/ VOLUME 81 JULY 14, 1977 NUMBER 14

JPCHAx

THE JOURNAL OF PHYSICAL CHEMISTRY

PUBLISHED BIWEEKLY BY THE AMERICAN CHEMICAL SOCIETY

THE JOURNAL OF

PHYSICAL CHEMISTRY

Published by the
AMERICAN CHEMICAL SOCIETY
BOOKS AND JOURNALS DIVISION
D. H. Michael Bowen, Director
Marjorie Laflin, Assistant to the Director

Editorial Department: Charles R. Bertsch, Head; Marianne C. Brogan, Associate Head; Celia B. McFarland, Joseph E. Yurvati, Assistant Editors
Magazine and Production Department: Bacil Guiley, Head
Research and Development Department: Seldon W. Terrant, Head

Advertising Office: Centcom, Ltd., 25 Sylvan Road South, Westport, Conn. 06880.

Published biweekly by the American Chemical Society at 20th and Northampton Sts., Easton, Pennsylvania 18042. Second class postage paid at Washington, D.C. and at additional mailing offices.

Editorial Information

Instructions for authors are printed in the first issue of each volume. Please conform to these instructions when submitting manuscripts.

Manuscripts for publication should be submitted to *The Journal of Physical Chemistry*, Department of Chemistry, University of Minnesota, Minneapolis, Minn. 55455. Correspondence regarding **accepted papers and proofs** should be directed to the Editorial Department at the ACS Easton address.

Page charges of $60.00 per page may be paid for papers published in this journal. Ability to pay does not affect acceptance or scheduling of papers.

Bulk reprints or photocopies of individual articles are available. For information write to Business Operations, Books and Journals Division at the ACS Washington address.

Requests for **permission to reprint** should be directed to Permissions, Books and Journals Division at the ACS Washington address. The American Chemical Society and its Editors assume no responsibility for the statements and opinions advanced by contributors.

Subscription and Business Information

1977 Subscription rates—including surface postage

	U.S.	PUAS	Canada, Foreign
Member	$24.00	$33.00	$34.00
Nonmember	96.00	105.00	106.00
Supplementary material	15.00	19.00	20.00

Air mail and air freight rates are available from Membership & Subscription Services, at the ACS Columbus address.

New and renewal subscriptions should be sent with payment to the Office of the Controller at the ACS Washington address. **Changes of address** must include both old and new addresses with ZIP code and a recent mailing label. Send all address changes to the ACS Columbus address. Please allow six weeks for change to become effective. **Claims for missing numbers** will not be allowed if loss was due to failure of notice of change of address to be received in the time specified: if claim is dated (a) North America—more than 90 days beyond issue date, (b) all other foreign—more than 1 year beyond issue date; or if the reason given is "missing from files". Hard copy claims are handled at the ACS Columbus address.

Microfiche subscriptions are available at the same rates hut are mailed first class to U.S. subscribers, air mail to the rest of the world. Direct all inquiries to Special Issues Sales, at the ACS Washington address or call (202) 872-4554. **Single issues** in hard copy and/or microfiche are available from Special Issues Sales at the ACS Washington address. Current year $4.75. Back issue rates available from Special Issues Sales. **Back volumes** are available in hard copy and/or microform. Write to Special Issues Sales at the ACS Washington address for further information. **Microfilm** editions of ACS periodical publications are available from volume 1 to the present. For further information, contact Special Issues Sales at the ACS Washington address. **Supplementary material** mentioned in the journal appears in the microfilm edition. Single copies may be ordered directly from Business Operations, Books and Journals Division, at the ACS Washington address.

	U.S.	PUAS, Canada	Other Foreign
Microfiche	$2.50	$3.00	$3.50
Photocopy			
1–7 pages	4.00	5.50	7.00
8–20 pages	5.00	6.50	8.00

Orders over 20 pages are available only on microfiche, 4 × 6 in., 24X, negative, silver halide. Orders must state photocopy or microfiche if both are available. Full bibliographic citation including names of all authors and prepayment are required. Prices are subject to change.

American Chemical Society
1155 16th Street, N.W.
Washington, D.C. 20036
(202) 872-4600

Member & Subscription Services
American Chemical Society
P.O. Box 3337
Columbus, Ohio 43210
(614) 421-7230

Editorial Department
American Chemical Society
20th and Northampton Sts.
Easton, Pennsylvania 18042
(215) 258-9111

Notice to Authors last printed in the issue of January 13, 1977

THE JOURNAL OF

PHYSICAL CHEMISTRY

Volume 81, Number 14 July 14, 1977

JPCHAx 81(14) 1343–1436 (1977)

ISSN 0022-3654

There is no supplementary material for this issue.

* In papers with more than one author, the asterisk indicates the name of the author to whom inquiries about the paper should be addressed.

AUTHOR INDEX

THE JOURNAL OF
PHYSICAL CHEMISTRY

VOLUME 81, NUMBER 14 JULY 14, 1977

Primary Products and Secondary Reactions in the Photodecomposition of Methyl Halides[1,2a]

G. A. Takacs[2b] and J. E. Willard*

Department of Chemistry, University of Wisconsin, Madison, Wisconsin 53706 (Received February 24, 1977)

Publication costs assisted by the U.S. Energy Research and Development Administration

CH_3I, CH_3Br, and CH_3Cl have been photolyzed at 184.9 nm and CH_3I at 253.7 nm, using CO, C_2H_4, C_2H_6, C_3H_8, C_3D_8, and CD_4 as scavengers to assist in the identification of the primary decomposition products. The quantum yield of methylene formation ($CH_3X + h\nu \rightarrow CH_2 + HX$) is less than $\sim 10^{-3}$ in all cases. Carbon–hydrogen bond rupture occurs with a quantum yield of $\sim 10^{-2}$ in the photolysis of CH_3I at 184.9 nm. Evidence is given on the relative effectiveness of CH_3I and hydrocarbons in thermalizing hot CH_3 radicals and on preferential abstraction from C–H bonds relative to C–D bonds by hot CH_3 radicals. Rupture of the carbon–halogen bond in CH_3Cl is the predominant path of photodecomposition, as earlier investigations (and the present work) show it to be in CH_3Br and CH_3I. The quantum yield of photosensitized CH_2 production by reaction of C_3H_8 with I_2 excited at 184.9 nm is shown to be $<10^{-3}$.

Introduction

When CH_3I absorbs at 253.7 or 184.9 nm, and when CH_3Br or CH_3Cl absorb at 184.9 nm, the transition is to an antibonding orbital localized on the C–X bond.[3] In each case, the absorbed energy is more than sufficient to cause decomposition of the methyl halide by any one of four paths:[2a]

$$CH_3X \rightarrow CH_3 + X \quad (1)$$

$$CH_3X \rightarrow CH_2X + H \quad (2)$$

$$CH_3X \rightarrow CH_2 + HX \quad (3)$$

$$CH_3X \rightarrow CHX + H_2 \quad (4)$$

In CH_3I[4] and CH_3Br[5] the quantum yield of path 1 is close to unity. However, evidence for H_2 production in the photolysis of CH_3I,[6a] HT formation in the photolysis of CH_2TI,[6b] and CH_2 formation in the photolysis of CH_3I[7] indicates some contribution by the other pathways, although this may be very small since the experiments were designed only to give qualitative evidence on products by sensitive tracer methods[6b,7] and no yields have been reported. Because of the inherent interest in the modes of rupture and because of the possibility that the methylenic fragments may be the precursors of chain lengthened products which have been observed in such systems, we have done experiments which set upper limits on the yields of CH_2 produced by activation of CH_3I at 253.7 nm and of CH_3I, CH_3Br, and CH_3Cl at 184.9 nm. Reactions with additives used in setting the limits include the following:

$$^1CH_2 + CO \rightarrow CH_2CO \quad (5)$$

$$^3CH_2 + CO \rightarrow CH_2CO \quad (6)$$

$$CH_2 + C_2H_4 \rightarrow c\text{-}C_3H_6 \quad (7)$$

$$\rightarrow C_3H_6 \quad (8)$$

$$^3CH_2 + C_3H_8 \rightarrow CH_3 + C_3H_7 \quad (9)$$

$$^1CH_2 + C_3H_8 \rightarrow C_4H_{10} \quad (10)$$

$$^1CH_2 + CD_4 \rightarrow CH_2DCD_3 \quad (11)$$

In addition to setting limits on the CH_2 yields, the investigation has provided information on H_2 and D_2 yields in CH_3I–C_3D_8 and CD_3I–C_3H_8 mixtures, including the relative importance of C–H (C–D) bond rupture and concerted H_2 (D_2) elimination. Knowledge of the prop-

erties of hot CH_3 radicals formed by the photolysis of CH_3I has been extended.

Some results in the literature which are of interest relative to the work reported here include the following: (1) Multiple fragmentation occurs in the vacuum UV photolysis of CH_3Cl in Ar and N_2 matrices at 14 K.[8] (2) Molecular rather than atomic elimination occurs in many other systems following various methods of excitation, e.g., H_2 from CH_4 at 123.6 nm,[9] HF from CH_3F at 147.0 nm,[10] other photon activated eliminations,[11] and decompositions activated by radical combination[12] and by nuclear recoil atoms.[13] Evidence had been obtained on the relative yields of the $^2P_{1/2}$ and $^2P_{3/2}$ states of iodine from the photolysis of CH_3I and other alkyl iodides.[14a-c] The lifetime of the excited states of CH_3I formed by 240–320-nm radiation is 7×10^{-14} s.[14d] About 12% of the energy in excess of the bond energy in the photodecomposition of CH_3I at 266.2 nm is present as vibrational energy.[14b]

Experimental[2] Section

Gaseous samples were photolyzed in a 10 cm long 22 mm i.d. cylindrical quartz cell with flat Suprasil end windows or in 9 mm i.d. Suprasil tubing. Each cell was connected through a graded seal and greaseless stopcock to a ground joint used for attachment to the vacuum line. After photolysis, the cells were cleaned with aqueous HF to remove brownish deposits which frequently formed on the windows.

Two Hanovia SC2537 low-pressure mercury arcs with Suprasil end windows irradiated the 22 mm i.d. cells simultaneously from both ends. About 1×10^{15} photons s^{-1} of 184.9-nm and 7.5×10^{15} photons s^{-1} of 253.7-nm radiation entered the cell when the lamps were 1 cm from the windows. The 9-mm i.d. vessels, irradiated in the center of a helical low pressure mercury arc, received $\sim 1 \times 10^{17}$ photons s^{-1} of 184.9 nm over an 11 cm length of the tubing.

For photolyses at 253.7 nm the radiation below 230.0 nm was cut out by a 2-mm thick Vycor filter, or by using a Vycor tube as the reaction cell with the spiral lamp. The Vycor transmitted ~75% of the 253.7-nm radiation. To remove 253.7 nm while transmitting 184.9 nm, an ozone filter[15a] with a transmittance of 50% at 184.9 nm and 0.1% at 253.7 nm was used with the spiral lamp. With the end-on lamps the 253.7-nm radiation was removed by γ-irradiated LiF filters[15b] which transmitted ~30% at 184.9 nm and <0.04% at 253.7 nm or by interference filters[15c] which transmitted ~24% at 184.9 and 0.09% at 253.7 nm. Since the lamp intensity at 253.7 nm is 7.5 times that at 184.9 nm, about 3% of the radiation transmitted by the interference filter is at 253.7 nm.

The radiation intensities incident on samples were determined by HBr actinometry at 184.9 nm[16] and HI actinometry at 253.7 nm.[15b] The optical densities were ≥2 for both the actinometers and samples. The decomposition of the actinometer gas was kept below 0.004 to preclude[16] error from the $H + X_2 \rightarrow HX + X$ reaction. The X_2 produced was determined spectrophotometrically using an extinction coefficient of 169 M^{-1} cm^{-1} for Br_2 at 420.0 nm[17] and of 578 M^{-1} cm^{-1} for I_2 at 500.0 nm.[18a]

Analyses for CH_2CO, H_2, HD, D_2, and deuterated alkanes were made with an AEI MS-10 mass spectrometer.[2a] Gas chromatography with a Poropak Q column was used for CH_4, C_2H_4, C_2H_6, C_3H_6, C_3H_8, c-C_3H_6, i-C_4H_{10}, and n-C_4H_{10}. A column of 20% SF 96 silicone oil on Chromosorb P was used for hydrocarbons with higher boiling points and for alkyl iodides.[2a] Product identification was assisted by plots of product emergence time vs. boiling point for known compounds. For each product studied quantitatively, a calibration curve of peak area vs. amount injected was determined.

TABLE I: Upper Limits of CH_2 from CH_3I at 253.7 nm and from CH_3I, CH_3Br, and CH_3Cl at 184.9 nm

System	CH_2 species	Φ (upper limit)
CH_3I-C_3H_8[a]	$^1CH_2$	4×10^{-6}
CH_3I-C_2H_4[a]	CH_2	5×10^{-5}
CH_3Br-C_2H_4	CH_2	1×10^{-3}
CH_3Cl-CO	$^1CH_2$	1×10^{-2}
CH_3Cl-CO	$^3CH_2$	6×10^{-3}
CH_3Cl-C_3H_8	$^1CH_2$	1×10^{-3}
CH_3I-C_2H_4	CH_2	2×10^{-2}
CH_3I-C_2H_4-O_2	$^1CH_2$	2×10^{-3}
CH_3I-CO	$^3CH_2$	2×10^{-3}
CH_3I-CO	$^1CH_2$	2×10^{-3}
CH_3I-CD_4	$^1CH_2$	2×10^{-2}
CH_3I-C_3H_8	$^1CH_2$	8×10^{-2}
CH_3I-C_3H_8-O_2	$^1CH_2$	2×10^{-2}
CH_3I-C_2H_6	$^1CH_2$	8×10^{-2}
CH_3I-C_2H_6-O_2	$^1CH_2$	2×10^{-3}

[a] 253.7-nm photolysis, all others 184.9 nm.

Reaction mixtures were prepared by standard vacuum line techniques. A liquid nitrogen trap separated the line from the mercury diffusion pump and a column of silver powder separated it from the mercury manometer. Stopcocks and ground joints were greased with Kel-F 90 or Halocarbon grease, or greaseless stopcocks with Teflon plugs and Viton O-rings were used. Known pressures of condensible reagents were obtained from reservoirs cooled by slush baths at temperatures chosen to give the desired vapor pressures. Following filling of the reaction cell at such a pressure, the vapor was condensed in a corner of the cell with liquid nitrogen. Additional condensible reagents were then condensed from calibrated volumes. Noncondensible additives (CH_4, CO, O_2) were allowed to fill the cell to pressures measured on the manometer while the cell was at room temperature except for the tip in which the condensibles were held at 77 K.

Methyl chloride (Matheson 99.5% purity) was degassed at 77 K. Methyl bromide (Matheson 99.5% purity) was degassed at dry ice temperatures which raised the purity to 99.9%. Eastman methyl iodide was purified from the 0.05% C_2H_4 which it contained by degassing at dry ice temperature or by preparative gas chromatography. The CO, CH_4, and C_2H_4 used were all of ≥99.5% purity as listed by the manufacturer (Matheson) or determined by us. Cyclopropane (Baker) was listed as 99.0%. Analytical checks for contaminants were made on unirradiated reaction mixtures in parallel with all irradiated samples.

Results

Upper Limits on CH_2 Yields. Upper limits set on the quantum yields for CH_2 production by photolysis of CH_3I, CH_3Br, and CH_3Cl are given in Table I. These estimates are based on the amount of light absorbed by the methyl halides,[18b] the observed product yields, and the fraction of the CH_2 expected to react with the scavenger relative to the halide, assuming the rate constant ratios of Table II. The data from which the limits were derived, and their interpretation, are discussed below.

CH_3Br–C_2H_4 Experiments. Six mixtures of ~35 Torr of CH_3Br and 100 Torr of C_2H_4 were photolyzed for times up to 1000 min at an absorbed intensity of 184.9-nm radiation of 3×10^{14} photons s^{-1}. The principal hydrocarbon products were CH_4 and C_3H_8, with quantum yields of $\sim 1 \times 10^{-2}$ and 1×10^{-3}, respectively. Trace amounts of propylene and the absence of detectable cyclopropane set an upper limit of $\sim 1 \times 10^{-4}$ on their quantum yields and

TABLE II: Relative Rate Constants for Reaction of Methylene[a]

Rate constant data, 300 K	Ref
$k(CH_3Br)/k(C_2H_4) = 1.3$	25
$^3k(CO)/^3k(CH_3Cl) = 3$–5	12b
$^1k(CO)/^1k(CH_3Cl) = 0.1$	12b
$^1k_3(CH_3Cl)/^1k(CH_3Cl) \sim \frac{^1k_3(CO)\,^1k(CH_2CO)}{^1k(CH_2CO)\,^1k(CH_3Cl)} = 0.072$	12b
$\frac{^1k_3(CO)}{^1k(CO)} = \frac{^1k_3(CO)\,^1k(CH_2CO)}{^1k(CH_2CO)\,^1k(CO)} =$ $(0.1)(1/0.12) = 0.83$	12b,26
$^1k_3(C_3H_8) = {}^1k(C_3H_8)$	27
$^1k(CH_3Cl) = {}^1k(C_3H_8)$	*b*
$^1k(CH_3I) = {}^1k(CH_3Cl)$	*c*
$^3k(CH_3I) = {}^3k(CH_3Cl)$	*b*
$k(CH_3I)/k(C_2H_4) = k(CH_3Br)/k(C_2H_4) = 1.3$	c,25
$^1k(C_2H_6) = {}^1k(C_3H_8)$	*b*
$k(I_2)/k(O_2) = \sim 25$	28
$^1k(O_2)/^1k(C_3H_8) < 0.46$	27
$^1k(I_2)/^1k(C_3H_8) \sim \frac{k(I_2)\,^1k(O_2)}{k(O_2)\,^1k(C_3H_8)} = 11.5$	27,28
$^1k(CD_4)/^1k_3(CD_4) = 1.19$	*d*
S/D = 1 for CH_2DCD_3* at 78 Torr of CD_4	*d*

[a] $^1k(X)$ and $^3k(X)$ are the rate constants for the reactions of $^1CH_2$ and $^3CH_2$ with X, respectively. $k(X)$ makes no distinction between singlet and triplet CH_2 reacting with X. $^1k_3(X)$ is the rate constant for deactivation of $^1CH_2$ to $^3CH_2$ by collision with X. [b] Assumed. [c] Assumed. These assumptions give a rate constant for the reaction of singlet methylene with CH_3I lower than it really is because the reaction of singlet methylene with a halide is electrophilic in nature (ref 12b) and therefore should be faster with the iodide than the bromide or chloride atoms. [d] Estimated from data in ref 34a. Uncertainties are introduced by the secondary isotope effect and the dependence of the stabilization/decomposition ratio of CH_2DCD_3* on the CH_2 energy.[34b]

TABLE III: Quantum Yields of Products of Photolysis of CH_3Cl at 184.9 nm[a]

CH_3Cl, Torr	Cl_2, Torr	Quantum yields CH_4	C_2H_4	C_2H_6
54	0	0.79	2.4×10^{-3}	1.5×10^{-3}
64	1	0.83	*b*	*b*
96	8	0.81	2.1×10^{-3}	6.9×10^{-4}

[a] Full intensity of the two end-window lamps on end-window cell, absorbed 184.9-nm intensity = 1.3×10^{15} photons s^{-1}. [b] Not determined.

an upper limit of 1×10^{-3} for the yield of CH_2 from CH_3Br.

The propylene and C_3H_8 found may arise from sources other than CH_2, in which case the quantum yield of the latter is less than the upper limit noted. Photolysis of 100 Torr of C_2H_4 for 1110 min with an absorbed 184.9-nm intensity of 1.8×10^{14} photons s^{-1} gave C_3H_6 and C_3H_8 quantum yields of 3.5×10^{-4} and 2.1×10^{-3}, respectively, but no cyclopropane or methane (quantum yields $<10^{-4}$). Hot *n*-propyl radicals, formed from addition of hot methyl radicals to ethylene, can produce propylene by unimolecularly decomposing, by abstracting a Br atom from CH_3Br to form C_3H_7Br which unimolecularly decomposes, and by disproportionation with methyl radicals after collisional stabilization. Propylene may also be produced by reaction of methyl radicals with C_2H_3 formed by abstraction of H from C_2H_4 by hot methyl radicals.[2]

CH_3Cl–CO Experiments. Two samples of 60 Torr of CH_3Cl and 300 Torr of CO were photolyzed for 8 and 18 min at 184.9 nm with an absorbed intensity of 1.0×10^{17} photons s^{-1}. No CH_2CO was found in the products. An amount equal to 0.6% of the CH_4 formed would have been detectable. This sets an upper limit of 6×10^{-3} on the quantum yield of $^3CH_2$ and 1×10^{-2} on the quantum yield of $^1CH_2$, by reasoning from reactions 12, 5, 6, and 13–16 for their formation and consumption.

$$CH_3Cl \xrightarrow{h\nu} {}^1CH_2(^3CH_2) + HCl \quad (12)$$

$$^1CH_2(^3CH_2) + CH_3Cl \rightarrow CH_2Cl + CH_3 \quad (13)$$

$$^1CH_2 + M \rightarrow {}^3CH_2 + M \quad (14)$$

$$CH_2CO^* + M \rightarrow CH_2CO + M \quad (15)$$

$$CH_2CO^* \rightarrow CH_2 + CO \quad (16)$$

The experiments were done at pressures in excess of the minimum required for collisional stabilization (reaction 15) of ketene produced from methylene formed by photolysis of ketene,[12b,29] or $Hg(^3P_1)$ photosensitized decomposition of ketene.[30] The energy available to be partitioned between the CH_2 and HCl of reaction 12 is 64 kcal mol^{-1}, whereas that from the $Hg^3(P_1)$ reaction gives 33 kcal mol^{-1} to the products of ketene decomposition. If the higher energy leads to significantly higher ketene decomposition, the CH_2 formed would react, at lower energy, with CO to re-form ketene.

Quantum yields from the photolyses of CH_3Cl without additive and in the presence of Cl_2 are given in Table III.

CH_3Cl–C_3H_8 Experiments. Photolysis of CH_3Cl at 184.9 nm in the presence of C_3H_8 produces CH_4 as the predominant hydrocarbon product, with much smaller amounts of C_2H_4, C_2H_6, and the isomeric butanes (Table IV).

The butanes may be formed by one or more of the following processes: (a) insertion of $^1CH_2$ into a C–H bond; (b) stabilization of the combination of CH_3 and C_3H_7 radicals; or (c) conceivably substitution of hot CH_3 for H in C_3H_8. The C_4H_{10} yields in the presence of Cl_2, which scavenges thermal radicals, place a limit of $\sim 4 \times 10^{-4}$ on the C_4H_{10} yield due to $^1CH_2$ insertion. The pressures used were within the region giving complete stabilization of hot butane molecules formed from $^1CH_2$ insertion into C_3H_8.[31] From these data, 10^{-3} is set as an upper limit for the primary quantum yield for the production of singlet methylene from photolysis of CH_3Cl at 184.9 nm.

CH_3I–CO Experiments. No ketene was found from the photolyses of CH_3I–CO mixtures with CO pressures from 51 to 346 Torr, CH_3I pressures from 9 to 19 Torr, absorbed 184.9-nm intensities from 1×10^{14} to 1×10^{17} photons s^{-1}, and total absorption of 2×10^{18} to 3×10^{20} photons.

TABLE IV: Quantum Yields from the Photolysis of CH_3Cl–C_3H_8 Mixtures at 184.9 nm

CH_3Cl, Torr	C_3H_8, Torr	Scavenger, Torr	Photolysis[a] time, min	Quantum yields × 10^3 CH_4	C_2H_4	C_2H_6	i-C_4H_{10}	n-C_4H_{10}
41	113	0	180	600	4	3	2	0.3
39	124	8 Cl_2	180	*b*	*b*	*b*	0.1	0.3
40	123	0	240	*b*	*b*	*b*	1.5	0.2
40	125	2.7 NO	240	200	1.8	2	1	0.2

[a] Full intensity of two end-window lamps on end-window cell, absorbed 184.9-nm intensity = 1.3×10^{15} photons s^{-1}. [b] Not determined.

TABLE V: Quantum Yields from the Photolysis of CH_3I-C_2H_4 Mixtures at 184.9 nm[a]

CH_3I, Torr	C_2H_4, Torr	O_2, Torr	Quantum yield × 10^3		
			C_3H_6	C_3H_6	c-C_3H_6
0	100	0	0.35	2.1	0
8.6	100	0	1.6	7	2.5
8.6	101	0	1.3	7.6	2.3
8.8	100	2.5	0.33	2	0.3

[a] Photolysis with two end-window lamps for 1110 min with absorbed intensities from 1.3×10^{14} to 1.8×10^{14} photons s^{-1}.

Ketene would have been observed if present at ≥2% of the CH_4 produced. The competing reactions for any CH_2 formed would be (5) and (6), competing with the CH_3I analogue of (13). From consideration of the rate constants and reactant ratios, it may be concluded that the quantum yields of singlet and triplet methylene are both less than 2×10^{-3}. The estimate assumes that the quantum yield of CH_4 was ~0.08, as it was for eight samples of 8.6 Torr of CH_3I photolyzed with similar intensities and doses.

CH_3I-C_2H_4 Experiments. Gas chromatographic analysis of CH_3I-C_2H_4 mixtures following photolysis at 184.9 nm showed five products, using the Porapak Q column: propylene, propane, cyclopropane, methane, and a peak in the region of the butanes. Table V gives typical quantum yields for the C_3 hydrocarbons, based on the total light absorbed by the mixtures.

The quantum yield of propylene from the photolysis of pure C_2H_4 is 3.5×10^{-4}. Assuming this yield is the same in the CH_3I-C_2H_4 mixtures which give a total propylene yield of $\sim 1.5 \times 10^{-3}$ and taking account of the different extinction coefficients and pressures of the CH_3I and C_2H_4, the propylene quantum yield due to absorption by CH_3I is determined to be 6.4×10^{-3}. The total propylene plus cyclopropane quantum yield due to CH_3I absorption is similarly determined to be $\sim 1.9 \times 10^{-2}$. If this yield were all due to CH_2 produced from CH_3I, the CH_2 quantum yield would be 2×10^{-2} (after correcting for loss of CH_2 by reaction with CH_3I and assuming the ratio of the rate constants for the reaction of CH_2 with CH_3I and C_2H_4 is the same as the ratio for reaction with CH_3Br and C_2H_4 (Table II)).

The total propylene yield sets a high limit on the CH_2 yield since the unimolecular decomposition of hot *n*-C_3H_7 radicals, formed by the addition of hot CH_3 to C_2H_4, is an important source of propylene in the pressure range studied.[2]

The presence of 2.5 mol % O_2 in CH_3I-C_2H_4 mixtures caused a large decrease in the C_3H_6 and c-C_3H_6 quantum yields (Table V). Singlet methylene reactions are relatively unaffected by the addition of O_2, while reactions involving $^3CH_2$ are greatly diminished.[32] The quantum yields of c-C_3H_6 (3×10^{-4}) and C_3H_6 (3×10^{-4}) formed in the presence of O_2 allow an estimate of 2×10^{-3} as the upper limit for the quantum yield of $^1CH_2$ produced from CH_3I.

Rowland and co-workers[7] have reported the formation of cyclopropane and propylene from the photolysis of CH_3I-C_2H_4 mixtures, but with no estimate of quantum yields.

CH_3I-Alkane Experiments at 184.9 nm. The quantum yields at 184.9 nm of propane from CH_3I-C_2H_6 mixtures (Table VI) and of butane from CH_3I-C_3H_8 mixtures (Table VII) in the absence of radical scavengers are ~0.04. These yields are greatly reduced by a few per cent of O_2 or NO which are used to distinguish between products formed by $^1CH_2$ and those originating from $^3CH_2$ or other radical precursors.[33] The CH_3I-C_2H_6 experiments in the absence of O_2 and with 5.8 Torr of O_2 set upper limits of 0.08 and 2×10^{-3} respectively for the quantum yield of $^1CH_2$. For the CH_3I-C_3H_8 experiments, the upper limit is 0.08, in the

TABLE VI: Quantum Yields from the Photolysis of CH_3I-C_2H_6 Mixtures at 184.9 nm[a]

CH_3I, Torr	C_2H_6, Torr	O_2, Torr	Final I_2, Torr	Quantum yields		
				CH_4	C_3H_8 × 10^3	I_2
8.5	129	0	0	0.9	43	0
8.6	131	1.4	0.10	0.1	9.4	0.068
8.5	130	2.8	0.16	0.091	3.9	0.098
8.8	129	5.8	0.20	0.086	0.73	0.13
8.5	133	30.8	0.36[b]	*c*	*c*	0.26[b]

[a] Absorbed 184.9-nm intensities: 1.5×10^{14} to 1.9×10^{14} photons s^{-1}. LiF filters used with end-window lamps and cell. Photolysis time 240 min. [b] The I_2 yield is a lower limit because some I_2 may have been left in the solid phase. If an average I_2 pressure during this experiment is taken as 0.2 Torr, then the quantum yield of I_2 due to radiation absorbed by CH_3I is calculated to be 0.51. [c] Not determined.

TABLE VII: Butane Quantum Yields from the Photolysis of CH_3I-C_3H_8 Mixtures at 184.9 nm[a]

C_3H_8, Torr	Scavenger, Torr	Final I_2, Torr	Quantum yields		
			Butane × 10^3	I_2 × 10^2	*i*-Bu/*n*-Bu
131	0	0.006	39.2	0.52	0.30
133	0	0.013	40.4	0.61	0.35
170	0	0.015	31.3	0.68	0.34
85	0	0.011	37.9	0.64	0.33
65	0	0.016	38.1	0.88	0.37
50	0	0.019	35.0	1.0	0.38
202	0	0.024	32.4	1.1	0.33
85	O_2,2.5	0.20	0	8.0	0
124	O_2,0.7	0.068	7.8	2.4	0.23
133	O_2,0.35	0.045	17.1	1.5	0.32
134	O_2,0.55	0.074	11.1	2.8	0.28
152	0	0.06	*b*	0.70	0.35
149	0	0.10	*b*	0.67	0.42
151	NO,2.7	*b*	Trace	*b*	0.46

[a] Using 8.7 Torr of CH_3I, 184.9-nm light intensities from end-window lamps with LiF filters of $(1.5 \pm 0.5) \times 10^{14}$ photons s^{-1} for first 11 experiments and $(3.2 \pm 0.4) \times 10^{14}$ for remainder. Photolysis times for the last three experiments were 625, 1000, and 1000 min, respectively, the rest were 300–400 min. [b] Not determined.

TABLE VIII: Quantum Yields from the Photolysis of CH_3I-C_3H_8 Mixtures at 253.7 nm[a]

Photolysis time, min	Quantum yields[b] CH_4	$C_2H_6 \times 10^4$	$I_2 \times 10^4$	Butanes
80	0.031	2.1	*c*	*c*
200	0.027	1.1	7.1	*c*
420	0.032	0.6	8.2	$<4 \times 10^{-6}$

[a] End-window lamps with Vycor filters. 8.4 Torr of CH_3I; 130 Torr of C_3H_8. [b] Trace amounts of ethylene also observed. [c] Below detectability limit.

absence of O_2, and 0.02 in the presence of 0.7 Torr of O_2. These values have been corrected for absorption of radiation by I_2.

The ratios CH_4/CH_3D and CD_3H/CD_4 for the CH_3I-C_3D_8 and CD_3I-C_3H_8 experiments (corrected to equal pressures of reactants) are 9 and 6, respectively, indicating significant isotope effects in the abstraction of an H (or D) atom by the hot methyl radicals produced from CH_3I by 184.9-nm radiation. Similarly, such hot methyl radicals produced in an equimolar mixture of CH_3I and CD_4 abstract preferentially from the C-H bonds relative to the C-D bonds, giving a CH_4/CH_3D ratio of 4.

The quantum yield of CH_2DCD_3 found for the 184.9-nm photolysis of CH_3I in CD_4 was $\sim 4 \times 10^{-3}$. Assuming this to all result from $^1CH_2$ insertion into CD_4, and correcting for the fraction of $^1CH_2$ converted to $^3CH_2$ by collision with CD_4 and the fraction of the CH_2DCD_3 which decomposes before collisional stabilization (see footnote *d*, Table II), an upper limit of 2×10^{-2} may be estimated for the quantum yield of $^1CH_2$.

CH_3I-Alkane Experiments at 253.7 nm. No cyclopropane ($\Phi < 5 \times 10^{-5}$) was found from the 253.7-nm photolysis of gaseous CH_3I-C_2H_4 mixtures and no butanes ($\Phi < 4 \times 10^{-6}$) from CH_3I-C_3H_8 mixtures (Table VIII), indicating that the yield of methylene from the photolysis of methyl iodide at this wavelength is very low.[2]

Hydrogen Production from CH_3I-C_3H_8 Systems. Photolyses at 184.9 nm of 8.6 Torr of CH_3I with 10 Torr of C_3D_8, 8.6 Torr of CD_3I with 11 Torr of C_3H_8, and 8.6 Torr of CH_3I with 11 Torr of C_3H_8 all yielded hydrogen, the ratios of the total hydrogen to total methane yield being 0.06, 0.09, and 0.10, respectively. The quantum yield for hydrogen formation is estimated to be ~ 0.01. The hydrogen distributions (H_2:HD:D_2) from the CH_3I-C_3D_8 and CD_3I-C_3H_8 mixtures were 2.7:6.2:1 and 3.3:7.8:1, respectively.

I_2-C_3H_8 Photolysis. I_2 molecules excited by 184.9-nm light in CH_4 initiate steps which produce C_2, C_3, and C_4 products in low quantum yields and such I_2^* molecules photosensitize HF elimination from CH_3F and CF_3H.[4,20,23] The possibility therefore had to be considered that I_2 formed in CH_3I-C_3H_8 mixtures might cause CH_2 formation. We have found no evidence for C_4H_{10} formation ($\Phi < 10^{-3}$) during 184.9-nm photolysis of I_2-C_3H_8 mixtures, indicating the absence of significant $^1CH_2$ formation.

Discussion

Methylene Yields. The results given in Table I indicate that the quantum yields of CH_2 from the 184.9-nm photolysis of CH_3I, CH_3Br, and CH_3Cl are less than $\sim 1 \times 10^{-3}$, and set an upper limit on the CH_2 yield from the 253.7-nm photolysis of CH_3I of 5×10^{-5}. Reactions of CH_2 cannot be a source of products in excess of these limits in photolyses of the methyl halides.

Products from CH_3Cl. The predominant process following absorption of 184.9-nm photons by CH_3Cl is rupture of the C-Cl bond, as indicated by the high CH_4 quantum yields with and without added hydrocarbons (Tables III and IV). Related work has shown that excited CH_2TCl^*[13a] and $CH_3{}^{38}Cl^*$[13b] molecules formed by substitution into CH_3Cl of ^3H and ^{38}Cl recoiling from nuclear reactions also decompose primarily by C-Cl bond rupture. The tritium recoil reaction in CH_3Cl-C_2H_4 mixtures gave little cyclopropane and propylene-*t* indicating little decomposition of CH_2TCl^* to give CH_2.[13a] The production of ClO from the flash photolysis of CH_3Cl-O_2 mixtures has also been cited as evidence for the $CH_3Cl \rightarrow CH_3 + Cl$ process.[35]

Methane formation from CH_3Cl must be due to abstraction of H from CH_3Cl by hot methyl radicals formed by the primary dissociation and to the reaction of thermal methyl radicals with HCl formed by abstraction of H atoms by Cl atoms. Reported activation energies for abstraction of H from CH_3Cl and HCl by methyl radicals are 9.4 and 2.3 kcal mol^{-1}, respectively;[36] for abstraction of H from CH_3Cl and C_3H_8 by Cl, they are 3.1,[37] 0.98 ± 0.13[38] (primary H), and 0.66 ± 0.13[38] (secondary H), respectively.

The rupture of CH_3-Cl bonds by 184.9-nm radiation results in 70.9 and 68.4 kcal mol^{-1} partitioned between the methyl radical and the chlorine atom in the $^2P_{3/2}$ and $^2P_{1/2}$ states, respectively.[2] Both states have been observed in photolyses of HCl, Cl_2, CCl_4, and CF_3Cl.[39] If 70.9 kcal mol^{-1} goes into translational energy of the $CH_3 + Cl$, the energy of the Cl atom is 20.5 kcal mol^{-1}. It is unlikely that the $Cl + CH_3Cl \rightarrow CH_3 + Cl_2$ reaction, for which an activation energy of 25 kcal mol^{-1} has been reported,[37] plays a significant role in the CH_3Cl system.

The ethane and ethylene formed in the 184.9-nm photolysis of CH_3Cl and CH_3Cl-C_3H_8 mixtures must result from the combination of $CH_3 + CH_3$ and $CH_3 + CH_2Cl$ to form excited ethane and ethyl chloride molecules. The hot C_2H_5Cl formed has ~ 91 kcal mol^{-1} excess vibrational energy, well above the critical energy of 55 kcal mol^{-1} for HCl elimination.[12b,40] The rate constant for HCl elimination is equivalent to the collisional frequency at 300 Torr of CH_3Cl.[41] In the experiments of Tables II and III, the majority of the hot C_2H_5Cl must have dissociated to give ethylene, with 1,2 elimination favored.[13a] The rates of dissociation of the hot ethane to $2CH_3$ and stabilization are equal at 240 Torr.[33] Hot 1,2-dichloroethane, formed by combination of two chloromethyl radicals, undergoes unimolecular HCl elimination with a rate constant equal to the collisional frequency at 16 Torr[12b,42] and therefore would be nearly completely stabilized at the pressures used. No attempt was made to detect this product.

CH_3Br-C_2H_4 Experiments. The low yields of hydrocarbons in the 184.9-nm photolyses of CH_3Br-C_2H_4 mixtures ($\Phi_{CH_4} = 1 \times 10^{-2}$, $\Phi_{C_3H_8} = 1 \times 10^{-3}$) indicate that most of the CH_3 radicals formed react with bromine-containing radicals or initiate polymer chains by addition to C_2H_4 (solid deposits were formed). Φ_{CH_3} is ~ 1.[5] C-Br rupture also predominates in excited CH_2TBr formed by tritium recoil atoms.[43] The CH_4 observed in the photolysis must result from abstraction of H from CH_3Br and C_2H_4 by hot CH_3. The reported activation energies for these reactions are 10.1 and 10 kcal mol^{-1}, respectively.[36] The CH_3 radicals from 184.9-nm photolysis of CH_3Br are formed with 72 or 63 kcal mol^{-1} of translational energy accompanying formation of $^2P_{3/2}$ and $^2P_{1/2}$ bromine atoms, respectively, if none of the energy of the photon enters vibrational modes. Hot CH_3 radicals also add to C_2H_4 to form excited n-C_3H_7,[2] the rate constant ratio[44] for abstraction relative to addition being 0.1.

The hot bromine atoms from the photolysis of CH_3Br in C_2H_4 may abstract H from CH_3Br and C_2H_4 and may

initiate chain reactions[45] by addition to C_2H_4 before or after thermalization. Only ground state ($^2P_{3/2}$) Br atoms have been observed from CH_3Br by kinetic spectroscopy, but CH_3Br has been shown to quench $^2P_{1/2}$ Br atoms from the photolysis of CF_3Br.[46]

CH_4 Yields from CH_3I and CH_3I Mixtures at 253.7 nm. The quantum yield for CH_4 production from the photolysis of 8.6 Torr of CH_3I at 253.7 nm is tenfold higher in the presence of 130 Torr of C_3H_8 (Table VIII) than in pure[4] CH_3I. This difference must be due to a higher probability per collision for abstraction of an H atom from C_3H_8 by hot CH_3 than from CH_3I. Similar results have been reported by Doepker and Ausloos[47] with CD_3I with and without $CH_3CD_2CH_3$ or $CD_3CH_2CD_3$ as additives. They report a 3.6-fold higher probability for abstraction of secondary hydrogen atoms than primary hydrogen atoms. Thermalization of hot CH_3 radicals by CH_3I may occur both by deactivation on collision without reaction $CH_3^* + CH_3I \rightarrow CH_3 + CH_3I$ and, quite possibly, by the iodine exchange reaction $CH_3^* + CH_3I \rightarrow CH_3I + CH_3$. Whittle[48] and Fox[49] have shown that thermalized CF_3 radicals abstract an I atom from methyl iodide about 10^2 times faster than an H atom from methyl iodide, and Henderson[50] found that the relative reactivities of hot methyl radicals from the 253.7-nm photolysis of CH_3I for abstraction of H and Cl from chlorinated hydrocarbons decrease with increasing thermal activation energy. If hot methyl radical abstract with the same ratio as thermalized CF_3 radicals, the yield for thermalization by the exchange reaction would be about 0.3, compared to the methane quantum yield of 3×10^{-3} found in pure CH_3I.

In contrast to our results in the gas phase, which show no evidence of cyclopropane, and hence of CH_2 production in the 253.7-nm photolysis of CH_3I–C_2H_4 mixtures, cyclopropane is produced in similar photolyses in the solid state.[51] Speculatively, this may be ascribed to reaction of C_2H_4 with CH_2 formed by disproportionation in the parent cage ($CH_3 + I \rightarrow CH_3I^* \rightarrow CH_2 + HI$) or to a concerted reaction of CH_3I^* with C_2H_4.

CH_4 Yields, Isotope Effects, and Hydrogen Yields from CH_3I and CH_3I Mixtures at 184.9 nm. As at 253.7 nm, the CH_4 yields from the photolysis of CH_3I at 184.9 nm are much higher in the presence of hydrocarbon additives. For example, we have found $\Phi_{CH_4} = 0.9$ with C_3H_8, after correction for absorption by the I_2 generated during photolysis, compared to 0.08 in pure CH_3I. This may be attributed to the same factors discussed for the 253.7-nm activation. The yield of CH_4 from pure CH_3I is about an order of magnitude higher at 184.9 nm than at 253.7 nm, as found both in the earlier work[4] and the present work. Since the energy available in excess of that necessary for bond rupture is much in excess of the activation energy for H abstraction both with 184.9- and 253.7-nm activation (76.6 and 34.7 kcal mol^{-1}, respectively, for $I(^2P_{1/2})$ production), it appears that the difference in yields must result from a difference in distribution of the energy between translational and internal. Photofragment spectroscopy studies[14b] of CH_3I dissociation at 266.2 nm have shown that the energy given the CH_3 radicals is primarily translational and moderation studies[4,52] on the radicals produced at 253.7 nm likewise indicate that their energy is primarily translational. Further evidence for a difference in vibrational–translational energy distribution of the CH_3 produced at 184.9 and 253.7 nm is our evidence for an isotope effect on the methane yields from photolysis of CH_3I–C_3D_8 and CD_3I–C_3H_8 mixtures at 184.9 nm as contrasted to the absence[48] of such an effect at 253.7 nm. Similarly, translationally hot CF_3 radicals produced by photolysis of CF_3I at 253.7 nm show only minor isotope effects on H abstraction[53] while vibrationally hot CF_3 from photolysis of CF_3Br at 184.9 nm abstract H atoms from CH_3CD_3 and CH_2D_2 5.3 times more readily than D atoms.[54]

The H_2:HD:D_2 distributions of 2.7:6.2:1 and 3.3:7.8:1 from the 184.9-nm photolysis of CH_3I–C_3D_8 and CD_3I–C_3H_8 mixtures requires that a major portion of the hydrogen results from C–H or C–D bond rupture in the photolytic act, followed by H or D abstraction by the ejected H or D atom. Hydrogen has been observed as a product of the photolysis of CH_3I at 184.9 nm by Martin,[6a] and subsequently Beverly and Martin[6c] found a value of 0.06 for the H_2/CH_4 ratio from the photolysis. Molecular elimination of H_2 has been reported.[6b] The ratios of total hydrogen to total methane yields found in our studies were 0.10, 0.06, and 0.09 for CH_3I–C_3H_8, CH_3I–C_3D_8, and CD_3I–C_3H_8 mixtures, respectively. The isotope effects preclude estimation of a quantum yield for molecular hydrogen elimination from our data, other than that it is less than the yield of C–H bond rupture by 184.9-nm radiation.

Production of D_2 in the CH_3I–C_3D_8 and H_2 in the CD_3I–C_3H_8 mixtures was unexpected. The most probable mechanism appears to be replacement of a hydrogen atom of propane by a hot methyl radical followed by hydrogen abstraction by the displaced atom. Evidence for such replacement reactions has been reported,[54] and questioned.[7]

Rationale for Differences in Methane Yields from Photolyses of CH_3Cl, CH_3Br, and CH_3I. The exothermicities for the 184.9-nm photolyses of CH_3I, CH_3Br, and CH_3Cl producing $^2P_{1/2}$ halogen atoms are not far different (76.6, 74.9, and 68.4 kcal mol^{-1}, respectively), yet the methane quantum yields are 0.08 ± 0.02, 0.020 ± 0.003,[5] and 0.81, respectively. The activation energies for the abstraction of an H from the methyl halides by a thermal methyl radical are all about 10 kcal mol^{-1}.[36] The activation energy for the abstraction of a Cl atom from CH_3Cl by CF_3 is ≥ 6 kcal mol^{-1} more than the activation energy for abstraction of an H atom from CH_3Cl.[49] For CH_3I and CH_3Br, the activation energy for the abstraction of the halogen atom is lower than the activation energy for hydrogen abstraction.[49] The same trend in reaction probabilities for abstraction of halogen and hydrogen from CH_3X by hot CH_3 is expected. Therefore, the lower methane quantum yield for the photolyses of CH_3I and CH_3Br than for the photolysis of CH_3Cl at 184.9 nm may result partially from a greater percentage of hot methyl radicals abstracting a halogen atom, and replacing a hot methyl radical with a thermal methyl radical. In the absence of additives, thermal methyl radicals must react primarily with each other at the onset of photolysis in all three media. As illumination proceeds, they must react with the I_2, HBr, and HCl products.

References and Notes

(1) This work has been supported in part by the U.S. Energy Research and Development Administration under Contract No. AT(1101)-1715 and by the W. F. Vilas Trust of the University of Wisconsin.
(2) (a) Further details of this work are given in the Ph.D. Thesis of G. A. Takacs, University of Wisconsin—Madison, 1970; (b) Present address, Department of Chemistry, Rochester Institute of Technology, Rochester, N.Y. 14623.
(3) (a) G. W. King and A. W. Richardson, *J. Mol. Spectrosc.*, **21**, 339, 353 (1966); (b) M. Ito, P. C. Huang, and E. M. Kosower, *Trans. Faraday Soc.*, **57**, 1662 (1961).
(4) G. M. Harris and J. E. Willard, *J. Am. Chem. Soc.*, **76**, 4678 (1954).
(5) P. C. Kobrinsky and R. M. Martin, *J. Chem. Phys.*, **48**, 5728 (1968).
(6) (a) R. M. Martin, Ph.D. Thesis, University of Wisconsin—Madison, 1964; (b) C. Tsao and J. W. Root, *J. Phys. Chem.*, **76**, 308 (1972); (c) G. Beverly and R. M. Martin, private communication.
(7) C. C. Chou, P. Angelberger, and F. S. Rowland, *J. Phys. Chem.*, **75**, 2536 (1971).

(8) M. E. Jacox and D. E. Milligan, *J. Chem. Phys.*, **53**, 2688 (1970).
(9) A. H. Laufer and J. R. McNesby, *J. Chem. Phys.*, **49**, 2272 (1968).
(10) E. Tschuikow-Roux and S. Kodama, *J. Chem. Phys.*, **50**, 5297 (1969).
(11) (a) M. J. Berry, *J. Chem. Phys.*, **61**, 3114 (1974); (b) H. Okabe and J. R. McNesby, *ibid.*, **34**, 668 (1961).
(12) (a) K. C. Kim and D. W. Setser, *J. Phys. Chem.*, **78**, 2166 (1974); (b) W. G. Clark, D. W. Setser, and E. E. Siefert, *ibid.*, **74**, 1670 (1970).
(13) (a) Y.-N. Tang and F. S. Rowland, *J. Am. Chem. Soc.*, **90**, 570, 574 (1968); (b) C. M. Wai and F. S. Rowland, *ibid.*, **90**, 3638 (1968); (c) Y.-N. Tang, W. S. Smith, J. L. Williams, K. Lowery, and F. S. Rowland, *J. Phys. Chem.*, **75**, 44 (1971); (d) A. Hosaka and F. S. Rowland, *ibid.*, **75**, 3781 (1971).
(14) (a) T. Donohue and J. R. Wiesenfeld, *J. Chem. Phys.*, **63**, 3130 (1975); (b) S. J. Riley and K. R. Wilson, *Faraday Discuss., Chem. Soc.*, **53**, 132 (1972); (c) R. J. Donovan and J. Husain, *Nature (London)*, **209**, 609 (1966); (d) M. Dzvonik, S. Yang, and B. Bersohn, *J. Chem. Phys.*, **61**, 4408 (1974).
(15) (a) L. C. Glasgow and J. E. Willard, *J. Phys. Chem.*, **74**, 4290 (1970); (b) R. M. Martin and J. E. Willard, *J. Chem. Phys.*, **40**, 2999 (1964); (c) D. J. Schroeder, *J. Opt. Soc. Am.*, **52**, 380 (1962).
(16) R. A. Fass, *J. Phys. Chem.*, **74**, 984 (1970).
(17) A. A. Passchier, J. D. Christian, and N. W. Gregory, *J. Phys. Chem.*, **71**, 937 (1967).
(18) (a) R. L. Strong and J. E. Willard, *J. Am. Chem. Soc.*, **79**, 2098 (1975). (b) The extinction coefficients used in M^{-1} cm^{-1} (with the reference number in parentheses) are: CH_3I, 380 at 253.7 nm (19) and 220 at 184.9 nm (20); C_2H_4, 0 at 253.7 nm and 80 at 184.9 nm (21); CH_3Br, 70, (this value and all the values below are at 184.9 nm) (5); CH_3Cl, 60 (2); CO, C_2H_6, C_3H_8, all 0 (22); I_2, 1×10^4 (23); Cl_2, 0 (24), NO 90 (22); O_2, 2 (22).
(19) D. Porret and C. F. Goodeve, *Proc. R. Soc. London, Ser. A*, **165**, 31 (1938).
(20) T. A. Gover and J. E. Willard, *J. Am. Chem. Soc.*, **82**, 3816 (1960).
(21) L. C. Glasgow and P. Potzinger, *J. Phys. Chem.*, **76**, 138 (1972).
(22) J. G. Calvert and J. N. Pitts, Jr., "Photochemistry", Wiley, New York, N.Y., 1966.
(23) L. C. Glasgow and J. E. Willard, *J. Phys. Chem.*, **77**, 1585 (1973).
(24) G. O. Wood and J. M. White, *J. Chem. Phys.*, **52**, 2613 (1970).
(25) R. L. Johnson and D. W. Setser, *J. Phys. Chem.*, **71**, 4366 (1967).
(26) R. A. Cox and K. F. Preston, *Can. J. Chem.*, **47**, 3345 (1969).
(27) R. D. Koob, *J. Phys. Chem.*, **73**, 3168 (1969).
(28) R. A. Gregory and D. W. C. Style, *Trans. Faraday Soc.*, **32**, 724 (1936).
(29) R. A. Cox and K. F. Preston, *Can. J. Chem.*, **47**, 3345 (1969).
(30) R. A. Cox and R. J. Cvetanovic, *J. Phys. Chem.*, **72**, 2236 (1968).
(31) G. Z. Whitten and B. S. Rabinovitch, *J. Phys. Chem.*, **69**, 4348 (1965).
(32) T. W. Eder and R. W. Carr, Jr., *J. Phys. Chem.*, **73**, 2074 (1969).
(33) M. L. Halberstadt and J. R. McNesby, *J. Am. Chem. Soc.*, **89**, 3417 (1967).
(34) (a) W. Braun, A. M. Bass, and M. Pilling, *J. Chem. Phys.*, **52**, 5131 (1970); (b) K. Shibuya, K. Obi, and I. Tanaka, *Bull. Chem. Soc. Jpn.*, **49**, 2178 (1976).
(35) J. P. Simons and A. J. Yarwood, unpublished data, quoted in J. R. Majer and J. P. Simons, *Adv. Photochem.*, **2**, 137 (1964).
(36) A. F. Trotman-Dickenson and G. S. Milne, "Tables of Bimolecular Gas Reactions", IUSRDS-NBS No. 9, U.S. Government Printing Office, Washington, D.C., 1967.
(37) G. Chiltz, P. Goldfinger, G. Huybrecht, G. Martens, and G. Verbeke, *Chem. Rev.*, **63**, 355 (1963).
(38) G. C. Fettis and J. H. Knox, *Prog. React. Kinet.*, **2**, 1 (1964).
(39) R. J. Donovan, D. Husain, A. M. Bass, W. Braun, and D. D. Davis, *J. Chem. Phys.*, **50**, 4115 (1969).
(40) K. Dees and D. W. Setser, *J. Chem. Phys.*, **49**, 1193 (1968).
(41) W. G. Clark, D. W. Setser, and K. Dees, *J. Am. Chem. Soc.*, **93**, 5328 (1971).
(42) D. W. Setser and E. E. Siefert, *J. Phys. Chem.*, **57**, 3613 (1972).
(43) F. S. Rowland, E. K. C. Lee, and Y.-N. Tang, *J. Phys. Chem.*, **73**, 4024 (1969).
(44) B. G. Dzantiev, S. T. Kozlov, Al. N. Mushkaev, and A. P. Shvedchikov, *High Energy Chem. (Engl. Trans.)*, **3**, 32 (1969).
(45) (a) R. J. Field and P. I. Abell, *Trans. Faraday Soc.*, **65**, 743 (1969); (b) P. I. Abell, chapter in "Free Radicals", Vol. 2, J. K. Kochi, Ed., Wiley-Interscience, 1973, p 63; (c) P. I. Abell, *Trans. Faraday Soc.*, **60**, 2214 (1964).
(46) R. J. Donovan and D. Husain, *Trans. Faraday Soc.*, **62**, 2643 (1966).
(47) R. D. Doepker and P. Ausloos, *J. Chem. Phys.*, **41**, 1865 (1964).
(48) W. G. Alcock and E. Whittle, *Trans. Faraday Soc.*, **61**, 244 (1965).
(49) R. J. Fox, F. W. Evans, and M. Swarz, *Trans. Faraday Soc.*, **57**, 1915 (1961).
(50) D. J. Henderson, Ph.D. Thesis, University of Wisconsin—Madison, 1968.
(51) (a) R. E. Rebbert and P. Ausloos, *J. Chem. Phys.*, **48**, 306 (1968); (b) J. H. Purnell, *Acta Chim. Acad. Sci. Hung.*, **51**, 175 (1967).
(52) J. K. Rice and F. K. Truby, *Chem. Phys. Lett.*, **19**, 440 (1973).
(53) R. A. Fass and J. E. Willard, *J. Chem. Phys.*, **52**, 1874 (1970).
(54) (a) J. Saunders and D. S. Urch, *Chem. Phys. Lett.*, **8**, 227 (1971); (b) J. W. Root and G. W. Mutch, Abstracts, 160th National Meeting of the American Chemical Society, Chicago, Ill., Sept, 1970.

Photolysis Mechanism of Aqueous Tryptophan[1]

J. F. Baugher and L. I. Grossweiner*

Biophysics Laboratory, Department of Physics, Illinois Institute of Technology, Chicago, Illinois 60616 *(Received July 14, 1976; Revised Manuscript Received May 3, 1977)*

Publication costs assisted by the U.S. Energy Research and Development Administration and the National Institutes of Health

Flash photolysis experiments indicate that monophotonic photoionization is the principal initial photolysis act in aqueous tryptophan under high intensity, 265-nm laser excitation, leading to the Trp^+ radical cation (λ_{max} 580 nm) with quantum yield 0.12 ± 0.01 and e_{aq}^- with quantum yield 0.10 ± 0.01 from pH 4 to 8. The neutral Trp radical (λ_{max} 510 nm) is formed by deprotonation with rate constant 1.5×10^6 s^{-1}. The disappearance of e_{aq}^- follows a complex decay inconsistent with homogeneous kinetics. The results are in agreement with a recombination model in which the electron diffuses through the medium as a quasi-free entity, during which period back reactions with the original radical, or electrons and radicals generated in nearby pairs, compete with scavenging by tryptophan or added solutes. The well-established result that Trp yield observed after electron decay is not enhanced by oxygen or other e_{aq}^- scavengers is attributed to the formation of an unstable intermediate product of the electron–radical back reaction which subsequently oxidizes additional tryptophan to Trp.

Introduction

Tryptophan (Trp) is a major chromophore in most proteins and has been the subject of numerous investigations of its electronic and photochemical properties.[2] Previous flash photolysis studies have shown that the initial products when aqueous Trp is irradiated in the 280-nm band are the triplet state ^3Trp (λ_{max} 460 nm), the neutral radical oxidation product Trp (λ_{max} 510 nm), and the radical cation Trp^+ (λ_{max} 580 nm).[3] The same radicals are formed by ionizing radiation when anion radicals such as Br_2^- or $(CNS)_2^-$ react with aqueous Trp.[4,5] The previous work has shown also that formation of the Trp radical in

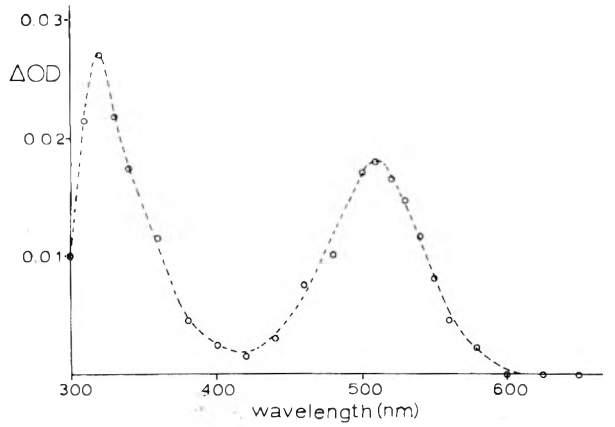

Figure 1. Transient absorption of Trp radical from 265-nm laser photolysis of 350 μM Trp at pH 11.3 (KOH), 0.2-μs time delay (O_2 saturated).

near-neutral solutions is accompanied by the hydrated electron e_{aq}^-.[6,7] In a recent laser flash investigation it was found that e_{aq}^- from Trp (and also *N*-methyltryptophan, tyrosine, I^-, and $Fe(CN)_6^{4-}$) disappears more rapidly than predicted by homogeneous reactions, with an approximately exponential initial decay stage at the same activation energy as the "inverse viscosity" of water.[8] A weakly bound complex between the electron and radical was postulated, in which the back reaction competes with separation into free species. The "loose complex" model was modified in a subsequent investigation proposing a new decay mechanism where the electron migrates a considerable distance from the radical, during which time it may react with the original radical, electrons, or radicals from other pairs or scavengers including the Trp solute.[9] The analysis led to a decay law based on random walk theory which is applied in the present work. However, *any* decay mechanism postulating electron–radical back reactions is faced with a surprising experimental result: the Trp yield in the presence of electron scavengers such as O_2 or N_2O is about the same or lower than in N_2.[3,8,10,17-19] By comparison, in the case of I^- photolysis the yield of I_2^-[9] and the permanent products[11,12] are markedly enhanced by electron scavenging. This paper constitutes an extension of ref 8 in which the analysis of ref 9 is applied to the Trp case.

Experimental Section

The flash photolysis measurements were made with a 150-MW Nd-glass laser system (Holobeam Model 631) with Pockel's cell Q-switching providing a 17-ns pulse at 265 nm after doubling with CDA and quadrupling with ADP crystals. The transient absorptions were measured in a 1-cm quartz cuvette with photoelectric detection, as described in ref 8. The actinometry was based on electron ejection from $Fe(CN)_6^{4-}$ as monitored at 650 nm taking $\epsilon_{650}(e_{aq}^-) = 15\,400$ L/mol cm with $\phi_{e^-} = 0.52$ at 265 nm from Shirom and Stein.[13] The initial e_{aq}^- yield (extrapolated to the time of the laser pulse) from $Fe(CN)_6^{4-}$ saturates at high laser intensities (see Figure 5) and the quantum yields in this paper are based on the linear region. (This saturation led to high initial e_{aq}^- yields in ref 8.) The solutions were made with triply distilled water and Aldrich Chemical Co. L-(−)-tryptophan used as received. The fluorescence spectra were measured with a Perkin-Elmer Model 204 recording fluorescence spectrometer.

Results

1. *Initial Products.* A typical flash spectrum of Trp at 0.2-μs delay in Figure 1 shows the 510- and 320-nm bands

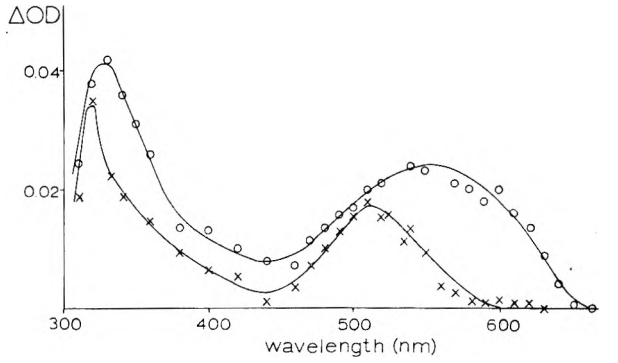

Figure 2. Transient spectra from 265-nm laser photolysis of 350 μM TRP (aqueous), O_2 saturated: (O) 0.3-μs time delay; (×) 2.3-μs time delay.

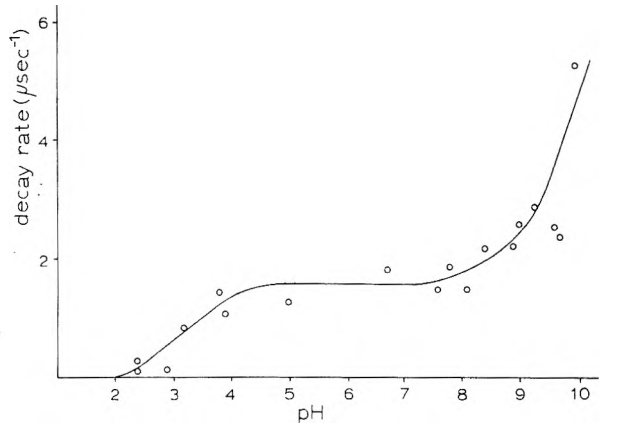

Figure 3. Decay rate of Trp^+ monitored at 580 nm (O_2 saturated).

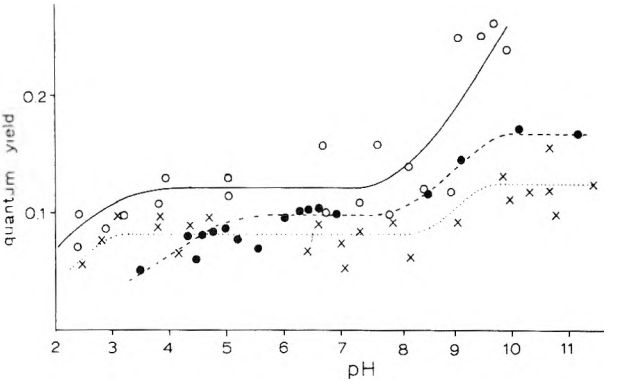

Figure 4. Yields for 265-nm laser photolysis of 350 μM Trp (aqueous): (O) Trp^+, 50-ns delay (O_2 saturated); (●) e_{aq}^-, 50-ns delay (N_2 saturated); (×) Trp, 2-μs delay (O_2 saturated).

of the neutral Trp radical. The measurement was made with O_2 saturation to quench the overlapping e_{aq}^- and ^3Trp bands and at pH 11.3 to promote the conversion of Trp^+ to Trp. Similar measurements at pH 6.4 (no buffer) in Figure 2 show the 580- and 330-nm bands of Trp^+ at 0.30-μs delay and the Trp spectrum at 2.3 μs. The conversion of Trp^+ to Trp was exponential in time with rate constant 1.5×10^6 s^{-1} from pH 5 to 8 (Figure 3). These data were obtained with O_2 saturation to inhibit Trp formation by the recombination of e_{aq}^- with Trp^+, as discussed below. The product quantum yields in Figure 4 show that the initial Trp^+ exceeds e_{aq}^- by 20% and the initial Trp^+ exceeds the Trp yield at 2 μs by 50% from pH 4 to 8. The e_{aq}^- yield is a linear function of laser intensity, with a regression line passing through the origin in this pH range (Figure 5), indicative of a monophotonic process. By constrast, the e_{aq}^- yield from $Fe(CN)_6^{4-}$ is linear at low laser intensities and saturates at high intensities. The

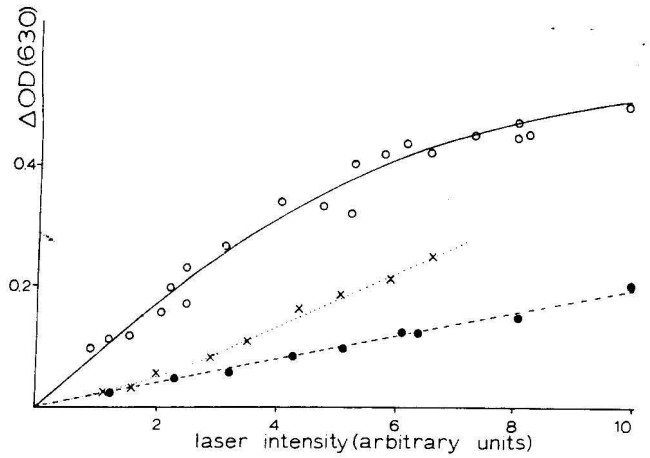

Figure 5. Dependence of initial electron yield on laser intensity: (O) 600 M $Fe(CN)_6^{4-}$; (X) 350 μM Trp (pH 10.9); (●) 350 μM TRP (aqueous) N_2 saturated.

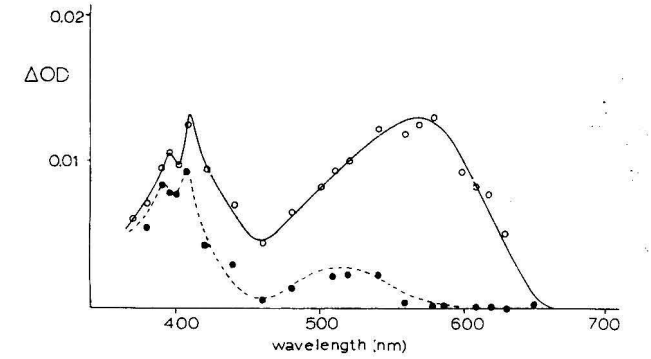

Figure 6. Transient spectra from 265-nm laser photolysis of 350 μM L-tryptophyl-L-tyrosine (aqueous), O_2 saturated, (O) 200 ns, (●) 1600 ns.

initial product yields increase at pH >9, attributed by Bent and Hayon[14] to dissociation of the Trp NH_3^+ group. The initial e_{aq}^- yield is nonlinear with laser intensity in alkaline solutions indicative of a biphotonic contribution to photoionization.

Laser photolysis of the dipeptide tryptophyltryosine generates radical spectra with a 580-nm band characteristic of Trp^+ and also a strong 410-nm band characteristic of the tyrosine phenoxyl radical (Figure 6). Since the fluorescence spectrum of this compound has no detectable tyrosine component, it is unlikely that the fluorescent state or triplet state is the precursor of the electron. This finding supports the observation of Bent and Hayon[14] that e_{aq}^- is generated faster than the decay of fluorescence. The growth of Trp^+ requires about 10^{-6} s in 2 M HCl with a 385-nm precursor that cannot be attributed to the H-atom adduct of Trp, which has been identified by pulse radiolysis with bands at 310 and 345 nm.[15] It may coincide with the unknown "product X" of Arce et al.[16] observed by flash photolysis of aqueous indole.

Transient product yields for 320 μM Trp at pH 6.4 are given in Table I including the effects of high Br^-. These runs were made in connection with the work of Volkert et al.[17] on Trp and *N*-acetyltryptophanamide (NATA) who found that Br^- enhances the yield of the triplet state and the radicals in parallel. The present work confirms that Br^- enhances ^3Trp, accompanied by quenching of the Trp fluorescence. However, the Trp radical yield at 2-μs delay was not altered by Br^- when the overlapping ^3Trp absorption was subtracted out. The present results do not rule out a secondary pathway of radical formation which may account for the 20% higher Trp^+ yield than e_{aq}^- (Figure 4). Table I shows also that the Trp yield at 2-μs

TABLE I: Transient Product Yields from 265-nm Laser Photolysis of 320 μM Tryptophan

Condition	Transient product: Trp[a]	Transient product: e_{aq}^-[b]	Transient product: ^3Trp[c]	Fluorescence efficiency[d]
N_2 satd	0.84	1.0	1.0	
O_2 satd	0.76	1.0	1.0	1.0
N_2 + 5 M Br^-		0.86		
O_2 + 0.2 M Br^-	0.76		1.8	0.85
O_2 + 1 M Br^-	0.76		3.6	0.60
O_2 + 5 M Br^-	0.76		5.1	0.18

[a] Measured at 510 nm; 2-μs delay; normalized to electron yield in N_2 taken as unity. [b] Measured at 650 nm; 20-ns delay; normalized to electron yield in N_2 taken as unity. [c] Measured at 440 nm; 20-ns delay; normalized to triplet yield in N_2 taken as unity. [d] Excited at 285 nm and measured at 340 nm with air saturation.

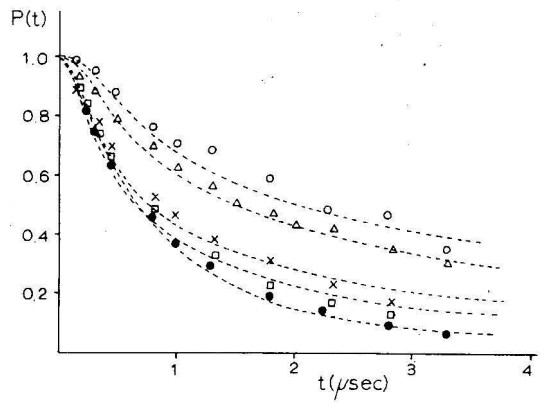

Figure 7. Fit of eq 3 to electron decays after laser photolysis of Trp: (O) 71 μM (aqueous), $a = 4.1 \times 10^{-4}$; (X) 330 μM (aqueous), $a = 2.5 \times 10^{-4}$; (□) 568 μM (aqueous), $a = 2.5 \times 10^{-4}$; (●) 1500 μM (aqueous), $a = 3.4 \times 10^{-4}$ (all $\beta' = 1$, $k_s = 3.6 \times 10^8$); (Δ) 350 μM (pH 10.9), $a = 3.5 \times 10^{-4}$, $\beta' = 1$, $k_s = 1.3 \times 10^8$.

delay is lower in O_2 than in N_2 in agreement with prior work.[3,8,10,17-19] The presence of O_2 would be expected to increase the radical yield by suppressing the electron–radical back reactions. The opposite effect provides definite evidence that Trp formation in the absence of e_{aq}^- scavengers cannot be explained simply by the deprotonation of Trp^+.

2. *Electron Decay Kinetics.* Typical decay curves for e_{aq}^- after laser photolysis of N_2-saturated Trp solutions are given in Figure 7. The initial e_{aq}^- yield in these runs ranged from 3 to 8 μM. If e_{aq}^- disappears by the usual bimolecular reaction at $k_2(e_{aq}^- + e_{aq}^-) = 1.1 \times 10^{10}$ L/mol s and scavenging by Trp at $k_1(e_{aq}^- + Trp) = 3.6 \times 10^8$ L/mol s,[20] then the solution to the rate equation for homogeneous reactions:

$$-d(e_{aq}^-)/dt = k_1(e_{aq}^-)(Trp) + k_2(e_{aq}^-)^2 \quad (1)$$

leads to

$$t_{1/2} = [1/k_1(Trp)] \ln [(2 + A)/(1 + A)] \quad (2)$$

with $A \equiv k_2(e_{aq}^-)_0/k_1(Trp)$. For $(e_{aq}^-)_0 = 5$ μM, (2) leads to $t_{1/2} = 11$ μs at (Trp) = 70 μM and $t_{1/2} = 1.2$ μs at (Trp) = 1.5 mM. However, the actual electron half-time varies from about 2 to 0.7 μs for this range of Trp concentrations, where the discrepancy exceeds the experimental variations. The data in Figure 8 show that $t_{1/2} \simeq 1$ μs and decreases slowly with increasing $(e_{aq}^-)_0$ for a constant value (Trp) = 350 μM. In this case, (2) predicts $t_{1/2} = 5$ μs for $(e_{aq}^-)_0 = 2$ μM and $t_{1/2} = 2.5$ μs for $(e_{aq}^-) = 20$ μM. It is apparent that homogeneous kinetics predicts a slower e_{aq}^- decay, by

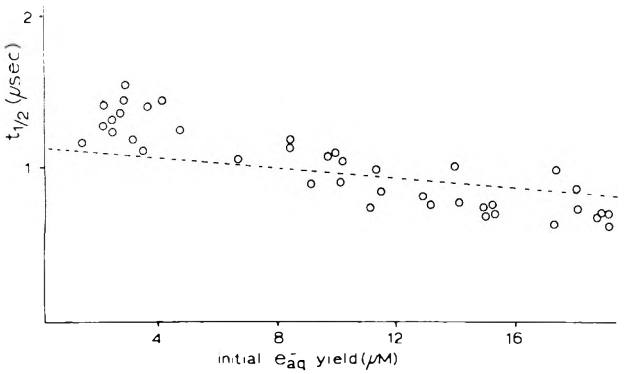

Figure 8. Dependence of e_{aq}^- decay half-time on initial electron yield after 265-nm laser photolysis of 350 μM Trp (aqueous) N_2 saturated. The dashed line is based on eq 5 taking $a = 3 \times 10^{-4}$, $\beta' = 1$, and $k_2 = 1.1 \times 10^{10}$.

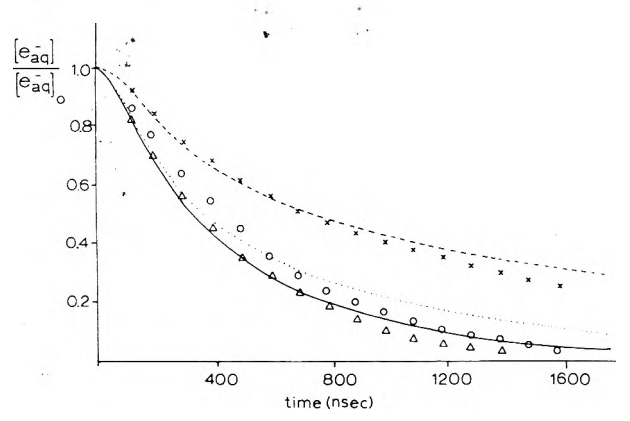

Figure 9. Fit of eq 3 to electron decays after 265-nm laser photolysis of 325 μM Trp (aqueous) N_2 saturated: (Δ) with 1.25 mM $ZnCl_2$, $a = 2.9 \times 10^{-4}$; (O) with 0.63 mM $ZnCl_2$, $a = 2.4 \times 10^{-4}$; (×) without $ZnCl_2$, $a = 2.6 \times 10^{-4}$; all for $k_5 = 1.0 \times 10^9$, $\beta' = 1$.

as much as 5 times in the case of lower initial electron yields and Trp concentrations, and a much stronger dependence of $t_{1/2}$ on both (e_{aq}^-) and (Trp). The results in Figure 9 show the effect of Zn^{2+} as an external e_{aq}^- scavenger on the decay of e_{aq}^- generated by Trp photoionization. In this case, the addition of 0.63 mM Zn^{2+} diminishes $t_{1/2}$ from about 0.8 to 0.4 μs. The prediction of (2) based on $k(e_{aq}^- + Zn^{2+}) = 1.0 \times 10^9$ L/mol s[20] as an additional scavenging contribution leads to $t_{1/2} = 0.8$ μs, two times higher than was observed.

Comparable discrepancies between the measured and calculated e_{aq}^- decays for various organic and inorganic solutes led to a new decay mechanism in which pairwise, electron–radical recombination was proposed as the principal process leading to electron disappearance.[9] The following semiempirical decay law was derived by assuming that the electron migration obeys three-dimensional random walk:

$$(e_{aq}^-)/(e_{aq}^-)_0 = e^{-k_s(S)t}[1 - \beta' \operatorname{erfc}(a/\beta')(\pi/t)^{1/2}] \quad (3)$$

where k_s is the bimolecular rate constant for scavenging by species S which may be the photolyte. The parameters a and β' were defined originally in conjunction with the Noyes theory of diffusional recombination,[21] although it is not assumed here that the solvent "cage" model is applicable because the observed electron lifetimes are $\sim 10^4$ times too long. Nevertheless, the physical interpretation of the parameters should remain valid on the longer time scale, where β' is the maximum probability of electron–radical recombination in the absence of scavengers and a is related to the recombination lifetime. (It was shown in ref 9 that the approximate recombination lifetime is $10 \cdot (a/\beta')^2$.) The dashed lines Figure 7 were calculated with (3) taking $\beta' = 1$ and adjusting for the best value of a in each case. The average value for four runs at pH 6.4 is $a = (3.1 \pm 0.6) \times 10^{-4}$ $s^{1/2}$, in agreement with $a = 3.5 \times 10^{-4}$ for the run at pH 10.9 where $k(e_{aq}^- + Trp) = 1.3 \times 10^{8}$.[20] The data in Figure 9 based on a different set of runs led to $a = (2.6 \pm 0.2) \times 10^{-4}$ $s^{1/2}$ with or without Zn^{2+}.

The dependence of $t_{1/2}$ on Trp concentration was treated by defining a mean decay lifetime: $\bar{t} = \int_0^\infty t\, dp / \int_0^\infty dp$, where $p(t)$ was taken as $(e_{aq}^-)/(e_{aq}^-)_0$ in (3). The straight-forward integration leads to:

$$1/\bar{t} = 0.693/t_{1/2} = (y^2/\pi)\frac{\beta' e^{-(2a/\beta')y} + 2ay + (1 - \beta')}{ay[1 + e^{-(2a/\beta')y}] + (1 - \beta')} \quad (4)$$

where $y \equiv [\pi k_s(S)]^{1/2}$. The results published as Figure 2 of ref 9 show that (4) is followed for a series of 29 runs where (Trp) was varied from 0.05 to 4 mM, taking $a = 3 \times 10^{-4}$ $s^{1/2}$, $\beta' = 1$, and $k_s = 3.6 \times 10^8$ L/mol s.

The applicability of (3) and (4) is limited to low initial electron yields, where the decay process is essentially completed prior to the time that an electron reacts with electrons or radicals generated in other pairs. The deviations of the data from the theoretical lines after about 0.5 μs in Figures 7 and 9 are attributed to the onset of such pair–pair processes. This case was treated in ref 9 by demonstrating that (3) is equivalent to a time-dependent, first-order decay rate constant: $k_t = k_s(S) + (a/t^{3/2})/[1 - \beta' \operatorname{erfc}(a/\beta')(\pi/t)^{1/2}]$ which when substituted for k_1 in (1) leads to a modified decay function valid for $t \gg \pi a^2/\beta'^2$ at high initial electron yields. The half-time deduced from this decay function should vary with $(e_{aq}^-)_0$ as

$$k_2(e_{aq}^-)_0 t_{1/2} + [(4t_0)^{-1/2} - k_2(e_{aq}^-)_0 t_0^{1/2}] t_{1/2}^{1/2} = 1 \quad (5)$$

where t_0 is the arbitrary initial time corresponding to $(e_{aq}^-)_0$ and approximately equal to $4a^2$ for $\beta' = 1$. The dashed line in Figure 8 shows the plot of (5) for $k_2 = 1.1 \times 10^{10}$ L/mol s, $a = 3 \times 10^{-4}$ $s^{1/2}$, and $\beta' = 1$. The good agreement is considered as strong support for the proposed recombination mechanism since no additional parameters are required except a and β' as determined previously from the decay curves.

In summary, the decay of e_{aq}^- generated by photoionization of aqueous Trp agrees with a new mechanism involving diffusive electron motions for periods $\sim 10^{-6}$ s, during which time recombination of the radicals is the dominant effect, in competition with scavenging by the Trp photolyte or added scavengers such as Zn^{2+}. This aspect of the process has been emphasized because the existence of significant recombination requires a new radical decay mechanism in order to explain why the Trp yields remain high even in the absence of effective scavengers such as O_2 or N_2O.

Discussion

An attempt is made in Table II to summarize the published work relevant to this study, in approximately chronological order, indicating the key observations and conclusions. The following are taken as reasonably firm on the basis of support from different investigations: The major initial photochemical act is photoionization leading to the Trp^+ monocation radical and e_{aq}^-. The conversion of Trp^+ to the neutral Trp radical is complex and may involve the back reaction of e_{aq}^- with Trp^+. The disappearance of e_{aq}^- does not obey homogeneous decay reaction kinetics. The electron is released to the medium from a

TABLE II: Published Results on Tryptophan Photolysis

Photolyte(s)[a]	Method[b]	Key results and conclusions[c]	Ref
Trp	Flash photol	e_{aq}^- initial product	6
Indole derivatives	Flash photol	e_{aq}^- plus radical spectra ~480 nm	7
Indole, 3-β-hydroxyethylindole	Products	e_{aq}^- from fluorescent state; high activation energy	22
Trp	Flash photol	$\phi(e^-)$ = 0.09 (pH 12); 0.06 (pH 7); e_{aq}^- + Trp^+ back reaction	23
Trp, 1-MeTrp	Flash photol	Trp^+ (600 nm), Trp (485 nm), ^3Trp (460 nm)	3
Trp, 1-MeTrp	Flash photol, products	$\phi(e^-)$ = 0.006 (pH 10-12); $^3Trp + O_2$ leads to products	19
Indole derivatives	Laser flash photol	$\phi(e^-)$ = 0.21 (pH 11), 0.08 (pH 6); Trp^+ (560 nm), Trp (530 nm); ^3Trp (450 nm); monophotonic e_{aq}^-; high activation energy	14
Trp, 1-MeTrp	Pulse radiolysis	Trp^+ (570 nm, 2600), Trp (510 nm, 1750)	4
Trp, 1-MeTrp	Laser flash photol	Trp^+ (580 nm, 2900), Trp (510 nm, 1800); complex e_{aq}^- decay; e_{aq}^- + Trp^+ back reaction	3
Indole	Flash photol	e_{aq}^- + I^+ leads to I	16
Trp, skatole	Laser flash photol	Complex e_{aq}^- decay	24
Trp derivatives	Flash photol	Complex e_{aq}^- decay; monophotonic Trp from ^3Trp	18
Trp	Laser flash photol	Biphotonic e_{aq}^-	25
Trp	Pulse radiolysis	Trp^+ (570 nm, 2500), Trp (520 nm, 1870); $pK_a(Trp^+)$ = 4.3	5
NATA	Flash photol	$pK_a(Trp^+)$ = 4.3; +1 charge on radical ion	26
NATA	Flash photol	Br^- promotes radical; 50% of radical not with e_{aq}^-	27
NATA	Flash photol	Common precursor to e_{aq}^-, radical cation and fluorescent state	28
NATA, Trp	Flash photol, laser flash photol	^3Trp (460 nm, 5000); Br^- promotes ^3Trp; radical cation, radicals	17

[a] Fluid aqueous solutions. [b] Flash photolysis (flash photol) ~5-50-μs resolution; laser flash photolysis (laser flash photol) 30-ns resolution, 265 nm. [c] $\phi(e^-)$ for Trp; band maxima and extinction coefficients (L/mol cm) in parentheses.

state shorter-lived than ^3Trp. Several pathways of radical formation are feasible, the importance of which depends on the irradiation conditions.

Several inconsistencies in the experimental parameters are now satisfactorily resolved. The initial yield of e_{aq}^- formation in near-neutral solutions is 0.010 ± 0.02, the extinction coefficients of Trp^+ at 580 nm and Trp at 510 nm are 2700 ± 200 and 1800 ± 50 L/mol cm, respectively, and pK_a of the radical is 4.3. The dependence of the e_{aq}^- yield on laser intensity remains an unresolved issue. The present work indicates that the photoionization process is monophotonic at near neutral pH and has a possible biphotonic contribution in alkaline solutions. This may be compared with Bent and Hayon[14] who reported a 1.25 power dependence on intensity at pH 7.5 and 1.2 power dependence at pH 11.8. The work of Lachish et al.[2,5] is in greater disagreement, who find the process to be biphotonic in the near-neutral case. The different intensity dependence of the e_{aq}^- yield reported in other work suggests that several photoionization pathways may be operative, depending on the actual irradiation conditions. However, the dipeptide result in Figure 6 is taken as strong supporting evidence of monophototonic photoionization in near-neutral conditions in the present work.

The formation of Trp from Trp^+ has been a source of confusion. When the electron is not involved (e.g., Figure 3) the exponential conversion is attributed to deprotonation:

$$Trp^+ \rightleftarrows Trp + H^+$$

Taking $k(-Trp^+) = 1.5 \times 10^6\ s^{-1}$ and $pK_a = 4.3$ leads to $k(Trp + H^+) = 3 \times 10^{10}$ L/mol s, in good agreement with other aromatic bases.[29] Since the deprotonation half-time of 0.5 μs is comparable to the e_{aq}^- lifetime in deaerated solutions, the electron–radical recombination takes place simultaneously with deprotonation and approximately 2/3 of the recombining e_{aq}^- would be expected to react with Trp^+. In order to explain why this process does not suppress Trp formation (e.g., Table I) it is postulated that the back reaction does not restore the original Trp. Instead, we suggest that an intermediate product Trp′ is formed, which can react in turn with the Trp solute leading to Trp and the Trp^- electron adduct:

$$Trp^+ + e_{aq}^- \rightarrow Trp'$$

$$Trp' + Trp \rightarrow Trp + Trp^-$$

It is well known that the recombination of electrons with aromatic radicals in rigid media leads to excited singlet and triplet states (e.g., luminescence studies on Trp by Moan and Steen,[30] Moan,[31] and Muller et al.[32]) in which case Trp′ might be a triplet state. The formation of Trp^- by the reaction of ^3Trp with Trp has been proposed by Volkert et al.[17] on the basis of a 350-nm band observed by laser photolysis of N_2O-saturated Trp, with 0.1 M *tert*-butyl alcohol to scavenger e_{aq}^- and OH radicals. Alternatively, a biradical might be formed that undergoes electron disproportionation with Trp. Another possibility is deamination of the radical cation by electron capture leading directly to a neutral indolyl radical after electron rearrangement whose absorption would not be distinguishable from Trp.[7] This type of process was proposed for the irradiation of crystalline valine with x rays at 77 K by Box et al.[33] and for 13 polycrystalline amino acids including Trp by Shield and Hamrick.[34]

The recombination mechanism leading to eq 3, 4, and 5 implies that the electron separates from the Trp^+ radical and diffuses through the medium for about 10^{-6} s, during which time it may react with the original radical, a sca-

venger molecule, or with the electron or radical from another pair if time is available. The time for the last process is comparable to the time required for the electron to diffuse from one Trp^+ to another, which depends on the initial e_{aq}^- yield. For example, for $(e_{aq}^-)_0 = 5\ \mu M$, the mean separation of Trp^+ radicals is about 400 Å. Taking $(2Dt)^{1/2}$ as the mean diffusion length and $D_{e^-} = 3 \times 10^{-5}\ cm^2/s$ leads to $t = 0.3\ \mu s$. This result is comparable to the times at which the decay curves depart from the predictions of (3) in Figures 7 and 9. A lower limit for the efficiency of recombination may be estimated by assuming that homogeneous kinetics are valid. The probability of scavenging per interaction of the electron with a Trp molecule is approximately the ratio of $k(e_{aq}^- + Trp)$ to the diffusion limited rate constant of $\sim 3 \times 10^{10}$ L/mol s or 0.012. Assuming that each $e_{aq}^- - Trp^+$ interaction is 100% efficient, the probability of recombination is $p_{rec} \simeq f/(f + 0.012)$, where f is the fraction of Trp converted to Trp^+ by the laser flash. Taking $f = 5\ \mu M/300\ \mu M = 0.017$ leads to $p_{rec} = 0.6$. Therefore, *homogeneous kinetics predicts a substantial degree of recombination under the typical flash irradiation conditions.* However, homogeneous kinetics predicts negligible bimolecular back reaction under steady irradiation conditions, while original-pair recombination in the proposed model is about 70% efficient at (Trp) = 350 μM even at low light intensities, based on eq 10 of ref 9.

The e_{aq}^- and Trp^+ yields measured at 20 ns may represent those initial products that escape geminate recombination in the solvent cage. In the case of the photoionization of $Fe(CN)^{4-}$ the mode locked laser techniques of Rentzepis et al.[35] show that the electron absorption changes from the infrared (1.06 μ) to the normal e_{aq}^- band within 4 ps. To our knowledge, there is no direct experimental evidence for electron–radical recombination during the period 10^{-10} to 10^{-11} s in fluid water, as predicted by the Noyes theory. Czapski and Ottolenghi[36] contend that the photochemical scavenging experiments of Stein[11] do not support the cage recombination model because the radical yields from flash photolysis of I^-, phenolate, and $Fe(CN)_6^{4-}$ were the same with 1.5 and 100% N_2O, and propose that the product yield data of Stein can be explained equally well by homogeneous competition kinetics. The work of ref 9 shows that the Stein results are quantitatively consistent with the mechanism proposed here, and represent an alternate method of monitoring the electron decay process.

Acknowledgment. The authors are indebted to Dr. W. A. Volkert of the University of Missouri for making available prepublication preprints of several references and to Dr. J. Y. Lee of this laboratory for providing the data in Figure 9.

References and Notes

(1) Work supported by ERDA Contract E(11-1)-2217 and PHS Grant GM-20117. This is COO-2217-18.
(2) L. I. Grossweiner, "Current Topics in Radiation Research Quarterly", Vol. II, M. Ebert and A. Howard, Ed., North Holland Publishing Co., Amsterdam, 1976, p 141.
(3) R. Santus and L. Grossweiner, *Photochem. Photobiol.*, **15**, 101 (1972).
(4) J. L. Redpath, R. Santus, J. Ovadia, and L. I. Grossweiner, *Int. J. Radiat. Biol.*, **27**, 201 (1975).
(5) M. L. Posner, G. E. Adams, P. Wardman, and R. B. Cundall, *J. Chem. Soc., Faraday Trans. 1*, **72**, 2231 (1976).
(6) L. I. Grossweiner, G. W. Swenson, and E. F. Zwicker, *Science*, **141**, 805 (1963).
(7) H. I. Joschek and L. I. Grossweiner, *J. Am. Chem. Soc.*, **88**, 3261 (1966).
(8) F. D. Bryant, R. Santus, and L. I. Grossweiner, *J. Phys. Chem.*, **79**, 2711 (1975).
(9) L. I. Grossweiner and J. F. Baugher, *J. Phys. Chem.*, **81**, 93 (1977).
(10) L. I. Grossweiner, A. G. Kaluskar, and J. F. Baugher, *Int. J. Radiat. Biol.*, **29**, 1 (1976).
(11) J. Jortner, M. Ottolenghi, and G. Stein, *J. Phys. Chem.*, **66**, 2037, 2042 (1962).
(12) F. S. Dainton and S. R. Logan, *Proc. R. Soc. London, Ser. A*, **287**, 281 (1965).
(13) M. Shirom and G. Stein, *J. Chem. Phys.*, **55**, 3372 (1971).
(14) D. V. Bent and E. Hayon, *J. Am. Chem. Soc.*, **97**, 2612 (1975).
(15) R. C. Armstrong and A. J. Swallow, *Radiat. Res.*, **40**, 563 (1969).
(16) R. Arce, A. Grimison, J. Revuelta, and G. A. Simpson, *Photochem. Photobiol.*, **21**, 397 (1975).
(17) W. A. Volkert, R. R. Kuntz, C. A. Ghiron, R. F Evans, R. Santus, and M. Bazin, *Photochem. Photobiol.*, in press.
(18) H. Templer and P. J. Thistlethwaite, *Photochem. Photobiol.*, **23**, 79 (1976).
(19) M. T. Pailthorpe, J. P. Bonjour, and C. H. Nichools, *Photochem. Photobiol.*, **17**, 209 (1973).
(20) M. Anbar, M. Bambenek, and A. B. Ross, *Natl. Stand. Ref. Data Ser., Natl. Bur. Stand.*, **No. 43** (1973).
(21) R. M. Noyes, *J. Am. Chem. Soc.*, **77**, 2042 (1955); **78**, 5486 (1956).
(22) J. Feitelson, *Photochem. Photobiol.*, **13**, 87 (1971).
(23) L. I. Grossweiner and Y. Usui, *Photochem. Photobiol.*, **13**, 195 (1971).
(24) M. Bazin, C. Hasselmann, G. Laustriat, R. Santus, and P. Walrant, *Chem. Phys. Lett.*, **36**, 505 (1975).
(25) U. Lachish, A. Shafferman, and G. Stein, *J. Chem. Phys.*, **64**, 4205 (1976).
(26) R. F. Evans, G. A. Ghiron, W. A. Volkert, and R. R. Kuntz, *Chem. Phys. Lett.*, **42**, 415 (1976).
(27) R. F. Evans, C. A. Ghiron, W. A. Volkert, R. R. Kuntz, R. Santus, and M. Bazin, *Chem. Phys. Lett.*, **42**, 39 (1976).
(28) R. F. Evans, C. A. Ghiron, R. R. Kuntz, and W. A. Volkert, *Chem. Phys. Lett.*, **42**, 415 (1976).
(29) M. Eigen, W. Kruse, G. Mass, and L. DeMaeyer, *Prog. React. Kinet.*, **2**, 287 (1964).
(30) J. Moan and H. B. Steen, *J. Phys. Chem.*, **75**, 2887 (1971).
(31) J. Moan, *J. Chem. Phys.*, **60**, 3859 (1974).
(32) D. Muller, M. Ewald, and G. Durocher, *Can. J. Chem.*, **52**, 407 (1974).
(33) H. C. Box, H. G. Freund, and E. E. Budzinskl, *J. Chem. Phys.*, **46**, 4470 (1967).
(34) H. Shields and P. H. Hamrick, Jr., *J. Chem. Phys.*, **64**, 263 (1976).
(35) P. M. Rentzepis, R. P. Jones, and J. Jortner, *J. Chem. Phys.*, **59**, 766 (1973).
(36) G. Czapski and M. Ottolenghi, *Isr. J. Chem.*, **6**, 75 (1968).

Kinetics and Equilibria of the Binding of Cobalt(II) to Adenosine 5′-Monophosphate

A. Peguy[1] and H. Diebler*

Max-Planck-Institute for Biophysical Chemistry, 34 Göttingen, Nikolausberg, West Germany *(Received January 1, 1977)*

Publication costs assisted by the Max-Planck-Gesellschaft

Equilibrium studies of the binding of Co^{2+} to adenosine 5′-monophosphate (AMP) have been carried out at 8.0 °C and ionic strength I = 0.2 M ($NaClO_4$) by means of potentiometric measurements. The following stability constants have been evaluated: K_{ML} = $[CoAMP]/[Co^{2+}][AMP^{2-}]$ = 225 ± 10 M^{-1} and K_{MLH} = $[CoAMPH^+]/[Co^{2+}][AMPH^-]$ = 21 ± 2 M^{-1}. The kinetics of the (fast) binding reactions have been studied by the temperature-jump relaxation technique. Values of the inverse relaxation time show a nonlinear dependence on the reactant concentrations. This observation is interpreted by a mechanism involving stepwise coordination of the metal ion to the ligand's phosphate and adenine groups. The rate constants which have been evaluated by a fitting procedure are consistent with those of other Co(II)-complex formation reactions.

Introduction

Because of their biological relevance, the interactions of metal ions with nucleotides have found great interest recently. Most of the studies in this field are concerned with structural properties and equilibrium data, and several review articles have appeared which summarize a large amount of experimental data.[2-5] Reports of the kinetics of metal ion–nucleotide interactions are less numerous, although kinetic properties are possibly of importance for the efficiency of metal-ion activation in certain types of enzymatic reactions involving nucleotides.[6] The majority of the kinetic studies have been carried out with adenosine triphosphate (ATP) and diphosphate (ADP). The results available so far have been discussed recently by Frey and Stuehr.[7] At low reactant concentrations the kinetic data are consistent with simple 1:1 complex formation reactions; data obtained over a wider concentration range, however, indicate more complicated reaction mechanisms. In case of Mg^{2+}, the behavior at higher concentrations was attributed to the stepwise formation of the species MgL and Mg_2L, where L = ADP or ATP. With Ni^{2+}, adenosine 5′-monophosphate (AMP) exhibits a behavior qualitatively similar to that of ADP and ATP,[7] although complexes M_2L are not known for L = AMP (M = divalent metal ion) and are not likely to be formed. Since it is well established that transition metal ions bind to the phosphate group and to adenine of these nucleotides,[2-5] the kinetic data are most conveniently explained by a mechanism which involves stepwise coordination of the transition metal ion to the phosphate group and to adenine, and in which the monocoordinate species does not represent a steady-state intermediate. The results of a kinetic study of binding of Ni^{2+} to AMP covering a wide concentration range and various H^+ concentrations were interpreted in terms of this mechanism and allowed the evaluation of all the rate constants involved.[8]

In order to test the proposed mechanism, it is desirable to extend such studies also to other metal ions. In the present paper, equilibrium constants and kinetic data are reported for the binding of Co^{2+} to adenosine 5′-monophosphate.

Experimental Section

5′-AMP (Merck, for biochemical purposes), cobalt(II) perchlorate (Fluka), sodium perchlorate (Koch-Light, AR), and other chemicals were of the highest quality commercially available and were used without further purification. Stock solutions of $Co(ClO_4)_2$ were standardized by titration with EDTA, using murexide as indicator,[9] and AMP solutions by pH titration. Low concentrations of cacodylate buffer (1×10^{-3} M) were added in the kinetic studies; under these conditions the buffer components do not interact significantly with Co(II) ions.

All measurements were carried out at 8 °C and 0.2 M ionic strength, adjusted with $NaClO_4$ (the low temperature was chosen because of the high rate of reaction). The protonation constants of adenosine monophosphate were determined from pH titrations of 4×10^{-3} M solutions of $AMPH_2$ with 0.05 M NaOH. Binding constants for the interaction of 5′-AMP with Co(II) were evaluated from pH titrations in the presence of various concentrations of metal ion. Measurements of pH were carried out by means of a Polymetron 42D pH meter and a Metrohm EA 125 combined electrode in which the KCl solution had been replaced by NaCl solution. The meter was calibrated at 8 °C using Radiometer buffer solutions (pH 4.0 and 7.0) of known temperature dependence. Nitrogen was bubbled through the reaction solution prior to, and over the surface during the measurement of pH.

Studies of the kinetics were carried out by the temperature-jump relaxation technique with spectrophotometric detection.[10] The relaxation process was followed in the UV region (274 nm) where the π–π^* transition of adenine occurs. The photographed oscilloscope curves were evaluated by means of an electronic device which produces exponential curves of variable time constant and amplitude. The relaxation time constants given in this paper are the mean values of five to seven individual measurements; the individual values were within ±10% of the mean value for any series of measurements.

Results

Equilibria. Under the conditions of this study the following protonation reactions of the dinegative anion of adenosine monophosphate, $AMP^{2-} = L^{2-}$, are of interest:

$$H^+ + L^{2-} = HL^- \qquad K_{HL} \tag{1}$$

$$H^+ + HL^- = H_2L \qquad K_{H_2L} \tag{2}$$

The first step (K_{HL}) corresponds to protonation of the phosphate group, and the second (K_{H_2L}) to protonation of adenine. Accepting 0.78 as the activity coefficient of H^+ under the given conditions,[11] the following constants were obtained from the titration curves:

$$K_{HL} = [HL^-]/[H^+][L^{2-}] = 1.06 \times 10^6\ M^{-1}$$
$$(pK_{HL} = 6.025)$$

$$K_{H_2L} = [H_2L]/[H^+][HL^-] = 1.23 \times 10^4\ M^{-1}$$
$$(pK_{H_2L} = 4.09)$$

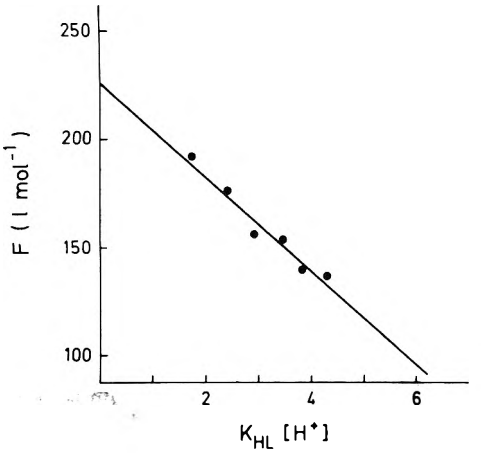

Figure 1. Plot of $F = (3K_{H_2L}K_{HL}[H^+]^2 + K_{HL}[H^+] - 1)/[M]$ vs. $K_{HL}[H^+]$ according to eq 5: 8 °C, I = 0.2 M.

(8 °C, I = 0.2 M).

The binding of metal ions yielding 1:1 complexes can be expressed as

$$M^{2+} + L^{2-} = ML \qquad K_{ML} \tag{3}$$

$$M^{2+} + LH^- = MLH^+ \qquad K_{MLH} \tag{4}$$

Binding studies have been carried out with total ligand $L_0 = 2 \times 10^{-3}$ M and total metal $M_0 = 5 \times 10^{-3}$–3×10^{-2} M. As in case of Ni^{2+} + AMP,[8] the possible formation of some complex ML_2 (ref 12) can be neglected under these conditions. There is also no evidence for the formation of M_2L with L = AMP.[8] The effect of Co(II) ions on the titration curves is most pronounced in the range where about 1.2–1.7 mol of NaOH per mole of total ligand (initial form $AMPH_2$) have been added. If exactly 1.5 mol of OH^- per mole of ligand are added, the following relationship may be derived[8] from eq 1–4 and the mass balance equations for the ligand species, $L_0 = [L] + [HL] + [H_2L] + [ML] + [MLH]$, and for hydrogen ion, $2L_0 = 2[H_2L] + [HL] + [H] + [MLH] + B - [OH]$ (charges omitted for simplicity), where B = total base added (=1.5L_0 in this case):

$$(3K_{H_2L}K_{HL}[H]^2 + K_{HL}[H] - 1)/[M] = K_{ML} - K_{MLH}K_{HL}[H] \tag{5}$$

A plot of the expression on the left-hand side of eq 5 vs. $K_{HL}[H]$ yields values for K_{ML} and K_{MLH}. The experimental data are shown in Figure 1. Initially, [M] was approximated by M_0 and approximate values for K_{ML} and K_{MLH} were derived which then have been used to calculate better values for [M]. From Figure 1 results $K_{ML} = [ML]/[M^{2+}][L^{2-}] = 225 \pm 10$ M^{-1} and $K_{MLH} = [MLH^+]/[M^{2+}][LH^-] = 21 \pm 2$ M^{-1} (8 °C, I = 0.2 M).

Kinetics. Kinetic studies of the interaction of Co^{2+} with AMP have been carried out at pH 5.0, 6.0, and 7.0, with $L_0 = 1 \times 10^{-4}$–2×10^{-4} M and M_0 = 0.001–0.04 M, always with at least a tenfold excess of metal ion over ligand. One relaxation effect was observed with all solutions; its time constant varied between 14.5 and 40 μs. The concentration and pH dependence of the inverse relaxation time $1/\tau$ is shown in Figure 2. The sum of the reactant concentrations, $[Co^{2+}] + \sum[L]$, where $\sum[L] = [L] + [LH] + [LH_2]$, was always very close to $[Co]_0$ (pseudo-first-order conditions). At pH 7.0 and 6.0 the plots of $1/\tau$ vs. $[Co^{2+}] + \sum[L]$ are clearly curved and appear to approach a limiting value at very high reactant concentrations, thus ruling out a simple complex formation process of the type M + L ⇌ ML. If outer-sphere association is taken into account, i.e., M + L ⇌ M,L ⇌ ML, where M,L denotes the outer-sphere complex, the outer-sphere stability constant $K_0 = [M,L]/[M][L]$ required to fit the experimental data at pH 7.0 would be about 60 M^{-1}. This value appears much too high; actually, a value close to $K_0 \simeq 9$ M^{-1} would be expected for reactants of the charge type +2,–2 under the conditions of this study.[13] It is most unlikely, therefore, that the curvature of the plots of Figure 2 is due to outer-sphere association, and the results are consequently discussed in terms of the general reaction scheme 6, which takes ex-

Figure 2. Dependence of $1/\tau$ on reactant concentrations for the reaction of Co^{2+} with 5′-AMP at pH 5.0 (○), 6.0 (●), and 7.0 (□); 8 °C, I = 0.2 M.

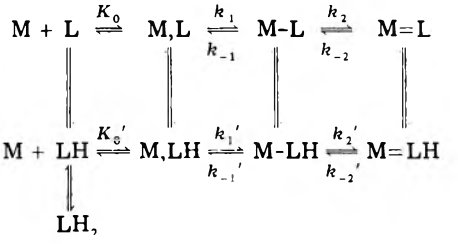

(6)

plicitly into account the stepwise binding process. M–L and M–LH denote monodentate species (mainly phosphate bound) and M=L and M=LH the bidentate (phosphate and adenine bound) species. If it is assumed that the protolytic reactions (vertical steps in reaction scheme 6) like the outer-sphere association processes may be considered as rapid preequilibria as compared to the substitution reactions at the Co(II) center, only two relaxation time constants are to be expected for the complex formation reactions of scheme 6. They are given by[10]

$$1/\tau_{+,-} = (1/2)\{(a_{11} + a_{22}) \pm [(a_{11} + a_{22})^2 - 4(a_{11}a_{22} - a_{12}a_{21})]^{1/2}\} \tag{7}$$

with

$$a_{11} = \frac{k_1K_0 + k_1'K_0'K_{HL}[H]}{K_1K_0 + K_1'K_0'K_{HL}[H]} + \frac{(k_1K_0 + k_1'K_0'K_{HL}[H])([M] + \Sigma[L])}{\beta + (K_0 + K_0'K_{HL}[H])([M] + \Sigma[L])}$$

$$a_{12} = \frac{k_1K_0 + k_1'K_0'K_{HL}[H]}{K_1K_0 + K_1'K_0'K_{HL}[H]}$$

$$a_{21} = \frac{k_2 + k_2'K_{Cl}[H]}{1 + K_{Cl}[H]}$$

$$a_{22} = \frac{k_2 + k_2'K_{Cl}[H]}{1 + K_{Cl}[H]} + \frac{k_{-2} + k_{-2}'K_{C2}[H]}{1 + K_{C2}[H]}$$

TABLE I: Kinetic and Equilibrium Data for the Interaction of Co^{2+} with 5′-AMP (8 °C, I = 0.2 M [$NaClO_4$])

K_{ML}, M^{-1}	225	k_1, s^{-1}	1.9×10^6
K_{MLH}, M^{-1}	21	k_1', s^{-1}	1.2×10^6
K_0, M^{-1}	9	k_{-1}, s^{-1}	2.6×10^5
K_0', M^{-1}	1.7	k_{-1}', s^{-1}	3.4×10^5
K_1	7.3	k_2, k_2', s^{-1}	6.6×10^4
K_1'	3.5	k_{-2}, k_{-2}', s^{-1}	2.9×10^4
K_2, K_2'	2.3		

and where

$$\beta = 1 + K_{HL}[H] + K_{HL}K_{H_2L}[H]^2$$

$$K_1 = k_1/k_{-1} \qquad K_1' = k_1'/k_{-1}'$$

$$K_{C1} = [M\text{-}LH]/[M\text{-}L][H] = K_1'K_0'K_{HL}/K_1K_0$$

$$K_{C2} = [M{=}LH]/[M{=}L][H] = K_2'K_1'K_0'K_{HL}/K_2K_1K_0$$

The curvature of the plots shown in Figure 2 can only be accounted for by the negative sign of the root of eq 7, whereas the corresponding plot for the positive sign would curve upward (at least for weak outer-sphere association). Therefore the observed relaxation effect is attributed to τ_-. The quantities in the expression for $1/\tau_-$ may then be fitted to the experimental data. In order to reduce the number of unknowns, calculated values[13] of the outer-sphere stability constants were used, $K_0 \simeq 9\ M^{-1}$ and $K_0' \simeq 1.7\ M^{-1}$, although it is realized that with a nonspherical ligand like AMP the calculations can provide only approximate values. K_1 was expressed in terms of K_{ML}, K_0, and k_2/k_{-2} ($K_{ML} = ([M,L] + [M\text{-}L] + [M{=}L])/[M][L] = K_0(1 + K_1 + K_1K_2)$, where $K_2 = k_2/k_{-2}$), and K_1' in terms of K_{MLH}, K_0', and k_2'/k_{-2}'. Furthermore, it is to be expected that the rate of forming and breaking the Co(II)–adenine bond does not strongly depend on the protonation state of the phosphate group, i.e., $k_2' \simeq k_2$ and $k_{-2}' \simeq k_{-2}$, thus $a_{21} \simeq k_2$ and $a_{22} \simeq k_2 + k_{-2}$. At a given pH the expression for $1/\tau_-$ can now be formulated in terms of only three unknowns, k_{1f}, k_2 ($=a_{21}$), and $k_2 + k_{-2}$ ($=a_{22}$), with

$$k_{1f} = k_1K_0 + k_1'K_0'K_{HL}[H^+] \qquad (8)$$

A computer evaluation of the best fit of these quantities to the experimental data for pH 7.0 yielded the values $k_{1f} = 20 \times 10^6\ M^{-1}\ s^{-1}$, $k_2 = 6.6 \times 10^4\ s^{-1}$, and $k_2 + k_{-2} = 9.5 \times 10^4\ s^{-1}$. These values of k_2 and $k_2 + k_{-2}$ were then used to evaluate k_{1f} at pH 6.0 and 5.0, giving $k_{1f} = 16 \times 10^6\ M^{-1}\ s^{-1}$ (pH 6.0) and $k_{1f} = 45 \times 10^6\ M^{-1}\ s^{-1}$ (pH 5.0). The values of $1/\tau_-$ which are calculated with these data are given by the solid lines of Figure 2 (at pH 6.0, this fit is not a particularly good one; a somewhat better fit at pH 6.0 is obtained with $k_{1f} = 20.9 \times 10^6\ M^{-1}\ s^{-1}$, $k_2 = 5.6 \times 10^4\ s^{-1}$, and $k_2 + k_{-2} = 8.4 \times 10^4\ s^{-1}$, broken line in Figure 2). Finally, plotting k_{1f} vs. $K_{HL}[H^+]$ (eq 8) yields $k_1K_0 = (1.7 \pm 0.3) \times 10^7\ M^{-1}\ s^{-1}$ and $k_1'K_0' = (2.1 \pm 0.3) \times 10^6\ M^{-1}\ s^{-1}$. A summary of the kinetic and equilibrium data for the system Co^{2+}–5′-AMP is shown in Table I. Some of the values of Table I contain an appreciable uncertainty (see Discussion).

Discussion

According to Taqui Khan and Martell,[14] the value of K_{ML} for the system Co^{2+}–AMP increases slightly with increasing temperature; certainly it will increase also with decreasing ionic strength. The value $K_{ML} = 225\ M^{-1}$ (8 °C, I = 0.2 M [$NaClO_4$]) which has been determined in the course of this study is therefore consistent with the literature reports $K_{ML} = 295\ M^{-1}$ (8 °C, I = 0.1 M [KNO_3]),[14] 340 M^{-1} (25 °C, I = 0.1 M [KNO_3]),[14] and 370 M^{-1} (25 °C, I = 0.1 M [KNO_3]),[15] but less so with $K_{ML} = 155\ M^{-1}$ (25 °C, I = 0.1 M [$NaClO_4$]).[16] A comparison with the equilibrium constant $[CoHPO_4]/[Co^{2+}][HPO_4^{2-}] = 150\ M^{-1}$ (25 °C, I = 0.1 M [$NaClO_4$])[17] reveals the extra stability of the Co^{2+}–AMP complex provided by the Co^{2+}–adenine bond.

The stability constants K_{ML} for Co^{2+}–AMP and Ni^{2+}–AMP ($K_{ML} \simeq 300\ M^{-1}$ at 25 °C, I = 0.1 M [$NaClO_4$][8]) are rather similar. The value of K_{MLH} is even larger for M = Co^{2+} (21 M^{-1} at 8 °C, I = 0.2 M [$NaClO_4$]) than for M = Ni^{2+} (11 M^{-1} at 25 °C, I = 0.1 M [$NaClO_4$][8]). Similar deviations from the Irving–Williams order[18] have also been observed for several other phosphate complexes of Co^{2+} and Ni^{2+}, e.g., with HPO_4^{2-}, pyrophosphate, and triphosphate.[17,19] It cannot be excluded, however, that the given values of K_{MLH} (i.e., the slopes of plots of the type shown in Figure 1) are slightly affected by the changes of the medium which are required in the equilibrium studies (replacement of sodium ions by metal(II) ions at constant ionic strength).

The kinetic data which have been evaluated (Table I) may be compared with those of other 1:1 complex formation reactions of Co^{2+}. A few representative examples are compiled in Table II. At 25 °C, the inner-sphere substitution rate constants k_i which have been evaluated from the second-order rate constants k_f are not far from $1 \times 10^6\ s^{-1}$ in almost all cases (only one of the values for glycine$^-$ is somewhat low), i.e., they do not show an appreciable dependence on the ligand involved. A similar value was reported for the rate of exchange of a water molecule of $Co(H_2O)_6^{2+}$ with bulk water, $k_{ex} = 2.2 \times 10^5\ s^{-1}$ at 25 °C.[25] These observations indicate that the rate-determining (first) substitution step proceeds by a dissociative mechanism (dissociative interchange or S_N1 mechanism), as has been found also for other divalent metal ions.[26] Consequently, the corresponding rate constants in the system Co^{2+}–AMP, k_i and k_i', are expected to be of the same magnitude. The agreement is not as perfect as it might appear on first sight, however, since the data of Table I refer to 8 °C. At this temperature the value of the exchange rate is $k_{ex} = 7.4 \times 10^5\ s^{-1}$ (from k_{ex} at 25 °C and $\Delta H^{\ddagger}$, ref 25) and the k_i values are usually close to $4 \times 10^5\ s^{-1}$ (Table II). In our opinion, the somewhat higher values for k_1 and k_1' given in Table I do not speak against the proposed mechanism but merely reflect the uncertainties of the evaluation of the rate constants for the first substitution step in case of AMP as ligand. In particular two factors have to be mentioned in this context.

TABLE II: Complex Formation Kinetics of Reactions Co^{2+} + L

L	k_f, $M^{-1}\ s^{-1}$	$k_i = k_f/K_o$, s^{-1}	Conditions	Ref
NH_3	6.9×10^4	4.6×10^5	11 °C, I = 0.1 M	20
	9.5×10^4	6.3×10^5	20 °C, I = 0.1 M	
		8×10^5	25 °C, I = 0.1 M	
phen	8.4×10^4	3×10^5[a]	7.5 °C, I variable	21
	3×10^5	1×10^6[a]	25 °C, I variable	
Glycine$^-$	4.6×10^5	2.6×10^5[b]	25 °C, I = 0.1 M	13
	1.5×10^6	7.5×10^5[b]	25 °C, I = 0.1 M	22
Serine$^-$	2.0×10^6	1×10^6	25 °C, I = 0.1 M	23
Malonate^{2-}	3.1×10^6		7 °C, I = 0.1 M	24
	9×10^6	6.9×10^5	25 °C, I = 0.1 M	
$HP_2O_7^{3-}$	9.3×10^7	1.4×10^6[c]	25 °C, I = 0.1 M	19, 7
$HP_3O_{10}^{4-}$	4.1×10^8	1.4×10^6[d]	25 °C, I = 0.1 M	19, 7

[a] With K_o = 0.3. [b] With K_o = 2.0. [c] With K_o = 67. [d] With K_o = 300.

First, the values of k_1, k_1', K_1, and K_1' are affected by the uncertainties in the calculation of K_0 and K_0'. Second, the fitting procedure described above is much more sensitive to the values of k_2 and $k_2 + k_{-2}$ than to the value of k_{1f}. This can be demonstrated explicitly by differentiating the expression for $1/\tau_-$ with respect to k_{1f}, k_2, and $k_2 + k_{-2}$, respectively. The reason for this behavior is easily rationalized in terms of the data of Table I: k_{-1} and k_{-1}' are appreciably larger than k_2 and k_2'; if they were *very* much larger, then the first substitution step would represent a rapid preequilibrium as compared to the second complexation step, and its rate constants could not be evaluated at all. As a consequence of these conditions, a reasonably good fit can still be obtained with values of k_{1f} which are about a factor 2 (but not much more) smaller than those given above. For instance, if k_{1f} at pH 7.0 is set equal to 10×10^6 M^{-1} s^{-1}, the fitting of k_2 and $k_2 + k_{-2}$, and then of k_{1f} for pH 6.0 and 5.0 leads finally to $k_1 = 9.5 \times 10^5$ s^{-1}, $k_1' = 6.8 \times 10^5$ s^{-1}, $k_2 = 5.1 \times 10^4$ s^{-1}, and $k_{-2} = 3.6 \times 10^4$ s^{-1}. The standard deviation of the experimental points from those calculated with these rate constants is only by a factor 1.22 larger than that obtained using the rate constants of Table I.

Also, estimates of the rates of the protolytic reactions under the conditions of this study (pH 5.0–7.0, [buffer] = 0.001 M; $pK_{buff} = 6.15$) based on the general rules for proton transfer processes[27] indicate that the assumption of rapid protolytic preequilibrations is only a rather crude approximation for some of the proton transfer steps of reaction scheme 6, if a very rapidly complexing metal ion like Co^{2+} is involved. At pH 7.0, protolytic equilibrations are not of importance since the concentrations of protonated species are small compared to those of the unprotonated species, and complex formation proceeds almost exclusively via the upper path of reaction scheme 6. Thus only the evaluation of k_1', but not of k_1, could possibly be affected thereby.

The rate constants k_2 and k_2' for ring closure (Table I) are about one order of magnitude lower than those for normal substitution reactions at Co^{2+} (k_i at 8 °C, Table II). Since the phosphate group is bound about as strongly as a water molecule to Co(II) (k_{-1} and k_{ex} are rather similar), this difference is probably not due to an inductive effect of the phosphate group already coordinated to the Co(II) which leads to a decrease in the rate of exchange of the other coordinated H_2O molecules, but indicates a steric hindrance in forming the chelate structure. This assumption appears most reasonable; an AMP molecule can adopt a wide variety of conformations, but ring closure can occur only when the adenine group is close to the Co(II)–phosphate moiety. The low value of k_2 therefore most likely reflects an entropy effect.

Finally, the data of Table I allow the calculation also of the time constants of the fast relaxation effect τ_+, which has not been observed experimentally. A pH 7.0, the values of τ_+ are about 12–14 times shorter than those of τ_- and vary between 1.2 and 2.6 μs. This is just outside the time range of the temperature-jump apparatus which has been used and the heating time of which was ca. 2 μs. Moreover, the amplitude of this relaxation effect is expected to be very small, since the first binding step (binding solely to the phosphate group) will hardly affect the spectral properties of the adenine group, and the coupling of the second step to the first step is rather weak with k_{-1} being appreciably larger than k_2.

Acknowledgment. A.P. is grateful to the Max-Planck-Gesellschaft for a fellowship, and to Professor M. Eigen for providing the facilities to carry out this work.

References and Notes

(1) Permanent address: Laboratoire de Chimie Physique Organique, Université de Nancy I, C.O. 140, 54037 Nancy Cedex, France.
(2) A. T. Tu and M. J. Heller in "Metal Ions in Biological Systems", Vol. 1, H. Sigel, Ed., Marcel Dekker, New York, N.Y., 1974, p 1.
(3) R. M. Izatt, J. J. Christensen, and J. H. Rytting, *Chem. Rev.*, **71**, 439 (1971).
(4) U. Weser, *Struct. Bond.*, **5**, 41 (1968).
(5) R. Phillips, *Chem. Rev.*, **66**, 501 (1968).
(6) H. Diebler, M. Eigen, and G. G. Hammes, *Z. Naturforsch. B*, **15**, 554 (1960); M. Eigen and G. G. Hammes, *Adv. Enzymol.*, **25**, 1 (1963).
(7) C. M. Frey and J. Stuehr in "Metal Ions in Biological Systems", Vol. 1, H. Sigel, Ed., Marcel Dekker, New York, N.Y., 1974, p 51.
(8) R. S. Taylor and H. Diebler, *Bioinorg. Chem.*, **6**, 247 (1976).
(9) G. Schwarzenbach and H. Flaschka, "Die komplexometrische Titration", 5th ed, Enke Verlag, Stuttgart, 1965, p 194.
(10) M. Eigen and L. De Maeyer, in "Technique of Organic Chemistry", Vol. VIII/2, 2nd ed, A. Weissberger, Ed., Interscience, New York, N.Y., 1963.
(11) R. A. Robinson and R. H. Stokes, "Electrolyte Solutions", 2nd ed, Butterworths, London, 1959, p 491. (The temperature dependence of the activity coefficients is very small, see p 481.)
(12) J. L. Banyasz and J. E. Stuehr, *J. Am. Chem. Soc.*, 96, 6481 (1974).
(13) See, e.g., G. G. Hammes and J. I. Steinfield, *J. Am. Chem. Soc.*, **84**, 4639 (1962).
(14) M. M. Taqui Khan and A. E. Martell, *J. Am. Chem. Soc.*, **89**, 5585 (1967).
(15) E. Doody, E. R. Tucci, R. Scruggs, and N. C. Li, *J. Inorg. Nucl. Chem.*, **28**, 833 (1966).
(16) H. Sigel and H. Brintzinger, *Helv. Chim. Acta*, **47**, 1701 (1964).
(17) H. Sigel, K. Becker, and D. B. McCormick, *Biochim. Biophys. Acta*, **148**, 655 (1967).
(18) H. Irving and R. J. P. Williams, *J. Chem. Soc.*, 3192, (1953).
(19) G. G. Hammes and M. L. Morrell, *J. Am. Chem. Soc.*, **86**, 1497 (1964).
(20) D. B. Rorabacher, *Inorg. Chem.*, **5**, 1891 (1966).
(21) R. H. Holyer, C. D. Hubbard, S. F. A. Kettle, and R. G. Wilkins, *Inorg. Chem.*, **4**, 929 (1965).
(22) G. Davies, K. Kustin, and R. F. Pasternack, *Inorg. Chem.*, **8**, 1535 (1969).
(23) R. L. Karpel, K. Kustin, and R. F. Pasternack, *Biochim. Biophys. Acta*, **177**, 434 (1969).
(24) F. P. Cavasino, *Ric. Sci.*, **35**, (II-A), 1120 (1965).
(25) P. E. Hoggard, H. W. Dodgen, and J. P. Hunt, *Inorg. Chem.*, **10**, 959 (1971).
(26) M. Eigen and R. G. Wilkins, *Adv. Chem. Ser.*, **No. 49**, 55 (1965).
(27) M. Eigen, *Angew. Chem., Int. Ed.*, **3**, 1 (1964).

Kinetic Studies of Potential Bifunctional Acid–Base Catalysts in Aqueous Solution. The Iodination of Acetone

J. Spaulding, J. E. Stein, and J. E. Meany*

Department of Chemistry, Central Washington State College, Ellensburg, Washington 98926 (Received February 22, 1977)

Publication costs assisted by the Central Washington State College Research Fund

The catalysis of the iodination of acetone by a series of general bases was studied in H_2O and in D_2O at 25.0 °C and at an ionic strength of 0.1 M. Catalytic rate coefficients were determined for general bases which possess removable protons: monohydrogen phosphate dianion, $k_{HPO_4^{2-}} = 1.56 \times 10^{-3}$ M^{-1} min^{-1}; monohydrogen arsenate dianion, $k_{HAsO_4^{2-}} = 2.80 \times 10^{-3}$ M^{-1} min^{-1}; imidazole, $k_{Im} = 1.12 \times 10^{-3}$ M^{-1} min^{-1} and those restricted to monofunctional general base catalytic action: diethylmalonate dianion, $k_{(C_2H_5)_2C(CO_2^-)_2} = 0.126 \times 10^{-3}$ M^{-1}; monomethyl phosphate dianion, $K_{CH_3PO_4^{2-}} = 0.522 \times 10^{-3}$ M^{-1} min^{-1}; monoethyl phosphate dianion, $k_{C_2H_5PO_4^{2-}} = 0.462 \times 10^{-3}$ M^{-1} min^{-1}; and *N*-methylimidazole, $k_{CH_3Im} = 1.18 \times 10^{-3}$ M^{-1} min^{-1}. Solvent deuterium isotope effects for both groups of catalysts were observed to be of similar magnitude, $k_B^{H_2O}/k_B^{D_2O} = \sim 1.2$. The application of the Brønsted catalysis law to take into account pK_a differences and statistical correction factors indicates normal catalytic behavior for all bases studied with the exception of $(C_2H_5)_2C(CO_2^-)_2$ which is less than one-tenth that expected. The corresponding analysis was applied to the hydration of acetaldehyde catalyzed by HPO_4^{2-}, $CH_3PO_4^{2-}$, and $(C_2H_5)_2C(CO_2^-)_2$. Again it was determined that the catalytic effectiveness of HPO_4^{2-} and $CH_3PO_4^{2-}$ are as expected whereas that for $(C_2H_5)_2C(CO_2^-)_2$ is abnormally low.

Introduction

A classic example of bifunctional acid–base catalysis is the 2-pyridone-catalyzed mutarotation of 2,3,4,6-tetramethylglucose in benzene solvent.[1,2] A wide variety of general acid–general base-catalyzed reactions have been found considerably more sensitive toward catalysis by the mono- and dianions of phosphate than other acids and bases of similar strength.[3-11] It has been suggested that catalysis by the components of phosphate buffers is abnormally high and reflects their capacity to act as bifunctional catalysts[9-13] (also referred to as tautomeric catalysts[12]). Such catalytic involvement is conceivable for ketone enolizations (reaction 1) and has been suggested

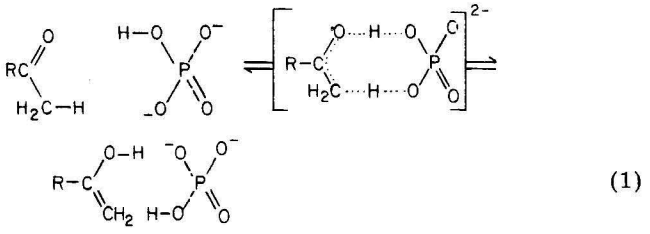

(1)

for the hydration of aldehydes.[4,12,13] For the hydration of acetaldehyde,[4] for example, it was found that monohydrogen phosphate dianion is 12 times more catalytic than diethylmalonate dianion, a base of similar pK_a but restricted to monofunctional catalytic behavior by virtue of the fact that it possesses no removable protons. Similarly, in the present study, we observed for the iodination of acetone that the magnitude of phosphate catalysis exceeds that of diethylmalonate dianion by a factor of 12.

The purpose of the present investigation is to explore the question of whether such comparative catalytic data indeed implies bifunctional catalysis by substances (such as the dianion of monohydrogen phosphate) which possess appropriately positioned acidic and basic sites.

This paper describes the general base-catalyzed iodination of acetone by phosphate, arsenate, diethylmalonate, monoalkyl phosphates, imidazole (Im), and *N*-methylimidazole (CH_3Im), bases which differ in structure and charge type but are of similar pK_a. Comparisons of kinetic parameters are made between potential "tautomeric" catalysts and catalysts structurally restricted so that only monofunctional action is possible. These results, in turn, are compared with those corresponding to the reversible hydration of acetaldehyde.

Experimental Section

The iodination of acetone was followed by the disappearance of the triiodide band at 353 nm (ϵ 24 500 M^{-1} cm^{-1})[14] by means of a Beckman Acta II recording spectrophotometer. The initiation of the kinetic runs and the determination of the observed rate constant, k_{obsd}, are described in earlier communications.[4,15] Values of k_{obsd} were generally reproducible to within +1%. The hydration of acetaldehyde was also followed spectrophotometrically by following the diminution of the carbonyl band at 278 nm (ϵ 16.2 M^{-1} cm^{-1}). The pseudo-first-order rate constants were determined as described in earlier work.[4]

Spectral grade acetone and reagent grade acetaldehyde were fractionally distilled immediately prior to use. Sodium 2,2-diethylmalonate was prepared from the commercially available diethyl ester (Eastman Kodak, White Label) by saponification. Monomethyl phosphoric acid and monoethyl phosphoric were separated from commercially available mixtures of the respective monoalkyl and dialkyl phosphoric acids (Stauffer Chemicals) by the selective precipitation of the corresponding barium monoalkyl phosphate salts.[16] The mono- and dialkyl phosphates were also separated by the ion exclusion method described by Cesarano and Lepscky.[17] Kinetic results using the monoalkyl phosphates isolated by the two techniques were found to be in strict accord. Since alkyl phosphate esters are known to undergo exceedingly slow hydrolysis,[17] their solutions were generally prepared directly prior to use. All other reagents used for buffer preparations were obtained from commercial sources in reagent grade or of comparable purity. The ionic strength of all buffer solutions was adjusted to 0.1 M by adding the appropriate quantities of reagent grade sodium chloride.

Results and Discussion

It has long been known that the rate-determining step in the halogenation of acetone is its enolization,[19,20] a

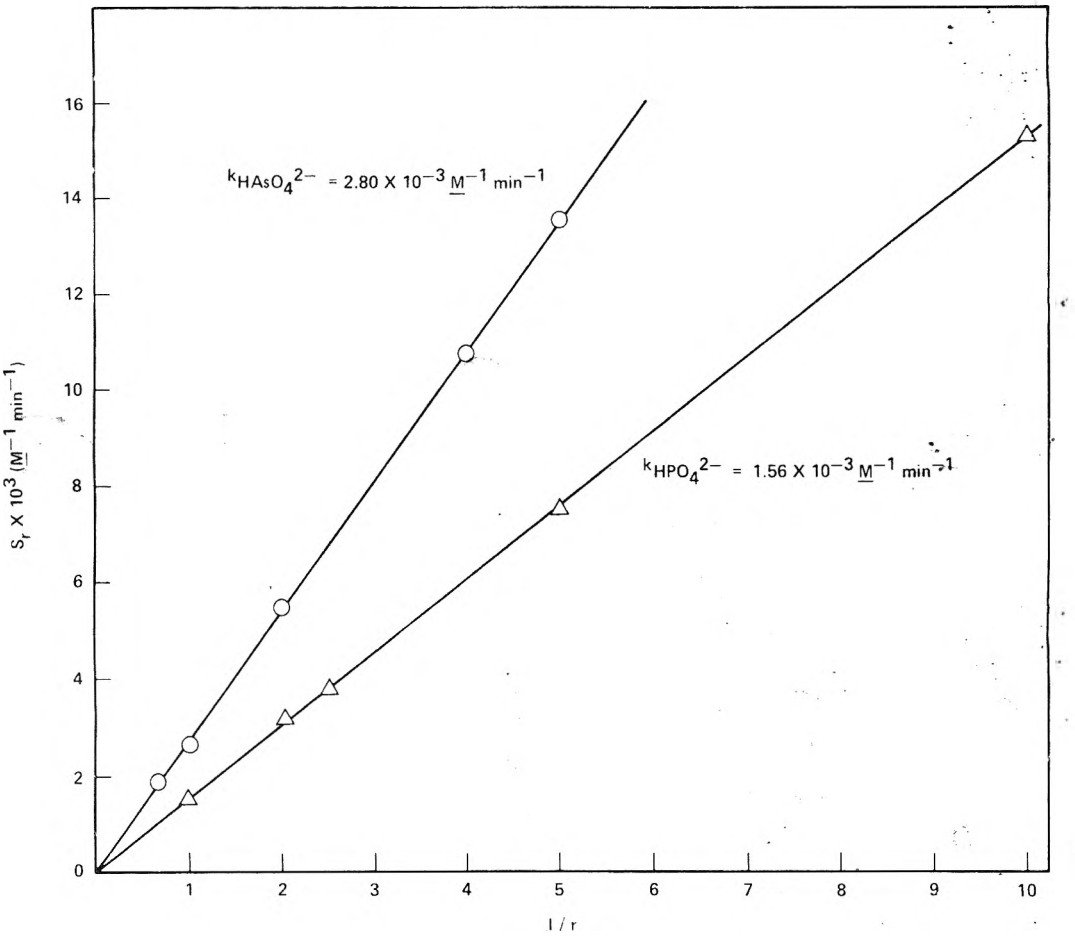

Figure 1. Catalysis of the idoination of acetone by arsenate (O) and phosphate (Δ) at various buffer ratios at 25.0 °C.

process which is subject to general acid and general base catalysis.[20-22] The observed rate constant for the reaction, k_{obsd}, may be represented by a sum of kinetic terms, one for each acidic component, A, and basic component, B, in the reaction solution:

$$k_{obsd} = k_0 + k_{L_3O^+}[L_3O^+] + k_{OH^-}[OH^-] + k_A[A] + k_B[B] \quad (2)$$

where k_0 is the spontaneous rate coefficient and L is used to denote either hydrogen or deuterium. In certain buffer systems, a product term, $k_{AB}[A][B]$, has been experimentally detected[21] which has, however, been analyzed and interpreted in a number of ways.[20-26]

Equation 2 can be written as

$$k_{obsd} = k_0 + k_{L_3O^+}[L_3O^+] + k_{OL^-}[OL^-] + [A](k_A + k_B/r) \quad (3)$$

where r is the buffer ratio [A]/[B]. If eq 3 describes the catalytic components for the reaction, plots of k_{obsd} vs. [A] at a given buffer ratio should be linear with a slope, $S_r = k_A + k_B/r$ and intercept $I_r = k_0 + k_{L_3O^+}[L_3O^+] + k_{OL^-}[OL^-]$. For arsenate and phosphate buffers, S_r was determined at various buffer ratios (Figure 1) allowing the evaluation of $k_{HAsO_4^{2-}}$ and $k_{HPO_4^{2-}}$, respectively. The intercept values, too small to be detected, indicate the absence of any significant catalysis by the conjugate acids, $H_2AsO_4^-$ and $H_2PO_4^-$. Accordingly, for the other buffer systems investigated in the present work, k_B was simply determined from the slopes of the lines obtained from plots of k_{obsd} vs. [B] at a buffer ratio of 1 (Figure 2). The linearity of these plots indicates the absence of any detectable simultaneous catalytic action of the acidic and basic components (A and B) for the buffer systems studied.

TABLE I: Catalytic Rate Coefficients for the Iodination of Acetone at 25.0 °C (Ionic Strength = 0.1 M)

Catalyst	pK_a[a]	p[b]	q[b]	10^3-$k_B^{H_2O}$ M^{-1} min^{-1}	10^3-$k_B^{D_2O}$ M^{-1} min^{-1}
HPO_4^{2-}	6.9	2	3	1.56	1.20
$HAsO_4^{2-}$	6.8	2	3	2.80	2.51
$(C_2H_5)_2C(CO_2^-)_2$	7.1	1	4	0.126	
$CH_3PO_4^{2-}$	6.4	1	3	0.522	0.444
$C_2H_5PO_4^{2-}$	6.6	1	3	0.462	
Im	6.9	2	1	1.12	
CH_3Im	7.0	1	1	1.18	

[a] Values obtained from pH measurements at buffer ratio, r = 1, ionic strength of 0.1 M. [b] As defined in text.

The general acid–general base-catalyzed hydration of acetaldehyde was investigated in methyl phosphate buffers. The overall pseudo-first-order rate constant again may be represented by eq 1 and 2. For this reaction, however, acidic buffer components with pK_a values around neutrality also contribute substantial catalysis.[4] The catalytic rate coefficients for the methyl hydrogen phosphate and methyl phosphate anions were determined by the analysis described in earlier work[4] ($k_{CH_3(H)PO_4^-}$ = 8.0 M^{-1} min^{-1}, $k_{CH_3PO_4^{2-}}$ = 15.0 M^{-1} min^{-1}).

A comparison of the catalytic effectiveness of the various buffer components studied for the iodination of acetone is illustrated in Figure 2 and Table I. A cursory inspection of the data in Table I would indicate that, taking into consideration differences of pK_a for the buffer systems investigated, the relative values of the observed catalytic coefficients are all rather comparable with the exception of the low value for diethylmalonate dianion. A more

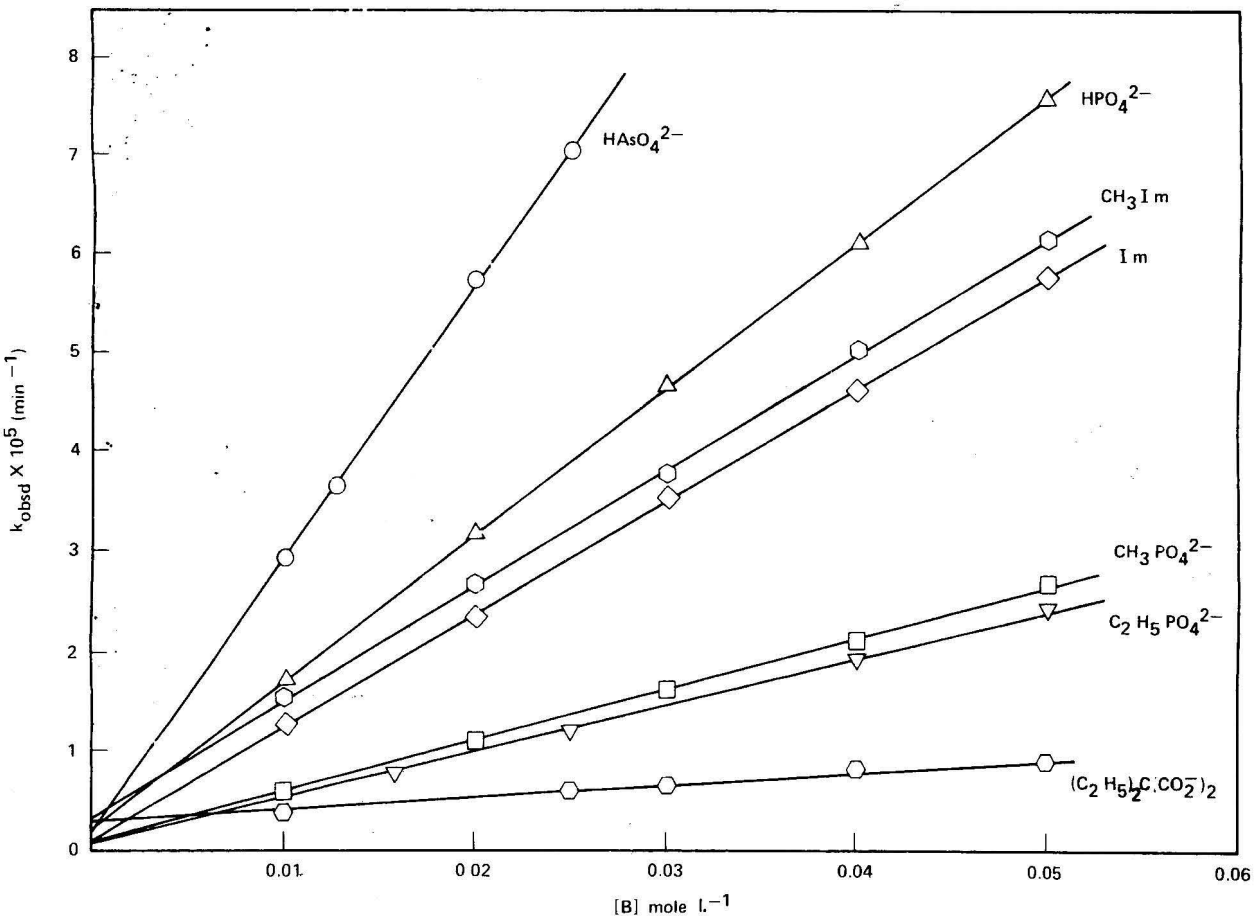

Figure 2. The general base-catalyzed iodination of acetone: (O) $k_{HAsO_4^{2-}} = 2.80$ M^{-1} min^{-1}; (Δ) $k_{HPO_4^{2-}} = 1.56$ M^{-1} min^{-1}; (○) $k_{CH_3Im} = 1.18$ M^{-1} min^{-1}; (◇) $k_{Im} = 1.12$ M^{-1} min^{-1}; (□) $k_{CH_3PO_4^{2-}} = 0.522$ M^{-1} min^{-1}; (▽) $k_{C_2H_5PO_4^{2-}} = 0.462$ M^{-1} min^{-1}; (○) $k_{(C_2H_5)_2C(CO_2^-)} = 0.126$ M^{-1} min^{-1}.

TABLE II: A Comparison of the Relative Catalytic Effectiveness of Bases for the Iodination of Acetone and the Hydration of Acetaldehyde

	Iodination of acetone			Hydration of acetaldehyde		
Catalyst	$10^3 k_B^{obsd}$ M^{-1} min^{-1}	$10^3 k_B^{calcd\,a}$ M^{-1} min^{-1}	k_B^{obsd}/k_B^{calcd}	k_B^{obsd} M^{-1} min^{-1}	$k_B^{calcd\,a}$ M^{-1} min^{-1}	k_B^{obsd}/k_B^{calcd}
HPO_4^{2-}	1.56	1.56	1.0	35.9[b]	35.9	1.0
$CH_3PO_4^{2-}$	0.522	0.31	1.7	15.0	16.0	0.94
$C_2H_5PO_4^{2-}$	0.462	0.46	1.0			
$(C_2H_5)_2C(CO_2^-)_2$	0.126	1.3	0.097	3.00[b]	38.0	0.079
$HAsO_4^{2-}$	2.80	1.2	2.3			
Im	1.12	1.3	0.86	3.90[b]	20.0	0.20[c]
CH_3Im	1.18	0.90	1.3			

[a] Values of k_B^{calcd} determined as described in text. [b] Reference 4. [c] It should be noted that imidazole reacts with acetaldehyde to form a complex.[4]

quantitative comparison of catalytic coefficients incorporating variations in pK_a may be achieved by the application of the Brønsted catalysis law.[27] Since the general bases investigated have similar values of pK_a, catalytic coefficients of the various bases were calculated (Table II) *in reference* to the experimental catalytic coefficient for the monohydrogen phosphate dianion. If it is assumed that log $k_{HPO_4^{2-}}$ falls directly on the Brønsted curve, the calculated catalytic coefficients, k_B^{calcd}, for the other bases studied may be evaluated:

$$k_B^{calcd} = k_{HPO_4^{2-}}\left(\frac{q_B}{q_{HPO_4^{2-}}}\right)\left(\frac{K_a^{HPO_4^{2-}} p_B q_{HPO_4^{2-}}}{K_a^{B} q_B p_{HPO_4^{2-}}}\right)^{\beta} \quad (4)$$

where $q_{HPO_4^{2-}}$ and $p_{HPO_4^{2-}}$, and q_B and p_B represent statistical correction factors. For the iodination of acetone the value $\beta = 0.88$ was used.[22] Again, based on this comparative analysis, it will be noted that with the exception of the dimethylmalonate dianion, the observed catalytic rate coefficients, k_B^{obsd}, are in rather close agreement with the corresponding calculated values, k_B^{calcd}.

The solvent deuterium isotope effects determined for the dianions of phosphate, arsenate, and methyl phosphate (Table I) are of similar magnitude,[28] $k_{H_2O}/k_{D_2O} = 1.1$–1.3. Earlier work showed almost identical isotope effects for the general base-catalyzed iodination of esters of pyruvic acid.[30] The close similarity in catalytic effectiveness of general bases in H_2O and D_2O may imply that, for these enolizations, the transition state involves the direct interaction between the general base and the methyl hydrogen of the substrate. This may be contrasted with the suggested intervention of one or more solvent "bridging" molecules in the general base-catalyzed hydration of aliphatic aldehydes[4,5,31] for which considerably larger ratios of k_{H_2O}/k_{D_2O} have been observed.[4]

The close similarity in solvent deuterium isotope effects for the dianions of inorganic phosphate, arsenate, and monomethyl phosphate and the comparable magnitude of

the relative catalytic effectiveness of these general bases strongly suggests that parallel mechanisms of catalysis are operative for the enolization of acetone. It would appear that since the dianions of the alkyl phosphate esters may act only as general bases, catalysis by the monohydrogen phosphate dianion is also monofunctional. The same is probably true in the case of arsenate.

The corresponding analysis (eq 4) was applied to the hydration of acetaldehyde for which the value of $\beta = 0.45$ was taken.[32] Again, for this reaction, HPO_4^{2-} is ca. 12 times more effective than diethylmalonate[4] despite the fact that the latter is slightly stronger in its basicity. This observation has previously been interpreted[4,12,13] as resulting from bifunctional catalytic behavior by HPO_4^{2-}. As indicated in Table II, however, the close correlation of values of k_B^{obsd} and k_B^{calcd} for monohydrogen phosphate and the monoalkyl phosphate dianions again implies that the former is a monofunctional catalyst for the hydration of acetaldehyde.

Imidazole could conceivably function as a tautomeric catalyst. Rony[12] has proposed that the related compounds pyrazole and 1,2,4-triazole function in this manner. For the iodination of acetone, however, the observed and calculated rate coefficients for imidazole and *N*-methylimidazole (Table II) indicate normal monofunctional catalytic behavior. This was also found to be the case for the imidazole-catalyzed hydrolysis of D-glucono-δ-lactone and certain of its methylated derivatives.[33] On the other hand, for the hydration of aliphatic aldehydes,[4,5] catalysis by imidazole was observed to be ca. one-ninth as effective as HPO_4^{2-}. This apparent anomally may in part be due to the fact that imidazole complexes with aliphatic aldehydes,[4] which in turn could reduce the effective concentration of the catalyst. We were unable to detect any complexation between acetone and imidazole through spectrophotometric measurements of the type described in earlier work.[4]

The present work shows that catalysis by diethylmalonate is considerably less effective than that by organic or inorganic phosphate for two reactions for which bifunctional catalysis by HPO_4^{2-} is obviously not operative. Thus, for the two reactions under consideration, catalysis by HPO_4^{2-} does not represent a positive deviation from the respective Brønsted plots, but rather diethylmalonate dianion represents a negative deviation (ca. 1.0–1.1 log units, Table II). A similar conclusion has been reached by Pocker and Dickerson[5] for the hydration of certain aliphatic aldehydes. From preliminary studies,[34] it appears that the abnormally low catalysis of the iodination of acetone by diethylmalonate is an effect caused largely by the entropy of activation ($\Delta S^{\ddagger}_{(C_2H_5)_2C(CO_2^-)_2} = -37.8$ eu vs $\Delta S^{\ddagger}_{HPO_4^{2-}} = -14.8$ eu) despite the fact that the slightly stronger base strength of diethylmalonate is reflected by a somewhat more favorable enthalpy of activation ($\Delta H^{\ddagger}_{(C_2H_5)_2C(CO_2^-)_2} = 14.0$ kcal/mol vs. $\Delta H^{\ddagger}_{HPO_4^{2-}} = 19.3$ kcal/mol).

There is an important advantage associated with the relatively low catalytic effectiveness of the buffer components of diethylmalonate. Buffers of diethylmalonate regulate pH at approximately physiological levels. Their experimental use in enzymatically catalyzed processes, which are also subject toward general acid–general base catalysis, allows the precise isolation of the enzymatic catalytic component from overall rates.[35]

Well founded examples of bifunctional catalysis by simple chemical systems in aqueous solution undoubtedly exist in the literature.[9,10,13] However, general acid–general base-catalyzed reactions may be prematurely labeled as involving bifunctional catalysis on the basis of the relative catalytic effectiveness of a limited number of acids or bases of similar acidic or basic strength. In hydroxylic solvents, the dual requirements of acidic and basic catalytic functional groups on a single catalytic species may be obviated by amphoteric solvent properties. Efforts have been made to establish criteria for predicting potential bifunctional catalytic pathways. Not only is it essential for the catalyst to possess special geometric structural requirements but there must exist the additional compatability of the acidic and basic properties of the substrate site and the catalyst.[36]

Acknowledgment. This work was partially supported by the Central Washington State College Research Fund.

References and Notes

(1) C. G. Swain and J. F. Brown, Jr., *J. Am. Chem. Soc.*, **74**, 2534, 2538 (1952).
(2) P. R. Rony, *J. Am. Chem. Soc.*, **90**, 2824 (1968).
(3) Y. Ogata, A. Kawaski, and I. Kishi, *J. Chem. Soc. B*, 703 (1968).
(4) Y. Pocker and J. E. Meany, *J. Phys. Chem.*, **71**, 3113 (1967), and earlier references quoted therein.
(5) Y. Pocker and D. G. Dickerson, *J. Phys. Chem.*, 73, 4005 (1969).
(6) Y. Pocker and E. Green, *J. Am. Chem. Soc.*, **95**, 113 (1973).
(7) R. P. Bell and P. G. Evans, *Proc. R. Soc. London, Ser. A*, **291**, 297 (1966)
(8) S. O. Eriksson and C. Holst, *Acta Chem. Scand.*, 20, 1892 (1966).
(9) B. A. Cunningham and G. L. Schmir, *J. Am. Chem. Soc.*, **88**, 551 (1966); **89**, 917 (1967).
(10) R. K. Chaturvedi and G. L. Schmir, *J. Am. Chem. Soc.*, **90**, 4413 (1968); E. G. Sander and W. P. Jencks, *ibid.*, **90**, 4377 (1968).
(11) D. R. Robinson and W. P. Jencks, *J. Am. Chem. Soc.*, **89**, 7088 (1967).
(12) P. R. Rony, *J. Am. Chem. Soc.*, **91**, 6090 (1969), and references quoted therein.
(13) W. P. Jencks, "Catalysis in Chemistry and Enzymology", McGraw-Hill, New York, N.Y., 1969, p. 215, and references quoted therein.
(14) W. J. Alberty, R. P. Bell, and A. L. Powell, *Trans. Faraday Soc.*, **61**, 1194 (1965).
(15) J. E. Meany, *J. Phys. Chem.*, **75**, 150 (1971).
(16) R. H. A. Plimmer and W. J. N. Burch, *J. Chem. Soc.*, 292 (1929).
(17) C. Cesarano and C. Lepscky, *J. Inorg. Nucl. Chem.*, **14**, 276 (1960).
(18) M. C. Bailly, *Bull. Soc. Chim. Fr.*, **9**, 314, 340, 405, 421 (1942); A. Desjobert, *Compt. Rend.*, **224**, 575 (1947).
(19) A. Lapworth, *J. Chem. Soc.*, **85**, 30 (1904); L. Zucker and L. P. Hammett, *J. Am. Chem. Soc.*, **61**, 2791 (1939).
(20) M. L. Bender, "Mechanisms of Homogeneous Catalysis from Protons to Proteins", Wiley-Interscience, New York, N.Y., 1971, p 117, and references quoted therein.
(21) H. M. Dawson and E. Spivey, *J. Chem. Soc.*, 2180 (1930); R. P. Bell and P. Jones, *ibid.*, 88 (1953).
(22) R. P. Bell and O. M. Lidwell, *Proc. R. Soc. London, Ser. A*, **176**, 96 (1940).
(23) C. G. Swain, *J. Am. Chem. Soc.*, **72**, 4578 (1950).
(24) C. G. Swain, A. J. DiMilo, and J. P. Cordner, *J. Am. Chem. Soc.*, **80**, 5983 (1958).
(25) F. J. C. Rossetti, *Nature (London)*, **188**, 936 (1960).
(26) E. A. Shilov and A. A. Yasnikov, *Ukr. Khim. Zh.*, **23**, 215 (1957); **27**, 506 (1961).
(27) J. N. Brønsted, *Chem. Rev.*, **5**, 322 (1928).
(28) The solvent deuterium isotope effects for the general bases studied in the present work are in close agreement with that observed for the acetate catalyzed halogenation of acetone,[31] $k_{H_2O}/k_{D_2O} = 1.15$.
(29) O. Reitz and J. Kopp, *Z. Phys. Chem.*, **A184**, 429 (1939); Y. Pocker, *Chem., Ind. (London)*, 1383 (1959).
(30) M. Hegazi and J. E. Meany, *J. Phys. Chem.*, **76**, 3121 (1972).
(31) R. P. Bell and P. G. Evans, *Proc. R. Soc. London, Ser. A*, **291**, 297 (1966); M. Eigen, *Discuss. Faraday Soc.*, **39**, 7 (1965).
(32) R. P. Bell, M. H. Rand, and K. M. A. Wynne-Jones, *Trans. Faraday Soc.*, **52**, 1093 (1956).
(33) Y. Pocker and E. Green, *J. Am. Chem. Soc.*, **96**, 166 (1974).
(34) J. Spaulding and J. E. Meany, unpublished results.
(35) Y. Pocker and J. E. Meany, *J. Am. Chem. Soc.*, **87**, 1809 (1965); *Biochemistry*, **4**, 2635 (1965); **6**, 239 (1967); Y. Pocker and D. G. Dickerson, *ibid.*, **7**, 1995 (1968); Y. Pocker and J. E. Meany, *ibid.*, **13**, 1411 (1974).
(36) W. P. Jencks, *Chem. Rev.*, **72**, 705 (1972); J. E. Critchlow, *J. Chem. Soc., Faraday Trans. 1*, 1774 (1972).

Conversion of Hydroxycyclohexadienyl Radicals of Methylated Benzenes to Cation Radicals in Acid Media

K. Sehested,* J. Holcman, and E. J. Hart

Accelerator Department, Risø National Laboratory, DK-4000 Roskilde, Denmark *(Received December 14, 1976)*

Publication costs assisted by Risø National Laboratory

Formation of radical cations from the OH adducts of methylated benzenes in acidic aqueous solutions is demonstrated. The radical cation is formed as an intermediate species in the water elimination reaction in which the OH adduct is transformed into the corresponding methylbenzyl radical. The radical cations are also produced in neutral aqueous solution by reacting SO_4^- radical ions with the methylated benzenes. The cations have two absorption bands, an UV band, 280–300 nm, and a visible band, 430–470 nm, with extinction coefficient of about 6500 and 2000 M^{-1} cm^{-1}, respectively. The formation of the radical cations from the OH adducts depends on the hydrogen ion concentration, $k_{OH\ adduct+H^+} = (1.5 \pm 0.5) \times 10^9$ M^{-1} s^{-1}. The radical cations decay in acid solution exclusively into the corresponding methylbenzyl radicals.

Introduction

The hydroxyl radical is known to react with aromatic compounds preferentially in an addition reaction forming the corresponding hydroxycyclohexadienyl radical.[1] In our recent paper[2] we have shown that the OH adduct in some cases undergoes a dissociation reaction forming the radical cation. Previously both an uncatalyzed and an acid catalyzed water elimination reaction were reported from the OH adducts of phenols,[3] hydroquinone,[4] and methylated benzenes.[5] Recently some papers appeared on the acid catalyzed formation of the radical cations of biphenyl[6] and methoxylated benzenes[7] and radical zwitterions from methoxylated benzoic acids.[8] In a previous paper[5] we reported the results from a pulse radiolysis study of the methylated benzenes in aqueous solution, and we tentatively assigned a transient species, appearing as an intermediate in the water elimination reaction in acid solution, in which the OH adduct is transformed into the corresponding methylbenzyl radical to the radical cation. The present report describes further experiments which confirm our previous assignment.

Experimental Section

The methylated benzenes of the highest available purity were obtained from Merck, BDH, Koch-Light, Fluka, and K & K, and used without further purification. The perchloric acid was reagent grade from G. F. Smith and the sodium hydroxide from Merck. The water was triply distilled and all glassware was preheated to 450 °C.

The pulse radiolysis system on the Linac was described previously[5,9] and the setup on the 2.3-MeV Febetron was essentially the same except for a faster detection system. The doses were measured with the hexacyanoferrate(II) dosimeter[10] using $g(e_{aq}^- + OH) = 5.25$ and $\epsilon(420\ nm) = 1000\ M^{-1}\ cm^{-1}$.

Solutions of the liquid methylated benzenes were deaerated and saturated by bubbling gas through the solution with an excess of the methylated benzene in a 100-mL syringe. Solutions of the solid compounds were prepared in a 1-L flask by repeated evacuation and saturation with the appropriate gas. The pH was adjusted with perchloric acid or sodium hydroxide and was measured on a digital pH meter, Radiometer PHM52.

Results and Discussions

Spectrum in Acid Solution. Aqueous solutions saturated with various methylated benzenes in the pH range 0–7 were pulse radiolyzed. Solutions at pHs ≥3 were N_2O saturated and at pHs <3 Ar or O_2 saturated. At high pH, the transient species are the hydroxycyclohexadienyl radical with the characteristic broad absorption band at 320–330 nm and a small yield of the methylbenzyl radical.[1,5] As the pH is lowered, two new bands form, one below 300 nm, the other in the visible region at 430–470 nm. These bands decay simultaneously yielding a product which is identified as the corresponding methylbenzyl radical.[5] These three spectra from *p*-xylene are shown in Figure 1.

In our previous paper[5] the new spectrum was tentatively assigned to the radical cation. The intermediate species from isodurene existing between the hydroxycyclohexadienyl radical and the methylbenzyl radical spectrum is illustrated in Figure 2. At 331 nm the OH adduct absorption decays into the radical cation species absorbing at 465 nm, which successively decays into the methylbenzyl radical absorbing at 331 nm.

The decay of the OH adducts at 320–330 nm changes from a second-order reaction in neutral to pseudo-first order in acid solution. The rate of this pseudo-first-order decay is found to be linearly dependent on the hydrogen ion concentration and corresponds exactly to the buildup of the absorption at 450 nm. This behavior has also been found for the formation of radical cations of biphenyl,[6] methoxylated benzenes,[7] and methoxylated benzoic acids,[8] where the OH adduct proves to be the precursor for the radical cation. A "clean" spectrum of the radical cations, without interference from the H adduct absorption, can be obtained in oxygen-saturated acid solution, since neither the absorption bands nor the kinetics of the radical cations are affected by oxygen. This spectrum can also be obtained at pH above 3 in N_2O-saturated solutions for the higher methylated compounds. In these cases the increase of the band height at 450 nm by a factor of 2 is demonstrated in N_2O-saturated solution compared to argon-saturated solutions. Moreover it was shown in our previous paper[5] that the OH adduct is quantitatively converted into the methylbenzyl radical in acid solution. This justifies the use of the corrected yield of OH radicals in the calculation of the extinction coefficient of the new species. The correction applied to the OH radical yield is due to the small fraction entering the reaction of the direct H-atom abstraction.[5] The extinction coefficients were then calculated from the absorptions in strong acid solution, pH 0–2, both in Ar and O_2 saturated, and the results are given in Table I.

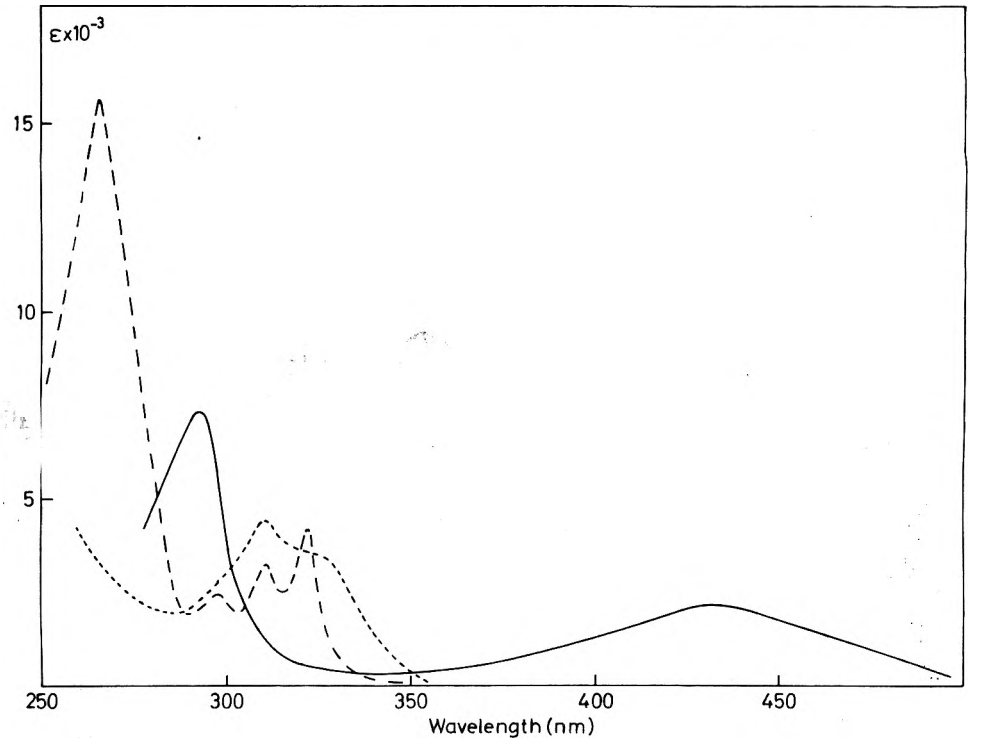

Figure 1. Spectra of transient species in the acid-catalyzed water elimination reaction of *p*-xylene: (····) OH adduct; (——) radical cation; (– – – – –) *p*-methylbenzyl radical.

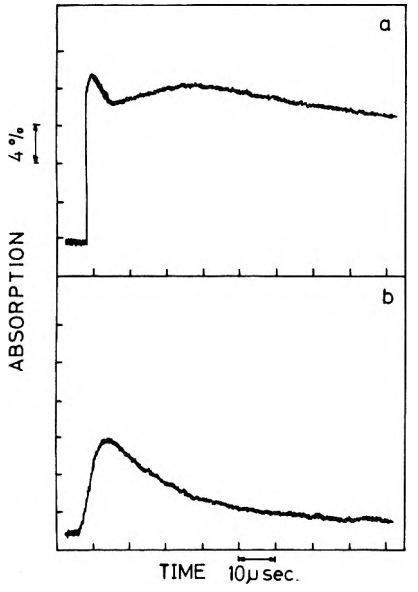

Figure 2. Oscilloscopic traces of the transients in isodurene solution, pH 3.45: (a) 331 nm (absorption of the OH adduct and the trimethylbenzyl radical); (b) 455 nm (absorption of the radical cation). The time scale in both traces is 10 μs per division.

TABLE I: Absorption Bands and Extinction Coefficients of the Radical Cations of Methylated Benzenes in Aqueous Solution

	λ_{max}, nm	ϵ, M^{-1} cm^{-1}
Toluene	285	
	430	
o-Xylene	290	6000
	430	2000
m-Xylene	285	6300
	450	2300
p-Xylene	290	7000
	435	2050
Mesitylene	292	6600
	475	2250
Hemimillitene	290	6700
	450	1950
Pseudocumene	285	7000
	445	2300
Isodurene	290	6500
	455	2200
Prehnitene	300	7000
	455	2000
Durene	295	5000
	465	~1800
Pentamethylbenzene	305	3750
	475	~1500

The high acid concentration was used in order to obtain instantaneous conversion of the OH adduct, which is necessary to get a fully developed spectrum of the radical cation of the low methylated compounds because of the fast first-order decay of their radical cations, even though the extinction coefficient for *o*- and *m*-xylene may be too low. For the same reason we are not able to offer an extinction coefficient for the toluene radical cation, because the formation and decay rate in 1 M acid is of the same order of magnitude. However, the spectrum of the toluene radical cation can be observed in even stronger acid (2–5 M), but at these acid concentrations the primary yields are not well known. The ability to observe the spectrum in very strong acid is due to a general increase of the lifetime of the radical cations of the methylated benzenes at acid concentrations above 0.5 M. This effect of acid concentration is not fully understood at the moment. For the high methylated benzenes the solubility is so low that the formation of the radical cation becomes controlled by the rate of reaction of the OH radicals with the substrate. This together with a fairly fast decay may result in a low value for the extinction coefficient for these compounds.

Formation of the New Transient Spectrum in Neutral Solution. Except for toluene and *o*- and *m*-xylene the radical cation can be observed in neutral solution by reacting SO_4^- radicals with the methylated benzenes. Persulfate is known to scavenge hydrated electrons with a rate constant of 1.1×10^{10} M^{-1} s^{-1}, producing SO_4^- radicals,[11] while the OH radical reacts much slower with the persulfate, $k \leq 10^6$ M^{-1} s^{-1}.[1] The sulfate radical reacts

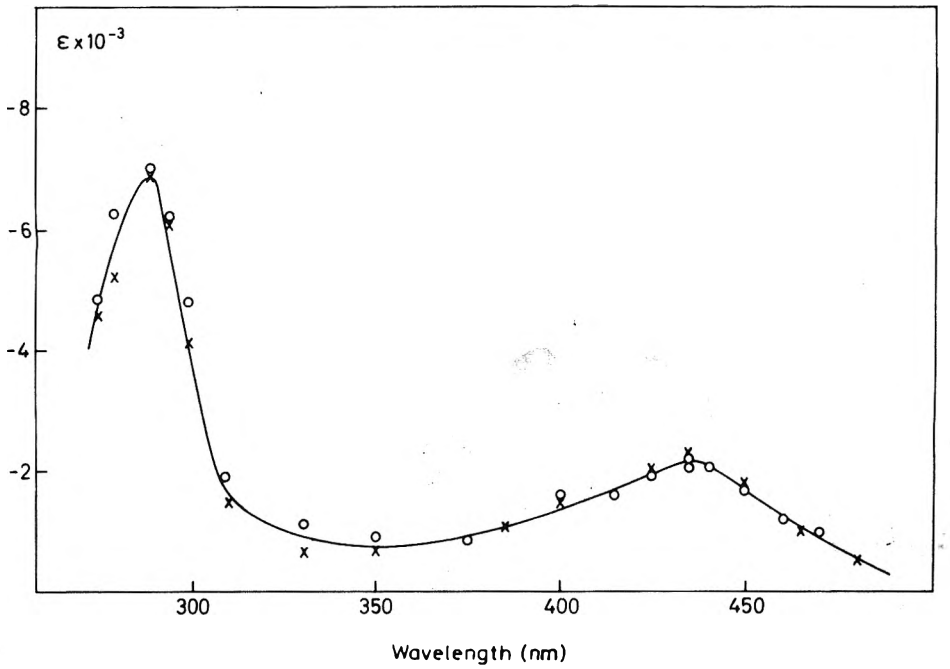

Figure 3. The spectrum of the *p*-xylene radical cation in aqueous solution: (X) O_2 saturated with 1 M $HClO_4$; (O) Ar saturated at pH 8.2, containing 5×10^{-3} M $S_2O_8^{2-}$ and 0.4 M *tert*-butyl alcohol; normalized at 435 nm.

with aromatic substrates yielding the radical cation[7,12-16] in several cases. No addition products were detected.[17]

In an Ar-saturated neutral solution of methylated benzenes containing 5×10^{-3} M $S_2O_8^{2-}$, the transient spectrum consists of absorption bands at 420–470, 320–330, and 280–300 nm. The OH radicals produce the adduct with a band at 320–330 nm, and the SO_4^- radical is believed to produce the radical cation. When the OH adduct absorption is subtracted from the spectrum, the remaining absorption is identical with the spectrum found in oxygen-saturated acid solution. Moreover the extinction coefficient based on $G_{SO_4^-} = g_{e_{aq}^-} = 2.7$ is identical with that obtained in acid solution, based on the corrected OH yield. A "clean" spectrum of the radical cation formed in the reaction with SO_4^-, free of the OH adduct absorption, may be obtained by scavenging the OH radicals by *tert*-butyl alcohol, since the SO_4^- radical reacts with the alcohol with a rate constant of $k = (9 \pm 1) \times 10^5$ M^{-1} s^{-1},[18] while the OH radical reaction has a rate constant of $k = 5.2 \times 10^8$ M^{-1} s^{-1}.[1] Using a concentration of *tert*-butyl alcohol two hundred times greater than the concentration of the methylated benzenes, more than 90% of the OH radicals are scavenged, while more than half of the SO_4^- radicals react with the methylated benzenes. The resulting spectrum at pH 8.2 is again identical with that obtained in acid solution. In Figure 3 the normalized spectrum of the *p*-xylene radical cation obtained in neutral solution containing *tert*-butyl alcohol and $S_2O_8^{2-}$ is compared with the spectrum observed in acid oxygen saturated solution.

The rate constants for the reaction of the SO_4^- radical with the various methylated benzenes were measured from the formation of the absorption band at 430 nm. These rate constants are generally three to five times lower than the rate constants for the OH radical reaction. The rate constants are all of the order of 1 to 2×10^9 M^{-1} s^{-1}. Some of the rates are rather difficult to determine accurately, however, because of the overlapping spectrum of the SO_4^- radical.

Assignment of the Transient Species. The assignment of the intermediate transient species to the radical cation is based on its identity with the species formed by the SO_4^- reaction and on the ionic strength dependency of the reaction of the species with ferrous and hydroxide ions. The reaction with Fe^{2+} was studied in N_2O-saturated sulfuric acid solution at pH 2.5–3.5. The ratio of the concentrations of the methylated benzene and the ferrous ions was adjusted so that most of the OH radicals react with the benzene. The pH was chosen as a compromise to avoid the H adduct formation and to obtain a fast transformation of the OH adduct into the radical cation. For this reason only tri- and tetramethylbenzenes were used. The reaction is a reduction of the radical cation to the parent compound and an oxidation of ferrous to ferric ions.

$$(CH_3)_n\dot{C}_6H_{6-n}^+ + Fe^{2+} \rightarrow (CH_3)_nC_6H_{6-n} + Fe^{3+} \quad (1)$$

The rate constant was determined at different ferrous ion concentrations by following the decay of the radical cation at 460 nm and the formation of ferric ions at 302 nm.[19] The rate of this reaction for pseudocumene and isodurene was $(6.0 \pm 1.0) \times 10^7$ M^{-1} s^{-1}. For the ionic strength measurements the sulfuric acid was substituted by perchloric acid and the ionic strength of the solution was adjusted with $NaClO_4$. The rate was measured from the decay of the radical cation and the rate constant was calculated from the equation

$$k_m = k_4 + k_1$$

where k_m is the measured first-order decay, k_4 the rate for the formation of the methylbenzyl radicals in acid solutions, and k_1 the rate constant for reaction 1. As was found for the anisole radical cation[20] the rate of reaction 1 is ionic strength dependent. Figure 4 shows the result for isodurene where the initial slope of the curve equals +2. This supports the conclusion that our species has a unit positive charge. k_4 proved to be independent of the salt concentration.

A second reaction supporting our assignment is the reaction with hydroxide ions yielding the OH adduct

$$(CH_3)_n\dot{C}_6H_{6-n}^+ + OH^- \rightarrow (CH_3)_n\dot{C}_6H_{6-n}OH \quad (2)$$

This reaction was studied in argon-saturated solutions at pH 8–11 containing $S_2O_8^{2-}$. The radical cation was formed

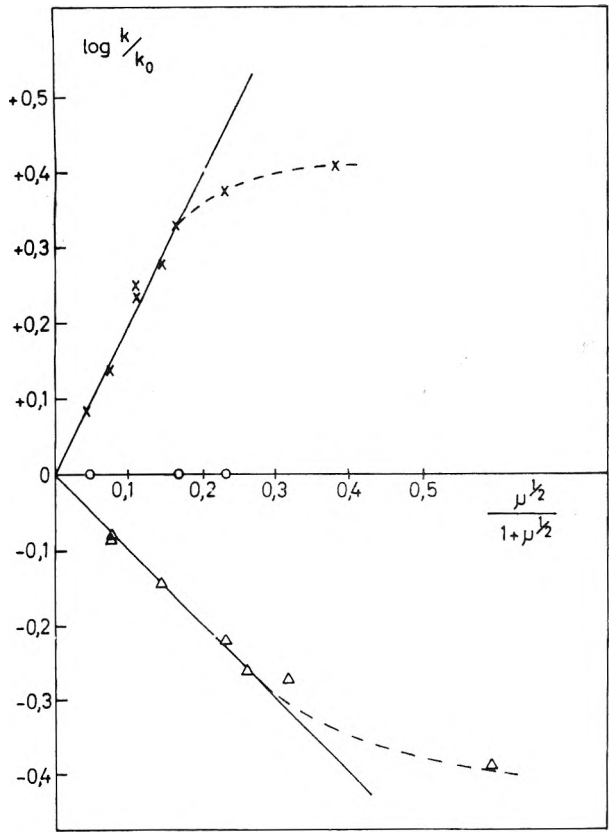

Figure 4. The effect of onic strength, μ, on the rate of the isodurene radical cation reactions: k, measured rate constant, k_0, rate constant extrapolated to zero ionic strength: (X) reaction with Fe^{2+}, pH 3.1; (O) decay into the trimethylbenzyl radical, pH 3.1; (Δ) reaction with OH^-, pH 10.5.

from SO_4^- radicals and the OH radicals formed the OH adduct. At pH 7 the radical cation decays faster than in acid solutions, and it is concluded from the additional formation of OH adduct that a reaction with water (reverse of reaction 3) competes with the formation of methylbenzyl radicals (reaction 4). This reaction will be described in a successive paper.[21] At higher pH the rate of the radical cation decay is proportional to the hydroxide ion concentration, and additional OH adduct is formed according to reaction 2 at the expense of methylbenzyl radicals. At pHs approaching 11 some minor part of the SO_4^- radicals contributes to the OH adduct formation directly through the reaction with hydroxide ions yielding OH radicals. The rate constant for this reaction is 7.3×10^7 M^{-1} s^{-1} [15] and will be significant only with compounds of low solubility. However, this reaction has no influence on the determination of the rate constant of reaction 2, as this is measured from the decay of the radical cation. The rate constant for reaction 2 was calculated from an equation analogous to (A), but instead of using k_4, which is considered to be pH independent, a rate constant as measured at pH 7 taking into account the reverse of reaction 3 is used, the reason being that reaction 2 is competing with reaction 4 as well as with the reverse of reaction 3. The rate constant for isodurene radical cation with OH^- (reaction 2) is 1.2×10^9 M^{-1} s^{-1} and, as shown in Figure 4, the curve for the rate constant as function of ionic strength has a slope of −1 again suggesting a unit positive charge for the transient species.

The cationic behavior of the species is additionally demonstrated by its unreactivity with oxygen. The spectra obtained for the negative ions of benzene, toluene, and *p*-xylene by dissolution of alkali metals in organic systems show essentially the same absorption maxima as the

TABLE II: Rate Constants for Reaction of OH Adducts of Methylated Benzenes with Hydrogen Ions

	$k_{\text{OH adduct} + H^+}$ $\times 10^{-9}$ M^{-1} s^{-1}
Toluene	
o-Xylene	>0.5
m-Xylene	
p-Xylene	>0.5
Mesitylene	>0.5
Hemimillitene	1.4 ± 0.3
Pseudocumene	1.5 ± 0.2
Isodurene	1.0 ± 0.3
Prehnitene	1.5 ± 0.2
Durene	1.1 ± 0.2
Pentamethylbenzene	1.5 ± 0.3

corresponding radical cations which should be expected for a one electron deficient original compound.[22] Furthermore the absorption energies of the toluene radical cation from the photodissociation spectra are 3.0 and 4.7 eV[23] compared to our values 2.9 and 4.35 eV in the aqueous phase. Thus our assignment of the species to the radical cation seems justified.

The Reaction Mechanism in Acid Solution. The formation and decay of the radical cation in acid solution can be rationalized by the reactions:

$$(CH_3)_n\dot{C}_6H_{6-n}OH + H^+ \rightarrow (CH_3)_n\dot{C}_6H_{6-n}^+ + H_2O \quad (3)$$

$$(CH_3)_n\dot{C}_6H_{6-n}^+ \rightarrow (CH_3)_{n-1}C_6H_{6-n}\dot{C}H_2 + H^+ \quad (4)$$

The dependency of the formation of the radical cation on the hydrogen ion concentration suggests a protonation of the OH adduct as the first step, followed by a rapid elimination of a water molecule. As we have not observed an absorption, which could be attributed to the protonated form of the OH adduct, the elimination reaction must then be very fast. An alternative mechanism could be an OH^- abstraction from the OH adduct caused by the high hydrogen ion concentration. In this case the adduct probably has to be in equilibrium with a charge-transfer complex. The OH^- elimination from OH adducts is suggested by Bansal and Henglein[24] in the cathodic process.

In the oxidation of benzene and its derivatives by the Fenton reagent and in related systems,[25,26] a reaction such as (3) involving the radical cation was suggested to explain the low yields of hydroxylated products in acid solution. Furthermore this reaction was postulated for the formation of radical cations from biphenyl[6] and methoxylated benzenes[7] and for the formation of zwitterions from methoxylated benzoic acids.[8]

Because of the complexity of the overall mechanism in the system, the formation of the radical cation from the OH adduct in acid solution is a combined effect of several reactions. The rate constant for reaction 3 cannot be accurately determined for the lower methylated compounds (one and two methyl groups) because of a fast decay of the radical cation and a back reaction with H_2O.[21] We estimate a lower limit of 5×10^8 M^{-1} s^{-1} for these compounds. For the slower decaying cations (three, four, and five methyl groups), the rate constant k(OH adduct + H^+) can be measured directly by the buildup of the positive ion transient as a function of the hydrogen ion concentration. The rate was found to be $k_3 = (1.5 \pm 0.5) \times 10^9$ M^{-1} s^{-1} for all the compounds, and we assume that this value also is valid for the lower methylated benzenes (Table II). This rate constant agrees with values reported for methoxylated benzenes.[7]

Reaction 4, a proton splitting reaction, is the main path of the decay of the radical cations of the methylated benzenes in acid solution. It was found that the conversion

of OH adducts to methylbenzyl radicals was quantitative.[5] This reaction was not observed in the study of anisole,[7,20] probably because its methyl group becomes more negative on ionization[27] contrary to the methylated benzene derivatives where the methyl group increases its positive charge. The fractional charge on the methyl group in toluene radical cation is calculated to be about 10% increasing to 20% for durene and pentamethylbenzene radical cations.[28]

Neither a dimerization of the radical cations nor a reaction with the solute, as were found in the anisole system,[20] was observed for the methylated benzenes. This may be due to the short lifetime of the radical cations and the low solubility of the methylated benzenes.

The reverse of reaction 3 is being studied in neutral solution with the radical cations formed from SO_4^-, and the results will appear in a later paper.[21]

Acknowledgment. We thank the operator staff of the accelerator at Risø for their assistance and we are indebted to W. L. McLaughlin and E. Bjergbakke for valuable discussions during the work.

References and Notes

(1) L. M. Dorfman and G. E. Adams, *Natl. Stand. Ref. Data Ser., Natl. Bur. Stand.*, **No. 46** (June 1973).
(2) J. Holcman and K. Sehested, to be published.
(3) E. J. Land and M. Ebert, *Trans. Faraday Soc.*, **63**, 1181 (1967).
(4) G. E. Adams and B. D. Michael, *Trans. Faraday Soc.*, **63**, 1171 (1967).
(5) K. Sehested, H. Corfitzen, H. C. Christensen, and E. J. Hart, *J. Phys. Chem.*, **79**, 310 (1975).
(6) K. Sehested and E. J. Hart, *J. Phys. Chem.*, **79**, 1639 (1975).
(7) P. O'Neill, S. Steenken, and D. Schulte-Frohlinde, *J. Phys. Chem.*, **79**, 2773 (1975).
(8) P. O'Neill, S. Steenken, and D. Schulte-Frohlinde, *J. Phys. Chem.*, **81**, 31 (1977).
(9) H. C. Christensen, G. Nilsson, P. Pagsberg, and S. O. Nielsen, *Rev. Sci. Instrum.*, **40**, 786 (1969).
(10) R. Rabani and M. S. Matheson, *J. Phys. Chem.*, **70**, 761 (1966).
(11) M. Anbar, M. Bambenek, and A. B. Ross, *Natl. Stand. Ref. Data Ser., Natl. Bur. Stand.*, **No. 43** (May 1973).
(12) G. Walling and D. M. Camaioni, *J. Am. Chem. Soc.*, **97**, 1603 (1975).
(13) M. E. Snook and G. A. Hamilton, *J. Am. Chem. Soc.*, **96**, 860 (1974).
(14) H. Zemel and R. W. Fessenden, *J. Phys. Chem.*, **79**, 1419 (1975).
(15) O. P. Chawla and R. W. Fessenden, *J. Phys. Chem.*, **79**, 2693 (1975).
(16) J. K. Kochi in "Free Radicals", Vol. 11, J. K. Kochi, Ed., Wiley, New York, N.Y., 1973, p 673.
(17) K. M. Bansal and R. W. Fessenden, *Radiat. Res.*, **67**, 1 (1976).
(18) E. Hayon, A. Treinin, and J. Wilf, *J. Am. Chem. Soc.*, **94**, 47 (1972).
(19) K. Sehested, E. Bjergbakke, O. L. Rasmussen, and H. Fricke, *J. Chem. Phys.*, **51**, 3159 (1969).
(20) J. Holcman and K. Sehested, *J. Phys. Chem.*, **80**, 1642 (1976).
(21) K. Sehested and J. Holcman, to be published.
(22) C. N. R. Rao, V. Kalyanaraman, and M. V. George, *Appl. Spectrosc., Rev.*, **3**, 153 (1970).
(23) R. C. Dunbar, *Chem. Phys. Lett.*, **32**, 508 (1975).
(24) K. M. Bansal and A. Henglein, *J. Phys. Chem.*, **78**, 160 (1974).
(25) C. Walling and R. A. Johnson, *J. Am. Chem. Soc.*, **97**, 363 (1975).
(26) C. R. E. Jefcoate and R. O. C. Norman, *J. Chem. Soc. B.*, **48** (1968).
(27) B. Cantone, F. Grasso, and S. Pignataro, *Mol. Phys.*, **11**, 221 (1966).
(28) A. B. King, *J. Chem. Phys.*, **47**, 2701 (1967).

The Spectral Properties of Methanol–Iodine and Ethanol–Iodine Complexes in *n*-Heptane Solution

Hing-Cheung Tse and Milton Tamres*

Chemistry Department, University of Michigan, Ann Arbor, Michigan 48109 *(Received January 27, 1977)*

Publication costs assisted by the National Science Foundation

The iodine complexes of ethanol and methanol in *n*-heptane were studied by the constant activity method, and their UV and visible spectral characteristics were determined. With decreasing alcohol concentration, the blue-shifted iodine band maxima of both complexes shift to longer wavelengths, whereas their charge-transfer band maxima shift to shorter wavelengths. The value of the blue-shifted iodine band maximum extrapolated to zero alcohol concentration is $\simeq 475 \pm 5$ nm for each complex. This is an appreciably longer wavelength than previously reported for the alcohol–iodine system. The estimated charge-transfer band maxima for ethanol–iodine and methanol–iodine are $\simeq 225 \pm 5$ and $\simeq 223 \pm 5$ nm, respectively. A model based on the self-association of alcohol and preferential solvation of the complex is proposed to explain the concentration dependence of the bands. The iodine interacts with an alcohol aggregate, the donor strength of which increases with an increase in degree of aggregation.

Introduction

Diethyl sulfide, diethyl ether, methanol, and ethanol are classical examples of *n*-type electron donors which interact with an iodine molecule to form charge-transfer complexes. These have been studied in solution before.[1-6] Results for the equilibrium constants and heats of complexation show that diethyl sulfide is a stronger donor than the ether and alcohols, the latter two being comparable in strength. According to Mulliken's theory,[7] the extent of the blue shift of the complexed iodine visible band should increase with increasing strength of the donor. Therefore, it would be expected that the blue-shifted (hereafter abbreviated by BS) iodine bands of the ether and alcohol complexes should appear in the same region of the spectrum but at appreciably longer wavelength than that of the sulfide complex. The literature data are not in accord with expectation. The often quoted values for the BS iodine band maximum (λ^{BS}) for ethanol–iodine is 443 nm and for methanol–iodine is 440 nm, these being from the work of de Maine who used carbon tetrachloride as the solvent.[5] Exactly, the same results were reported by Voigt[8] for iodine in pure ethanol and in pure methanol. These maxima are rather close to that of 435 or 437 nm reported for the diethyl sulfide–iodine complex,[1,2] but are quite far from the value of 470 nm obtained for the diethyl ether–iodine complex.[9]

Another point to consider is the intensity of the BS iodine band when complexed with donors containing an

oxygen atom. The molar absorptivities at the BS iodine band maxima (ϵ^{BS}) for the iodine complexes with diethyl ether, water, and the alcohols range from 700 to 1100 M^{-1} cm^{-1}. They are rather low, being close to or even less than those of iodine in *n*-heptane and of the aromatic hydrocarbon–iodine complexes. Mulliken and Person,[7b] in their classic book in this field, took particular note of this low intensity. They raised the question whether these values are spurious as a result of possible reaction of the water or of the alcohols with iodine, or whether they are real since the data seem reproducible.

Recently, the constant activity method based on saturated iodine solutions from tetramethylammonium polyiodides was introduced to study iodine complexes.[9] This method allows precise determination of the position of the BS iodine band. It also allows direct determination of the relative molar absorptivities of the charge-transfer band (ϵ^{CT}) and the BS iodine band. Thus, it circumvents the errors and difficulties in separating the molar absorptivity (ϵ) and equilibrium constant (K_C) from the $K_C\epsilon$ product, a problem which is present in the conventional Benesi–Hildebrand method for weak complexes. In this paper the constant activity method has been employed to investigate the ethanol–iodine and methanol–iodine systems to clarify the above points.

Experimental Section

Apparatus. A Cary 14 recording spectrophotometer was used to measure the spectra. A Varian Co. thermostattable cell jacket for the Cary 14 spectrophotometer was installed in the sample and reference cell compartments. A solution of ethylene glycol in water (1:1 mixture by volume) was circulated through the cell jackets from a constant temperature circulator (Haake FK10). The temperature within the cells was controlled to ±0.05 °C by a fixed setting mercury temperature regulator (H-B Instrument Co.) and was measured by thermocouples inserted into the cell jackets and touching the wall of the cells. Matched far-UV silica cells (Beckman Co.) with ground glass stoppers were used. Ground glass stoppers were more effective than teflon stoppers in preventing the evaporation of *n*-heptane. The cell lengths used were 10.00 cm for the visible studies and 1.00 cm for the UV studies.

Reagents. Ethanol (USP absolute) and anhydrous methanol (Mallinckrodt, Analytical Reagent) were distilled over their respective magnesium alkoxide through a 20-cm Vigreux column in a dry nitrogen atmosphere.[10] The middle cuts were taken and analyzed by vapor-phase chromatography which showed the sample to be better than 99.9% pure. The alcohols were stored in a dry box under a nitrogen atmosphere.

Spectrograde *n*-heptane (Matheson Coleman and Bell) was distilled over fresh calcium metal in a dry nitrogen atmosphere. It was also stored in the dry box.

Analytical grade iodine (Baker, Analyzed Reagent) was purified by mixing with analytical grade potassium iodide (Baker, Analyzed Reagent) and subliming twice.[4a]

Tetramethylammonium pentaiodide ($TMAI_5$) was prepared and recrystallized as described in the literature[11] (mp observed 129 °C; lit. 129–130 °C).

Procedure. In order to prevent formation of the triiodide ion[6] and to minimize the possibility of absorbance at wavelengths shorter than 240 nm due to contact charge-transfer bands of alcohol or *n*-heptane with oxygen,[12] the donors and solvent were distilled and stored in a dry box in a nitrogen atomsphere and all solutions were prepared inside the box. After filling the spectrophotometric cell, the stopper was covered with a small rubber cap and the cap was wrapped with Parafilm (American Can Co.). With these precautions, no triiodide ion was detected when iodine was added to prepare the solutions for the experiments to determine the isosbestic point. [The absorbance of the solutions at 360 nm, where triiodide ion absorbs intensely ($\epsilon \simeq 25\,000$ M^{-1} cm^{-1}),[13,14] was less than 0.004.] However, when tetramethylammonium pentaiodide was used as the constant activity iodine source, small amounts of triiodide ion were present no matter what precautions were taken.

All stock solutions and sample solutions were prepared inside the dry box using a Sargent-Welch gold chain semimicrobalance weighing to ±0.1 mg. The concentration of the iodine solutions was checked by measuring the absorbance at 520 nm using the known molar absorptivity from the literature (ϵ 918 M^{-1} cm^{-1}).[9]

To determine the isosbestic point of the system, the sample solutions were prepared in calibrated volumetric flasks using known weights of alcohol and *n*-heptane, and weighed equal aliquots of iodine stock solution. For the constant activity method, the alcohol solutions were prepared in the same way except that no iodine stock solution was used. Instead an excess of tetramethylammonium pentaiodide crystals was added directly into the cell. (0.2 g of $TMAI_5$ was used for the 10-cm cell and 0.08 g for the 1-cm cell.)

Measurement. In the determination of the isosbestic point (using pure *n*-heptane as the reference), the cells were equilibrated in the thermostattable cell jackets for 4 h with occasional shaking. In the constant activity method the cells were allowed to equilibrate in the thermostattable cell jackets for at least 48 h with occasional shaking followed by slight tapping to assure that no $TMAI_5$ crystals were attached to the cell windows.

Visible spectra were measured in the usual way, such as reported by Childs.[9] To measure the spectrum due to complex only in the UV region, a tandem arrangement of cells was used to compensate for the absorption of both ethanol and *n*-heptane at wavelengths shorter than 230 nm. The sample compartment contained two 1.00-cm cells, one with pure *n*-heptane and the other with known $[D]_0$ and $TMAI_5$ solid in *n*-heptane. The reference compartment contained two 1.00-cm cells, one with $[D]_0$ in *n*-heptane and the other with $TMAI_5$ solid in *n*-heptane. In this arrangement, the slit-width of the spectrophotometer opened to its maximum at wavelengths shorter than 210 nm; therefore, absorbance readings at these shorter wavelengths were discarded.

Treatment of Data. In the presence of liquids with a high dielectric constant (ethanol, 24.3; methanol, 32.6), the tetramethylammonium polyiodide solids will ionize slightly in solution to give triiodide ion. In the most concentrated alcohol solution used in this study, the triiodide ion concentration was estimated to be around 1×10^{-5} M, based on the reported molar absorptivity of 25 000 M^{-1} cm^{-1} at 360 nm, in ethylene chloride solution.[13,14] This is sufficiently large so that correction for the absorption due to triiodide ion has to be made in both the visible and UV regions in order to obtain the spectrum of the complex only.

Resolution of overlapping bands into its components can be achieved by a least-squares procedures.[15–17] In this study, a computer program similar to that of Fraser and Suzuki[16] was used. In the initial resolution attempts, the component bands were assumed to be a composite of Gaussian and Lorentzian shapes. The results showed that the contribution from the Lorentzian shape was small. This is consistent with what has been observed in most cases.[18] A Gaussian band shape was then assumed in all

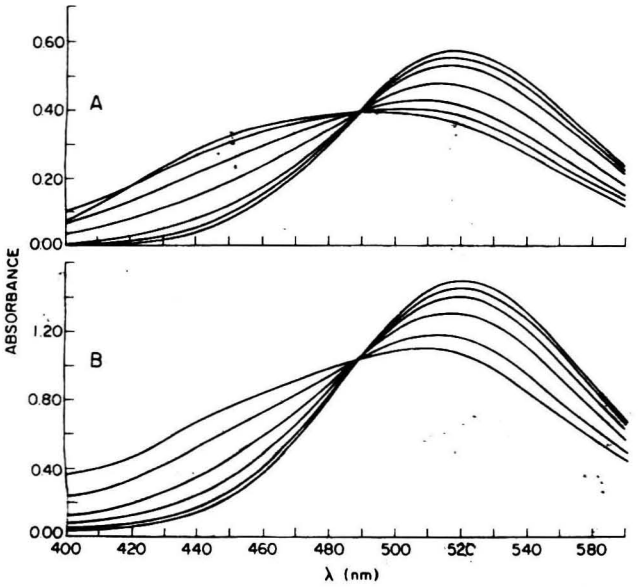

Figure 1. Isosbestic point of alcohol–iodine complexes in *n*-heptane: (A) ethanol–iodine, t = 25.0 °C, cell path = 1.00 cm; $[I_2]_0 = 6.38 \times 10^{-4}$ M, $[D]_0$ = 0.00–0.726 M; (B) methanol–iodine, t = 22.5 °C, cell path = 10.00 cm; $[I_2]_0 = 1.59 \times 10^{-4}$ M, $[D]_0$ = 0.00–0.691 M.

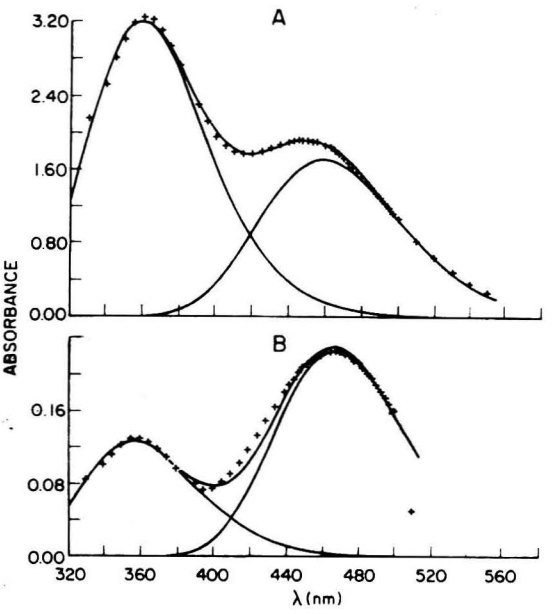

Figure 2. Visible spectra of ethanol–iodine complex in *n*-heptane obtained by the constant activity method: t = 24.8 °C, cell path = 10.00 cm (5.00-cm cell used when the absorbance exceeded 2 in the 10.00-cm cell), $[I_2]_0 = 1.94 \times 10^{-4}$ M; (+++) actual absorbance data, (—) computer resolved component bands and their sum: (A) $[D]_0$ = 0.644 M; (B) $[D]_0$ = 0.101 M.

subsequent resolutions. No asymmetric factor was used in the fitting because, experimentally, all the component bands except the CT band appeared to be symmetric. For the CT band, no absorbance data were obtained at wavelengths much shorter than the band maximum (about 225 nm) because the solution was not transparent. Hence, a Gaussian band shape was used for the CT bands as well, although it is reported that they generally are asymmetric in shape.[18,19]

Results

Figures 1a and 1b show the isosbestic points of the complexes of ethanol–iodine (at 490.8 ± 1 nm) and methanol–iodine (at 491.3 ± 1 nm). The molar absorptivity of iodine in *n*-heptane at these wavelengths is 628 and 637 M^{-1} cm^{-1}, respectively. Over the range of solutions used the isosbestic point for both complexes does not change with alcohol concentration.

The visible spectra for two solutions of ethanol–iodine obtained by the constant activity method are shown in Figures 2a and 2b, with total ethanol of 0.644 and 0.101 M, respectively. It is evident that resolution into two components, based on Gaussian shapes, matches closely the observed spectrum. The blue-shifted iodine band maximum (λ^{BS}) in Figure 2a is at 458.6 nm while in Figure 2b it is at 467.2 nm. An examination of the spectra obtained at different total ethanol concentrations revealed that the λ^{BS} is shifted to shorter wavelengths with increasing ethanol concentration. The methanol–iodine complex has similar behavior. The spectral characteristics of the BS iodine band obtained from different solutions of the two complexes are shown in Tables Ia and Ib. The variation of λ^{BS} with total alcohol concentration is plotted in Figures 3a and 3b. Since the BS iodine bands are quite broad there is an uncertainty in determining the exact maximum, and the estimated error limit is shown for each band maximum in Figure 3. Drawing a curve through the points in the figure and extrapolating to infinite dilution of alcohol gives a limiting value of λ^{BS} at ~475 ± 5 nm for both alcohol–iodine complexes.

From the spectrum obtained by the constant activity method, the molar absorptivity of the blue-shifted iodine band maximum (ϵ^{BS}) is found from the ratio of the absorbance at λ^{BS} (A^{BS}) to the absorbance at the isosbestic

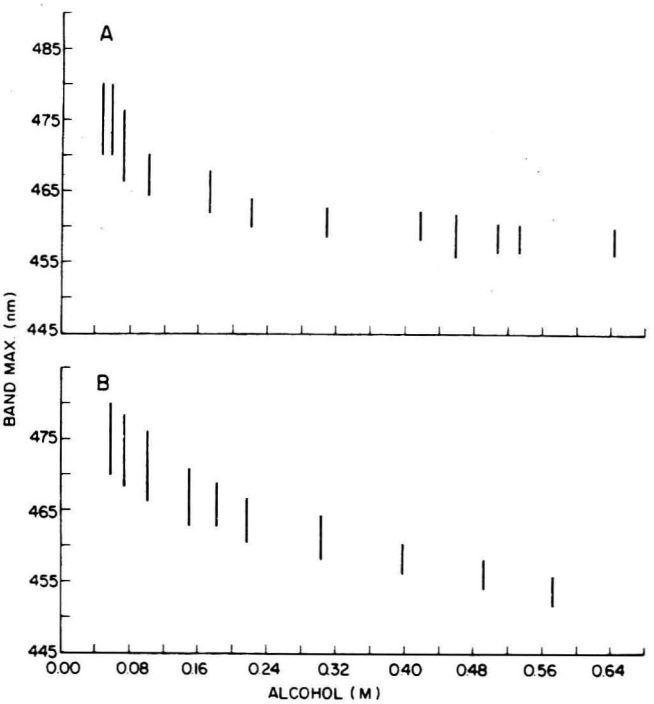

Figure 3. Variation of blue-shifted iodine band maximum with concentration of alcohol: (A) ethanol; (B) methanol.

point (A^{isos}). Since for both complexes λ^{BS} shifts to longer wavelengths (i.e., toward the isosbestic point) with decreasing alcohol concentration whereas the isosbestic point is unchanged, the ratios of A^{BS} to A^{isos} must decrease with dilution. Therefore, ϵ^{BS} also decreases with dilution. This is shown in the last column of Tables Ia and Ib which give the individual values of ϵ^{BS} at each concentration for the two complexes. The correlation of A^{BS} and A^{isos} for solutions with different alcohol concentrations is plotted in Figure 4. A least-squares treatment of the data with the line forced through the origin gives the regression lines for the two complexes shown in Figures 4a and 4b. From the slope of the line and the known molar absorptivity of the

TABLE I: Visible Band Spectral Data in *n*-Heptane Obtained by the Constant Activity Method[a]

$[D]_0$, M	λ^{BS}, nm	$\Delta\nu_{1/2}{}^{BS}$, cm^{-1}	A^{BS}	ϵ^{BS},[c] M^{-1} cm^{-1}
		(a) Ethanol–Iodine Complex		
0.644	458.6 ± 2	4261 ± 158	1.719 ± 0.048	929 ± 150
0.533	458.7 ± 2	4052 ± 82	1.344 ± 0.024	876 ± 60
0.507	458.8 ± 2	4084 ± 72	1.299 ± 0.018	895 ± 50
0.458[b]	459.0 ± 3	4074	1.130	865
0.417	460.4 ± 2	4143 ± 75	1.034 ± 0.014	861 ± 50
0.309	460.8 ± 2	4090 ± 66	0.760 ± 0.009	852 ± 45
0.222	462.0 ± 2	3995 ± 76	0.530 ± 0.007	830 ± 40
0.173[b]	465.0 ± 3	4024	0.391	792
0.101	467.2 ± 3	3805 ± 315	0.226 ± 0.008	776 ± 120
0.0721[b]	471.3 ± 5	3853	0.153	728
0.0583[b]	475.0 ± 5	4155	0.110	652
0.0466[b]	475.0 ± 5	4010	0.092	680
Av		4043 ± 230		
		(b) Methanol–Iodine Complex		
0.572	453.8 ± 2	4562 ± 100	1.312 ± 0.086	936 ± 130
0.491	456.1 ± 2	4515 ± 62	1.082 ± 0.029	892 ± 50
0.398	458.3 ± 2	4420 ± 143	0.815 ± 0.013	854 ± 60
0.302	461.2 ± 3	4457 ± 131	0.601 ± 0.008	809 ± 50
0.217	463.6 ± 3	4596 ± 153	0.437 ± 0.005	780 ± 55
0.182	465.8 ± 3	4496 ± 100	0.342 ± 0.003	754 ± 30
0.149	466.8 ± 4	4683 ± 128	0.290 ± 0.003	745 ± 45
0.100	471.1 ± 5	4424 ± 127	0.180 ± 0.002	708 ± 40
0.0743	473.3 ± 5	4499 ± 195	0.129 ± 0.003	690 ± 60
0.0584	475.4 ± 5	4418 ± 117	0.095 ± 0.001	665 ± 80
Av		4507 ± 180		

[a] The temperature was 24.8 °C, cell path length 10.00 cm. The iodine concentration was 1.94×10^{-4} M. All values were obtained by the least-squares procedure except where noted. The error limits are for one standard deviation. [b] For these solutions the values were obtained by experimental estimation as described in ref 15. [c] The error limits are estimated from the errors of the absorbance readings.

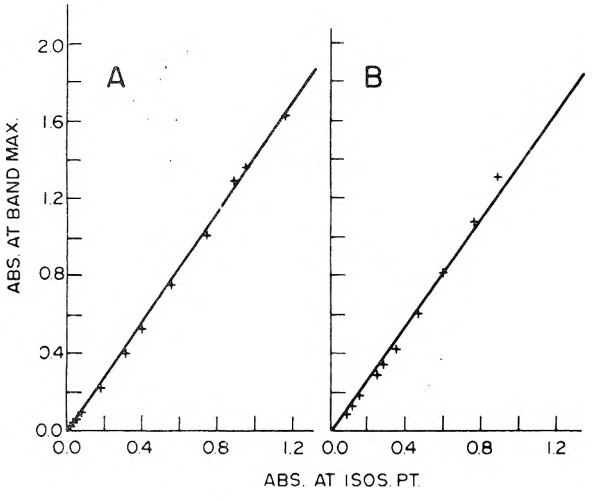

Figure 4. Molar absorptivity of the blue-shifted iodine band (with the regression line forced through the origin): (A) ethanol–iodine complex; (B) methanol–iodine complex.

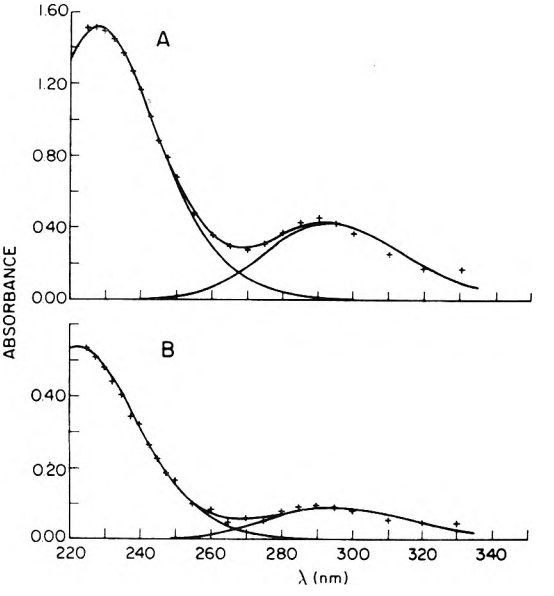

Figure 5. Ultraviolet spectra of ethanol–iodine complex in *n*-heptane obtained by the constant activity method: t = 24.8 °C, cell path = 1.00 cm, $[I_2]_0 = 1.94 \times 10^{-4}$ M; (+++) actual absorbance data, (—) computer resolved component bands and their sum; (A) $[D]_0$ = 0.475 M; (b) $[D]_0$ = 0.190 M.

complex at the isosbestic point, ϵ^{BS} was determined to be 884 ± 15 M^{-1} cm^{-1} for ethanol–iodine and 874 ± 20 M^{-1} cm^{-1} for methanol–iodine. The ϵ^{BS} so determined is a weighted regression value for the solutions.

Two UV spectra of the ethanol–iodine complex obtained by the constant activity method are shown in Figures 5a and 5b. The charge-transfer band maximum (λ^{CT}) for the concentrated ethanol solution is at 227.7 nm and for the dilute solution it is at 222.6 nm. The λ^{CT} shifts to shorter wavelengths with dilution. The methanol–iodine complex behaves similarly. Tables IIa and IIb give the spectral characteristics of the charge-transfer band for the two complexes obtained from different solutions. No solution with an alcohol concentration of 0.1 M or less was used because, during sitting in the thermostattable cell jackets for at least 24 h to attain equilibrium, some oxygen gas may diffuse into the cell. Contact charge-transfer spectra of oxygen with alcohol and with *n*-heptane appear at wavelengths below 240 nm. For concentrated solutions the small absorbance from these contacts will not lead to large error, but for dilute solutions such error would be relatively large.

Tables IIa and IIb clearly show that λ^{CT} for both complexes shifts to shorter wavelengths with dilution. The direction of this shift is opposite to that observed for λ^{BS}. Extrapolation to infinitely dilute solution is not precise because no solution with alcohol concentration less than 0.1 M was studied. Nonetheless, it appears that λ^{CT} would fall within the range of ~225 ± 5 nm for ethanol–iodine

TABLE II: UV Band Spectral Data in *n*-Heptane Obtained by the Constant Activity Method at 24.8 °C[a]

$[D]_0$, M	λ^{CT}, nm	$\Delta\nu_{1/2}^{CT}$, cm^{-1}	A^{CT}
	(a) Ethanol–Iodine Complex		
0.475	227.7 ± 2	7046 ± 411	1.518 ± 0.029
0.350	226.3 ± 2	7288 ± 527	1.139 ± 0.031
0.285	226.5 ± 2	6973 ± 100	0.946 ± 0.055
0.260	225.7 ± 2	7231 ± 504	0.804 ± 0.023
0.190	222.6 ± 2	7310 ± 631	0.537 ± 0.030
Av		7170 ± 200	
	(b) Methanol–Iodine Complex		
0.572	225.5 ± 2	6739 ± 442	1.249 ± 0.033
0.491	224.9 ± 2	6861 ± 658	1.224 ± 0.048
0.398	223.7 ± 2	7140 ± 830	0.961 ± 0.050
0.302	223.2 ± 2	6824 ± 611	0.592 ± 0.021
0.182	223.2 ± 2	6696 ± 714	0.357 ± 0.020
0.101	222.0 ± 2	6356 ± 522	0.176 ± 0.010
Av		6769 ± 413	

[a] All values were obtained by the least-squares resolution of bands. The error limits are for one standard deviation.

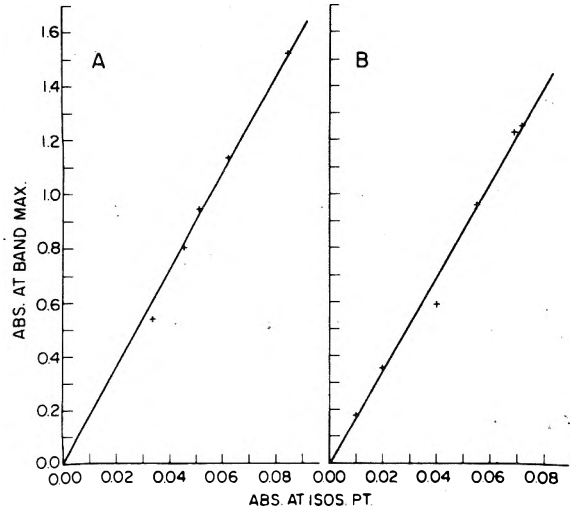

Figure 6. Molar absorptivity of the charge-transfer band (with the regression line forced through the origin): (A) ethanol–iodine complex; (B) methanol–iodine complex.

and ~223 ± 5 nm for methanol–iodine.

By studying the full spectrum, i.e., both the visible and UV regions, using 1-cm cells, it is possible to establish directly the ratio of the absorbance at the CT band maximum to the absorbance at the isosbestic point. This ratio (A^{CT}/A^{isos}) does not change systematically with dilution. Figure 6 shows the plot of this ratio for the two complexes. The linear regression line forced through the origin is also shown. From the slope of the line the molar absorptivity of the charge-transfer band is determined as 11 200 ± 200 M^{-1} cm^{-1} for ethanol–iodine and 11 000 ± 240 M^{-1} cm^{-1} for methanol–iodine.

Discussion

The Blue-Shifted Iodine Band. The trend and magnitude of the shift of λ^{BS} to longer wavelength with decreasing alcohol concentration seems real (Table I), being beyond the error limits of the computer resolution of overlapping bands. It might be noted for the same solutions that the band position and half-intensity bandwidth of the triiodide ion and the half-intensity of the blue-shifted iodine bands are not concentration dependent.

To check the possibility that the trend might be caused by the correction for the triiodide absorption, which is larger in more concentrated alcohol solutions, some solutions were deliberately exposed to air after the initial visible spectrum was taken. This resulted in an increase in the formation of triiodide ion. The visible spectrum was rerun and reanalyzed. The same result for λ^{BS} was obtained before and after exposure to air, eliminating this as a factor.

Childs,[9] in his study of the diethyl ether–iodine complex by the same constant activity method, did not detect any shift in λ^{BS} for the dilute solutions, although he did detect a very slight shift when the diethyl ether concentration was in excess of 1 M. Apparently, the concentration dependence of λ^{BS} in dilute solutions has not been noted previously except in one case. Reid and Mulliken[20] reported that the λ^{BS} of the pyridine–iodine complex in *n*-heptane solution shifted toward shorter wavelengths when the pyridine concentration was gradually increased above 0.1 M. For very dilute solutions, no shift in λ^{BS} for this system was detected.[9]

Solvent effects on the electronic spectra of molecules have been the subject of many studies (e.g., Bayliss,[21,22] Ooshika,[23] McRae,[24] Lippert,[25] Bakhshiev,[26] Weigang,[27] Abe,[28] and Liptay[29]), and several reviews (e.g., Suppan,[30] Tamres,[31] Nicol,[32] and Davis[33]). Although the theories are developed for solvent effects on the spectrum of a stable compound going from the vapor phase to solution, they should be applicable to the effects on the spectrum in different solution environments. The theories point out two broad categories of solvent effects, namely, specific and nonspecific effects (although precise distinction may not be possible). The former include hydrogen bonding, electron or proton transfer between solute and solvent, ionization, isomerization, complexation, etc. The nonspecific effects include solvent cage strains, dispersion, and polarization forces.

Considering first the specific effects, the association of ethanol and methanol in nonpolar solvents is a well-known phenomenon. Singh and Rao[34] studied the infrared spectra of ethanol and methanol, and showed that the alcohols formed dimers or trimers in carbon tetrachloride solutions as dilute as 0.01 M. An NMR study by Dixon[35] of methanol in carbon tetrachloride solution also showed that dimers, trimers, or higher polymers could exist even in solutions as dilute as 0.004 mole fraction in methanol. Tucker et al.[36] have pointed out that, in *n*-hexadecane solution, ethanol forms trimers or octamers even though its formal concentration is as low as 0.2 M. Thus, it is quite safe to assume that ethanol or methanol associates through hydrogen bonding in *n*-heptane solution.

The process of self-association and preferential solvation will result in a complex which seems to consist of an iodine molecule interacting with an aggregate containing many alcohol molecules. The number of alcohol molecules in the aggregate is concentration dependent because of different degrees of self-association and solvation. For two solutions of different alcohol concentration, we may assume that in the more dilute solution there is an average of *m* alcohol molecules in the aggregate while in the more concentrated solution there is an average of *n* alcohol molecules in the aggregate where $n > m$ and *n* and *m* are not necessarily integers.

The donor strength of the alcohol may change after association. Molecular orbital calculations on the association of water, of methanol, and of other hydrogen-bonded molecules show that the charge distribution of the polymeric molecule is different from that of the monomer.[37-40] The negative charge on the oxygen atom in the molecule acting as the proton donor increases when the hydrogen bond is formed, and increases still more if a

trimer is formed. Since the negative charge on this oxygen atom is greater than that on the oxygen in the molecule acting as the proton acceptor, and also because of more favorable steric factors, it would be expected that complexation with iodine occurs through the oxygen in the molecule which is the proton donor. The donor strength of the alcohol should parallel the increase in negative charge on the oxygen resulting from association, i.e., trimer > dimer > monomer. In general, then, the $(alcohol)_n$ aggregate in concentrated solution should be a stronger donor than the $(alcohol)_m$ aggregate in dilute solution.

The absorption band at 520 nm of molecular iodine in *n*-heptane solution arises from electron excitation from the antibonding Π_g^* molecular orbital to the antibonding σ_u^* molecular orbital (a $^1\Sigma$ to a $^3\Pi$ transition). Mulliken[7] has pointed out that the strongly antibonding σ_u^* molecular orbital must be larger in size than the outer occupied molecular orbitals in the ground state of the iodine molecule. On excitation of the iodine molecule in a complex, its suddenly swollen size introduces an exchange repulsion between it and the partner molecule.[7a] This repulsion energy, and thus the blue shift in absorption frequency, should be greater the stronger the complex. In the present case of alcohol–iodine complexes, the $(alcohol)_n$ aggregate in concentrated solution interacting with an iodine molecule should give a larger blue shift for the visible iodine band than that given by the $(alcohol)_m$ aggregate in dilute solution. Hence, the specific effect of hydrogen bonding of alcohols can account for the concentration dependence of λ^{BS}.

Among the possible nonspecific effects is that due to the solvent cage. If a molecule in the vapor phase is dissolved in a solvent, its electronic spectrum can be altered by the solvent cage.[29] It has been discussed that the shift observed in comparing solutions with different alcohol concentrations probably is not due to the cavity size of the $(alcohol)_m$ and $(alcohol)_n$ aggregates,[15] but more likely due to the change in the intermolecular D–A distance. Since weak complexes have a shallow potential energy minimum, in the ground state, the internal pressure of the solvent cage is more effective in compressing the intermolecular D–A distance. As has been pointed out by Prochorow et al.,[41] Kroll,[42] and Trotter,[43] this results in the charge-transfer band being shifted to lower frequency in going from the vapor to solution. This shortening in intermolecular D–A distance should have an effect on the blue-shifted iodine band as well. However, the shortening in the D–A distance with increasing alcohol concentration may not be due solely to the increase in solvent compression. As mentioned, the specific effect of hydrogen bonding, by increasing the donor strength of the alcohol, also will shorten the D–A distance and similarly shift λ^{BS}.

Nonspecific effects due to dispersion and polarization, dipole–induced dipole, and other electrical interactions also have received attention. The so-called dielectric theories quite successfully correlate the solvent shift of the absorption band of a compound to the macroscopic properties of the solvent.[21-30] In general, the absorption energy in solution, or more precisely the change in absorption energy in going from the vapor phase to solution, is approximately a linear function of $(d - 1)/(2d + 1)$ or $(d - 1)/(d + 2)$, where d is the static dielectric constant of the solvent. The absorption energy change is also a linear function of $(n_0^2 - 1)/(2n_0^2 + 1)$, where n_0 is the refractive index of the solvent at zero frequency or at very long wavelength of the electromagnetic wave (although the refractive index at the sodium D line, n, is commonly used). Other quantities, for example, $[(d - 1)/(2d + 1)] - [(n^2 - 1)/(2n^2 + 1)]$, also are shown to correlate with the solvent shift.[29,32]

Although it is known that the blue-shifted iodine band in complexes is solvent dependent, similar kinds of correlations between the frequency, ν^{BS}, and the dielectric constant or refractive index of the solvent have not been reported. A survey of the literature revealed that only a few studies have been made of λ^{BS} for weak complexes in different solvents. For example, the visible spectrum of benzene–iodine was studied in six different solvents,[44,45] with a reported λ^{BS} range between 497 and 523 nm. These ν^{BS} results do not correlate with either the $(d - 1)/(2d + 1)$ or the $(n^2 - 1)/(2n^2 + 1)$ function.

The visible and UV spectra of the strong complex pyridine–iodine have been studied in many different solvents by different investigators.[2c,46-49] Reid and Mulliken[20] studied it in *n*-heptane and noticed a shift of λ^{BS} to shorter wavelengths with increasing pyridine concentration. They attributed this shift in λ^{BS} to solvation of the complex by pyridine molecules, causing the complex to become more polar. This is analogous to the specific effect cited earlier for the alcohol–iodine complex, although it has been discussed[15] that the nonspecific effects may contribute to the shift also.

Since the dielectric constant of ethanol (24.30) and of methanol (32.60) are higher than that of *n*-heptane (1.924) the dielectric constant of the alcohol–*n*-heptane solution will increase with alcohol concentration. For dilute solutions, where there is difficulty in measuring the dielectric constant experimentally, it can be approximated by the additivity of molar polarizations of the solvent (P_1) and the solute (P_2) as long as the solutions are ideal.[50,51] In this study, the highest concentration of ethanol and methanol used was around 0.6 M. Taking 0.600 M as an exact value, this corresponds to a mole fraction $X_1 = 0.9160$ and $X_2 = 0.0840$ for the ethanol solution, and to $X_1 = 0.9168$ and $X_2 = 0.0832$ for the methanol solution. (1 refers to the solvent and 2 refers to the solute.)

Smyth and Stoops[52] studied a series of ethanol–*n*-heptane solutions at different temperatures and obtained plots of the molar polarization of the solution (P) vs. mole fraction of ethanol. When X_2 of ethanol is less than 0.18, the experimental P is in fact given by the sum of X_1P_1 and X_2P_2. The same result was shown by Debye[53] for ethanol–benzene solutions when X_2 is less than 0.18. Rodebush et al.[54] measured the dielectric constant of very dilute 1-butanol–carbon tetrachloride solutions. They also showed that, when X_2 is less than 0.14, $P = X_1P_1 + X_2P_2$. Thus it appears valid that, for the concentration range of ethanol and methanol solutions used in the present study, the molar polarization and therefore the dielectric constant of the solution can be calculated. The change in dielectric constant from that in pure *n*-heptane (1.924) to that of a 0.600 M solution of alcohol in *n*-heptane is rather small, becoming 2.056 for the ethanol solution and 2.024 for the methanol solution.

For these same dilute solutions, the refractive index at the sodium D line can be calculated in a similar way. The change from pure *n*-heptane (1.388) is only to 1.390 and to 1.391 for the ethanol and methanol solutions, respectively. It may be noted that measurements by Poltz[57] showed that over the entire concentration range of 2-propanol–*n*-hexane solutions the additivity of molar refraction holds.

Further, the function $(d - 1)/(2d + 1)$ increases from 0.1906 (pure *n*-heptane) to 0.2066 (ethanol–*n*-heptane) and to 0.2029 (methanol–*n*-heptane), and the function $(n^2 - 1)/(2n^2 + 1)$ increases from 0.1909 (pure *n*-heptane) to 0.1916 (ethanol–*n*-heptane) and to 0.1920 (methanol–

n-heptane). The small changes in these functions when the concentration of alcohol is increased from 0.0 to 0.6 M makes it unlikely that the nonspecific effects of dispersion and polarization interactions between the complex and the solvent medium will shift the λ^{BS} by as much as observed in this study. It must be noted, however, that the above calculated dielectric constant and refractive index are bulk properties which apply to the solution as a homogeneous medium. The actual dielectric constant and refractive index of the medium as felt locally by the complex may be much greater than these bulk values because of preferential solvation and self-association of the alcohol. If this is true, the dispersion and polarization effects may change λ^{BS} (or ν^{BS}) in a way similar to that observed for the pyridine–iodine complex in different solvents. Unfortunately, it is not possible to determine the properties of the medium in the immediate vicinity of the complex. Thus, the proposal that the shift in λ^{BS} with concentration is due to local medium changes around the complex cannot be treated quantitatively. However, it must be pointed out that this model of a local medium effect on the complex is not different from that of the effect attributed to an alcohol aggregate on the complexed iodine molecule.

One other possibility for the shift in λ^{BS} with alcohol concentration is that the molar absorptivity of the free iodine in alcohol–*n*-heptane solutions may be different from that in pure *n*-heptane, thereby resulting in a difference when correcting for the free iodine absorbance. Again, the fact that the dielectric constant and refractive index of even the most concentrated solution used in this study do not differ much from those of pure *n*-heptane makes it unlikely that the molar absorptivity of iodine changes sufficiently to shift λ^{BS} by as much as is observed.

The literature results of λ^{BS} for ethanol–iodine and methanol–iodine are 443 and 440 nm, respectively, and come from the work of de Maine[5] and of Voigt.[8] In the former study, the concentration of alcohol ranged from a mole fraction of about 0.06 to 0.95 in carbon tetrachloride solution, i.e., a molarity of about 0.64 to 15.76 M for ethanol and about 0.64 to 21.95 M for methanol. In the latter study, iodine was dissolved in the pure alcohols. These high concentrations of alcohol probably were the main cause for the observed short λ^{BS} values. A more meaningful procedure is to extrapolate λ^{BS} for the alcohol–iodine complex to infinite dilution of alcohol, as in Figure 4. The result is 475 ± 5 nm for both alcohol–iodine complexes. (If ν^{BS} is plotted against concentration the same limiting values of λ^{BS} are obtained.)

The Charge-Transfer Band. Tables IIa and IIb show that the charge-transfer band maximum, λ^{CT}, of both the ethanol–iodine and methanol–iodine complexes shifts to shorter wavelengths with decreasing alcohol concentration, the shift being in the opposite direction to that observed for λ^{BS}. The same factors discussed above as affecting λ^{BS} can be considered as to their contribution to the shift in λ^{CT}.

From theory, a simplified equation applicable to weak electron donor–acceptor complexes[42] is

$$h\nu^{CT} \simeq I_D^V - E_A^V - \frac{e^2}{d r_{DA}} \quad (1)$$

where I_D^V is the vertical ionization potential of the donor, E_A^V is the vertical electron affinity of the acceptor, e is the electron charge, d is the dielectric constant of the solution, and r_{DA} is the equilibrium intermolecular D–A distance. Since self-association increases the negative charge on the oxygen atom in the alcohol molecule, making it a stronger donor, I_D^V is expected to decrease with increasing alcohol aggregation. Also, e^2/dr_{DA} ought to increase because of the small shortening in r_{DA} for a stronger donor and the approximate constancy in d over the concentration range studied. The net result is a predicted smaller value of $h\nu^{CT}$ in the concentrated solution, which is consistent with the experimentally observed trend.

A trend toward longer λ^{CT} with increasing functions such as $(d-1)/(2d+1)$ and $(n^2-1)/(2n^2+1)$ was observed for aromatic hydrocarbon donors by Voigt[55] for TCNE complexes and by Ham[56] for iodine complexes. However, these bulk properties cannot account for the shift in the present study because the alcohol range covered is so small.

Finally, Julien[6] pointed out that the molar absorptivity of free iodine in the UV region in alcohol–*n*-heptane solution is concentration dependent because of the anomalous dispersion and charge-transfer contacts formed by alcohol–iodine and *n*-heptane–iodine. This may be true in the concentrated solutions. (Julien used ethanol solutions with concentrations between 0.34 and 2.73 M.) In the present study, the solutions were much more dilute so that a small change in the molar absorptivity of the free iodine cannot alone account for the large shift in λ^{CT}.

Stability of the Isosbestic Point. Since the blue-shifted iodine band maximum is concentration dependent, it may be suspected that the isosbestic point of the systems varies with concentration too. No such dependence was observed over the alcohol concentration range of 0.05 to 0.7 M.

Its stability also was tested as follows. The equilibrium constant of complex formation depends upon the temperature. In a single solution composed of alcohol, *n*-heptane, and molecular iodine, the concentrations of the complexed and free iodine vary with temperature, but the total iodine concentration remains the same. Thus, the isosbestic point of the system can be determined by measuring the spectra of this single solution at different temperatures. This was done over a temperature range of 10–40 °C for both alcohol–iodine complexes. The spectra were measured by the conventional Benesi–Hildebrand method using an *n*-heptane blank. For those solutions whose ethanol concentration was higher than 0.3 M and with a fixed iodine concentration of 1.59×10^{-4} M, the spectral curves at different temperatures did indeed go through an isosbestic point at 490.8 ± 1 nm. (For the temperature range studied the change in density of the solution is less than 4%.) For those solutions where the ethanol concentration was less than 0.3 M, the concentration of the weak complex formed is small and the change in absorbance with temperature is even smaller. In these cases the spectral curves at different temperatures were practically the same in the wavelength region from 480 to 500 nm, and it can only be estimated for these dilute solutions that the isosbestic point lies perhaps intermediate between these wavelengths. The methanol–iodine system showed similar behavior. The above test confirmed the observation that the isosbestic point of both alcohol–iodine systems is indeed stable over the concentration range of the solutions used.

The isosbestic point will be stable if the species present in the concentrated solution [$(alcohol)_n$–iodine] and that present in the dilute solution [$(alcohol)_m$–iodine] have the same molar absorptivity as the free iodine at this particular wavelength. Since the blue-shifted iodine band position does change with concentration, but not the isosbestic point, either its molar absorptivity or its half-intensity bandwidth has to change. (This is discussed below.)

It also is possible that the molar absorptivity of $(alcohol)_n$–iodine at the isosbestic point is slightly different

from that of $(alcohol)_m$–iodine, with both being near that of the free iodine. If the difference is small and considering that the concentration of complex formed is also small, it may be difficult to detect experimentally the variation of the isosbestic point with concentration since, for both complexes, it may lie within the narrow range of ±1 nm for the concentrations studied.

The Half-Intensity Bandwidth and the Molar Absorptivity of the Blue-Shifted Iodine Band. The half-intensity bandwidth of an electronic absorption band at a particular temperature depends on the slope of the potential energy curve of the excited state.[18] Usually it is not affected very much by the environment.[31-33] Tables Ia and Ib show the half-intensity bandwidths of the blue-shifted iodine band, $\Delta\nu_{1/2}^{BS}$, of the ethanol–iodine and methanol–iodine complexes. Both values of $\Delta\nu_{1/2}^{BS}$ remain constant within the error limits of the computer analyses over the whole range of concentrations. The average value of $\Delta\nu_{1/2}^{BS}$ for the ethanol–iodine complex is 4043 ± 230 cm^{-1} and that for the methanol–iodine complex is 4507 ± 180 cm^{-1}. These values are quite close to those reported by de Maine.[5]

In the constant activity method the ϵ^{BS} of the complex is determined by the ratio of A^{BS} to A^{isos}. Figure 4 shows the plot of A^{BS} vs. A^{isos}, and Tables Ia and Ib give ϵ^{BS} for the individual solutions for the two alcohol–iodine complexes. The errors associated with A^{BS} and A^{isos}, hence also the errors in ϵ^{BS}, are quite large for the dilute solutions. Nevertheless, there seems to be a systematic trend of decreasing ϵ^{BS} with decreasing alcohol concentration. In their study of the pyridine–iodine complex, Reid and Mulliken[20] also noticed a decrease of ϵ^{BS} with dilution.

The solvent effects on the intensity of an absorption band are more complicated and are still not clearly understood.[21-29,32,58] Many workers have shown that the oscillator strength, f, is some function of the refractive index at the sodium D line. Chako[59] reported a linear relation between f and $(n^2 + 2)^2/9n$. Other reported relations are f is a function of $12n^2/(2n^2 + 1)(n^2 - 1)$[60] and a function of $(n^2 + 2)^2/9n$ or of $(n^2 - 1)/(2n^2 + 1)$.[27] Liptay[29d] showed that in many cases f is directly proportional to the wavenumber of the absorption band maximum, ν^{max}, and Abe[28] related f to both $9n^2\nu^{max}/(2n^2 + 1)^2$ and to $\nu^{max}(n^2 + 2)^2/9n^2$.

As discussed earlier, the bulk refractive index and dielectric constant of the alcohol solutions do not change much. Therefore, the molar absorptivity of the blue-shifted iodine band cannot correlate with any of the functions suggested by Chako, by Weigang, or by Schuyer. (In the alcohol–iodine complexes, since $\Delta\nu_{1/2}$ is unchanged over the range of solutions, ϵ^{BS} and f are directly proportional.) When the refractive index remains constant, Abe's equations reduce to Liptay's result, i.e., ϵ^{BS} is a linear function of ν^{BS}. Figure 7 is a plot of ϵ^{BS} vs. ν^{BS} for the two complexes, and it clearly shows the linear relation between these terms as the treatments of Liptay and of Abe would indicate.

The intensification of the blue-shifted iodine band in complexes also can be explained by a reason suggested by Mulliken.[7] The locally excited $^3\Pi_u$ state of the iodine molecule is shifted to higher energies on complex formation and its mixing with the charge-transfer state or with other excited states will increase. The shift and mixing should be greater the stronger the complex, leading to a greater borrowing of intensity and, therefore, a more intense band.

Figure 4 shows the linear regressions for the plots of A^{BS} vs. A^{isos}. For the ethanol–iodine complex the regression lines gives a value for ϵ^{BS} of 884 ± 15 M^{-1} cm^{-1}, and for the

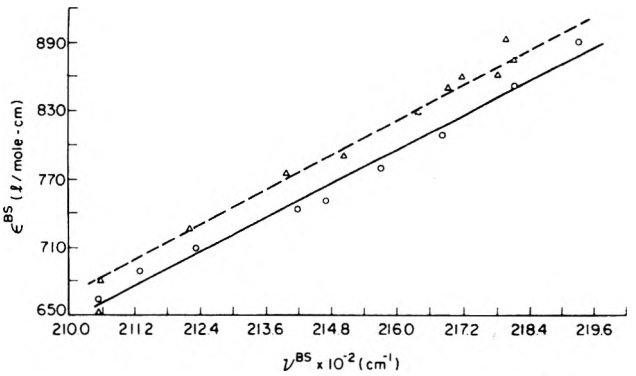

Figure 7. ϵ^{BS} vs. ν^{BS} for the alcohol–iodine complexes: (Δ) ethanol–iodine; (O) methanol–iodine.

methanol–iodine complex the regression value is 874 ± 20 M^{-1} cm^{-1}. Because of the concentration dependence of λ^{BS} and ϵ^{BS}, it is the limiting value of ϵ^{BS} for the infinitely dilute solution which ought to be considered. The large error of each ϵ^{BS} for different solutions makes it difficult to plot ϵ^{BS} vs. $[D]_0$ to find the limiting value. Therefore, it was calculated from the data for the average $\Delta\nu_{1/2}^{BS}$ and the known ϵ_{I_2} at the isosbestic point assuming a Gaussian band shape. The value for λ^{BS} at infinite dilution was found to be at 475 ± 5 nm for both complexes. The variation in the isosbestic point is of the order of ±1 nm, with a slight trend toward a longer wavelength on dilution. Therefore, the upper limit of the isosbestic point is used, i.e., 491.8 nm for the ethanol–iodine complex and 492.3 nm for the methanol–iodine complex. At these wavelengths, ϵ_{I_2} is 645 and 652 M^{-1} cm^{-1}, respectively. Hence, the calculated values of ϵ^{BS} at infinite dilution for ethanol–iodine and methanol–iodine are 704 ± 20 and 702 ± 20 M^{-1} cm^{-1}, respectively.

The data show that the λ^{BS} obtained in the present study for both alcohol–iodine complexes is at nearly the same or even at a slightly longer wavelength than that for the diethyl ether–iodine complex. This is a very different result from those which have been reported in the literature. Considering the relative donor strengths, the new values are more in line with Mulliken's theory.

The regression values for ϵ^{BS} from the present study for both alcohol–iodine complexes are in the same range as that for the diethyl ether–iodine case. All three values are seemingly smaller than that for ϵ^{max} of free iodine in *n*-heptane. The values at infinite dilution of ϵ^{BS} for the alcohol–iodine complexes are even lower, and make the difference more pronounced. The oscillator strength of the free iodine band and of its complexes with the alcohols and with diethyl ether are all comparable, the spread being too small for quantitative comparison.

The Half-Intensity Bandwidth and the Molar Absorptivity of the Charge-Transfer Band. Tables IIa and IIb show the half-intensity bandwidth for the charge-transfer band, $\Delta\nu_{1/2}^{CT}$, of the two alcohol–iodine complexes. Like the blue-shifted iodine band and other cases,[31,42] $\Delta\nu_{1/2}^{CT}$ is not affected much by the change in solvent environment.

The plots of A^{CT} vs. A^{isos} for the two complexes are shown in Figure 6. The ϵ^{CT} of each complex remains constant within experimental error for the entire alcohol concentration range. This is different from the effect observed on ϵ^{BS}. Liptay[29] has related the solvent dependence of the transition dipole moment of the electronic transition, and hence the intensity, as follows:

$$\mu(sol) = \mu(vap) + \alpha\overline{F} + \frac{2(n^2 - 1)}{r^3(2n^2 + 1)}Z \qquad (2)$$

where μ(sol) and μ(vap) are the transition dipole moment of the molecule in solution and in the vapor phase, respectively, α is the transition polarizability tensor, $\bar{F}$ is the reaction field exerted by the solvent on the molecule, r is the diameter of the molecule, Z is the effect of dispersion on the transition dipole moment, and n is again the refractive index. Usually, for a molecule with a large dipole moment the last term in the above equation can be neglected. Furthermore, for an electronic excitation with a sufficiently large transition dipole moment, μ(vap), the transition polarizability tensor, α, makes a relatively small contribution. Thus the intensity of a strong absorption band is affected relatively little by the solvent.

For the case of the alcohol–iodine complexes, the value of μ for the charge-transfer band is around 4 D which is much greater than that of around 1 D for the blue-shifted band. Hence, the solvent effect on ϵ^{CT} should be very small, whereas that on ϵ^{BS} ought to be relatively large.

Mulliken[18] showed that the transition dipole moment for the charge-transfer band, μ_{VN}, is

$$\mu_{VN} = a^*b(\mu_1 - \mu_0) + (aa^* - bb^*)(\mu_{01} - S_{01}\mu_0) \quad (3)$$

where 0 refers to the no-bond structure, and 1 refers to the dative bond structure of the complex, $\mu_0 = \int \psi_0 \bar{\mu} \psi_0 d\tau$ and μ_1 and μ_{01} have similar meaning ($\bar{\mu}$ is the dipole moment operator), and a, b, a^*, and b^* are the coefficients in the no-bond and dative-bond wave functions of the ground and excited states, respectively.

The first term shows the dependence of μ_{VN} on the difference in the dipole moment between the dative and no-bond structures, and the second on the fraction of the electron transfer between the ground and excited states. Mulliken[18] also pointed out that, for a strong complex, the first term $a^*b(\mu_1 - \mu_0)$ is important in giving an intense absorption band. However for some weak complexes the second term, which depends on the overlap integral S_{01}, might be large enough to contribute considerable intensity. In the present case of the alcohol–iodine complexes, the terms μ_1, μ_0, μ_{01}, S_{01} and the coefficients a, b, etc., are all concentration dependent because the size and charge distribution of the donor should change as a consquence of the self-association of the alcohol. The somewhat opposing effects on $a^*b(\mu_1 - \mu_0)$ and on $(\mu_{01} - S_{01}\mu_0)(aa^* - bb^*)$ with change in alcohol concentration and, hence, change in the strength of the complex, may be such as to result in a negligible overall change in intensity with concentration.

Julien[6] applied the Liptay method in his study of the ethanol–iodine charge-transfer band and found a trend in the values of ζ_{ij} (the ratio of the absorbance of solution j at wavelength i to the absorbance of solution j at wavelength λ) as a function of total ethanol concentration. He attributed this to a change of molar absorptivity of the free iodine with alcohol concentration. However, this trend in ζ_{ij} also can be accounted for by the variation of λ^{CT} with increasing alcohol concentration.[15]

Acknowledgment. One of the authors (H.C.T.) thanks the Horace H. Rackham School of Graduate Studies at The University of Michigan for a predoctoral fellowship. This research was supported in part by the National Science Foundation through Grant No. GP-38403X.

References and Notes

(1) M. Tamres and S. Searles, *J. Phys. Chem.*, **66**, 1099 (1962).
(2) H. Tsubomura and R. P. Lang, *J. Am. Chem. Soc.*, **83**, 2085 (1961).
(3) M. Good, A. Major, J. Nag-Chaudhuri, and S. P. McGlynn, *J. Am. Chem. Soc.*, **83**, 4329 (1961).
(4) (a) M. Brandon, M. Tamres, and S. Searles, *J. Am. Chem. Soc.*, **82**, 2129 (1960); (b) M. Tamres and M. Brandon, *ibid.*, **82**, 2134 (1960).
(5) P. A. D. de Maine, *J. Chem. Phys.*, **26**, 1192 (1957).
(6) (a) L. M. Julien, Ph.D. Dissertation, The University of Iowa, 1966. (b) L. M. Julien, W. E. Bennett, and W. B. Person, *J. Am. Chem. Soc.*, **91**, 6915 (1969).
(7) (a) R. S. Mulliken, *Recl. Trav. Chim. Pays-Bas.*, **75**, 845 (1956); (b) R. S. Mulliken and W. B. Person "Molecular Complexes", Wiley-Interscience, New York, N.Y., 1969, Chapter 10.
(8) E. M. Voigt, *J. Phys. Chem.*, **72**, 3300 (1968).
(9) (a) J. D. Childs, Ph.D. Dissertation, The University of Oklahoma, **1971**. (b) J. D. Childs, S. D. Christian, and J. Grundnes, *J. Am. Chem. Soc.*, **94**, 5657 (1972).
(10) (a) A. I. Vogel, "A Textbook of Practical Organic Chemistry, Including Qualitative Organic Analysis", 3rd ed., Longmans Green and Co., London, 1956. (b) J. A. Riddick and E. E. Toops, Jr., in "Technique of Organic Chemistry, Vol. VII, Organic Solvents", A. Weissberger, Ed., Interscience, New York, N.Y., 1955.
(11) (a) *Inorg. Syn.*, 5, 172 (1957); (b) F. D. Chattaway and G. Hoyle, *J. Chem. Soc.*, **123**, 654 (1923).
(12) H. Tsubomura and R. S. Mulliken, *J. Am. Chem. Soc.*, **82**, 5966 (1960).
(13) R. E. Buckles, J. P. Yuk, and A. I. Popov, *J. Am. Chem. Soc.*, **74**, 4379 (1952).
(14) A. I. Popov and R. F. Swensen, *J. Am. Chem. Soc.*, **77**, 3724 (1955).
(15) H. C. Tse, Ph.D. Dissertation, The University of Michigan, 1976.
(16) (a) R. D. B. Fraser and E. Suzuki, *Anal. Chem.*, **38**, 1770 (1966); (b) *ibid.*, **41**, 37 (1969); (c) R. D. B. Fraser and E. Suzuki in "Physical Principles and Techniques in Protein Chemistry", Part C, S. J. Leach, Ed., Academic Press, New York, N.Y., 1973, Chapter 21.
(17) (a) K. Nagano and D. E. Metzler, *J. Am. Chem. Soc.*, **89**, 289 (1967); (b) D. B. Siano and D. E. Metzler, *J. Chem. Phys.*, **51**, 1856 (1969).
(18) R. S. Mulliken and W. B. Person, "Molecular Complexes", Wiley-Interscience, New, York, N.Y., 1969, Chapters 3 and 8.
(19) G. Briegleb, "Electron-Donator-Acceptor Komplexe", Springer-Verlag, Berlin, 1961.
(20) C. Reid and R. S. Mulliken, *J. Am. Chem. Soc.*, **76**, 3869 (1954).
(21) N. S. Bayliss, *J. Chem. Phys.*, **18**, 292 (1950).
(22) N. S. Bayliss and E. G. McRae, *J. Phys. Chem.*, **58**, 1002 (1954).
(23) Y. Ooshika, *J. Phys. Soc., Jpn.*, **9**, 594 (1954).
(24) E. G. McRae, *J. Phys. Chem.*, **61**, 562 (1957).
(25) (a) E. Lippert, *Z. Naturforsch. A*, **10**, 541 (1955); (b) *Z. Elektrochem.*, **61**, 962 (1957).
(26) N. G. Bakhshiev, *Opt. Spectrosc.*, **10**, 379 (1961).
(27) (a) O. E. Weigang, Jr., and D. D. Wild, *J. Chem. Phys.*, **37**, 1180 (1962); (b) O. E. Weigang, Jr., *ibid.*, **41**, 1435 (1964).
(28) T. Abe, *Bull. Chem. Soc., Jpn.*, **38** 1314 (1965).
(29) (a) W. Liptay, *Z. Naturforsch. A*, **20**, 1441 (1965); (b) W. Liptay, "Modern Quantum Chemistry", Part II, O. Sinanoglu, Ed., Academic Press, New York, N.Y., 1965, Chapter 5; (c) W. Liptay, *Z. Naturforsch. A*, **21**, 1605 (1966); (d) *Angew. Chem. Int. Ed. Engl.*, **8**, 177 (1969).
(30) P. Suppan, *J. Chem. Soc. A*, 3125 (1968).
(31) M. Tamres, "Molecular Complexes", Vol. I, R. Foster, Ed., Crane, Russak and Co., New York, N.Y., 1973, Chapter 2.
(32) M. F. Nicol. *Appl. Spectrosc. Rev.*, 8, 183 (1974).
(33) K. M. C. Davis, "Molecular Association", Vol. I, R. Foster, Ed., Academic Press, London, 1975, Chapter 5.
(34) S. Singh and C. N. R. Rao, *J. Phys. Chem.*, **71**, 1074 (1967).
(35) W. B. Dixon, *J. Phys. Chem.*, **74**, 1396 (1970).
(36) E. E. Tucker, S. B. Farnham, and S. D. Christian, *J. Phys. Chem.*, **73**, 3820 (1969).
(37) J. R. Hoyland and L. B. Kier, *Theor. Chim. Acta (Berl.)*, **15**, 1 (1969).
(38) (a) A. S. N. Murthy, R. E. Dairs, and C. N. R. Rao, *Theor. Chim. Acta (Berl.)*, **13**, 81 (1969); (b) A. S. N. Murthy, S. N. Bhat, and C. N. R. Rao, *J. Chem. Soc. A*, 1251 (1970).
(39) H. Morita and S. Nagakura, *Theor. Chim. Acta (Berl.)*, **27**, 325 (1972).
(40) J. E. Del Bene, *J. Chem. Phys.*, **55**, 4633 (1971).
(41) J. Prochorow and A. Tramer, *J. Chem. Phys.*, **44**, 4545 (1966).
(42) M. Kroll, *J. Am. Chem. Soc.*, **90**, 1097 (1968).
(43) P. J. Trotter, *J. Am. Chem. Soc.*, **88**, 5721 (1966).
(44) H. A. Benesi and J. H. Hildebrand, *J. Am. Chem. Soc.*, **71**, 2703 (1949).
(45) B. B. Bhownik, *Spectrochim. Acta, Part A*, **27**, 321 (1971).
(46) H. D. Bhist and W. B. Person, *J. Phys. Chem.*, **71**, 2750 (1967).
(47) K. R. Bhaskar and S. Singh, *Spectrochim. Acta, Part A*, **23**, 1155 (1967).
(48) P. V. Huong, N. Platzer, and M. L. Josien, *J. Am. Chem. Soc.*, **91**, 3669 (1969).
(49) W. J. McKinney and A. I. Popov, *J. Am. Chem. Soc.*, **91**, 5215 (1969).
(50) (a) C. P. Smyth, "Dielectric Constant and Molecular Structure", The Chemical Catalog Co., New York, N.Y., 1931. (b) C. P. Smyth, "Dielectric Behavior and Structure", McGraw-Hill, New York, N.Y., 1955.
(51) (a) C. J. F. Böttcher, "Theory of Electric Polarization", Elsevier, Amsterdam, 1952. (b) C. J. F. Böttcher, O. C. Van Belle, P. Bordewijk, and A. Rip, "Theory of Electric Polarization", 2nd ed., Vol. 1, Elsevier Scientific, Amsterdam, 1973.
(52) C. P. Smyth and W. N. Stoops, *J. Am. Chem. Soc.*, **51**. 3312 (1929).

(53) P. Debye, "Polar Molecules", The Chemical Catalog Co., New York, N.Y., 1929, reprinted by Dover Publication, New York, N.Y.
(54) W. H. Rodebush, C. R. Eddy, and L. D. Eubank, *J. Chem. Phys.*, **8**, 889 (1940).
(55) E. M. Voigt, *J. Chem. Phys.*, **70**, 598 (1966).
(56) J. Ham, *J. Am. Chem. Soc.*, **76**, 388 (1954).
(57) H. Poltz, *Z. Phys. Chem.*, **B32**, 243 (1936).
(58) S. F. Abdulnur, *J. Chem. Phys.*, **58**, 4175 (1973).
(59) N. Q. Chako, *J. Chem. Phys.*, **2**, 644 (1934).
(60) J. Schuyer, *Recl. Trav. Chim. Pays-Bas.*, **72**, 933 (1953).

The Thermodynamic Properties of Methanol–Iodine and Ethanol–Iodine Complexes in *n*-Heptane Solution

Hing-Cheung Tse and Milton Tamres*

Chemistry Department, University of Michigan, Ann Arbor, Michigan 48109 *(Received January 27, 1977)*

Publication costs assisted by the National Science Foundation

Thermodynamic properties of the ethanol–iodine and methanol–iodine complexes in *n*-heptane solution were investigated using both the constant activity method and the Benesi-Hildebrand-Scott method. The applicability of the latter method was examined in view of the changing spectral characteristics of the complex with change in alcohol concentration. The equilibrium constants at 25 °C and heats of complexation obtained by the two methods are, respectively, as follows: (a) ethanol–iodine 1.50 ± 0.03 M^{-1} and −3.2 ± 0.2 kcal/mol, and 0.95 ± 0.06 M^{-1} and −3.5 ± 0.2 kcal/mol; (b) methanol–iodine 1.29 ± 0.09 M^{-1} and −3.0 ± 0.4 kcal/mol, and 0.65 ± 0.11 M^{-1} and −3.0 ± 0.2 kcal/mol. The equilibrium constants and heats of complexation are analyzed in terms of an aggregate model based on the self-association of alcohol.

Introduction

In an earlier paper,[1] the positions of the complexed visible iodine band and charge-transfer (CT) band of the ethanol–iodine and methanol–iodine complexes were reported to vary with alcohol concentration. A model based on the aggregation of alcohol molecules was proposed to explain these observations, i.e., the donor ability of the alcohol increases with increasing aggregation which causes a blue shift of the complexed visible iodine band and a red shift of the CT band. These effects necessitate looking more closely at the determination of the equilibrium constant.

In the work of Childs,[2] based on a constant activity method, it has been shown that the equilibrium constant of a complex can be determined for a single solution from data at the isosbestic point. Therefore one can test if there is a systematic change in the equilibrium constant with increasing alcohol concentration.

Furthermore, in using the Benesi-Hildebrand and Scott equations, the absorbance of the complex at a chosen wavelength is assumed to follow Beer's law. This cannot strictly hold for the alcohol–iodine complexes because of the variation in the absorption band maxima with alcohol concentration.[1] In this paper the applicability of the Scott equation to the absorbance data of the alcohol–iodine complexes in the visible region is also investigated.

Both methods enable determination of the heat of complexation ($\Delta H_C°$). For ethanol–iodine, $\Delta H_C°$ has been reported as −2.1 kcal/mol (in CCl_4 by de Maine),[3] −4.5 kcal/mol (in *n*-heptane by Julien),[4] −4.1 kcal/mol (in methylene chloride by Julien),[4] and −3.3 kcal/mol (in *n*-hexane by Amako).[5] The $\Delta H_C°$ of methanol–iodine has been reported as −1.9 kcal/mol (in CCl_4 by de Maine)[3] and −3.5 kcal/mol (in methylene chloride by Julien).[4] These variations are rather large, even among solvents considered to be relatively "inert", especially so if quantitative relations between donor strength and the blue-shifted iodine band are sought.

Experimental Section

The methods for purifying the reagents and preparing the samples and the procedures for determining spectral bands are described in the earlier paper.[1]

In the determination of $\Delta H_C°$ by the constant activity method, an alcohol solution was prepared in the dry box and put into a 10.00-cm cell with excess crystals of tetramethylammonium pentaiodide ($TMAI_5$). The cell was placed in a thermostattable cell jacket in the sample compartment. A matched 10.00-cm cell, containing pure *n*-heptane and $TMAI_5$ crystals, was put in a thermostattable cell jacket in the reference compartment. The temperature of the jackets was cooled to 10 °C and dry cool air was purged through the compartments to prevent condensation of moisture on the windows of the cell. The cells were shaken frequently and the visible spectrum taken after at least 24 h. The temperature of the jackets was raised to 40 °C in increments of 5 °C and the visible spectrum was taken at each temperature after equilibrium was attained. Base line corrections were determined at each temperature.

Determination of $\Delta H_C°$ by the constant activity method requires prior determination of the heat of solution of the following equilibrium:

$$(CH_3)_4NI_5(s) \rightleftharpoons (CH_3)_4NI_3(s) + I_2(sol) \quad (1)$$

This is obtained from a van't Hoff plot of the temperature dependence of the absorbance at 520 nm for eq 1. *n*-Heptane and excess $TMAI_5$ crystals were placed in a flask which was stoppered with a plastic cap and wrapped with Saran Wrap. The flask was placed in a constant temperature bath (Haake circulator), shaken frequently, and allowed to attain equilibrium for at least 24 h. The solution then was pipetted into a 1.00-cm cell and the absorbance at 520 nm was measured against an *n*-heptane blank using a Beckman DU spectrophotometer.

The sample and reference solutions for the Scott method also were prepared in the dry box from stock solutions.

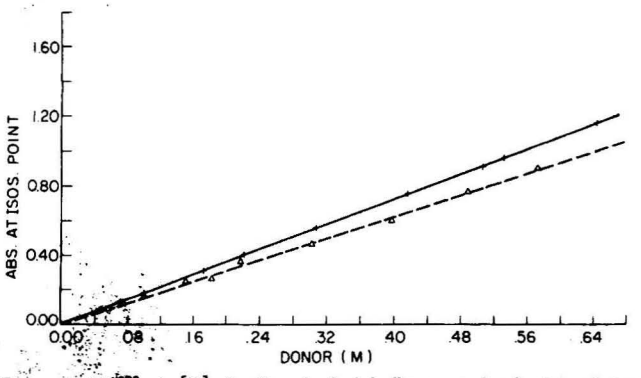

Figure 1. A^{isos} vs. $[D]_0$ for the alcohol–iodine complex in *n*-heptane studied by the constant activity method: t = 24.8 °C, cell path = 10.00 cm; (+) ethanol–iodine; (Δ) methanol–iodine.

Results and Discussion

The Equilibrium Constant. In the constant activity method the equilibrium constant at a particular temperature, K_C^S, can be expressed as[2]

$$K_C^S = \frac{[C]}{[D]\,[I_2]_{0,t}} = \frac{A^{isos}}{\epsilon_{I_2}^{isos} b [I_2]_{0,t}([D]_0 - [C])} \quad (2)$$

where [C] is the equilibrium concentration of the complex, [D] and $[D]_0$ are the equilibrium and initial concentrations of the donor, respectively (for a weak complex they are practically the same), $[I_2]_{0,t}$ is the equilibrium concentration of the free iodine at temperature t which is controlled by the $TMAI_5/TMAI_3$ equilibrium described by eq 1, A^{isos} is the absorbance of the complex at the isosbestic point, $\epsilon_{I_2}^{isos}$ is the molar absorptivity of the free iodine at the isosbestic point (which is the same as that of the complex at this wavelength), and b is the cell length. [C] can be found directly by measuring the increase in absorbance at the isosbestic point if $\epsilon_{I_2}^{isos}$ has been determined. In addition, as seen by rearranging eq 2, plotting A^{isos} against [D] should give a straight line with a slope equal to $K_C^S \epsilon_{I_2}^{isos} b [I_2]_{0,t}$.

Figure 1 gives a plot of A^{isos} vs. $[D]_0$ for ethanol–iodine and methanol–iodine. Both plots show good linearity to the highest alcohol concentration used, about 0.65 M. (A quadratic regression analysis carried out for the points gave no improvement over the linear analysis.) The K_C^S at 24.8 °C for ethanol–iodine is 1.50 ± 0.03 M^{-1} and for methanol–iodine it is 1.29 ± 0.09 M^{-1}. Christian et al.[6] have pointed out that K_C^S actually includes both a specific interaction (complex formation) and nonspecific interactions between donor and iodine. They also suggested using the solubility parameters of the donor, acceptor, and solvent to estimate the correction term due to the nonspecific interactions. These are obtained from heats of vaporization and molar volume data (Hildebrand and Scott).[7] According to Stull et al.[8] the heats of vaporization of ethanol and methanol at 25 °C are 10.08 and 8.96 kcal/mol, respectively. Thus the solubility parameters[7] were calculated to be 12.73 $cal^{1/2}\ cm^{-3/2}$ for ethanol and 14.33 $cal^{1/2}\ cm^{-3/2}$ for methanol. Applying Childs'[2,6] method, the correction term in the K_C^S due to the nonspecific interactions would be –0.44 and –0.38 M^{-1}, giving the corrected equilibrium constants (K_C^{th}) of 1.06 ± 0.03 M^{-1} for ethanol–iodine and 0.91 ± 0.09 M^{-1} for methanol–iodine. However, as has been pointed out,[7,9b] for highly associated systems such as ethanol and methanol, solubility parameters so calculated are too large. Therefore, the correction term for the K_C^S calculated above is overestimated, so that K_C^{th} represents a lower limit. If the effective solubility parameter of ethanol and methanol is close to that of diethyl ether (a nonassociated liquid), the correction term due to nonspecific interactions is around zero and the K_C^{th} values are approximately equal to the K_C^S values.

The linearity of the plots in Figure 1 means that K_C^S stays the same in all solutions. This seems contradictory to the model whereby with increasing alcohol concentration, and hence increasing aggregation, the iodine supposedly interacts with a stronger donor. This poses the question as to the physical interpretation of K_C^S.

According to the proposed model, iodine in concentrated solution interacts with an alcohol aggregate, D_n, where n is the average number of alcohol molecules in the aggregate:

$$D_n + I_2 \rightleftarrows D_n\text{–}I_2 \quad (3)$$

The equilibrium constant for reaction 3 is

$$K_n = [D_n\text{–}I_2]/[D_n]\,[I_2]_{0,t} \quad (4)$$

where $[D_n]$ is the equilibrium concentration of the uncomplexed alcohol aggregate, which for a weak complex is practically the same as the total concentration of the alcohol aggregate, and $[D_n\text{–}I_2]$ is the equilibrium concentration of the complex. Similarly for the dilute solution, which differs from the above case only in that the average number of alcohol molecules in the aggregate is m instead of n, where $m < n$

$$K_m = [D_m\text{–}I_2]/[D_m]\,[I_2]_{0,t} \quad (5)$$

Since a larger aggregate is considered to be the stronger donor, it is expected that $K_n > K_m$.

Actually, eq 3–5 summarize a more complicated physical system. In a solution of an alcohol–iodine complex, the actual number of alcohol molecules in the aggregate is not likely to be unique. We may assume that in a solution there are many different kinds of alcohol polymers, e.g., $D_1, D_2, \ldots, D_i$ where the index i refers to the number of alcohol molecules in the aggregate. Each aggregate interacts with iodine to form a different complex species, and the following equations exist:

$$D_1 + I_2 \rightleftarrows D_1\text{–}I_2 \qquad K_1 = [D_1\text{–}I_2]/[D_1]\,[I_2]_{0,t} \quad (6)$$

$$D_2 + I_2 \rightleftarrows D_2\text{–}I_2 \qquad K_2 = [D_2\text{–}I_2]/[D_2]\,[I_2]_{0,t} \quad (7)$$

$$D_i + I_2 \rightleftarrows D_i\text{–}I_2 \qquad K_i = [D_i\text{–}I_2]/[D_i]\,[I_2]_{0,t} \quad (8)$$

or

$$[D_i\text{–}I_2] = K_i[D_i]\,[I_2]_{0,t} \quad (9)$$

If there are p different kinds of aggregates in solution there will be p equations similar to eq 8. (The number p is not necessarily the same as the number i.) The measured absorbance, A, of the solution at a given wavelength is the sum of the absorbances of all the complex species

$$A = \sum_p (A_i)_p \quad (10)$$

The absorbance of each species, A_i, follows Beer's law, i.e., $A_i = \epsilon_i b [D_i\text{–}I_2]$. Therefore

$$A = \sum_p (\epsilon_i b [D_i\text{–}I_2])_p \quad (11)$$

The total concentration of complexed iodine is $\sum_p([D_i\text{–}I_2])_p$; and the total concentration of complexed alcohol is $\sum_p(i[D_i\text{–}I_2])_p$. For a weak complex, these two concentration terms of complexed species are small compared to

the total initial concentration of alcohol. Renaming the total complexed iodine concentration as $[D_n\text{-}I_2]$, that is

$$[D_n\text{-}I_2] = \sum_p ([D_i\text{-}I_2])_p \quad (12)$$

and choosing a constant, ϵ_n, such that

$$b\epsilon_n[D_n\text{-}I_2] = A = \sum_p (b\epsilon_i[D_i\text{-}I_2])_p \quad (13)$$

leads to the following by combining eq 12 and 13:

$$\epsilon_n = \sum_p (\epsilon_i[D_i\text{-}I_2])_p / \sum_p ([D_i\text{-}I_2])_p \quad (14)$$

Let the initial alcohol concentration in terms of monomer be $[D]_T$, which equals the sum of the alcohol molecules in all the free and complexed aggregates

$$[D]_T = \sum_p (i[D_i])_p + \sum_p (i[D_i\text{-}I_2])_p \quad (15)$$

If for the present we choose to define $[D_n]$ as

$$[D_n] = \frac{[D]_T - \sum_p (i[D_i\text{-}I_2])_p}{n} \quad (16)$$

where n is a number (not necessarily an integer), then dividing eq 12 by eq 16 and by $[I_2]_{0,t}$ gives

$$\frac{[D_n\text{-}I_2]}{[D_n][I_2]_{0,t}} = \frac{\sum_p ([D_i\text{-}I_2])_p}{(\{[D]_T - \sum_p (i[D_i\text{-}I_2])_p\}/n)[I_2]_{0,t}} \quad (17)$$

For a solution of a particular alcohol concentration in equilibrium with polyiodide, all the terms on the right-hand side of eq 17 are constant. Therefore eq 17 becomes

$$[D_n\text{-}I_2]/[D_n][I_2]_{0,t} = K_n \quad (18)$$

and leads to the result such that eq 18 seems to represent the equilibrium constant of a single species of an alcohol aggregate D_n interacting with iodine for the following conditions in the constant activity method:

$$D_n + I_2 \rightleftarrows D_n\text{-}I_2 \quad (19)$$

initial concentration:

$$[D_n]_0 = \frac{[D]_T}{n} \qquad [I_2]_{0,t} \qquad 0.0$$

equilibrium concentration:

$$[D_n] = \frac{[D]_T}{n} - [D_n\text{-}I_2] \qquad [I_2]_{0,t} \qquad [D_n\text{-}I_2]$$

Here, the equilibrium constant

$$K_n = [D_n\text{-}I_2] \Big/ \left\{ \frac{[D]_T}{n} - [D_n\text{-}I_2] \right\} [I_2]_{0,t} = \frac{[D_n\text{-}I_2]}{[D_n][I_2]_{0,t}} \quad (20)$$

is identical with that in eq 17 and 18.

The meaning of the number n can be seen by combining eq 12, 16, 18, and 20:

$$[D_n] = \frac{[D]_T - \sum_p (i[D_i\text{-}I_2])_p}{n} = \frac{[D]_T}{n} - [D_n\text{-}I_2] \quad (21)$$

that is

$$n = \frac{\sum_p (i[D_i\text{-}I_2])_p}{[D_n\text{-}I_2]} = \frac{\sum_p (i[D_i\text{-}I_2])_p}{\sum_p ([D_i\text{-}I_2])_p} \quad (22)$$

n is the weighted average number of alcohol molecules in the aggregates complexing with iodine. For all practical purposes, the solution can be treated as consisting of only one kind of aggregate, D_n, with the complex species represented by $D_n\text{-}I_2$. The constant K_n is a representative equilibrium constant. The constant ϵ_n from eq 14 is a weighted average molar absorptivity of all the complex species, and can be treated as the molar absorptivity of the unique representative species $D_n\text{-}I_2$.

Turning to the physical interpretation of K_C^S, which is defined as

$$K_C^S = \frac{\text{total complexed iodine concentration}}{\text{(total alcohol concentration as monomer} - \text{total complexed alcohol concentration as monomer)(free iodine concentration)}}$$

and, using terms defined previously, this becomes

$$K_C^S = \frac{\sum_p ([D_i\text{-}I_2])_p}{\{[D]_T - \sum_p (i[D_i\text{-}I_2])_p\}[I_2]_{0,t}} \quad (23)$$

Substituting eq 15 and 16 into eq 23 gives

$$K_C^S = \frac{\sum_p ([D_i\text{-}I_2])_p}{n[D_n][I_2]_{0,t}} = \frac{\sum_p ([D_i\text{-}I_2])_p}{\{\sum_p (i[D_i])_p\}[I_2]_{0,t}} \quad (24)$$

and substituting eq 9 into eq 24 gives

$$K_C^S = \frac{\sum_p (K_i[D_i][I_2]_{0,t})_p}{\{\sum_p (i[D_i])_p\}[I_2]_{0,t}} = \frac{\sum_p (K_i[D_i])_p}{\sum_p (i[D_i])_p} \quad (25)$$

Comparing eq 17, 18, and 23 then gives

$$K_C^S = K_n/n \quad (26)$$

Equation 25 shows that K_C^S is a weighted average of all the equilibrium constants for all different aggregates complexing with iodine in that solution.

For a dilute solution, similar equations apply, e.g.

$$K_C^{S'} = \frac{\sum_{p'} (K_i[D_i]')_{p'}}{\sum_{p'} (i[D_i]')_{p'}} = \frac{K_m}{m} \quad (27)$$

where the primes refer to the quantities in dilute solution.

Further, since the overall alcohol concentration range used in this study is relatively small, the variation of the weighted average of the equilibrium constant may be too small to be detected, and then $K_C^S \simeq K_C^{S'}$. However, even if K_C^S and $K_C^{S'}$ are equal, this does not mean that the representative equilibrium constants K_n and K_m are equal. Equations 26 and 27 show that K_n ($= nK_C^S$) will be greater than K_m ($= mK_C^{S'}$) because n is larger than m. Hence, there is no contradiction between the aggregate model and the experimental result for K_C^S in different solutions.

The aggregate number expressed by eq 22 probably is only very slightly different, under the experimental conditions, from that in a system of an alcohol solution free of iodine as considered by Tucker and Christian.[9] It is of interest to use their data on vapor pressure measurements of methanol and ethanol in n-hexadecane to estimate the magnitude of n and m. Assuming the extent

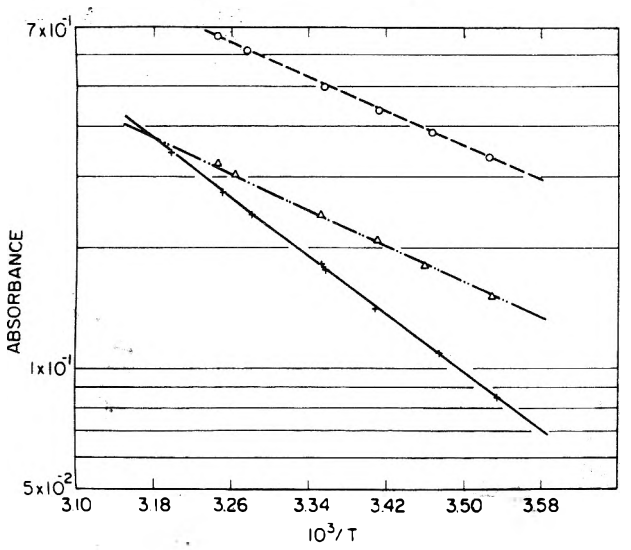

Figure 2. log A vs. $10^3/T$ (in n-heptane solution): (+) A at 520 nm for $TMAI_5$–$TMAI_3$ equilibrium; (O) A at isosbestic point for ethanol–iodine complex studied by the constant activity method, $[D]_0 = 0.280$ M; (Δ) A at isosbestic point for methanol–iodine complex studied by the constant activity method, $[D]_0 = 0.159$ M.

of association of the alcohols in n-heptane is the same as that in n-hexadecane, it is found that for both ethanol and methanol solutions the aggregate number will increase from 1.2 to 4.1 when the total (or formal) concentration of alcohol increases from about 0.04 to 0.6 M.

The Heat of Complexation. At any given temperature and wavelength, eq 2 for a weak complex can be rewritten as

$$K_C{}^S = \frac{A}{\epsilon_C b [I_2]_{0,t} [D]_0} \tag{28}$$

where ϵ_C is the molar absorptivity of the complex. Taking the logarithm of eq 28, the derivative with respect to $1/T$, and then rearranging the terms give

$$\frac{d \log K_C{}^S \epsilon_C}{d(1/T)} = \frac{-\Delta H_C^\circ}{2.303R} = \frac{d \log A}{d(1/T)} - \frac{d \log [I_2]_{0,t}}{d(1/T)} - \frac{d \log [D]_0}{d(1/T)} \tag{29}$$

provided that the temperature dependence of ϵ_C is essentially zero. The middle term on the right-hand side of eq 29 corresponds to the heat of solution of $TMAI_5$ in n-heptane. The last term of eq 29 is the temperature dependence of the initial donor concentration which, for a dilute solution, is essentially the same as the density variation of the pure solvent. Therefore, ΔH_C° can be determined by a temperature dependence study of the absorbance of the complex using only a single solution of donor with excess pentaiodide.

The van't Hoff plot of the absorbance of iodine at 520 nm from the $TMAI_5/TMAI_3$ equilibrium in n-heptane solution is shown in Figure 2. This equation follows the relation $\log (A/b) = -1788.21/T + 5.2522$ from which the heat of solution is 8.18 ± 0.14 kcal/mol. Topol[10] determined the heat of reaction of the following solid system by emf measurement and reported a value of 2.2 ± 0.1 kcal/mol:

$$(CH_3)_4NI_5(s) \rightleftarrows (CH_3)_4NI_3(s) + I_2(s) \tag{30}$$

Using this value and the solubility data of iodine in n-heptane reported by Hildebrand and Jenk[11] (from which the heat of solution is calculated to be 6.8 kcal/mol) gives a heat of solution of $TMAI_5$ in n-heptane of 9.0 kcal/mol. This differs by 0.8 kcal/mol from the one obtained in the present study. However, using the heat of reaction of eq 30 reported by Foote and Fleischer,[12] the heat of solution of $TMAI_5$ becomes 8.5 kcal/mol which is close to the one found in this study.

$TMAI_5$ solutions with ethanol concentrations of 0.121 and 0.280 M and with methanol concentrations of 0.159 and 0.130 M were studied to determine the heats of complexation. Higher alcohol concentrations were not used because these solutions gave too high an absorbance at higher temperatures and because the correction for the triiodide ion absorbance was quite large. Absorbance data at the isosbestic point rather than those at the blue-shifted iodine band maximum (λ^{BS}) were used in the van't Hoff plot because, for λ^{BS}, there is a slight shift in band position with temperature and the correction for the triiodide ion absorption is larger. Figure 2 shows the plot of log A^{isos} vs. $1/T$ for iodine in the solutions of higher alcohol concentration, from which the enthalpy change for this term in eq 29 is calculated to be 4.82 ± 0.22 kcal/mol for ethanol–iodine and 5.02 ± 0.40 kcal/mol for methanol–iodine. Data for the dilute solutions gave practically the same value for the two complexes.

The correction of the enthalpy due to the density change of the solution with temperature was calculated using the data for pure n-heptane in Timmermans,[13] and is −0.22 kcal/mol. Combining the three enthalpy values corresponding to the terms in eq 29 gives the heat of complexation for ethanol–iodine as −3.2 ± 0.2 kcal/mol and for methanol–iodine as −3.0 ± 0.4 kcal/mol.

The values for the heats of complexation must be considered as representing a composite result for alcohol–iodine of different alcohol aggregation, i.e.

$$\Delta H_C^\circ = \frac{\sum_p (\Delta H_i^\circ [D_i\text{–}I_2])_p}{\sum_p ([D_i\text{–}I_2])_p} \tag{31}$$

Since the donor strength increases with increasing alcohol aggregations, it would be expected that ΔH_C° is larger for a more concentrated solution. The fact that the same results were obtained for the two solutions of different alcohol concentration may be due to the small range of the alcohol, so that the results are comparable within experimental error.

Results Obtained by the Benesi–Hildebrand–Scott Method. The alcohol–iodine complexes also were studied in the visible region by the Scott modification of the Benesi–Hildebrand method. Six solutions with an iodine concentration around 1.6×10^{-4} M and alcohol concentrations ranging from 0.1 to 0.6 M were used. Figures 3a and 3b show the difference spectra in the visible region of the most dilute and most concentrated ethanol–iodine and methanol–iodine solutions in n-heptane run vs. an iodine–n-heptane reference. For both complexes the apparent band maximum changed from 455 to 447.5 nm when the alcohol concentration increases. From the measured absorbance

$$A = b[C](\epsilon_C - \epsilon_{I_2}) = b[C]\epsilon_C' \tag{32}$$

it is clear that, if at a particular wavelength ϵ_{I_2} does not change appreciably with alcohol concentration but ϵ_C' does change, then the actual molar absorptivity of the complex (ϵ_C) must also change with alcohol concentration. Thus the spectra from the conventional Benesi–Hildebrand method also indicate that the blue-shifted iodine band of these two complexes moves to longer wavelength upon dilution, as reported in the earlier paper.[1]

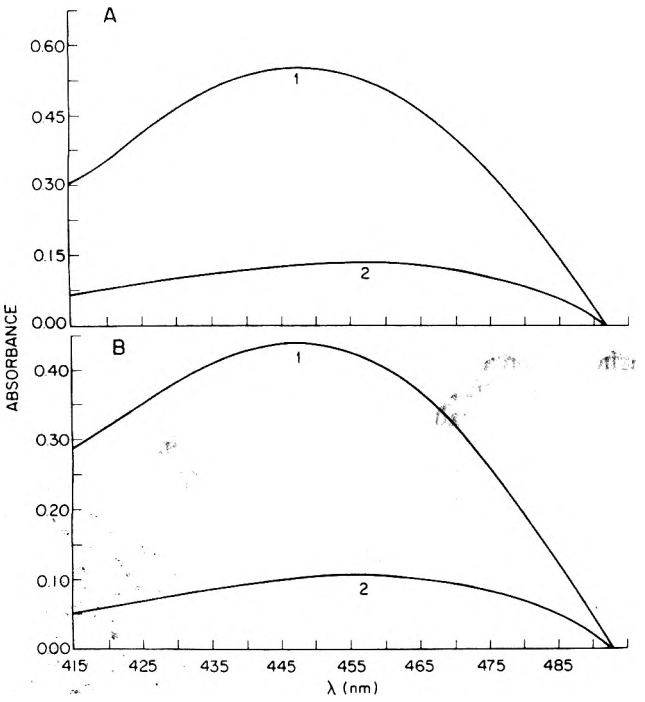

Figure 3. Visible spectrum of the alcohol–iodine complex in *n*-heptane studied by the Benesi–Hildebrand method: t = 24.8 °C, cell path = 10.00 cm, $[I_2]_0$ in reference cell; (A) ethanol–iodine complex: (1) $[D]_0$ = 0.5935 M and $[I_2]_0$ = 1.589 × 10^{-4} M, (2) $[D]_0$ = 0.1015 M and $[I_2]_0$ = 1.589 × 10^{-4} M; (B) methanol–iodine complex: (1) $[D]_0$ = 0.5433 M and $[I_2]_0$ = 1.608 × 10^{-4} M, (2) $[D]_0$ = 0.1003 M and $[I_2]_0$ = 1.608 × 10^{-4} M.

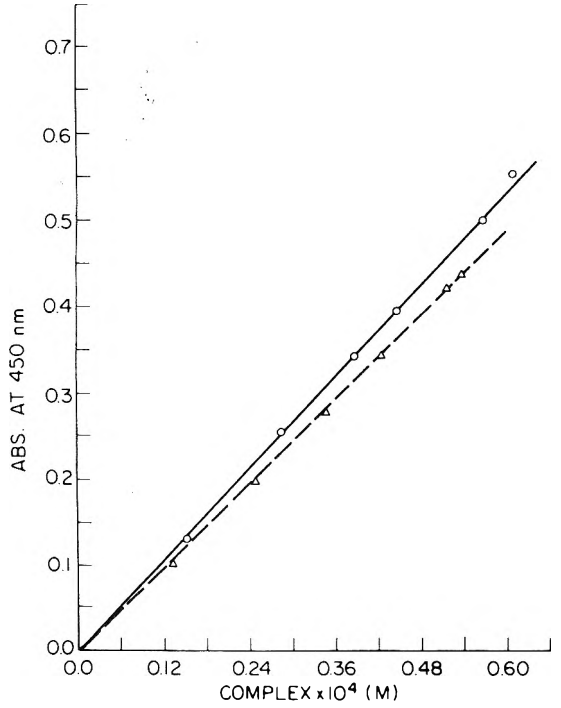

Figure 4. Alcohol–iodine complex in *n*-heptane studied by the Benesi–Hildebrand method. Test of Beer's law at λ 450 nm: (O) ethanol–iodine; (Δ) methanol–iodine.

In the Scott equation, it is assumed that Beer's law holds. As mentioned, this assumption is not strictly true for the alcohol–iodine complexes. However, by choosing a fixed intermediate wavelength, namely 450 nm, it was observed that the absorbance was quite close to the maximum value for all the spectral curves (considering that the maxima are generally broad). Therefore, at 450 nm the change in ϵ_C' with dilution is relatively small and

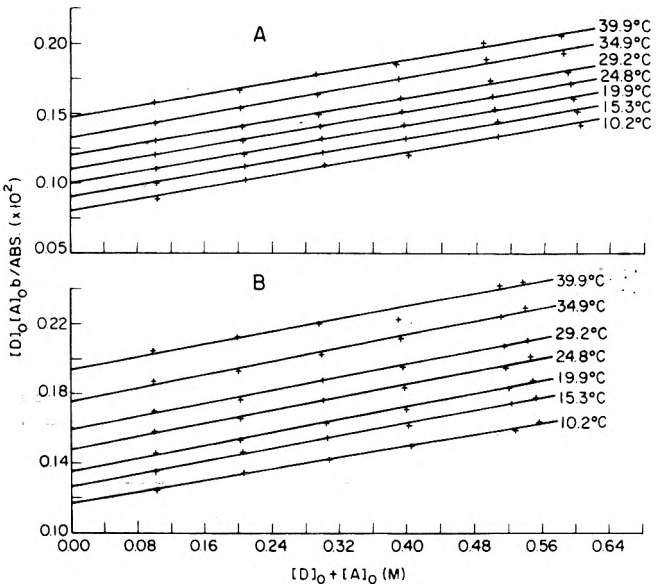

Figure 5. Scott plot of the alcohol–iodine complex in *n*-heptane at λ 450 nm: (A) ethanol–iodine; (B) methanol–iodine.

TABLE I: Alcohol–Iodine Complexes in *n*-Heptane Studied by the Benesi–Hildebrand Method[a]

Temp, °C	$K_C^{BH}\epsilon_C'$, M^{-2} cm^{-1}	K_C^{BH}, M^{-1}	ϵ_C' at 450 nm, M^{-1} cm^{-1}
	Ethanol-Iodine		
39.9	678.8 ± 24.1	0.69 ± 0.12	983.6 ± 133.2
34.9	755.3 ± 27.7	0.81 ± 0.12	930.8 ± 110.2
29.2	835.0 ± 25.9	0.86 ± 0.11	968.3 ± 90.6
24.8	911.1 ± 15.9	0.95 ± 0.06	959.1 ± 45.6
19.9	1001.1 ± 28.2	1.04 ± 0.01	962.1 ± 67.0
15.3	1109.4 ± 39.5	1.16 ± 0.13	953.2 ± 74.7
10.2	1248.6 ± 85.9	1.32 ± 0.26	946.3 ± 125.4
	Methanol-Iodine		
39.9	517.3 ± 27.5	0.48 ± 0.17	1081.9 ± 322.8
34.9	571.3 ± 18.1	0.56 ± 0.10	1028.3 ± 156.5
29.2	629.3 ± 14.4	0.60 ± 0.73	1055.0 ± 107.5
24.8	679.3 ± 22.9	0.65 ± 0.11	1050.0 ± 144.1
19.9	740.8 ± 18.3	0.69 ± 0.08	1069.8 ± 99.9
15.3	792.0 ± 16.9	0.73 ± 0.07	1086.2 ± 83.0
10.3	857.2 ± 17.4	0.71 ± 0.07	1204.4 ± 88.8

[a] Absorbance data at 450 nm were used and the error limits are at the 95% confidence level.

probably not much beyond experimental error in reading the absorbance, especially at the lower concentrations. This assumption was tested in the following way. It had been pointed out by Childs[2,6] that the corrected equilibrium constant (K_C^{th}) obtained by the constant activity method is close to the equilibrium constant obtained by the Benesi–Hildebrand method (K_C^{BH}). Therefore K_C^{th} at 24.8 °C was used to calculate the concentration of the complex present in each of the different solutions studied by the Benesi–Hildebrand method. Plots of the measured absorbance at 450 nm vs. the calculated concentration of the complex for the two alcohol–iodine complexes are shown in Figure 4. From the linearity, it appears that Beer's law holds within experimental error. Similar linearity also is observed if K_C^S is used.

Consequently, the absorbance at 450 nm was used for the Scott plot. Figures 5a and 5b show these plots at seven different temperatures. At each temperature there is a good straight line passing through all the data points which also indicates that Beer's law holds. The $K_C^{BH}\epsilon_C'$ product and the separated K_C^{BH} and ϵ_C' values at each temperature are given in Table I.

The results at 24.8 °C are compared in Table II with those obtained by the constant activity method. This table

TABLE II: Comparison of the Results Obtained by the Constant Activity Method and by the Benesi-Hildebrand Method

	Constant activity method				Benesi-Hildebrand method		
Donor[a]	K_C^{th}, M^{-1}	K_C^{s}, M^{-1}	$(\epsilon_C^{CT})^s$, M^{-1} cm^{-1}	$K_C^s(\epsilon_C^{CT})^s$, M^{-2} cm^{-1}	K_C^{BH}, M^{-1}	$(\epsilon_C^{CT})^{BH}$, M^{-1} cm^{-1}	$K_C^{BH}(\epsilon_C^{CT})^{BH}$, M^{-2} cm^{-1}
Benzene	0.15	0.356	8080	2880	0.203	14200	2880
Toluene	0.28	0.500	6900	3450	0.315	10700	3370
o-Xylene	0.37	0.641	6520	4190	0.423	9680	4100
p-Xylene	0.40	0.642	5710	3660	0.411	8860	3640
m-Xylene	0.46	0.698	6550	4570	0.539	8990	4850
Diethyl ether	1.44	1.44	5720	8230	1.23	5560	6840

Donor[b]	K_C^{th}	K_C^{s}	$(\epsilon_C')^s$	$K_C^s(\epsilon_C')^s$	K_C^{BH}	$(\epsilon_C')^{BH}$	$[K_C^{BH}(\epsilon_C')^{BH}]$
Ethanol	1.06 ± 0.03	1.50 ± 0.03	710 ± 20	1065	0.95 ± 0.06	959	911
Methanol	0.91 ± 0.09	1.29 ± 0.09	708 ± 28	913	0.65 ± 0.11	1050	679

[a] Childs' data[2a] in the UV region. [b] This work in the visible region at 450 nm; $\epsilon_C' = \epsilon_C - \epsilon_{I_2}$.

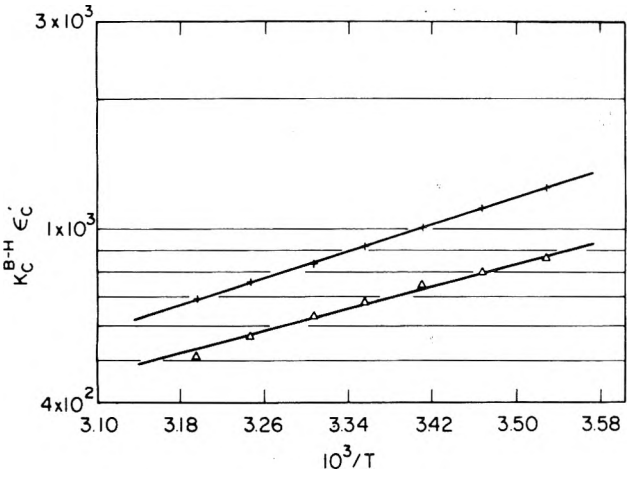

Figure 6. Van't Hoff plot of log $K_C^{BH}\epsilon_C'$ vs. $10^3/T$ for alcohol–iodine in *n*-heptane studied by the Benesi-Hildebrand method: (+) ethanol–iodine, (Δ) methanol–iodine.

includes similar data from the work of Childs[2,6] on iodine complexes studied in the UV region. The $(\epsilon_C')^s$ in the table was obtained by subtracting the known value of ϵ_{I_2} from the value of $(\epsilon_C)^s$ at 450 nm. The $(\epsilon_C)^s$ was calculated by using the average value of $\Delta\nu_{1/2}^{BS}$, the weighted regression value of ϵ^{BS}, the appropriate λ^{BS} for each solution, and assuming a Gaussian band shape. In the different solutions ranging from 0.6 to 0.1 M alcohol the $(\epsilon_C')^s$ values for the ethanol–iodine complex (in units of M^{-1} cm^{-1}) are 729 ± 10, 728 ± 10, 721 ± 12, 718 ± 12, 706 ± 20, and 660 ± 40. For the methanol–iodine complex, they are 740 ± 3, 735 ± 7, 726 ± 10, 711 ± 10, 696 ± 20, and 634 ± 40. Except perhaps for the last result for the most dilute solution, where the error is appreciably larger, it can be seen that $(\epsilon_C')^s$ at 450 nm for both complexes does not change very much with alcohol concentration. This is consistent with the previous results for the test of Beer's law at 450 nm (Figure 4). The average $(\epsilon_C')^s$ for ethanol–iodine over the concentration range is 710 ± 20 M^{-1} cm^{-1} and for methanol–iodine it is 708 ± 28 M^{-1} cm^{-1}. The corresponding $K_C^s(\epsilon_C')^s$ is 1065 and 913 M^{-2} cm^{-1}, respectively (Table II).

The values of $K_C^{BH}\epsilon_C'$ at different temperatures were used in the van't Hoff plot shown in Figure 6 for the two complexes. The heat of complexation so determined is −3.5 ± 0.2 kcal/mol for ethanol–iodine and −3.0 ± 0.2 kcal/mol for methanol–iodine. These values are very close to those obtained by the constant activity method.

It has been pointed out by Ham[14] and later others[15] that the heat of complexation can be correlated with the blue shift of the visible iodine band, ΔW_{vis} (= $h\nu^{BS} - h\nu_{I_2}$). Mulliken and Person[15a] have plotted ΔW_{vis} vs. $-\Delta H_C°$ for a large variety of iodine complexes. A trend is noted,

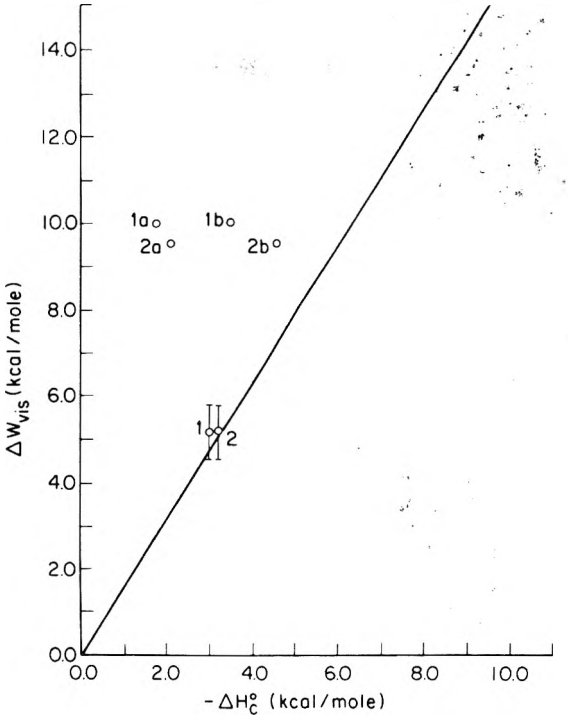

Figure 7. Correlation of the blue shift of the visible complexed iodine band with the heat of complexation; slope from Mulliken and Person:[15a] (1) methanol–iodine; (2) ethanol–iodine: no letter (this work), a (ref 3), b (ref 4).

although the data are rather scattered. Their best line through the points gave a slope of 1.57, as shown in Figure 7. It can be seen in this figure that the data for the alcohol–iodine complexes from the present study show appreciably less scatter from the line than the earlier literature results. It should not be construed, however, that the scatter for other donors arises solely from imprecise data. Recently, Paetzold and co-workers[16] have reported that a quite good linear correlation exists for iodine complexes with homologous series of donors, but the slope is different for each different homologous series.

Acknowledgment. One of the authors (H.C.T.) thanks the Horace H. Rackham School of Graduate Studies at The University of Michigan for a predoctoral fellowship. This research was supported in part by the National Science Foundation through Grant No. GP-38403X.

References and Notes

(1) H. C. Tse and M. Tamres, *J. Phys. Chem.*, preceding paper in this issue.
(2) (a) J. D. Childs, Ph.D. Dissertation, The University of Oklahoma, 1971. (b) J. D. Childs, S. D. Christian, and J. Grundnes, *J. Am. Chem. Soc.*, **94**, 5657 (1972).

(3) P. A. D. de Maine, *J. Chem. Phys.*, **26**, 1192 (1957).
(4) (a) L. M. Julien, Ph.D. Dissertation, The University of Iowa, 1966. (b) L. M. Julien, W. E. Bennett, and W. B. Person, *J. Am. Chem. Soc.*, **91**, 6915 (1969).
(5) Y. Amako, *Sci. Rep. Tohohu Univ., Ser 1*, **40**, 147 (1956).
(6) (a) S. D. Christian, J. D. Childs, and E. H. Lane, *J. Am. Chem. Soc.*, **94**, 6861 (1972); (b) E. H. Lane, S. D. Christian, and J. D. Childs, *ibid.*, **96**, 38 (1974).
(7) (a) J. H. Hildebrand and R. L. Scott, "The Solubility of Nonelectrolytes", Reinhold, New York, N.Y., 1950. (b) J. H. Hildebrand, J. M. Prausnitz, and R. L. Scott, "Regular and Related Solutions", Van Nostrand-Reinhold, New York, N.Y., 1970.
(8) D. R. Stull, E. F. Westrum, Jr., and G. C. Sinke, "The Chemical Thermodynamics of Organic Compounds", Wiley, New York, N.Y., 1969.
(9) (a) E. E. Tucker, S. B. Farnham, and S. D. Christian, *J. Phys. Chem.*, **73**, 3820 (1968); (b) E. E. Tucker and S. D. Christian, private communication.
(10) L. E. Topol, *Inorg. Chem.*, **10**, 736 (1971).
(11) J. H. Hildebrand and C. A. Jenk, *J. Am. Chem. Soc.*, **42**, 2180 (1920).
(12) H. W. Foote and M. Fleischer, *J. Phys. Chem.*, **57**, 122 (1953).
(13) J. Timmermans, "Physico-Chemical Constants of Pure Organic Compounds", Elsevier, New York, N.Y., 1965.
(14) J. Ham, *J. Am. Chem. Soc.*, **76**, 3875 (1954).
(15) (a) R. S. Mulliken and W. B. Person, "Molecular Complexes", Wiley-Interscience, New York, N.Y., 1969. (b) G. Briegleb, "Electronen-Donator-Acceptor Komplexe", Springer-Verlag, Berlin, 1961.
(16) (a) R. Paetzold and K. Niendorf, *Z. Phys. Chem.*, **256**, 361 (1975); (b) R. Paetzold, *Z. Chem.*, **15**, 377 (1975).

Reduction Potentials of Complex Ions. The Bis(2,6-pyridinedialdoxime)iron(III–II) System

G. I. H. Hanania,* M. S. Michailides, and D. H. Irvine†

Department of Chemistry, American University of Beirut, Beirut, Lebanon *(Received March 24, 1976; Revised Manuscript Received March 31, 1977)*

The reduction potential of aqueous bis(2,6-pyridinedialdoxime)iron(III–II) couple was measured potentiometrically covering a range of pH, ionic strength, and temperature. The equilibrium constant for formation of the iron(II) bis complex was spectrophotometrically determined. Numerical analysis was applied to the redox and equilibrium data as a whole to obtain a self-consistent set of parameters: E_i, the reduction potential at the limit of high pH (eq 4b); K_{ii}, formation constant for the iron(II) complex at the limit of low pH; four H^+ dissociation constants of oxime groups in the reductant ion, the iron(II) complex; and two of the four oxime H^+ dissociation constants in the oxidant ion, the iron(III) complex. From ionic strength and temperature dependence of the parameters, thermodynamic quantities were obtained. Enthalpy and entropy contributions to the free energy of the cell reaction and its related equilibria are discussed, with special reference to pH effects. The system is suitable as a model for the study of some thermodynamic aspects of the redox properties of hemoproteins.

Introduction

One of the factors which determine reactivities and relative stabilities of oxidation states in aqueous complex ions is the intramolecular electrostatic environment of the metal. This is evident in hemoproteins and metallo-enzymes where the dominant effects of pH on equilibria and kinetics of reactions indicate the role of side group ionizations. Since one cannot unequivocally assign thermodynamic parameters to individual groups in such complicated molecules, the relevance is seen of seeking model coordination systems incorporating redox and ionization properties with the desired structural features.

In an earlier study[1] of the complex ion system tris(2-pyridinealdoxime)iron(III–II) it was shown that the observed pH variation of reduction potential could be accounted for in terms of three H^+ dissociation equilibria of oxime side groups in each of the oxidant and reductant ions. For the parent cell reaction involving protonated species, the potential was about 1 V, a value characteristic of octahedral iron complexes with neutral N-heterocyclic ligands, and for the case involving fully ionized species at high pH the potential dropped to the lower limit of 0.35 V. The corresponding N-coordinated iron complexes in the hemoproteins cytochrome c, hemoglobin, and myoglobin have iron(III–II) reduction potentials of 0.3, 0.2, and 0.1 V, respectively.

As an N-terdentate ligand, 2,6-pyridinedialdoxime forms octahedral bis complexes of iron like the tris complexes of 2-pyridinealdoxime. However, since it has two =NOH oxime groups per ligand molecule, there are four rather than three ionizing groups in each of its oxidant and reductant ions. Thus a second system is available for testing the generality of the observation about the effect of side group ionizations on the thermodynamics of the cell reaction for complex ions. In this paper, we report a potentiometric study of the reduction potential of the bis-(2,6-pyridinedialdoxime)iron(III–II) couple covering a range of pH, ionic strength, and temperature, and an evaluation of some thermodynamic quantities for the cell reaction and its related equilibria.

The ligand reacts readily with ferrous salts in acidic aqueous solution to form a stable red bis complex with an overall equilibrium constant, K = (complex)/(iron)(ligand)^2, defined in terms of total molar concentrations at given pH, ionic strength, and temperature. The specific ionic species will of course depend on what ionization and other equilibria are involved. The $Fe^{2+}(aq)$ ion is known to undergo hydrolysis as well as ion association, but at low pH and low salt concentration these side reactions may be neglected as a first approximation. The neutral ligand, PH_2, has two weakly acidic oxime groups with ionization pK values of 10.1 and 10.9, respectively.[2] There are

* Visiting Professor, Department of Chemistry, Indiana University, Bloomington, Ind. 47401.
† Vice-chancellor, University of Guyana, Georgetown, Guyana.

therefore four successive oxime ionizations involving the bis(2,6-pyridinedialdoxime)iron(II) ion:

$$FeP_2H_4^{2+} \rightleftharpoons FeP_2H_3^{+} \rightleftharpoons FeP_2H_2 \rightleftharpoons FeP_2H^{-} \rightleftharpoons FeP_2^{2-} \quad (1)$$

with four corresponding ionization constants K_1, K_2, K_3, and K_4. Since practical considerations require the confinement of measurements to the acidic pH range, where contributions from oxime ionizations in the free ligand are negligible, it follows that the observed equilibrium constant, K, for the formation of the bis complex, will vary with pH according to the approximate relation:

$$K = K_{ii}(1 + (K_1/h) + (K_{12}/h^2) + (K_{123}/h^3) + (K_{1234}/h^4)) \quad (2)$$

where $K_{12} = K_1K_2$, etc., h is the hydrogen ion activity, and K_{ii} is the equilibrium constant for the parent formation reaction involving fully protonated species at the limit of low pH. A corresponding relation can be derived to include K_i, the equilibrium constant for the hypothetical formation reaction involving fully ionized species at the limit of high pH; in this case, however, account must be taken of oxime ionizations in the free ligand. Equation 2 enables one to obtain the value of K_{ii}, at constant ionic strength and temperature, from experimental data on pH and the observed equilibrium constant K, with four parameters (ionization constants K_1 through K_4) to be determined by numerical analysis of the data. Actually, K_4 is accurately known from spectrophotometric titration of the complex.[2] At the other pH extreme, the equilibrium constant K_i can similarly be computed from the data.

The ligand also reacts with ferric salts to form a bis complex, but the reaction is slower than that of ferrous salts, and the complex has a narrower range of stability. The Fe^{3+}(aq) ion is known to undergo extensive hydrolysis and ion association, as well as the formation of binuclear oxobridged complexes.[3] These side reactions can be minimized but are not entirely eliminated by confining measurements to low pH and salt concentration, and the results are that much less accurate. By analogy with eq 1, there are four successive oxime ionizations involving bis(2,6-pyridinedialdoxime)iron(III) ion:

$$FeP_2H_4^{3+} \rightleftharpoons FeP_2H_3^{2+} \rightleftharpoons FeP_2H_2^{+} \rightleftharpoons FeP_2H \rightleftharpoons FeP_2^{-} \quad (3)$$

with the four corresponding ionization constants K_1' through K_4' primed to distinguish them from those of the iron(II) complex. Similarly, an equation analogous to eq 2 can be written for pH variation of the equilibrium constant K' which refers to formation of the iron(III) complex. In this case, however, some account must be taken of hydrolysis and other equilibria, thereby adding to the uncertainty in K' values thus obtained.

Reduction Potential. The reduction potential, E, referring to the bis(2,6-pyridinedialdoxime)iron(III–II) couple, is defined for equimolar concentrations of oxidant and reductant ions at given pH, ionic strength, and temperature. The pH variation of E will be determined by four oxime ionization constants in the oxidant (K_1' through K_4') and the corresponding four in the reductant (K_1 through K_4). Two pH-independent reduction potentials can be defined: E_{ii} for the cell reaction involving fully protonated species at the limit of low pH, and E_i for the same cell reaction involving fully ionized species at the limit of high pH:

$$FeP_2H_4^{3+} + {}^1/_2H_2 = FeP_2H_4^{2+} + H^+ \quad (E_{ii}) \quad (4a)$$

$$FeP_2^{-} + {}^1/_2H_2 = FeP_2^{2-} + H^+ \quad (E_i) \quad (4b)$$

In both cases, the parent reaction includes the redox couple vs. standard hydrogen electrode. If the only ionic equilibria which affect the free energy change for the cell reaction are oxime group ionizations, then the pH variation of E will be given by:

$$E = E_{ii} + (RT/F) \times \ln \frac{(1 + (K_1/h) + (K_{12}/h^2) + (K_{123}/h^3) + (K_{1234}/h^4))}{(1 + (K_1'/h) + (K_{12}'/h^2) + (K_{123}'/h^3) + (K_{1234}'/h^4))} \quad (5a)$$

$$= E_i + (RT/F) \times \ln \frac{(1 + (h/K_4) + (h^2/K_{34}) + (h^3/K_{234}) + (h^4/K_{1234}))}{(1 + (h/K_4') + (h^2/K_{34}') + (h^3/K_{234}') + (h^4/K_{1234}'))} \quad (5b)$$

where $K_{12} = K_1K_2$ etc. and h is the hydrogen ion activity as in eq 2, and the Nernst parameter $(2.303RT/F) = 59.16$ mV at 25 °C. Equations 5a and 5b enable one to obtain E_{ii} and E_i which are the upper and lower limits of reduction potential, from the observed variation of E with pH at constant ionic strength and temperature. Numerical analysis of the data also yields values for the various ionization constants.

To obtain the thermodynamic reduction potential for the cell reaction in eq 4b, a Debye–Hückel function $f(I) = I^{1/2}/(1 + 2I^{1/2})$ may be used for the ionic strength variation assuming 0.6 nm as ion size parameter. It then follows that

$$E_i = E_i^{\circ} + 3A(2.303RT/F)(I^{1/2}/(1 + 2I^{1/2})) \quad (6)$$

where $A = 0.510$ for water at 25 °C, making the linear slope of the ionic strength variation of E_i equal to 90.5 mV. Equation 6 can be used for testing the data within a range of ionic strength sufficiently low for the above assumptions to be acceptable. Furthermore, assuming that ionic activities are constant within the range of temperature covered, the temperature coefficient of reduction potential may be assumed independent of ionic strength at low I, so that $dE_i/dT = dE_i^{\circ}/dT$, the value at zero ionic strength. Accordingly, enthalpy and entropy changes for the cell reaction in eq 4b are given by the thermodynamic relations (with reduction potentials expressed in volts):

$$\Delta H^{\circ}\ (\text{kJ mol}^{-1}) = 96.5(T(dE_i^{\circ}/dT) - E_i^{\circ})$$

$$\Delta S^{\circ}\ (\text{J K}^{-1}\ \text{mol}^{-1}) = 96.5 \times 10^3(dE_i^{\circ}/dT) \quad (7)$$

Experimental Section

Reagents. 2,6-Pyridinedialdoxime (Aldrich) was recrystallized from water to constant melting point 212 °C. All other chemicals were of analytical grade. By titration against standard reagents, the ferrous salt $Fe(NH_4)_2(SO_4)_2{\cdot}6H_2O$ was found to be 99.9% pure, and ferric salt $Fe(NH_4)(SO_4)_2{\cdot}12H_2O$ was 98.6%; both were used from freshly opened small bottles. Glass-distilled deionized water was used throughout.

Solutions. Stock solutions of the iron salts were made just before an experiment, in most cases at a concentration of 1.00×10^{-2} M and containing 2:1 molar ratio of $HClO_4$/Fe to repress hydrolysis. 2,6-Pyridinedialdoxime was dissolved in warm water or buffer, limited in solubility to about 10^{-2} M. Buffer solutions were made from phthalate–HCl or phthalate–NaOH mixtures adjusted to the requisite ionic strength with KCl. Phosphate buffers were used for some measurements beyond pH 6. All solutions were made in freshly boiled water.

Complexes. The iron(II) complex of 2,6-pyridinedialdoxime formed rapidly upon mixing the stock solutions,

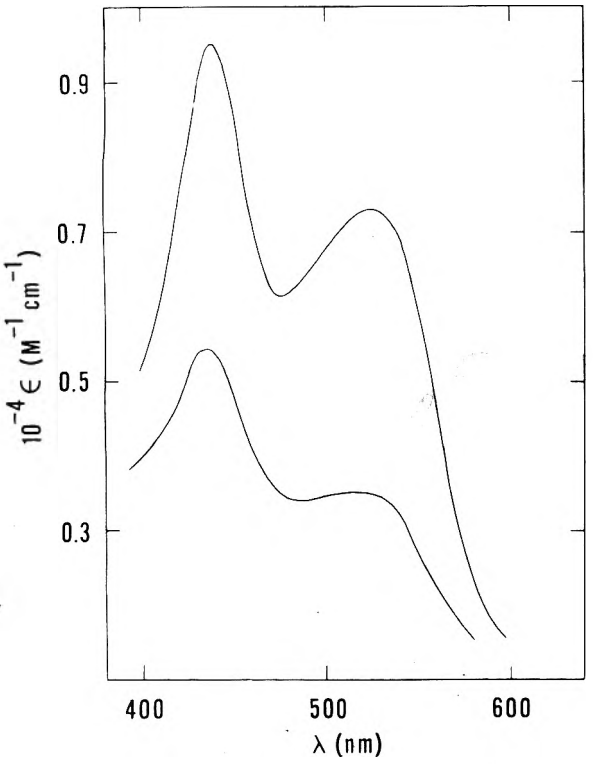

Figure 1. Absorption spectra, in the visible region, at room temperature and pH 4, for bis(2,6-pyridinedialdoxime)iron(II) complex, upper curve, and for the corresponding iron(III) complex, lower curve. Both spectra shift a little with change in pH (see text).

with excess ligand, letting stand for a few minutes, and then adding dilute buffer or alkali to adjust pH. The iron(III) complex was prepared in a similar manner, using the maximum possible excess of ligand, 20:1 molar ratio. Both complexes are red. Figure 1 shows that they have similar absorption spectra in the visible region. The iron(II) complex has bands at 445 and 540 nm at pH 5 which shift to 435 and 510 nm at pH 3, with about a 15% drop in absorbance. The iron(III) complex has one band at 448 nm and a shoulder near 540 nm at pH 5; the band maximum shifts toward 440 nm as the pH drops, while the shoulder is rather insensitive to pH change. The situation is quite unlike that of the corresponding complexes containing phenanthroline or dipyridyl ligands which form binuclear oxo-bridged iron(III) complexes and where the absorption spectra of their two oxidation states are markedly different.

The composition of each complex was determined by a spectrophotometric method of continuous variation, at 25 °C and I = 0.020 M, at concentration levels between 1×10^{-4} and 4×10^{-3} M, within the range of pH 3 to 6 for the iron(II) complex, and pH 2 to 4 for the iron(III) complex. The 1:2 stoichiometry was evident, as has already been reported for Co(II), Mn(II), Ni(II), and Zn(II) complexes of the same ligand.[4]

The overall formation constant for the iron(II) complex was determined by a semimicro titration method, carried out in the thermostated compartment of a Unicam SP500 spectrophotometer. The data fitted well 1:2 stoichiometry over a wide range of metal and ligand concentrations. The same technique was applied in determining the overall formation constant for the iron(III) complex. In this case, however, the complications arising from competition for Fe^{3+} by OH^-, salt anions, and possibly the oxo ligand permitted only approximate measurements and calculations.

Reduction Potential. The reduction potential was measured in a thermostated two-compartment cell with a salt bridge (saturated KCl in agar). A reference calomel electrode was equilibrated in saturated KCl, and was periodically tested against a matched pair of AgCl|Ag(s) electrodes as previously described.[5] The other half-cell contained 5-mL equimolar mixture of the oxidant and reductant complexes. Rhodium metal electrodes were found superior to platinum or gold in speed of equilibration and in reproducibility. The solution could be stirred magnetically or by bubbling N_2 gas. Cell emf was read to 0.1 mV on a Radiometer PHM4 potentiometer. pH was measured before and also after emf measurement, using NBS calibration standards.[6] Temperature was measured with a calibrated thermometer (National Physical Laboratory, London). In a typical experiment, the complexes were made, let stand for a few minutes, and were then diluted to 2.5 mL each, at the required pH and ionic strength. They were then mixed in the cell compartment, and emf measurements were taken at 1-min intervals. After an initial small drift, the potential remained steady. The mixture was normally about 5×10^{-4} M in each of the oxidant and reductant ions, and the ligand to metal ratio was nearly 20:1. The reduction potential E (millivolt) was measured within the range of pH 3 to nearly 7, ionic strength 0.060 to 0.0065 M, and at four temperatures from 15 to 30 °C.

Data Analysis. In view of the extensive data and the large number of variables, numerical analysis was carried out in two stages, using Powell's conjugate direction method.[7,8] The pH variation of K was first examined with reference to eq 2, taking the ten experimental sets of pH and K values from each series of measurements at constant ionic strength and temperature. The analysis gave a self-consistent set of parameters: K_{ii} and the ionization constants K_1 through K_4, from which K_i could then be calculated. The pH variation of E was likewise examined, using about 20 determinations of E and pH in each set. Analysis based on eq 5b gave a consistent set of parameters: E_i and the same four ionization constants K_1 through K_4, as well as K_4' and K_3' (the other two constants K_2' and K_1' being greater than 10^{-2}).

The two independent analyses of equilibrium and redox data yielded mean values for K_4 and K_3 concordant to within 2%, but the corresponding values for K_2 and K_1 differed by 20%. The discrepancy may be attributed to unequal precision of the equilibrium and redox data under varying pH conditions. Nevertheless, in order to obtain total internal consistency of results, the same method of numerical analysis was next applied to the simultaneous solution of eq 2 and 5b, using the combined 30 sets of pH, K, and E values, to fit together all the parameters involved. Since starting values of the parameters had already been obtained above, only a few iterations led to convergence and a minimum error factor, the result being a compromise on the unequal precisions involved. This procedure was repeated on every set of equilibrium and redox measurements, at each of the various ionic strengths and temperatures.

Results

Table I summarizes the results obtained by numerical analysis of the data at 25.0 °C and I = 0.025 M. It gives E_i, the limiting value of reduction potential at high pH for the cell reaction involving ionized species (eq 4b), K_{ii}, the limiting value at low pH of the formation constant for the iron(II) complex, and K_i, its limit at high pH, as well as the four oxime ionization constants K_1 through K_4 in the iron(II) complex (eq 1), and two of the four oxime ionization constants, K_3' and K_4', in the iron(III) complex (eq 3), the other two K_1' and K_2' being greater than 10^{-2}.

TABLE I: Results of the Combined Numerical Analysis of Redox and Equilibrium Data at 25.0 °C and I = 0.025 M Obtained from pH Variation of Reduction Potential E for the Bis(2,6-pyridinedialdoxime)iron(III-II) Couple, and Formation Constant K for the Iron(II) Bis Complex[a]

Iron(II) complex	Iron(III) complex	Redox couple
$K_1 = 3.00 \times 10^{-3}$	$K_1' > 10^{-2}$	
$K_2 = 3.30 \times 10^{-5}$	$K_2' > 10^{-2}$	
$K_3 = 1.26 \times 10^{-5}$	$K_3' = 5.02 \times 10^{-3}$	
$K_4 = 6.15 \times 10^{-8}$	$K_4' = 1.25 \times 10^{-6}$	
$K_{ii} = 2.4 \times 10^{5}$		
$K_i = 4.5 \times 10^{27}$		213.5 ± 0.5 mV

[a] The first column gives oxime ionization constants K_1 through K_4, formation constants K_{ii} at the limit of low pH, and K_i at the limit of high pH. The second column shows the corresponding ionization constants in the oxidant (formation constants are uncertain because K_1' and K_2' are unknown). The third column gives the reduction potential E_i for the cell reaction at the limit of high pH (eq 4b) (an estimate of E_{ii} is made in the discussion). Theoretical curves and experimental points are shown together in Figure 2.

TABLE II: Variation of E, the Measured Reduction Potential of the Bis(2,6-pyridinedialdoxime)iron(III-II) Couple, with Ionic Strength I at 25.0 °C and Fixed pH 6.30[a]

I, M	E, mV	E_i, mV	E_i°, mV
0.060	261.2	215.5	200.5
0.040	261.0	213.5	200.5
0.025	261.4	212.5	201.5
0.010	260.8	209.0	201.5
0.0065	260.6	207.5	201.5

[a] E_i is the potential at the limit of high pH obtained using eq 5b as described in the text. The cell reaction 4b involves fully ionized species. The last column gives E_i°, calculated from eq 6 as the corresponding thermodynamic reduction potential, with mean value 201.0 ± 0.5 mV. Precision of E measurements is 0.2 mV; the derived quantities E_i and E_i° are given to the nearest 0.5 mV.

Putting all these parameters into eq 2 and 5b yields the calculated pH variation of reduction potential and that of formation constant for the iron(II) complex. Figure 2 shows the theoretical curves and experimental points under the conditions specified. Since stable potentials could not be obtained beyond pH 7 it was not possible directly to reach the pH-independent region, but the trend is clear.

The variation of reduction potential with ionic strength was examined at 25.0 °C and fixed pH 6.30, covering the range I = 0.060 to 0.0065 M. Table II shows that E appears to be independent of I. However, it is E_i that one needs to look at. E_i can be obtained from eq 5b if the ionization constants are known at each ionic strength. The latter can be calculated from the data in Table I by assuming a Debye–Hückel variation with the appropriate charges in each case. Actually, only K_4, K_3, K_2, and K_4' need be considered, since the other ionizations have negligible effect at pH 6.30. Substitution into eq 5b now yields the E_i values (third column of Table II) which are seen to vary systematically with ionic strength. The apparent constancy of E may therefore be attributed to fortuitous balancing of ionic strength effects on the different ionization parameters. The theoretical variation of E_i with ionic strength is given by eq 6 which also enables one to calculate the thermodynamic reduction potential E_i° for the cell reaction 4b. The last column in Table II shows that the data fit the assumed relations, and that at 25.0 °C, E_i° = 201.0 ± 0.5 mV.

Keeping ionic strength constant at 0.025 M, the pH variation of E was studied at 15.0, 20.0, 25.0, and 30.0 °C. The same treatment of data was applied as above, yielding

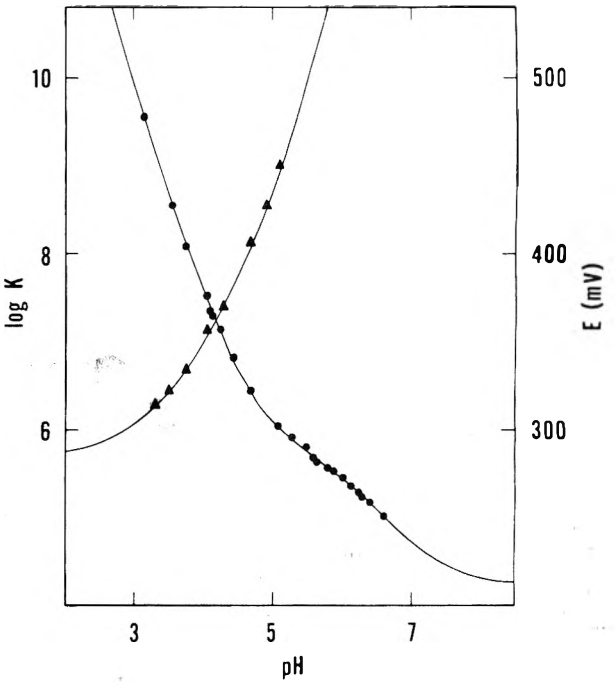

Figure 2. Variation with pH, at 25 °C and I = 0.025 M, of log K, the observed formation constant for the iron(II) complex, eq 2 (rising curve) and E, the reduction potential of the couple bis(2,6-pyridinedialdoxime)iron(III–II), eq 5b (falling curve). Experimental points are shown in each case. The smooth curves represent the theoretical pH variation of log K and of E, using the parameters in Table I.

at each temperature a set of parameters corresponding to those given in Table I for 25.0 °C. From the four resulting E_i values, $(dE_i/dT) = -2.40 \pm 0.14$ mV/deg, which was assumed equal to the value at zero ionic strength dE_i°/dT. Using eq 7, it follows that for the range of temperature covered, $\Delta H^\circ = -88 \pm 5$ kJ mol^{-1} and $\Delta S^\circ = -230 \pm 10$ J K^{-1} mol^{-1}.

As already stated, data analysis also yields the formation and the ionization constants at each temperature. For the iron(II) complex, the formation constant is K_{ii} at the limit of low pH (eq 2), and K_i at the other limit of high pH. At 25.0 °C, log K_{ii} = log K_{ii}° = 5.38, there being no significant ionic strength effect on the formation reaction since the latter involves no changes in charge; and the linear slope of log K_{ii} vs. $1/T$(K) is 1.5 ± 0.2, assumed independent of ionic strength. On this basis, $\Delta H_{ii}^\circ = -30 \pm 5$ kJ mol^{-1} and $\Delta S_{ii}^\circ = 0 \pm 5$ J K^{-1} mol^{-1}. Under the same conditions, but using a Debye–Hückel variation with the appropriate charges for the ionic strength effect, log K_i° = 28.14; the linear slope of log K_i vs. $1/T$(K) is 6.3 ± 0.5, assumed independent of ionic strength. On this basis, $\Delta H_i^\circ = -120 \pm 10$ kJ mol^{-1} and $\Delta S_i^\circ = 135 \pm 10$ J K^{-1} mol^{-1}. The oxime ionization equilibria were treated the same way.

Table III summarizes the results obtained. It gives thermodynamic quantities corresponding to the data in Table I, for the redox couple bis(2,6-pyridinedialdoxime)iron(III–II), for the formation of the iron(II) complex, and for oxime group ionizations in oxidant and reductant with the charge type (acid/conjugate base) indicated in each case. In view of the unequal errors involved, all ionization pK values have been rounded off to two significant figures, and enthalpy and entropy changes (and mean deviations) have been recorded as multiples of 5.

One factor which could effect the reliability of the results is the possible formation of iron(III) oxo-bridged binuclear complexes. In the present work, which was confined to low pH and very dilute solutions, no spectral changes characteristic of bridged complexes were observed, and

TABLE III: Standard Thermodynamic Quantities for the Redox, Formation, and Ionization Data in Table I[a]

	(at 25.0 °C) I = 0	ΔH°, kJ mol^{-1}	ΔS°, J K^{-1} mol^{-1}
E_i, mV	201	−88 (5)	−230 (10)
log K_i	28.14	−120 (10)	135 (10)
log K_{ii}	5.38	−30 (5)	0 (5)
pK_1(+2/+1)	2.34	0 (5)	−45 (5)
pK_2(+1/0)	4.41	0 (5)	−85 (5)
pK_3(0/−1)	4.96	5 (5)	−80 (5)
pK_4(−1/−2)	7.40	5 (5)	−125 (5)
pK_1'(+3/+2)	<2		
pK_2'(+2/+1)	<2		
pK_3'(+1/0)	2.24	0 (5)	−45 (5)
pK_4'(0/−1)	5.96	5 (5)	−95 (5)

[a] Oxime ionization pK and pK' equilibria are listed in the first column together with their charge type (acid/base). Estimates of uncertainty are mean deviations (given within braces).

there was no perceptible deviation from the expected stoichiometry for formation or for redox equilibria. It may be concluded that such side reactions probably occur to an insignificant extent under present experimental conditions.

Discussion

The above results may be considered from two thermodynamically equivalent viewpoints: the influence of side group ionizations on redox potential of the complex ion, and the effect of coordination to the metal on the acidity of oxime side groups in the ligand.

The first conspicuous feature of the results is the low reduction potential observed for an iron(III–II) couple. It is well known that ligands such as 2,2′-dipyridyl and 1,10-phenanthroline, which possess the bidentate ferroin chelating group –N=C–C=N–, form octahedral low-spin tris-ferrous complexes of high stability relative to the ferric state, reflected by a high reduction potential of about 1 V, and that substitution into the ligand by neutral groups does not perturb the reduction potential outside the limits 1.2 to 0.9 V.[9] In all these cases, the formal charges of oxidant/reductant are +3/+2. By marked contrast, the tris(2-pyridinealdoxime)iron(III–II) couple, whose bidentate ligand also contains the ferroin chelating group, has the much lower reduction potential 0.35 V at the limit of high pH where three oxime side group ionizations lead to oxidant/reductant charges 0/−1; and when account is taken of ionization equilibria, the reduction potential rises to about 1 V at the limit of low pH where the ligand is neutral.[1] It is clearly of interest to find out whether the bis(2,6-pyridinedialdoxime)iron(III–II) couple of the present study, being structurally similar to the above systems in that its tridendate ligand possesses a double ferroin group –N=C–C–N–C–C=N–, follows the same pattern of behavior.

Table IV gives some comparative thermodynamic data for this purpose. The reference +3/+2 couples with neutral N-heterocyclic ligands show the characteristic 1 V reduction potential, a highly exothermic cell reaction, and a negative entropy change. As the positive charge on the complex ion drops so does its reduction potential, a drop which is reflected partly in decreased exothermicity and partly in a more negative entropy change for the cell reaction. The effect is most pronounced in the −1/−2 couple of the present study, clearly indicating the role of oximate anionic side groups at the high pH limit (reaction 4b).

However, to complete the comparison one still needs E_{ii} at the low pH limit (reaction 4a). Table III gives the data

TABLE IV: Comparative Thermodynamic Data on Redox Couples of Some Iron(III–II) Octahedral Complexes with N-Heterocyclic Ligands in Aqueous Solution at 25 °C and Zero Ionic Strength[a]

	Charge (O/R)	E°, V	ΔH°, kJ mol^{-1}	ΔS°, J K^{-1} mol^{-1}	Ref
Fe(phen)$_3$	(+3/+2)	1.14	−137	−90	10
Fe(bpy)$_3$	(+3/+2)	1.12	−137	−95	10
Fe(bpyMe$_2$)$_3$	(+3/+2)	0.94	−112	−70	11
Fe(pyrald)$_3$	(0/−1)	0.35	−87	−180	1
Fe(pyrdiald)$_2$	(−1/−2)	0.20	−88	−230	This work

[a] Columns give, respectively, the charge type (oxidant/reductant), standard reduction potential, enthalpy and entropy of the cell reaction vs. standard hydrogen electrode, and the reference. Values have been rounded off. phen = 1,10-phenanthroline; bpy = 2,2-bipyridyl; bpyMe$_2$ = 4,4-dimethyl-2,2′-bipyridyl; pyrald = 2-pyridinealdoxime; pyrdiald = 2,6-pyridinedialdoxime. The last two cases refer to fully ionized species.

except for K_1' and K_2'. Since only a rough estimate is required, we may assure K_1' = 10 and K_2' = 1 with ΔH° = −5 kJ mol^{-1} for each. Substitution into eq 5a then gives E_{ii} = 0.91 V, and from the temperature variation one gets ΔH° = −103 kJ mol^{-1} and ΔS° = −50 J K^{-1} mol^{-1} indicating, as expected, the trend toward the +3/+2 reference parameters in Table IV. Of course, one would not expect full agreement since the polar =NOH side groups should have some influence on charge distribution in the complex ion and on its interaction with the solvent water.

The converse but thermodynamically equivalent effect is the role of the metal in controlling the acidic properties of oxime side groups in these complex ions. The effect of coordination to iron on the ionization of side groups in iron(II) complexes of 2,6-pyridinedialdoxime and analogous ligands has already been studied.[2] The acid strength of an ionizing group in a ligand undergoes very marked increase as a result of coordination of the ligand to aqueous metal cation. The effect is characterized by two main features: (a) the drop in ionization pK is reflected in decreased endothermicity of ionization and, to a lesser extent, in more favorable (less negative) entropy change; (b) the effect is cumulative, its magnitude depending upon the electrostatic charge of the metal, and also on the extent of enhanced electronic stabilization of the conjugate base of the ionizing group. The results of the present study provide further quantitative measures of these two factors. In the free ligand, the first oxime ionization has pK° = 10.08, ΔH° = 22 kJ mol^{-1}, and ΔS° = −118 J K^{-1} mol^{-1} (data from ref 2). The corresponding equilibrium in the iron(II) complex is the third oxime ionization (data for pK_3 are in Table III). The acid strength of this oxime group is seen to have increased by 10^5 as a result of coordination, even though the formal charges in the two systems are the same (0/−1), the ionization is 17 kJ mol^{-1} less endothermic, and the entropy term is 38 J K^{-1} mol^{-1} less negative. pK_2(+1/0) and pK_1(+2/+1) show the progressive effects of increasing positive charge. In the latter case, the change is so great that the thermodynamic quantities are unrecognizable as pertaining to an =NOH group. Similar patterns emerge from a comparison of the ligand's second oxime ionization with pK_4 in the iron(II) complex (followed by three stages of increasing positive charge in pK_3, pK_2, pK_1), and also in a parallel comparison with available data for the iron(III) complex.

To summarize, the redox, formation, and ionization equilibria can be grouped in cycles as shown in eq 8. Steps are identified by their equation numbers where possible, and vertical arrows refer to oxime ionizations. Iron(III)

TABLE V: Summary of Thermodynamic Data for the Redox, Formation, and Ionization Equilibria which Form the Cycles in Eq 8[a]

Reaction	Parameter	ΔG°, kJ	ΔH°, kJ	$T\Delta S^\circ$, kJ	Ref
4a	E_{ii}	−90	−105	−15	Discussion
4b	E_i	−20	−90	−70	Table III
1	$pK_1 \ldots pK_4$	110	10	−100	Table III
3	$pK_1' \ldots pK_4'$	40	−5	−45	Discussion
i	Free ligand pK	240	100	−140	Ref 2
e	E ($Fe^{+3/+2}$)	−75			Ref 12
f	K_{ii}	−30	−30	0	Table III
g	K_i	−160	−120	40	Table III
f′	K_{ii}'	−15			Discussion
g′	K_i'	−215			Discussion

[a] Values have been rounded off in multiples of 5 kJ.

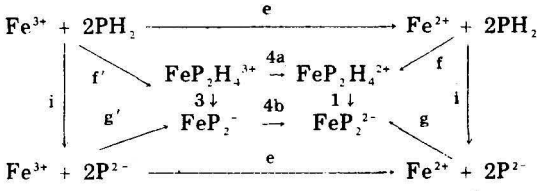

(8)

is on the left, iron(II) on the right. Free energy, enthalpy, and entropy data, rounded off in multiples of 5 kJ, are listed in Table V.

The central redox–ionization cycle (4a,1;3,4b) shows the effect of pH on the free energy of the cell reaction (the drop from E_{ii}, step 4a at the limit of low pH, to E_i, step 4b at the limit of high pH) is a thermodynamic consequence of the difference between the free energy of ionizing four oxime groups in the oxidant and reductant ions. The difference, 70 kJ, is a measure of the extent to which the extra positive charge in the iron(III) complex strengthens the acidity of oxime side groups (compare pK' with pK values in Table III). The decrease in exothermicity of the cell reaction is the difference between the total enthalpy of ionization in the two cases, a small effect of 15 kJ in comparison with the 55 kJ difference in $T\Delta S$.

The formation–ionization cycle of the iron(II) complex (f,1;i,g) can be viewed in the same manner. The effect of pH on formation constant is equivalent to the 130 kJ difference between the free energy of oxime group ionization of 2 mol of ligand and that of four oxime groups in 1 mol of the bis complex. Here, the enthalpy factor predominates, the effect of coordination accounting for the 90 kJ decrease in exothermicity of the formation reaction and 40 kJ decrease in $T\Delta S$.

From the two redox-formation cycles, on top (e,f;f′,4a) and at bottom (e,g;g′4b) of eq 8, we now obtain $\Delta G^\circ = -15$ kJ for step f′ and −215 kJ for step g′. This completes the iron(III) cycle on the left. The effect of pH on formation constant for the iron(III) complex is seen to be, as expected from charge considerations, even greater than it is in the case of iron(II) complex (200 kJ compared with 130 kJ in free energy; no reliable enthalpy and entropy data are available).

The iron complexes of 2,6-pyridinedialdoxime and analogous ligands may also be viewed as models for hemoproteins. The latter are proteins incorporating N-heterocyclic iron complexes with asymmetric octahedral structures and low reduction potentials. For hemoglobin and myoglobin, with E about 0.15 V, the cell reaction ΔH is about −60 kJ mol^{-1} and $\Delta S = -160$ J K^{-1} mol^{-1}; cytochrome c has slightly higher E whereas peroxidase and catalase have much lower reduction potentials.[13] Since the formal charge on iron(III) is +1 in all four cases, the widely varying redox properties of hemoproteins probably reflect the differences in structural, electronic, and electrostatic environment of their active sites. In this respect, data on simple coordination systems may be helpful in providing estimates of enthalpy and entropy contributions arising from specific structural features which influence the net redox behavior of complex molecules.

References and Notes

(1) G. I. H. Hanania, D. H. Irvine, and F. R. Shurayh, *J. Phys. Chem.*, **72**, 1355 (1968).
(2) G. I. H. Hanania, D. H. Irvine, and F. R. Shurayh, *J. Chem. Soc.*, 1149 (1965).
(3) K. S. Murray, *Coord. Chem. Rev.*, **12**, 1 (1974).
(4) S. P. Bag, Q. Fernando, and H. Freiser, *Anal. Chem.*, **35**, 719 (1963).
(5) G. I. H. Hanania, D. H. Irvine, W. A. Eaton, and P. George, *J. Phys. Chem.*, **71**, 2022 (1967).
(6) R. G. Bates, "Determination of pH", Wiley, New York, N.Y., 1964 Chapters 4 and 5.
(7) M. J. D. Powell, *Comput. J.*, **7**, 155 (1964).
(8) R. C. Marshall, private communication.
(9) J. C. Tomkinson and R. J. P. Williams, *J. Chem. Soc.*, 2010 (1958).
(10) P. George, G. I. H. Hanania, and D. H. Irvine, *J. Chem. Soc.*, 2548 (1959).
(11) D. H. Irvine, *J. Chem. Soc.*, 2977 (1959).
(12) L. G. Sillen and A. E. Martell, *Chem. Soc. Spec. Publ.*, **No. 17** (1964).
(13) P. George, G. I. H. Hanania, and W. A. Eaton, in "Hemes and Hemoproteins", B. Chance, Ed., Academic Press, New York, N.Y., 1966, p 267.

Interfacial Tension Near the Critical Point and the Density-Gradient Term in the Free Energy

O. K. Rice

Department of Chemistry, University of North Carolina, Chapel Hill, North Carolina 27514 *(Received February 7, 1977)*

A simplified theory of interfacial tension is presented; this focuses especially on the free-energy term arising from the density gradient in the interface. The energy and entropy parts of the free energy are considered in terms of a characteristic length related to the range of molecular forces, which may be different for energy and entropy, and, especially in the case of binary liquid systems, for different contributions to the entropy. The relations derived are analyzed with the aid of experimental data on interfacial tension, thickness of the interface, and other thermodynamic properties, for both liquid–vapor and binary–liquid systems; this is especially valuable in the latter case where the standard procedures are not so readily applicable. It is shown that the density-gradient term is unimportant near the critical temperature for several thermodynamic properties other than the free energy.

1. Liquid–Vapor Systems

Recently there have been a number of discussions of the interface between two phases and its behavior near the critical point.[1] These have focused largely on the dependence on intermolecular forces and the profile of the interface. In this paper we shall adopt a somewhat different point of view. We wish to regard the interface in as simple a way as possible. We start with the van der Waals–Cahn and Hilliard assumption that the Helmholtz free energy per molecule ϕ may be divided into two parts

$$\phi = \phi_1 + \phi_2 \tag{1.1}$$

where, in a one-component (liquid–vapor) system, ϕ_1 is a function of the molecular (number) density ρ at a particular point in the system, whereas ϕ_2 may depend upon such quantities as $\partial\rho/\partial z$ and $\partial^2\rho/\partial z^2$, where z is the distance coordinate in the direction normal to the surface. z is measured from a geometrical surface defined for a plane interface by the equation

$$\int_{-\infty}^{0}(\rho - \rho_v)\,dz + \int_{0}^{\infty}(\rho - \rho_l)\,dz = 0 \tag{1.2}$$

where ρ_v and ρ_l are the densities of the bulk vapor and liquid phases, respectively. Our special interest will be in an analysis of ϕ_2.

The reason that ϕ_2 has a value different from zero is because a particular molecule suffers a different interaction with molecules at a z smaller than its own than its interaction with those at a larger z. Let us suppose that the central molecule will be affected as if the molecules on the left were at an average distance $-\delta z$ and those on the right at an average distance δz, with average densities $\delta\rho_-$ and $\delta\rho_+$, respectively. Then we can write, to second order, assuming at first, to fix the procedure, that ϕ is not to be analyzed into its energy and entropy components:

$$\phi_2 = {}^1/_2\{(\partial\phi_1/\partial\rho)(\delta\rho_+ + \delta\rho_-) + {}^1/_2(\partial^2\phi_1/\partial\rho^2)[(\delta\rho_+)^2 + (\delta\rho_-)^2]\} \tag{1.3}$$

and

$$\delta\rho_+ = (d\rho/dz)\delta z + {}^1/_2(d^2\rho/dz^2)(\delta z)^2$$

$$\delta\rho_- = -(d\rho/dz)\delta z + {}^1/_2(d^2\rho/dz^2)(\delta z)^2$$

so that

$$\delta\rho_+ + \delta\rho_- = (d^2\rho/dz^2)(\delta z)^2 \tag{1.4}$$

and, to second order

$$(\delta\rho_+)^2 = (\delta\rho_-)^2 = (d\rho/dz)^2(\delta z)^2 \tag{1.5}$$

Using eq 1.4 and 1.5 in 1.3

$$\phi_2 = {}^1/_2(\partial\phi_1/\partial\rho)(d^2\rho/dz^2)(\delta z)^2 + {}^1/_2(\partial^2\phi_1/\partial\rho^2)(d\rho/dz)^2(\delta z)^2$$

$$= {}^1/_2(d/dz)[(\partial\phi_1/\partial\rho)(d\rho/dz)](\delta z)^2 \tag{1.6}$$

As the interfacial tension is the excess of free energy in unit surface, it is given by

$$\sigma = \int_{-\infty}^{0}(\rho\phi_1 - \rho_v\phi_{1,v})\,dz + \int_{0}^{\infty}(\rho\phi_1 - \rho_l\phi_{1,l})\,dz + \int_{-\infty}^{\infty}\rho\phi_2\,dz \tag{1.7}$$

Noting that at $z = -\infty$ and $z = \infty$ the gradient $d\rho/dz$ vanishes, we may integrate the last term by parts, calling it σ_2, and obtain

$$\sigma_2 = -{}^1/_2(\delta z)^2\int_{-\infty}^{\infty}(\partial\phi_1/\partial\rho)(d\rho/dz)^2\,dz = -{}^1/_2(\delta z)^2\int_{\rho_v}^{\rho_l}(\partial\phi_1/\partial\rho)(d\rho/dz)\,d\rho \tag{1.8}$$

At this point, we shall make a further simplification: we shall assume that $d\rho/dz$ is constant between ρ_l and ρ_v (see Figure 1) and shall write

$$d\rho/dz = (\rho_l - \rho_v)/\Delta z \tag{1.9}$$

where Δz is the thickness of the interface. We may then write

$$\sigma_2 = -{}^1/_2(\delta z)^2(\phi_{1,l} - \phi_{1,v})(\rho_l - \rho_v)/\Delta z \tag{1.10}$$

We now note that the Gibbs free energy per molecule is equal to $\phi_1 + P/\rho$, where P is the pressure, and since the Gibbs free energy must be the same in the coexisting phases we may write

$$\phi_{1,l} - \phi_{1,v} = P(\rho_v^{-1} - \rho_l^{-1}) = P(\rho_l - \rho_v)/\rho_l\rho_v \approx P(\rho_l - \rho_v)/\rho_c^2 \tag{1.11}$$

where ρ_c is the critical density, so we obtain

$$\sigma_2 = -{}^1/_2 P(\delta z)^2(\rho_l - \rho_v)^2/\rho_c^2\Delta z \tag{1.12}$$

It will be observed that eq 1.12 makes σ_2 negative, which would be inconsistent with the stability of the interface. We must, therefore, seek the factors which make it positive. We note first that if ρ could be treated as constant, or its variation counteracted across the interface, in the last integral in eq 1.7, then σ_2 would vanish. It seems

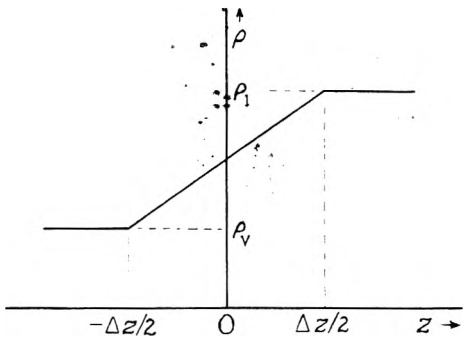

Figure 1. Illustrating assumed structure of the surface and notation.

probable that δz will depend on the density, and if δz were proportional to $\rho^{-1/2}$ it would, indeed, conteract the effect of the ρ factor in the integral, while if it were proportional to a more negative power of ρ the integral would be positive. Actually, δz is unlikely to vary more rapidly than proportionally to the distance between molecules, or $\rho^{-1/3}$, which would not make the integral positive, but would make it less negative. Actually the variation in δz is likely to be considerably less than this because around the critical point the variation in density probably reflects a change in the amount of open space, rather than the molecular distance.

However, in the calculation we have made it is assumed that the energy and the entropy (times T) are affected equally by the density gradient. If this is not so (and it has been explicitly assumed[2] that the entropy is, indeed, independent of the gradient) this could be expressed by assigning different values of $(\delta x)^2$ to the energy and entropy. Suppose that $(\delta x)^2$ refers to the energy and let $(\delta x)^2(1 + b)$ refer to the entropy. Then, in place of eq 1.10 we would find (neglecting the effect of ρ on δx)

$$\sigma_2 = -{}^1/_2(\delta z)^2[(\phi_{1,l} - \phi_{1,v}) - bT(s_{1,l} - s_{1,v})](\rho_l - \rho_v)/\Delta z \quad (1.13)$$

Since the entropy of condensation, $s_{1,l} - s_{1,v}$, is negative is it seen that if b is sufficiently negative, this could make σ_2 positive. The energy of condensation, $e_{1,l} - e_{1,v}$, and $T(s_{1,l} - s_{1,v})$ are both large in absolute value compared to their difference $\phi_{1,l} - \phi_{1,v}$. By the Clapeyron equation

$$s_{1,l} - s_{1,v} = (dP/dT)(\rho_l^{-1} - \rho_v^{-1}) \quad (1.14)$$

Inserting this and eq 1.11 into eq 1.13 we obtain, instead of eq 1.12

$$\sigma_2 = -{}^1/_2(\delta z)^2(P + bT\,dP/dT)(\rho_l - \rho_v)^2/\rho_c{}^2\Delta z \quad (1.15)$$

The fact that σ_2 must be positive if a stable interface is to result leads, as we have noted, to a negative value of b. Since dP/dT is considerably larger than P/T, it seems likely that the dP/dT term predominates. However, it is seen that, as P and dP/dT do not have singularities in the neighborhood of the critical point, the exact value of b does not affect the general form of the expression, unless, indeed, the combination $P + bT\,dP/dT$ has a singularity.

We now turn to a brief discussion of the other part of σ which we designate as σ_1. Under the approximation of Figure 1 we may write

$$\sigma_1 = [\Delta z/(\rho_l - \rho_v)][\int_{\rho_v}^{\rho_c}(\rho\phi_l - \rho_v\phi_{1,v})\,d\rho + \int_{\rho_c}^{\rho_l}(\rho\phi_l - \rho_l\phi_{1,l})\,d\rho]$$
$$= [\Delta z/(\rho_l - \rho_v)][\int_{\rho_v}^{\rho_l}\rho\phi_l\,d\rho - \rho_v\phi_{1,v}(\rho_c - \rho_v) - \rho_l\phi_{1,l}(\rho_l - \rho_c)] \quad (1.16)$$

Integrating by parts

$$\int_{\rho_v}^{\rho_l}\rho\phi_l\,d\rho = {}^1/_2(\phi_{1,l}\rho_l{}^2 - \phi_{1,v}\rho_v{}^2) - {}^1/_2\int_{\rho_v}^{\rho_l}\rho^2(d\phi_l/d\rho)\,d\rho$$
$$= {}^1/_2(\phi_{1,l}\rho_l{}^2 - \phi_{1,v}\rho_v{}^2) - {}^1/_2\int_{\rho_v}^{\rho_l}P\,d\rho \quad (1.17)$$

Using eq 1.11, and assuming that near the critical point the coexistence curve is sufficiently symmetrical to set $\rho_l - \rho_c = \rho_c - \rho_v = (\rho_l - \rho_v)/2$, we may reduce eq 1.16 to

$$\sigma_1 = {}^1/_2P\Delta z - {}^1/_2[\Delta z/(\rho_l - \rho_v)]\int_{\rho_v}^{\rho_l}P\,d\rho$$
$$= {}^1/_2\Delta z(P - \bar{P}) \quad (1.18)$$

and

$$\sigma = {}^1/_2\Delta z(P - \bar{P}) - {}^1/_2(\delta z)^2(P + bT\,dP/dT)(\rho_l - \rho_v)^2/\rho_c{}^2\Delta z \quad (1.19)$$

We may minimize σ with respect to variation of Δz (a similar procedure was carried out by Yang, Fleming, and Gibbs[3]); this shows (in agreement with more general treatments) that the two terms must be equal. Thus

$$\sigma = \Delta z(P - \bar{P}) = -(\delta z)^2(P + bT\,dP/dT)(\rho_l - \rho_v)^2/\rho_c{}^2\Delta z \quad (1.20)$$

The first of these expressions is what one would get from the mechanical discussion of surface tension. It depends on the deviation from exact asymmetry of the pressure under the coexistance curve about the critical density. Since this deviation is not very great, one would expect that $P - \bar{P}$ should go to zero at the critical point to a higher than the first power of the relative deviation $t = (T_c - T)/T_c$ of the temperature from the critical temperature. It will thus be of some interest to stop at this point to examine the temperature behavior of these quantities. We define the critical exponent μ for σ by $\sigma \propto t^\mu$; we also have by definition $\rho_l - \rho_v \propto t^\beta$, and, if we grant that Δz varies as the correlation length, $\Delta z \propto t^{-\nu'}$, we find from (1.20)

$$\mu = 2\beta + \nu' \quad (1.21)$$

also

$$P - \bar{P} \propto t^{2\beta+2\nu'} \approx t^2 \quad (1.22)$$

It is also known that[4]

$$\mu = \gamma' + 2\beta - \nu' \quad (1.23)$$

where γ' is the exponent for the compressibility. If this is combined with eq 1.21 we find

$$\gamma' = 2\nu' \quad (1.24)$$

which would not differ from the scaling law $\gamma' = 2\nu' - \nu'\eta$ if the exponent η were zero. It therefore appears that the approximations involved in this discussion are equivalent to taking $\eta = 0$.

This may be tentatively explained in the following way. A more exact theory (still containing some approximations but precise enough for this discussion) gives (see ref 3)

$$\sigma_2 = (kT/12)\int_{-\infty}^{\infty}\int_0^{\infty} r^2\,C(r, \rho)(d\rho/dz)^2\,d^3r\,dz \quad (1.25)$$

where r is the distance of a molecule from some molecule at a particular z, where d^3r is the corresponding volume element, and where $C(r, \rho)$ is the direct correlation function of Ornstein and Zernicke. If we now make the assumption that $d\rho/dz = (\rho_l - \rho_v)/\Delta z$ this can be written

$$\sigma_2 = [(kT/12)(\rho_l - \rho_v)/\Delta z]\int_{\rho_v}^{\rho_l}\int_0^\infty r^2\, C(r,\rho)\, d^3r\, d\rho$$
$$= [(kT/12)(\rho_l - \rho_v)^2/\Delta z]\langle\int_0^\infty r^2\, C(r,\rho)\, d^3r\rangle \quad (1.26)$$

The quantity in angular brackets is the average of the second moment of the direct correlation function, and it, in effect, takes the place of $(\delta z)^2$ in eq 1.12 and 1.15. It could diverge weakly, but, from its physical meaning, δz should remain finite. Thus, we conclude that Δz as defined by eq 1.26 differs slightly from Δz in 1.12 or 1.15, and its divergence may be slightly different, and, in either case, may differ slightly from the divergence of Δz in the expression for σ_1; eq 1.23 depends on σ_1.

It may be of interest to observe that my derivation[5] of eq 1.23 and a proof given by Yang, Fleming, and Gibbs that Δz is proportional to the correlation length both depend on a common assumption, namely, that the average of a thermodynamic function through the surface varies with the temperature with the same exponent as it does on the coexistence curve. We may also note that we have performed integrations through the surface on the assumption that the thermodynamic quantities do not have singularities in the surface (that is, under the coexistence curve). This may not be true,[6] in which case the integrals could be carried out only if it were possible to treat the singularity as the limit of a smooth function. In any case, the discrepancy in the exponent relationship is not very great for a three-dimension system.

2. Binary-Liquid Systems

Although the formula 1.20, which relates the surface tension to thermodynamic and structural properties of the surface, is of some interest in itself, it must be granted that the surface tension may be successfully represented by more exact theories, especially if one knows the pair distribution functions. In the case of a binary-liquid system, however, it is much more difficult to apply the exact theories. However the theory which we have outlined in section 1 can be carried through in this case rather readily.

A binary-liquid system may be expected to exhibit some differences from a liquid–vapor system. The density is generally considerably greater than that near the critical point in a liquid–vapor system, and further it will vary little across the coexistence curve, although it now constitutes an extra variable, in addition to the mole fraction, x_a or x_b, of one or the other of the components A and B, which cannot be entirely ignored. Both of these can affect the intensive, or field, variables, the chemical potentials, and the pressure, which will not vary monotonically through the interface. In a binary system the Helmholtz free energy can be expressed in terms of the partial molecular Helmholtz free energies by

$$\phi_1 = x_a\phi_{a1} + x_b\phi_{b1} \quad (2.1)$$

where the subscript 1 is used in the same sense as in section 1.

Our first task will be to set up an equation analogous to (1.6). However, we will have to deal separately with the energy and the entropy from the beginning. If we had a regular solution we could write the partial entropies as

$$\bar{s}_{a1}{}^r = s_{a1}{}^\circ - k\ln x_a$$
$$\bar{s}_{b1}{}^r = s_{b1}{}^\circ - k\ln x_b = s_{b1}{}^\circ - k\ln(1 - x_a) \quad (2.2)$$

Since this depends only upon the number of different arrangements of the molecules, and effectively assumes that the intermolecular forces do not influence this number, it may be expected that the range of influence δz for this entropy would be very small and we shall take it as zero. This is equivalent to the assumption made by Debye[7] in considering the fluctuations near the critical point. We may use (2.2) as a norm from which real systems depart. Changes of entropy are also caused by grouping of molecules arising from the forces between them. These may be considered as producing increments to $\bar{s}_{a1}$ and $\bar{s}_{b1}$ whose δz is the same as that applying to the energy. These increments we shall designate $\hat{s}_{a1}$ and $\hat{s}_{b1}$, so $\bar{s}_{a1} = \bar{s}_{a1}{}^r + \hat{s}_{a1}$ and $\bar{s}_{b1} = \bar{s}_{b1}{}^r + \hat{s}_{b1}$.

The eq 2.2 should be satisfactory as long as the molecules of the two components have roughly the same size. If one of them is considerably larger than the other, then it may be more accurate to substitute volume fractions for mole fractions in the mixing entropies.[8] However, unless the molecular densities of the pure liquids and the critical mole fractions both differ by more than a factor of 3 the difference in the final results is so small as to be scarcely noticeable, and we shall use eq 2.2 for the purposes of this paper.

In setting up the analogue of eq 1.3 we note that it must apply separately to the components A and B. We retain the variable ρ, which may not be important in this case, but then we must note that there will be similar terms in which x_a, x_{a+}, and x_{a-} will appear in place of ρ, ρ_+, and ρ_-; finally there will be a term

$$\tfrac{1}{2}(\partial^2\phi_{a1}/\partial\rho\partial x_a)(\delta\rho_+\,\delta x_{a+} + \delta\rho_-\,\delta x_{a-})$$
$$= (\partial^2\phi_{a1}/\partial\rho\,\partial x_a)(d\rho/dz)(dx_a/dz)(\delta z)^2 \quad (2.3)$$

and similar terms in which ϕ_{b1} replaces ϕ_{a1}. Also the resulting equation applies separately to $\bar{e}_{a1}$, $\bar{e}_{b1}$, $\hat{s}_{a1}$, and $\hat{s}_{b1}$. Then, in place of eq 1.6 we find

$$\sigma_2 = \frac{1}{2}x_a\frac{d}{dz}\left[\left(\frac{\partial\bar{e}_{a1}}{\partial\rho}\right)_{x_a}\frac{d\rho}{dz} + \left(\frac{\partial\bar{e}_{a1}}{\partial x_a}\right)_\rho\frac{dx_a}{dz}\right](\delta z)^2$$
$$+ \frac{1}{2}x_b\frac{d}{dz}\left[\left(\frac{\partial\bar{e}_{b1}}{\partial\rho}\right)_{x_a}\frac{d\rho}{dz} + \left(\frac{\partial\bar{e}_{b1}}{\partial x_a}\right)_\rho\frac{dx_a}{dz}\right](\delta z)^2$$
$$- \frac{1}{2}Tx_a\frac{d}{dz}\left[\left(\frac{\partial\hat{s}_{a1}}{\partial\rho}\right)_{x_a}\frac{d\rho}{dz} + \left(\frac{\partial\hat{s}_{a1}}{\partial x_a}\right)_\rho\frac{dx_a}{dz}\right](\delta z)^2$$
$$- \frac{1}{2}Tx_b\frac{d}{dz}\left[\left(\frac{\partial\hat{s}_{b1}}{\partial\rho}\right)_{x_a}\frac{d\rho}{dz} + \left(\frac{\partial\hat{s}_{b1}}{\partial x_a}\right)_\rho\frac{dx_a}{dz}\right](\delta z)^2$$
$$= \tfrac{1}{2}(x_a d^2\bar{e}_{a1}/dz^2 + x_b d^2\bar{e}_{b1}/dz^2)(\delta z)^2$$
$$- \tfrac{1}{2}T(x_a d^2\hat{s}_{a1}/dz^2 + x_b d^2\hat{s}_{b1}/dz^2)(\delta z)^2 \quad (2.4)$$

Integration of $\sigma_2 = \int_{-\infty}^{\infty}\rho\phi_2\, dz$ by parts, neglecting the variation in ρ since it is so much smaller than that of x_{a1}, now yields

$$\sigma_2 = -\tfrac{1}{2}(\delta z)^2\rho[\int_{-\infty}^{\infty}(dx_a/dz)(d\bar{e}_{a1}/dz)\, dz$$
$$+ \int_{-\infty}^{\infty}(dx_b/dz)(d\bar{e}_{b1}/dz)\, dz$$
$$- T\int_{-\infty}^{\infty}(dx_a/dz)(d\hat{s}_{a1}/dz)\, dz$$
$$- T\int_{-\infty}^{\infty}(dx_b/dz)(d\hat{s}_{b1}/dz)\, dz] \quad (2.5)$$

Let us now set $dx_a/dz = -dx_b/dz = (x_{a,l} - x_{a,v})/\Delta z$ within the surface and assume that the derivatives are zero elsewhere, in analogy to Figure 1, still using the subscripts l and v to distinguish the two phases, though now they are both liquid phases. Then (2.5) reduces to

$$\sigma_2 = \tfrac{1}{2}(\delta z)^2\rho(x_{a,l} - x_{a,v})[\Delta\bar{e}_{b1} - \Delta\bar{e}_{a1} - T\Delta\hat{s}_{b1}$$
$$+ T\Delta\hat{s}_{a1}]/\Delta z \quad (2.6)$$

where $\Delta\bar{e}_{b1} = \bar{e}_{b,l,l} - \bar{e}_{b1,v}$ etc. Since $\Delta\mu_{a1} = \Delta\mu_{b1} = 0$, and, since the pressure (P/ρ) terms are negligible for a liquid we see that the terms in (2.6) will cancel except that the

$\Delta\bar{s}^r$ terms from eq 2.2 are left over:

$$\sigma_2 = {}^1/_2(\delta z)^2\rho(x_{a,l} - x_{a,v})T(\Delta\bar{s}_{bl}{}^r - \Delta\bar{s}_{al}{}^r)/\Delta z \tag{2.7}$$

Since $(\partial\bar{s}_{al}{}^r/\partial x_a)_T$ and $(\partial\bar{s}_{bl}{}^r/\partial x_a)_T$ may be evaluated from eq 2.2 and are finite and nonzero at the critical point we may write

$$\sigma_2 \approx {}^1/_2(\delta z)^2\rho(x_{a,l} - x_{a,v})^2kT/x_{a,c}(1 - x_{a,c})\Delta z \tag{2.8}$$

It is to be noted that this expression is always positive. In cases where there are strong interactions between the different species, as when there are hydrogen bonds between them, it is quite possible for the entropy of each species to *decrease* upon its dilution, so that $\bar{s}_a$ is lower in the solution poor in A, and $\bar{s}_b$ lower in the solution poor in B. This results in a lower critical solution temperature. However the residual, which appears in eq 2.8, arising from the ideal or regular entropy of mixing, is always positive, and eq 2.8 applies equally to upper or lower critical solution points. In this respect, then, the approximations which have gone into eq 2.8 appear to be satisfactory.

To discuss the first two integrals of eq 1.7 we may proceed as in section 1, remembering, however, that now

$$d\phi_1/d\rho = \partial\phi_1/\partial\rho + (\partial\phi_1/\partial x_a)\, dx_a/d\rho \tag{2.9}$$

We then obtain, assuming ρ is linear with z or with x_a in the surface and constant elsewhere, i.e., that the linear assumption applies to ρ as well as x_a,

$$\begin{aligned}\sigma_1 &= \frac{\Delta z}{\rho_l - \rho_v}\left[\frac{1}{2}\rho_l\rho_v(\phi_{1,l} - \phi_{1,v}) - \frac{1}{2}\int_{\rho_v}^{\rho_l}\rho^2\frac{d\phi_1}{d\rho}\,d\rho\right] \\ &= \frac{\Delta z}{\rho_l - \rho_v}\left[\frac{1}{2}\rho_l\rho_v(\phi_{1,l} - \phi_{1,v}) - \frac{1}{2}\int_{\rho_v}^{\rho_l}P\,d\rho - \frac{1}{2}\int_{x_{a,v}}^{x_{a,l}}\rho^2\left(\frac{\partial\phi_1}{\partial x_a}\right)_\rho dx_a\right]\end{aligned} \tag{2.10}$$

the latter from eq 2.9. Further we note that the ϕ's can be expressed in terms of the chemical potentials

$$\phi_{1,l} = x_{a,l}\mu_{al,l} + x_{b,l}\mu_{bl,l} - P/\rho_l \tag{2.11}$$

and

$$\phi_{1,v} = x_{a,v}\mu_{al,v} + x_{b,v}\mu_{bl,v} - P/\rho_v \tag{2.12}$$

and recalling that $x_{a,l} - x_{a,v} = x_{b,v} - x_{b,l}$, that $\mu_{al,l} = \mu_{al,v} \approx \mu_{al,c}$ and that $\mu_{bl,l} = \mu_{bl,v} \approx \mu_{vl,c}$ we see that eq 2.10 becomes

$$\begin{aligned}\sigma_1 = {}&{}^1/_2\Delta z(P - \bar{P}) + {}^1/_2\Delta z\rho_l\rho_v(x_{a,l} \\ &- x_{a,v})(\mu_{al,c} - \mu_{bl,c})/(\rho_l - \rho_v) \\ &- {}^1/_2\Delta z\int_{x_{a,v}}^{x_{a,l}}\rho^2(\partial\phi_1/\partial x_a)_\rho\, dx_a/(\rho_l - \rho_v)\end{aligned} \tag{2.13}$$

It is seen that σ_1 varies as Δz, so minimizing $\sigma_1 + \sigma_2$ with respect to Δz will again give the result that $\sigma_1 = \sigma_2$ and

$$\sigma = 2\sigma_1 = 2\sigma_2 \tag{2.14}$$

Since we know from the mechanical discussion of interfacial tension that $\sigma = \Delta z(P - \bar{P})$ we infer that the last two terms of eq 2.13 must cancel. I have not found it possible to prove this directly, because of the difficulty in disentangling the effects of the two variables.

TABLE I: Application to Experimental Results

	Xe $b = -{}^1/_2; -1)$	C_6H_{12}-$C_6H_5NH_2$	C_6H_{12}-CH_3OH
T_c, K	290	303	319
ρ_c, mol/cm^3		0.98×10^{-2}	1.32×10^{-2}
P_c, atm	58.2		
σ, dyn/cm	$55t^{1.287}$	$35t^{1.30}$	$100t^{1.23}$
Δz, Å	$4 \times 1.8t^{-0.57}$	$2.1t^{-0.62}$	$9.4t^{-0.67}$
$(dP/dT)_c$, atm/deg	1.13		
$(\rho_l - \rho_v)/\rho_c$	$3.55t^{0.345}$		
$x_{a,l} - x_{a,v}$		$2.24t^{0.333}$	$1.87t^{0.333}$
$x_{a,c}(1 - x_{a,c})$		0.245	0.250
δz,[a] Å	5.2; 3.3	1.2	4.4

[a] δz is calculated on the basis that $\mu = 2\beta + \nu'$. This is well fulfilled except for cyclohexane-methanol, for which μ has the abnormally small value 1.23. This makes δz appear to depend on t, the value of δz given then being the hypothetical value at $t = 1$. At $t = 10^{-3}$ this δz would be 46% higher.

3. Application to Experiment

We have applied eq 1.20 to xenon, assigning b (which could have values from about −0.2 to −1) the value −1/2 or −1. Equation 2.8, with eq 2.14, has been applied to the cyclohexane–aniline system and the cyclohexane–methanol system. These calculations are summarized in Table I, where we have used the experimental data to calculate δz.

The thermodynamic data for xenon are taken from Guggenheim,[9] Hunter and Rowlinson,[10] and Buff and Lovett.[11] The value of Δz is obtained from the correlation length as measured by Giglio and Benedek.[12] The correlation length has been multiplied by 4 to get Δz, since Huang and Webb[13] (who measured the actual profile of the surface in a binary-liquid system) found that the distance across the interface was about 4 times the length characteristic of the exponential drop-off at the wings of the interface. The latter length they believed to be related to the correlation length of the Orstein–Zernike theory, which is what would be measured optically. The smaller value of δz, obtained for $b = -1$, seems somewhat more reasonable than the larger value, for $b = -1/2$.

The data for the cyclohexane–aniline system have been summarized previously,[5] and those for the cyclohexane–methanol system have been taken from Huang and Webb,[13] Warren and Webb,[14] and Eckfeldt and Lucasse.[15]

The values of δz which are obtained appear to be very reasonable. That for the cyclohexane–aniline system seems somewhat small, but I have previously noted[5] that the value of Δz, which is found from the effect of an impurity on the system, may be somewhat uncertain, and should possibly be nearer the value for the cyclohexane–methanol system. On the other hand, δz for cyclohexane–methanol turns out to be rather large, to a considerable degree on account of the large value of the interfacial tension. The latter depends upon the difference in density between the two phases, and the difference in this case is very small, since cyclohexane and methanol have almost the same density (in g/cm^3). The large value of σ was noted by Warren and Webb, but they did not believe that errors in the density difference could account for it.

There is one peculiar property of eq 1.20. Since dP/dT falls off rapidly below T_c, the values of δz will increase, which is hardly to be expected. However, as we get away from the critical temperature the densities of the two phases begin to differ considerably, and the behavior of δz across the interface then comes in doubt, so that it seems that eq 1.20, which is an approximation in any case,

becomes less valid away from the critical point.

While none of the equations are exact, we believe that the results obtained indicate that the physical picture incorporated in them is at least roughly correct.

4. The Gradient Term for Other Thermodynamic Quantities than the Free Energy

The free energy function is of course of primary importance in considering equilibria between phases and the interfacial tension. Because of the minimization of the free energy of the surface, the gradient term, integrated across the surface, is of equal importance with the other term, which we may describe as the localized free-energy term. This may not be the case with thermodynamic functions other than the free energy. The fact that the dependence of the entropy on gradients is often neglected, indicates that this statement is believed to apply to the entropy.

It is clear from the preceding discussion that in general T times the gradient term for the entropy is of the same order magnitude as the interfacial tension σ. If we differentiate σ with respect to T we get the surface entropy s_σ. Near the critical point $-s_\sigma = \partial\sigma/\partial T \approx T_c^{-1}\,\partial\sigma/\partial t$. Since $\partial\sigma/\partial t$ removes from σ a small factor t, it is clear that, at least near the critical point, s_σ is much larger than σ/T_c and than the gradient term for entropy, and the latter can, indeed, be neglected. The surface energy e_σ is of the same general order as Ts_σ and also considerably larger than σ, so the conclusion will also hold that e_σ is much larger than its corresponding gradient term.

In a recent paper[5] we considered the solubility of an impurity across the interface, and did not take into account the effect of the density gradient on the solubility λ. If we assume that the effect of the gradient on λ can be formulated in the same way as its effect on $\bar{e}_a$, or $\bar{s}_a$, for example, we can say that the effect of the gradient on the adsorption Γ_3 of the impurity at the interface will be given by

$$\Gamma_{3,2} = {}^1/_2(\delta z)^2 a_3(\rho_l - \rho_v)(\lambda_v - \lambda_l)/\Delta z$$

where a_3 is the activity of the solute. We have shown that $\lambda_v - \lambda_l \propto x_{a,l} - x_{a,v}$ and hence as t^β, and $\Delta z \propto t^{-\nu'}$. Thus, recalling also that $\rho_l - \rho_v$ (besides being very small) is proportional to $x_{a,l} - x_{a,v}$.

$$\Gamma_{3,2} \propto t^{2\beta + \nu'}$$

On the other hand, we have shown that the adsorption contributed directly by the local solubility is related to t by

$$\Gamma_{3,1} \propto t^{\gamma' + 2\beta - \nu' - 1}$$

Since $\gamma' \approx 2\nu'$

$$2\beta + \nu' > \gamma' + 2\beta - \nu' - 1$$

and, therefore, near the critical point where t is small, $\Gamma_{3,1} \gg \Gamma_{3,2}$.

Our guess then is that, near the critical point, the gradient term is important only for the free energy.

Acknowledgment. I am grateful to the National Science Foundation for support of this research. I wish to thank Professor Benjamin Widom for reading the manuscript and suggesting the second moment of the direct distribution function as the clue to the discrepancy between eq 1.21 and 1.23.

References and Notes

(1) For reviews and further references see J. A. Barker and D. Henderson, *Rev. Mod. Phys.*, **48**, 587 (1976); S. Toxvaerd in "Specialist Periodical Reports, Statistical Mechanics", K. Singer, senior reportor, The Chemical Society, Vol. 2, Chapter 4; B. Widom in "Montroll Birthday Symposium Volume", U. Landman, Ed., to be published.
(2) E.g., V. Bongiorno, L. E. Scriven, and H. T. Davis, *J. Colloid Interface Sci.*, **57**, 462 (1976).
(3) A. J. M. Yang, P. D. Fleming, III, and J. H. Gibbs, *J. Chem. Phys.*, **64**, 3732 (1976).
(4) B. Widom, *J. Chem. Phys.*, **43**, 3892 (1965); "Phase Transitions and Critical Phenomena", Vol. 2, C. Domb and M. S. Green, Ed., Academic Press, New York, N.Y., 1972.
(5) O. K. Rice, *J. Chem. Phys.*, **64**, 4362 (1976).
(6) O. K. Rice and D. R. Chang, *Physica*, **83A**, 18 (1976).
(7) P. Debye, *J. Chem. Phys.*, **31**, 680 (1959).
(8) J. H. Hildebrand and R. L. Scott, "The Solubility of Nonelectrolytes", 3d ed, Reinhold, New York, N.Y., 1950, pp 107 *ff*.
(9) E. A. Guggenheim, *J. Chem. Phys.*, **13**, 253 (1945).
(10) P. J. Hunter and J. S. Rowlinson in "Simple Dense Fluids", H. L. Frisch and Z. W. Salsburg, Ed., Academic Press, New York, N.Y., 1968.
(11) F. P. Buff and R. A. Lovett in ref 10; also see B. L. Smith, P. R. Gardner, and E. C. H. Parker, *J. Chem. Phys.*, **47**, 1148 (1967).
(12) M. Giglio and G. B. Benedek, *Phys Rev. Lett.*, **23**, 1145 (1969).
(13) J. S. Huang and W. W. Webb, *J. Chem. Phys.*, **50**, 3677 (1969).
(14) C. Warren and W. W. Webb, *J. Chem. Phys.*, **50**, 3694 (1969).
(15) E. L. Eckfeldt and W. W. Lucasse, *J. Phys. Chem.*, **47**, 164 (1943).

Surface Reactions of Oxygen Ions. 1. Dehydrogenation of Alkanes by O^- on MgO

Ken-ichi Aika and Jack H. Lunsford*

Department of Chemistry, Texas A&M University, College Station, Texas 77843 *(Received February 18, 1977)*

Publication costs assisted by the National Science Foundation

Surface reactions occur between C_1 to C_4 alkanes and O^- ions on MgO at minimum temperatures approaching the normal boiling points of the alkanes. The corresponding alkenes were observed in the gas phase when the reactions were carried out at 25 °C; however, the products reached a maximum when the systems were subsequently heated above 300 °C. Following the reaction of butane with O^-, butadiene also appeared as a product. The selectivity for the dehydrogenation reactions was 30 to 45%. A stoichiometry of one alkane per one O^- ion was determined. It is proposed that an alkoxide intermediate is formed on the surface since similar thermal desorption products were observed following the adsorption of the corresponding alcohols on MgO. Methane also reacted with O^- ions, apparently forming methoxide ions which decomposed at 450 °C to give mainly hydrogen.

Introduction

Ion/molecule reactions involving the O^- species have been reported in gas and liquid phases, as well as at the surface of metal oxides. Bohme et al.,[1] working in the gas phase, have shown that with simple olefins the oxygen ion adds only to ethylene, and with the higher olefins it reacts by either abstracting a hydrogen atom or a proton. For simple alkanes hydrogen atom abstraction was the only observed reaction.[2] Likewise, in liquid solution Neta and Schuler[3] have demonstrated that the addition of O^- to double bonds and aromatic systems is relatively slow so that in most cases hydrogen atom abstraction dominates.

The electron paramagnetic resonance (EPR) technique has been used to confirm the existence of the O^- ion on several metal oxides.[4] The simplest ion/molecule reactions that have been studied on surfaces are those in which stable paramagnetic radicals are formed. Examples of such reactions are[5-8]

$$O^- + O_2 \rightarrow O_3^- \quad (1)$$

$$O^- + CO \rightarrow CO_2^- \quad (2)$$

$$O^- + CO_2 \rightarrow CO_3^- \quad (3)$$

$$O^- + C_2H_4 \rightarrow C_2H_4O^- \quad (4)$$

$$O^- + CH_3OH \rightarrow \cdot CH_2OH + OH^- \quad (5)$$

In all of these cases the paramagnetic reaction product was detected by EPR spectroscopy. With other reactants, however, it is reasonable to expect that subsequent surface reactions may lead to diamagnetic intermediates. Only recently has there been an attempt to understand the gas phase products in terms of the surface reactions involving O^-. Kazusaka and Lunsford[9] concluded that the O^- ion was not a reactive intermediate in the low-temperature oxidation of CO with N_2O over supported molybdenum oxide.

The purpose of this research was to determine the reactions that occur between simple alkanes and O^- on the surface of magnesium oxide. This material was chosen because the magnesium cation has only one oxidation state and it is diamagnetic; therefore, each O^- ion formed on the surface may be detected by EPR. Similarly, radical intermediates could be detected if they had sufficiently long lifetimes on the surface. The situation is not so clear, for example, with molybdena supported on silica where the molybdenum ions may take on several paramagnetic oxidation states, and the observed O^- ion must be coordinated only to isolated Mo^{6+} ions.

Since the products of the reactions in this study were not paramagnetic and the concentrations of the surface species were small, the reactions were followed by observing the gas phase after desorption or decomposition of surface intermediates. By comparing thermal desorption data of the reaction intermediates with that obtained from known surface complexes it is possible to infer the elementary steps in the heterogeneous ion/molecule reaction.

Experimental Section

The magnesium oxide was prepared according to the method reported previously.[10] It was evacuated at 500 °C overnight before every reaction cycle in order to eliminate hydrocarbons, carbon dioxide, and water. The surface area of the MgO was approximately 160 m^2/g. Two samples (1.60 g in reactor A and 0.82 g in reactor B) were used for all of the experiments in which thermal desorption data were acquired. It should be noted that the concentration of O^- ions was determined for these particular samples.

The O^- ion was produced in the quartz reactor R (Figure 1) in the same manner as reported previously;[10] i.e., N_2O was allowed to react with electrons trapped at oxide ion vacancies on the surface of MgO. The EPR spectra of O^- were obtained with a Varian E-6S, X-band spectrometer. The g values were evaluated by using a phosphorus-doped silicon standard having a g value of 1.9987. The concentration of O^- ion was evaluated by a double integration of the EPR spectrum using both the phosphorus-doped silicon and a $CuSO_4 \cdot 5H_2O$ single crystal as standards. Both standards gave the same O^- concentration within a difference of 3%.

The alkanes (methane, ethane, propane, and n-butane) were obtained from commercial sources, and were purified by several distillations. For methane a zeolite adsorbent was used in the purification. The alkanes were stored and used as a 1% mixture in helium.

Reactants and products were analyzed using a Carle AGC-311 gas chromatograph with both a thermal conductivity detector (TCD) and a flame ionization detector (FID). The chromatograph was connected directly to the reaction system (Figure 1). The column packings were Porapack Q for the separation of CH_4, C_2H_4, C_2H_6, C_3H_6, C_3H_8, N_2O, and CO_2; bis(ethoxy)ethyl adipate for the separation of butane, butenes, butadiene, alcohols, aldehydes, and ethylene oxide; and 5A molecular sieve for

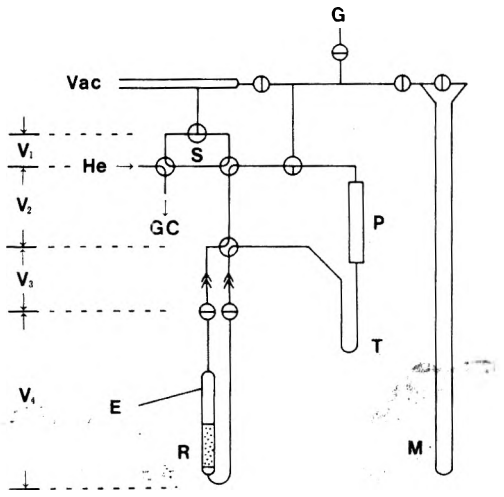

Figure 1. Reaction apparatus. The symbols listed are as follows: G, gas inlet; S, sampler; P, circulation pump; T, trap; R, quartz reactor; E, quartz tube for EPR measurement; M, manometer; GC, gas chromatograph; V_1, 1.2 mL; V_2, 20.6 mL; V_3, 2.3 mL; V_4, 32.3 mL for reactor A and 15.2 mL for reactor B.

the separation of H_2, O_2, N_2 and CO. Mass spectra of inorganic gases were obtained using a CEC residual gas analyzer.

After recording the EPR spectrum of the O^- ions on magnesium oxide, contained in the quartz sidearm E, the reactor was attached to the closed circulation system shown in Figure 1 and N_2O was evacuated. A known amount of alkane (0.1 or 1.0 Torr) was introduced and circulated over the MgO at 25 °C for 1–2 h. The reactants and products were analyzed by means of sampler S. The reactor was then heated according to a temperature program of 150 °C for 1–2 h, 300 °C for 1–2 h and 450 °C for 1–2 h, and the desorbed gases with the exception of methane were collected in the trap which was at −196 °C. In some cases the temperature was raised only to 300 °C for 1–2 h. After isolating the reactor from the system the trap was warmed to 25 °C, and the gas phase molecules were analyzed. The same program was applied when products of alcohol and acetaldehyde decomposition were thermally desorbed.

Infrared spectra of the MgO with adsorbed molecules were obtained in a manner described elsewhere,[11] using both an IR-9 spectrophotometer and a Fourier transform infrared spectrometer

Results

EPR Evidence for the Reaction between O^- and Alkanes. After recording the EPR spectrum of O^- on MgO at −196 °C 1 Torr of alkanes was introduced to the sample which, for this experiment, was contained in a cylindrical tube of 4 mm diameter. In order to examine the decay of the O^- signal as a function of temperature the sample was warmed by transferring it to a constant-temperature bath for 5 min. After cooling the sample to −196 °C the EPR spectrum was again recorded. The EPR signal of O^- disappeared at −130 to −150 °C for methane, −80 to −90 °C for ethane, −20 to −40 °C for propane, and 0 to −10 °C for *n*-butane. It is interesting to note that these temperatures are almost the same as the boiling points for each alkane, thus the reaction of O^- with an alkane is apparently rate limited by the diffusion of the alkane through the column of MgO.

When a trace amount of oxygen was present in the nitrous oxide gas the EPR spectrum of the O_3^- ion appeared[5] together with that of O^-. Upon the introduction of an alkane to such a sample only the O^- signal disappeared, and the O_3^- signal remained unchanged up to 25 °C. This indicates the high reactivity of O^- relative to the O_3^- ion. During the reactions no new paramagnetic species were detected.

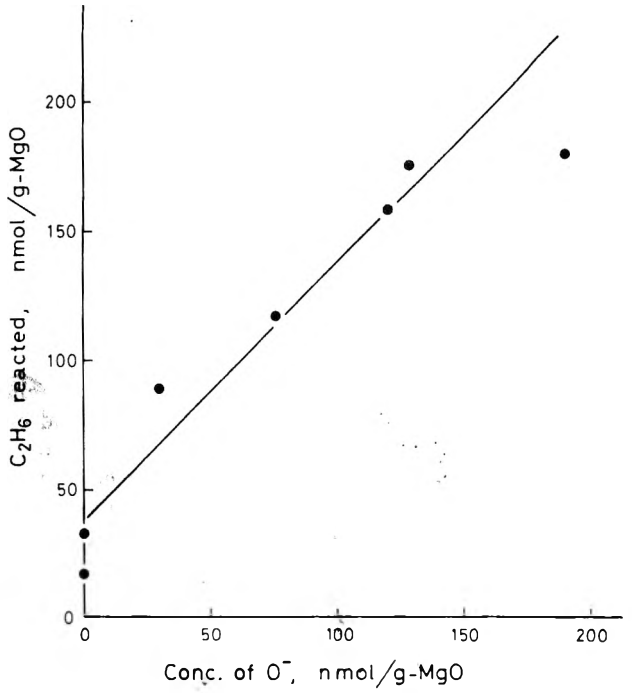

Figure 2. Variation of ethane reacted with O^- at 25 °C as a function of the concentration of O^- evaluated from its EPR spectrum.

Product Determination. When 0.1 or 1 Torr of an alkane was introduced on MgO which had not been treated with N_2O, no alkene was obtained following thermal desorption up to 300 °C, even though S centers (electrons trapped at oxide ion vacancies) were present. A small amount of other alkanes was obtained from such a system; for example, CH_4 and C_2H_6 were obtained from C_3H_8 and C_2H_6 was obtained from CH_4 at 25 °C. The amount of these products was approximately 1–2 nmol/g of MgO after 16 h of reaction. Thermal desorption up to 450 °C did not increase the quantity of these products.

The corresponding alkenes were obtained even at 25 °C when about 0.1 Torr of ethane, propane, or *n*-butane was introduced on MgO with O^-. The amount of ethane reacted is shown in Figure 2 as a function of O^- concentration evaluated from the EPR spectrum. A small amount of ethane reacted to give ethylene even when the EPR spectrum of O^- was not detectable, although it was necessary that the MgO be exposed to N_2O. As shown in the figure the amount of ethane reacted increased linearly with respect to the O^- concentration up to a concentration of ca. 150 nmol of O^-/g of MgO. The slope of unity suggests a one-to-one stoichiometry for the reaction of ethane and O^-.

The total amounts of gas phase products as a function of the thermal desorption program are shown in Figures 3–5. The amount of alkene increased upon thermal desorption up to 300 °C but remained at a steady value at higher temperatures. Cracked carbon species, e.g., methane and carbon dioxide in case of ethane, were detectable only at temperatures higher than 450 °C. Although carbon dioxide was observed as the principal inorganic product from C_2 to C_4 alkanes, the quantity is shown only in Figure 3 because of difficulty of measurement with the TCD detector. Hydrocarbons having a greater carbon number than the reactant were not observed except in the case of ethane, for which a small amount of propylene and 1,3-butadiene were detected at

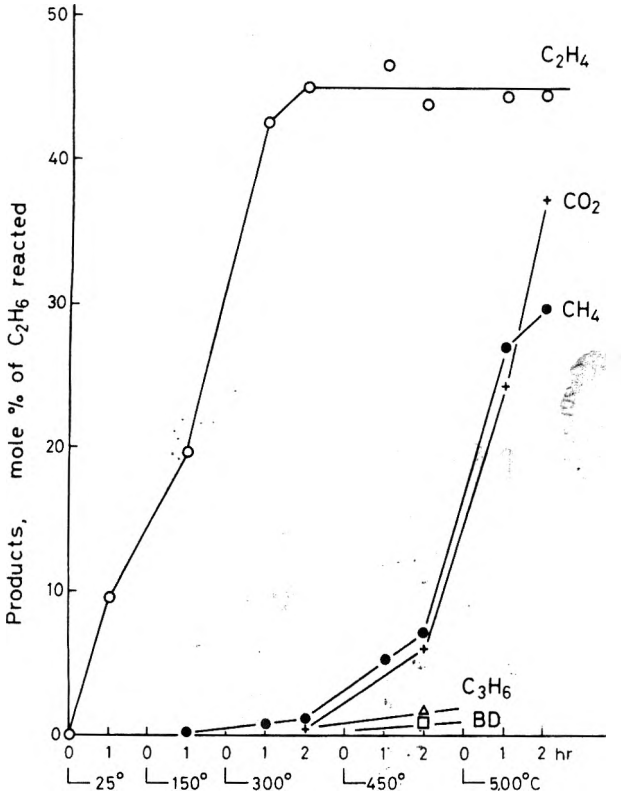

Figure 3. Variation of products as a function of the thermal desorption program following the reaction of ethane with O^- at 25 °C. (BD indicates butadiene.)

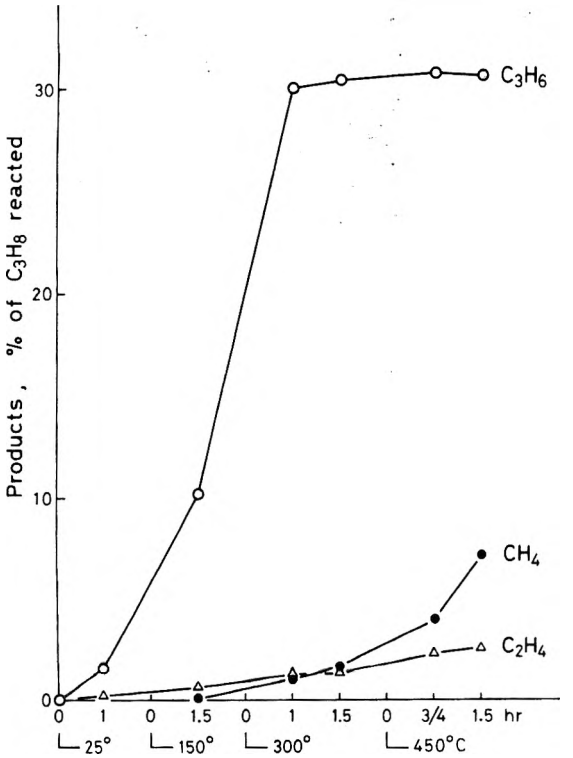

Figure 4. Variation of products as a function of the thermal desorption program following the reaction of propane with O^- at 25 °C.

450 °C. No oxygen containing species such as alcohols, aldehydes, or the corresponding epoxides were detected. The reaction of butene with O^- yielded 1,3-butadiene, as well as the *cis*- and *trans*-2-butene and 1-butene isomers in essentially equilibrium ratios. The selectivities for the corresponding alkenes or alkenes and dienes in the case of butene were 45% for ethane, 30% for propane, and 38%

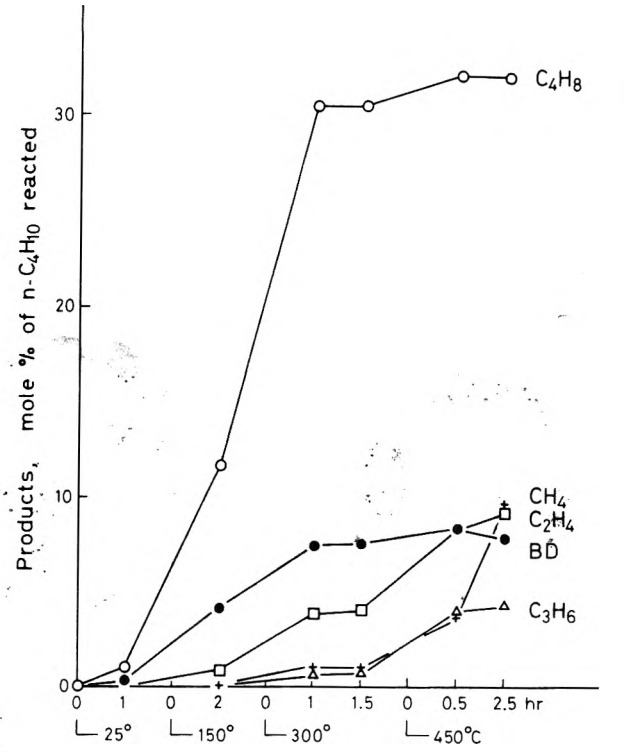

Figure 5. Variation of products as a function of the thermal desorption program following the reaction of *n*-butane with O^- at 25 °C. (BD indicates butadiene.)

for *n*-butane with a deviation of ±8%, respectively.

The reaction of 2.1 Torr of methane with O^- gave no hydrocarbon product except for a trace amount of ethane which was at the same level as in the blank run. No detectable amount of inorganic species as detected by TCD was observed after 2 h of thermal desorption; however, hydrogen was observed by means of mass spectrometry after thermal desorption at 450 °C. The amount of hydrogen obtained from the system with 292 nmol/g of MgO of O^- was 90 and 220 nmol/g of MgO for 1.5 and 21 h of thermal desorption, respectively, at 450 °C. A trace amount of carbon dioxide (2–14 nmol/g of MgO) was found at 450 °C. The amount of carbon monoxide could not be evaluated due to a background N_2 peak. Another experiment with 0.15 Torr of methane revealed that the amount of methane adsorbed (350 nmol/g of MgO) was almost equivalent to the O^- concentration (290 nmol/g of MgO) and that the adsorbed methane was not recovered even after thermal desorption for 13 h at 450 °C.

Competitive Reactions. Since alkanes yield no other alkanes below 300 °C and unreacted alkanes are recovered above 150 °C (see below), a relative rate between two alkanes may be evaluated by allowing a mixture of the alkanes to compete for the same O^- ions. A mixture of ethane and propane, with each at a pressure of 0.1 Torr, was introduced at 25 °C to a sample of MgO which contained O^- ions, and the reactants and products were collected after thermal desorption at 300 °C for 1–2 h. The conversion χ (reacted alkane/alkane introduced) was obtained for each alkane. The ratio for the conversion of propane vs. ethane (χ_3/χ_2) was 1.27 ± 0.03. Similar competitive runs between *n*-butane and ethane and between methane and ethane gave the conversion ratios (χ_4/χ_2) of 0.67 ± 0.12 and (χ_1/χ_2) of 0.50 ± 0.02. The relative reactivities between alkanes are summarized in Table I and compared to results from gas phase reactions.[2]

Up to this point it has been implied that an alkane reacts rapidly with O^- at 25 °C, giving some intermediate which is strongly adsorbed on MgO and is desorbed or decom-

TABLE I: Relative Reactivity of Alkanes with O^- Ions

	O^- on MgO	O^- in gas phase[a]
Temp	25 °C	22.5 °C
Alkane pressure, Torr	0.1	0.23
CH_4	0.50	0.14
C_2H_6	1.00	1.00[b]
C_3H_8	1.27	1.33
n-C_4H_{10}	0.67	1.7

[a] Reference 2. [b] Absolute rate constant is 7.0×10^{-10} cm^3/s.

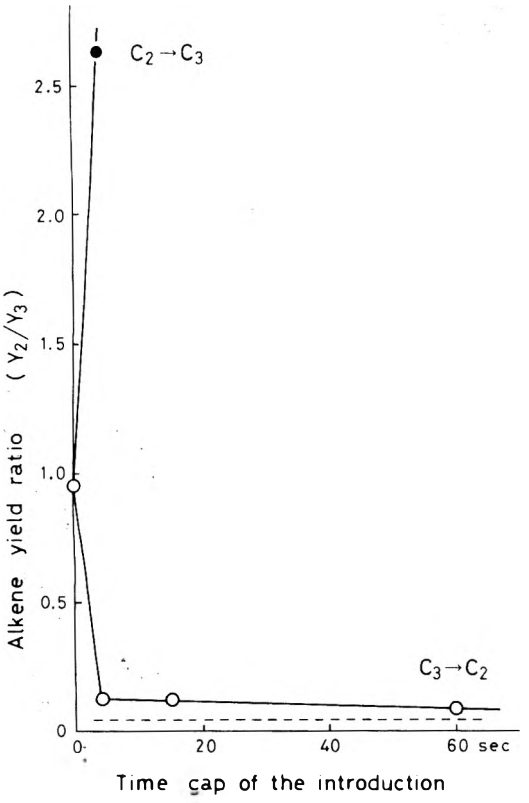

Figure 6. Variation of the alkene yield ratio following the reaction of ethane and propane with O^- as a function of the time gap between the introduction of the respective gases in the sequence indicated by the arrows. The dotted line is the amount of ethylene from propane. Pressures of alkanes were ca. 1 Torr. Products were obtained through the thermal desorption at 300 °C for 1–2 h.

posed only at 300 °C. This may be reasonable since the O^- signal disappeared when an alkane was admitted to the sample at a low temperature and since dehydrogenated products reached a maximum value only after the sample was heated to 300 °C. There is, however, a possibility that upon introducing an alkane the O^- might be converted to another nonparamagnetic oxygen-containing species (such as OH^-) which might react with an alkane slowly at 25 °C and quickly at 300 °C, giving the observed alkene. In order to explore this possibility, 1 Torr of ethane was added at a predetermined time after 1 Torr of propane had been introduced to the sample. The two gases were circulated well, and the products were analyzed after thermal desorption at 300 °C for 1–2 h. The alkene yield ratio (Y_2/Y_3) is given as a function of the time delay in Figure 6. The results show that when the time gap is longer than 4 s, the ethylene produced is only the amount expected as a by-product from the propane reaction. A similar result was obtained when the order of alkane introduction was reversed, as shown in Figure 6, although the amount of propylene produced was somewhat greater than expected. These results indicate that the alkanes indeed react rapidly with O^-, forming a thermally stable surface intermediate.

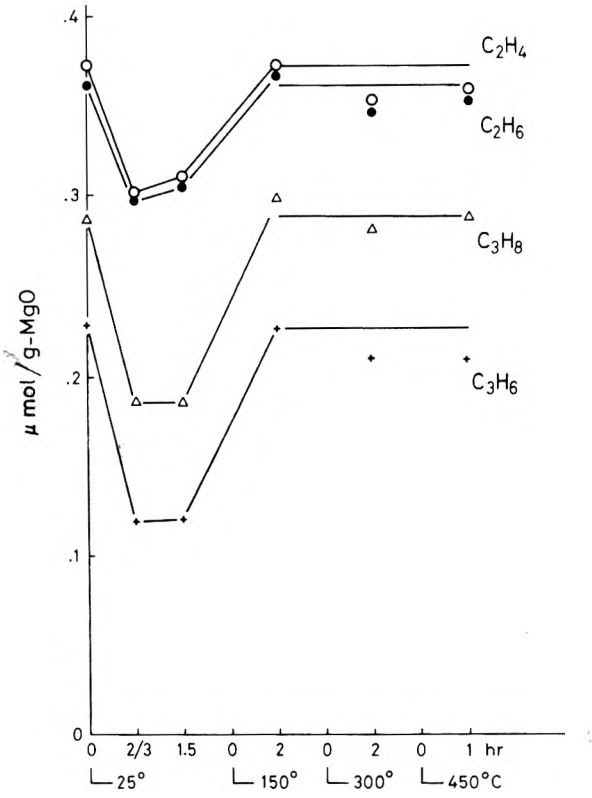

Figure 7. Variation of gaseous hydrocarbons over MgO as a function of the thermal desorption program following adsorption at 25 °C. The equilibrium pressures range from 0.044 to 0.115 Torr at 25 °C.

The active oxygen is consumed within at most a few seconds at 25 °C.

Adsorption and Thermal Desorption on MgO. In order to determine the nature of the surface intermediate adsorption and thermal desorption properties of alkenes, alcohols, and acetaldehyde were examined. Amounts of alkanes and alkenes comparable to those produced during a reaction were adsorbed at 25 °C on the same MgO sample without O^-, and thermally desorbed into a trap under a similar program as in the reaction with O^- ions. The amount of material remaining in the gas phase is shown as a function of the thermal desorption program in Figure 7. Both alkanes and alkenes were observed to be desorbed completely at 150 °C. Adsorption isotherms of alkanes and alkenes at 25 °C over the pressure range from 0 to 1 Torr show that these hydrocarbons are physically adsorbed on MgO. This suggests that strongly adsorbed alkenes are not the stable intermediates formed by the reaction of alkanes with O^- ions.

After approximately 3.7 μmol/g of MgO of ethanol was introduced on the same MgO the adsorption and thermal desorption results were obtained as described in Figure 8. Although ethanol adsorbed completely at 25 °C, none was desorbed up to 450 °C. Instead, a small amount of ethylene was obtained in the gas phase at 150 °C, and above 300 °C the moles of ethylene were almost the same as that of the original ethanol adsorbed. It should be noted that the desorption characteristics observed with ethanol are similar in many respects to those depicted in Figure 3.

Following the adsorption of 1.4 μmol/g of MgO of methanol on MgO at 25 °C only a comparable amount of hydrogen (0.3–2.2 μmol/g of MgO) and a small amount of CO and CO_2 (below 0.1 μmol/g of MgO each) were detected as desorption products at 450 °C. This has essentially the same thermal desorption spectrum as that obtained from the reaction between methane and O^- ions.

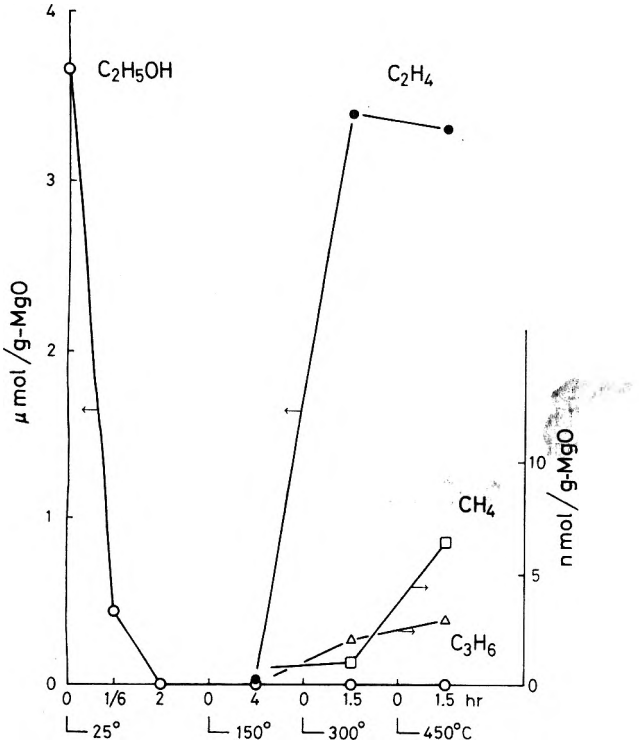

Figure 8. Variation of gas phase composition as a function of the thermal desorption program following the adsorption of ethanol on MgO at 25 °C.

Acetaldehyde may also be considered as a possible surface intermediate which might decompose to give ethylene. It was observed, however, that following the decomposition of 0.84 μmol/g of MgO of acetaldehyde only a small amount of ethylene (15 nmol/g of MgO) was observed with the sample at 300 °C. At 450 °C the acetaldehyde decomposed to give hydrogen and methane as the principal products and carbon dioxide as the minor product.

Infrared Study. In an effort to determine the identity of the surface intermediate the O^- ion was prepared on an MgO wafer which was suitable for obtaining infrared spectra in the transmission mode. After the introduction of 1 Torr of ethane, the spectrum was recorded using both a conventional scan and a Fourier transform spectrometer; however, no peaks were obtained except those due to adsorbed N_2O and the MgO background. The maximum concentration of the surface species was only ca. 300 nmol/g of MgO, which is apparently below the limits of detection.

Since the surface intermediate produced by the adsorption of ethanol gave essentially the same thermal desorption products as observed when ethane reacted with O^- ions, it was of interest to obtain the infrared spectrum following the reaction of ethanol with MgO. The positions of the bands are summarized in Table II where a comparison is made with the spectrum of liquid ethanol and magnesium ethoxide.[12] The results indicate that the ethoxide intermediate is formed on the surface.

Discussion

Initial Surface Reactions. The surface reactions of O^- with hydrocarbons may best be understood in light of the analogous gas phase reactions. For example, ethylene is the only alkene which reacts by addition to O^- as observed by Naccache and co-workers.[6,7] This same behavior has been observed for gas phase reactions of O^- with alkenes.[1] As stated earlier hydrogen atom or proton abstraction was noted for all other simple alkanes and alkenes.

TABLE II: IR Spectra of Adsorbed Alcohol on MgO, Magnesium Ethoxide, and Ethanol (cm^{-1})

Assignment[b]	Adsorbed C_2H_5OH on MgO[a]	$Mg(OC_2H_5)_2$[b]	C_2H_5OH[b] (liq)
ν(E)CH_3	2955	2964	2973
$2\delta_1$CH	2920	2922	2926
ν(B)CH_2	2855	2850	
ν(A)CH_2	2825	2850	
$2\delta_2$CH	2700	2720	
δ_1CH	1443	1447	1461
δ_2CH	1381	1382	1377
δ_3CH		1319	1328
νC-O	1110~1138	1123	1086
νC-O	1067	1070	1059
νC-C	889	893	881

[a] Obtained after 10-min evacuation following adsorption of ethanol for 5 h at 25 °C. [b] Reference 12.

Since no hydroxyl radical was observed on the surface, even at low temperatures, it seems unlikely that the abstraction of a proton prevailed on MgO. One could argue that the OH· radical rapidly abstracted a hydrogen atom from the same molecule but this would lead to the formation of radical anions which also were not observed by EPR spectroscopy.

Hydrogen atom abstraction seems to be a more likely reaction path, but again no alkyl radicals were observed. Radical recombination did not occur since no dimers were detected. We propose that alkyl radicals are indeed formed, but that they react mainly with surface O^{2-} ions as indicated in the following mechanism for ethane:

$$C_2H_6 + (O^-)_s \rightarrow \cdot C_2H_5 + (OH^-)_s \quad (6)$$

$$\square + \cdot C_2H_5 + (O^{2-})_s \rightarrow (OC_2H_5^-)_s + \square \quad (7)$$

where $\square$ denotes an electron trapped at an oxide ion vacancy at the surface. This mechanism, of course, results in the formation of a stable surface alkoxide. Our failure to observe the alkyl radicals suggests that reaction 7 must be rapid compared to reaction 6. The relative rates of reaction 6 for various alkanes is believed to be controlled by diffusion, and it is not surprising that the relative rates given in Table I are not the same as those observed in the gas phase.[2]

Since some ethylene appeared in the gas phase even at 25 °C, it is reasonable to expect that the following competing reactions may also occur:

$$\cdot C_2H_5 + \square \rightarrow C_2H_5^+ + \square \quad (8)$$

$$C_2H_5^+ + (O^{2-})_s \rightarrow C_2H_4 + (OH^-)_s \quad (9)$$

As depicted in reaction 9 the ethyl carbonium ion would be unstable on a basic oxide surface. Evidence for the oxidation of an alkyl radical to the carbonium ion by copper(II) has been obtained by Kochi.[13] The ultimate reaction product is an alkene, although rearrangement of the carbonium ion may occur.

A similar mechanism to that described above has been proposed by Tench et al.[8] to explain the reaction between H_2 and O^- on MgO. Upon exposure of O^- to H_2 the O^- signal disappeared and the EPR spectrum of trapped electrons at the surface was observed. This may be explained by the reactions:

$$H_2 + (O^-)_s \rightarrow (OH^-)_s + H\cdot \quad (10)$$

$$\square + H\cdot + (O^{2-})_s \rightarrow (OH^-)_s + \square \quad (11)$$

Independent evidence has been gained for reaction 11 through a study of the interaction of hydrogen atoms with magnesium oxide which results in the formation of trapped electrons at the surface.[14] These reactions parallel the

formation and subsequent radical reactions described in eq 6–9.

If reactions 7 and 8 indeed occur, one must explain why the EPR signal due to trapped electrons was not observed. First, it should be pointed out that ethylene reacted with these S centers, though rather slowly. (Ethane did not react with S centers.) It is also expected that the EPR spectrum of the trapped electrons would be destroyed by the radical-coupling reaction:

$$\cdot C_2H_5 + \square \rightarrow \overset{CH_2CH_3}{\square} \quad (12)$$

The resulting surface species may be the source of methane and carbon dioxide via a decomposition reaction at elevated temperatures. Both the reaction of S centers with ethylene and the radical-coupling reaction would account for the relatively low selectivity for the formation of ethylene. In fact, a selectivity of 50% would be predicted if all of the trapped electrons produced by reactions 7 and 8 were destroyed by reaction 12, and the decomposition of the alkoxide ion went cleanly to form ethylene.

The small amount of alkene produced on surfaces which had no O^- signal, as indicated in Figure 2, may be attributed to the interaction of ethane with O^- which was formed by the thermal reaction of N_2O with a transition metal impurity. Iron for example is known to be present in the MgO at a level of about 2 μmol/g of MgO. An O^- ion formed on such an impurity would not be observable by EPR. In this respect it should be noted that exposure of the sample to N_2O was required before a detectable amount of the alkene was produced.

Decomposition of Surface Intermediates. Alkoxide ions appear to be the most probable intermediate which decomposes to give alkenes at elevated temperatures; however, it is difficult to establish this directly because the concentration of these species is below the detection limits of infrared spectroscopy. Nevertheless it is instructive to examine the thermal desorption of known molecules in order to resolve the nature of the intermediate. Ethanol is known to be adsorbed as an alkoxide on Al_2O_3 or MgO. At high surface coverages ethoxide on Al_2O_3 decomposed thermally to give mainly ethanol at temperatures below 80 °C, a good amount of diethyl ether at 80–140 °C, and mainly ethylene above 140 °C.[15] When the surface coverage is low, the ethoxide is considered to be so strongly bound to Al atoms that it is decomposed mainly to ethylene. At high surface coverages ethoxide on MgO decomposed to give mainly ethanol below 330 °C and mainly 1,3-butadiene above 330 °C.[16] No acetaldehyde was observed, although this is a main product under catalytic conditions at 360 °C. In both of these cases it appears that strongly bonded surface complexes favor dehydration reactions. Indeed, we have observed that ethanol reacts with MgO, forming the ethoxide ion, and that the adsorption of small amounts of ethanol (ca. 5×10^{-3} monolayers) results in the formation of ethylene as the principal decomposition product. The similarity between the decomposition profiles depicted in Figures 3 and 8 suggests that the alkoxide intermediate is formed upon the reaction of O^- with alkanes.

Propyl and butyl alkoxides are considered to give corresponding alkenes when thermally desorbed. However, methoxide which has no corresponding alkene was found to decompose to H_2, CO, and CO_2 at higher temperatures on MgO, as has been reported elsewhere for Al_2O_3.[17] The carbon species, i.e., CO and CO_2, are considered to be complexed so strongly that only 10% of those molecules are observed to be desorbed after 16 h at 450 °C. Since methane was also found to react with O^- and to give the same thermal desorption spectra as that observed following the adsorption of methanol, it appears that the methoxide ion was formed in both cases.

The final step in the production of alkenes by the reaction of alkanes with O^- on MgO can be written as follows:

$$(OR^-)_s \xrightarrow{\text{slow}} \text{alkene} + (OH^-)_s \quad (13)$$

$$(OCH_3^-)_s \xrightarrow{\text{very slow}} CO(a) + {}^3/_2 H_2 \quad (14)$$

A stable form of adsorbed CO has been shown to exist on MgO at temperatures in excess of 400 °C.[18]

Conclusions

It is evident from this study that surface O^- ions react with simple alkanes at a rate which is governed by the transport of the hydrocarbon. Although alkyl radicals are not directly observed, the net reaction involves hydrogen abstraction, similar to the mechanism previously reported for the gas phase and solution studies. Furthermore, these results suggest that the O^- ion may be involved in the oxidative dehydrogenation of hydrocarbons, particularly when N_2O is employed as the oxidizing agent. Even in the absence of an external source of oxygen, it is reasonable to expect that O^- ions would be in dynamic equilibrium with oxide ions on certain transition metal oxides. The most favorable cases would be those oxides in which the metal ion is present in a high oxidation state.

Acknowledgment. The authors wish to acknowledge the support of the National Science Foundation under Grant No. CHE 75-15456.

References and Notes

(1) D. K. Bohme and L. B. Young, *J. Am. Chem. Soc.*, **92**, 3301 (1970).
(2) D. K. Bohme and F. C. Fehsenfeld, *Can. J. Chem.*, **47**, 2717 (1969).
(3) P. Neta and R. H. Schuler, *J. Phys. Chem.*, **79**, 1 (1975).
(4) J. H. Lunsford, *Catal. Rev.*, **8**, 135 (1973).
(5) N.-B. Wong and J. H. Lunsford, *J. Chem. Phys.*, **56**, 2664 (1972).
(6) C. Naccache and M. Che, "Catalysis", J. Hightower, Ed., North Holland Publishing Co., Amsterdam, 1973, pp 1389–1400.
(7) C. Naccache, *Chem. Phys. Lett.*, **11**, 323 (1971).
(8) A. J. Tench, T. Lawson, and J. F. J. Kibblewhite, *J. Chem. Soc., Faraday Trans. 1*, **68**, 1169 (1972).
(9) A. Kazusaka and J. H. Lunsford, *J. Catal.*, **45**, 25 (1976).
(10) N.-B. Wong and J. H. Lunsford, *J. Chem. Phys.*, **55**, 3007 (1971).
(11) M. J. Lin and J. H. Lunsford, *J. Phys. Chem.*, **79**, 892 (1975).
(12) A. I. Grigorov and N. Ya Turova, *Dokl. Acad. Nauk. SSSR.*, **162**, 98 (1965).
(13) J. K. Kochi, *J. Am. Chem. Soc.*, **85**, 1958 (1963).
(14) D. R. Smith and A. J. Tench, *Chem. Commun.*, 1113 (1968).
(15) H. Arai, J. Take, Y. Saito, and Y. Yoneda, *J. Catal.*, 9, 146 (1967).
(16) N. Takezawa, C. Hanamaki, and H. Kobayashi, *J. Catal.*, **38**, 101 (1975).
(17) T. Matsushima and J. M. White, *J. Catal.*, **44**, 183 (1976).
(18) F. S. Stone and A. Zecchina, *Proc. Int. Congr. Catal., 6th*, in press.

Poisoning Titration Technique for Determining the Number of Active Centers in a Supported Platinum Catalyst

L. Gonzalez-Tejuca,† K. Aika, S. Namba, and John Turkevich*

Chemistry Department, Princeton University, Princeton, New Jersey 08540 (Received February 14, 1977)

Publication costs assisted by Princeton University

A method has been developed for determining the number of active centers on platinum responsible for the catalytic hydrogenation of olefins and equilibration of hydrogen–deuterium mixtures. Alternate pulses of poison (titrant) and reactant (indicator) were introduced into a hydrogen stream which passed over the catalyst in a microreactor. The number of pulses of the poison (titrant) just necessary to decrease to zero the hydrogenation reaction (indicator) permits the calculation of the number of catalytically active centers. The following titrants were examined: carbon disulfide, carbonyl sulfide, carbon monoxide, hydrogen sulfide, sulfur dioxide, and thiophene. Carbon disulfide was found to be the best titrant for platinum. A number of reactions were used as indicators: hydrogenation of ethylene, propylene, butylene, cyclohexene, and benzene and the equilibration of hydrogen–deuterium mixtures. The reproducibility of the titration of active catalytic centers was determined to be 7% of a series of monodispersed supported platinum catalysts with particle diameter from 19 to 53 Å. The number of active centers was usually found to be equal to those determined by hydrogen chemisorption if it is assumed that one carbon disulfide molecule poisons two platinum atoms. However, evidence was obtained that, under certain conditions of catalyst treatment, chemisorption of hydrogen occurs on platinum clusters that are not catalytically active. These clusters seem to be molecularly dispersed platinum atoms on the support lacking catalytic activity for hydrogenation of ethylene. Evidence was also obtained for the presence of a geometric factor in the hydrogenation of benzene. The turnover number for the hydrogenation of ethylene based on the number of centers determined by poison titration is constant in the particle range of 19 to 53 Å.

Introduction

The problem of determining the number of active centers on a catalytic surface and the activity of each center is crucial in experimental catalytic investigations. It has had a long history. The total surface area of a catalyst preparation can be reliably determined by the BET method[1] while the extent of chemisorption has been identified with the number of active centers in a nonsupported catalyst. This chemisorption approach has been refined for supported catalysts by the elegant variation of first adsorbing oxygen on the catalyst and then determining the amount of hydrogen necessary to displace the oxygen and chemisorb the hydrogen.[2] In a recent publication we have reported good agreement between the particle size as determined by ultrahigh resolution electron microscopy (resolution of 1.2 Å) and the Benson–Boudart chemisorption method for monodisperse platinum on alumina and silica.[3]

In this paper we wish to report the use of poison titration technique for determining the number of active centers on supported platinum catalysts, and to correlate the results obtained with the number of surface atoms as determined by chemisorption techniques.

In the poison titration of the number of active centers on the catalyst surface, a pulse microreactor is used with a carrier gas which can be a reactive gas such as hydrogen or an inert one such as helium. A pulse of the reactant (in our case either an olefin, benzene, or deuterium), which is an indicator of the status of the catalyst, is introduced and its conversion measured. Then a poison pulse is introduced. This is adsorbed on the surface. This is followed by a reactant pulse. This cycle of poison and reactant is carried out until a sufficient number of pulses of the poison are introduced to completely "kill" the activity of the catalyst. Knowing the platinum content of the sample and the number of adsorptive centers in the poison, the percentage of atoms that are catalytically active can be determined. This number can be correlated either with crystal structure of the catalyst, as in the case of zeolites,[4] or with the number of surface atoms.[5] The poison is a titrant and the catalytic reaction is the indicator.

The poison titration method has a number of advantages over the chemisorption method. In the first place, it measures the number of catalytically active centers under dynamic conditions where the time scale for the gas–solid interactions is milliseconds compared to minutes used in chemisorption work. Furthermore, the poison titration method has wide flexibility. A number of poisons can be used for the titration and a number of reactions can be used as indicators. The poison must be strongly adsorbed under reaction conditions and not react either with the carrier gas or the indicator. It is also desirable that the poison be readily removed either by desorption at a higher temperature or by oxidation. Another advantage of the method over chemisorption is that only a small amount of catalyst is necessary, corresponding to 10^{16} active centers. Further, the method is rapid permitting a number of determinations to be made in a day.

The poisoning titration method has been used in the Princeton Laboratories for determining the number of acid centers in zeolites using quinoline as a poison and the cracking of cumene as an indicator.[4] Here the active centers were shown to be Brønsted acid sites associated with the aluminum in the large zeolite cavities. The number of active centers were also determined on monodisperse palladium (range of 55 to 600 Å uniform diameter with standard deviation of 12%) supported on fibrous Baymol alumina for ethylene hydrogenation using carbon monoxide as a poison.[5] It was shown that all the palladium atoms on the surface were active.

With the availability of monodisperse platinum in the particle range of 19 to 60 Å either on alumina or silica, it was of interest to investigate in detail the poison titration method, to determine the number of active centers in various preparations, and to study the relation of a number of active centers determined by the poisoning technique

† Instituto de Catalisis y Petroleoquimica, Madrid, Spain.

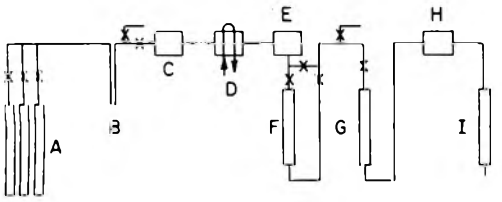

A GAS TANKS
B DRYING TUBE
C,H THERMAL CONDUCTIVITY CELLS
D PULSER FOR OLEFIN
E PORT FOR POISON (LIQUID SAMPLE)
F REACTOR
G CHROMATOGRAPHY COLUMN
I FLOW METER

POISON TITRATION APPARATUS

Figure 1. Poison titration apparatus.

to the number of centers determined by hydrogen chemisorption.

In this work poisoning experiments were carried out using CO, COS, H_2S, SO_2, C_4H_4S, and CS_2, as poisons, and the hydrogenations of ethylene, propylene, 1-butene, cyclohexene, and benzene and the H_2–D_2 exchange as indicators; also the chemisorption of hydrogen and kinetics of ethylene hydrogenation were studied. As catalysts, samples of colloidal platinum on alumina, with different modes of preparations and different particle sizes, were used, and also platinum silica catalysts furnished by Professor Burwell of Northwestern University. Two techniques were employed: a pulse technique for the poisoning and kinetics experiments and a static system for the chemisorption experiments.

Experimental Section

Materials. The following gases and liquids were used: hydrogen (prepurified grade from Matheson Gas Products, East Rutherford, N.J.); deuterium, ethylene, propylene, butene-1, carbon monoxide, hydrogen sulfide, carbonyl sulfide (CP grade from Matheson); helium (grade A from Liquid Carbonic Co.); carbon disulfide (ACS Reagent grade from Fisher Scientific Co., Fairlawn, N.J.); cyclohexene and thiophene (Aldrich Chemical Co., Milwaukee, Wisc.); benzene (Spectral quality, Matheson).

The following catalysts were examined: monodisperse platinum on alumina prepared via colloidal synthesis of monodisperse platinum and adsorption on platelike alumina, 0.45% of 32 Å, 0.47% of 43 Å. We also received through the courtesy of Professor R. W. Burwell of Northwestern University platinum on silica catalysts obtained by impregnation or cation exchange of silica by either chloroplatinic acid or platinum tetramine ion: 0.49% of 19-Å, 1.17% of 32-Å, and 1.48% of 47-Å platinum particles. We also studied a commerical preparation of 0.3% of 20-Å platinum particles on alumina (Lot C-5206 Engelhard Industries, Newark, N.J.).

Methods. Pulse Apparatus. The experimental setup for the pulse technique is shown in Figure 1. The carrier gas, hydrogen (A), was passed through a deoxy hydrogen purification unit (Engelhard Industries, Murray Hill, N.J.), and a trap containing 13X zeolite (B), cooled with liquid nitrogen. (When oxygen was passed, the trap was cooled with dry ice.) The carrier gas was then passed through the reference side of a thermal conductivity cell (Aerograph Wilkens Instruments and Research, Inc.) with tungsten filaments (C), a six-port, heated nut type G.S.V. pulser (Varian Aerograph, Walnut Creek, Calif.), D, for gas samples, an injection unit for liquid samples and poisons (E), and the reactor containing the catalysts under study (F). The reaction products were separated by means of a chromatography column (150 × 0.45 cm) filled with activated silica (G). The stream then passed through the detector side of the conductivity cell (H) and a flow meter (I). The outlet was isolated from the atmosphere with a mineral oil trap. The signal from the Wheatstone bridge, two arms of which consist of the filaments of the thermal conductivity cell was sent to a dc amplifier (Kintel Cohu Electronics, Inc.) and recorded on a recorder (Brown Instrument Co., Minneapolis; Honeywell Regulator Co., Philadelphia, Pa.) with 12-mV range.

The reactor, a Pyrex (or quartz) tube, 20 cm long with an internal diameter of 0.55 cm, was attached to the metallic line through two Kovar seals. The flow rate was controlled by a needle valve (Matheson, Model 4171).

For the H_2–D_2 exchange, a column, 2 m long, of alumina coated with Fe_2O_3, similar to the one described in ref 4, was used. It was operated at liquid nitrogen temperature with helium gas as carrier. The reaction products were passed through a 20 cm long tube of 4 mm diameter, filled with copper oxide, heated to 450 °C. There they were oxidized to H_2O, HDO, and D_2O which were then detected by thermal conductivity in a helium stream.

Poisoning Titration Procedure. A portion of 15–20 mg of catalyst sieved through 100 mesh was weighed and thoroughly mixed with 1–3 g of corundum support or alundum RR, 60 mesh, Norton (Fisher Scientific Co., Fairlawn, N.J.). The mix was homogenized in a Wig-L-Bug vibrator (Crescent Dental Mfg. Co., Chicago, Ill.) for 40 s and put into the reactor. In this way, a small amount of catalyst was dispersed in a 2–5 cm length of reactor, permitting ready access of the catalyst to reactants and poisons.

The various mixtures of poison and carrier gas were prepared in the following way. For CS_2–H_2 a reservoir of 2-L capacity was evacuated for 16 h on a high vacuum system. A small amount of liquid CS_2 was transferred to an appropriate bulb and cooled to liquid nitrogen temperature. The system was again evacuated for 2 h. Pumping continuously, the dewar was removed from the bulb several times for brief periods to permit the oxygen and nitrogen which might have been trapped at the start to be pumped out completely. A portion of CS_2 vapor was admitted to the reservoir by raising the temperature of the solid CS_2 and its pressure measured by a mercury manometer separated from the rest of the system by a small trap filled with crumpled gold foil. The remaining CS_2 was eliminated by removing the bulb and pumping the system for a reasonable period of time (usually an additional 2 h). Then H_2 or He was passed through a trap containing 13X zeolite at liquid nitrogen temperature and admitted to the system in quantity sufficient to raise the total pressure of the mixture to 1 atm. The reservoir was closed and kept protected from sunlight.

The gas mixture ranged from 2.5 to 5% in CS_2, the latter being the composition most widely used in this study. No differences of behavior in poisoning experiments were observed using H_2–CS_2 or He–CS_2. The gaseous poisons (CO, COS, H_2S, SO_2) were introduced into the storage reservoir directly from their containers. A small piece of Pyrex tube was fused to each reservoir. A rubber septum was attached to the tube using silicone grease as sealant. This arrangement held vacuum well for a test period of several days.

Before an experiment was carried out, the catalyst sample was treated first with oxygen at 135–300 °C and

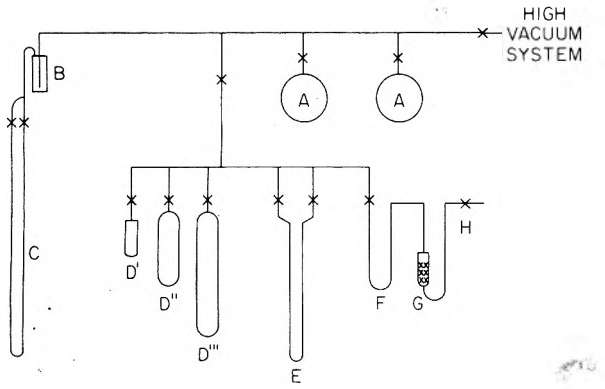

Figure 2. Chemisorption apparatus.

then with hydrogen from 0 to 450 °C, for 0.5 to 4 h each. These oxidation and reduction treatments regenerated completely the catalytic surface. A flow rate of 1 or 0.5 mL/s of hydrogen was maintained during each run. The temperatures of the column were 60, 100, 150, 225, and 225 °C for ethylene, propylene, 1-butene, cyclohexene, and benzene hydrogenation, respectively. The retention times at lower flow rate at these temperatures were 6 and 8 min for ethane–ethylene; 7 and 11 min for propane–propylene, butane–1-butene, and cyclohexane–cyclohexene; and 7 and 14 min for cyclohexane–benzene.

For ethylene, propylene, and 1-butene, the sampling loop used in the pulser had a volume of 304 μL. For cyclohexene and benzene injections of 4 and 1 μL of liquid were used.

After warming the filaments for a few minutes the experiment was started. A pulse of unsaturated hydrocarbon was let into the hydrogen stream to check the initial catalytic activity of the catalyst. The rubber septum for the introduction of poison must be checked periodically for leaks. After that, successive injections of poison and hydrocarbon were made and the percentage conversion measured. When the catalytic surface had been completely deactivated, the desorption of the poison was followed by passing hydrogen through the catalyst at the same flow rate and temperature used in the poisoning experiment and measuring the percentage conversion at certain intervals for several hours. Then the surface was reactivated by oxidation and reduction and the following experiment started.

H_2–D_2 Exchange. Pulses of 2 mL of an equimolecular mixture of hydrogen and deuterium were injected into the helium stream. At a flow rate of 2.3 mL/s, the retention times for H_2O, HDO, and D_2O, of 17, 19, and 21 min, respectively, gave satisfactory separation.

Hydrogenating Activity Measurements. Since in these experiments no poison was used, the sample underwent, between two successive experiments, only the treatment with hydrogen. A 20 mg of catalyst was diluted with 1 g of alundum, and homogenized as described earlier. The conversions measured within the temperature range −50 to 30 °C were all less than 100%. The pulse volume was 304 μL and the flow rates were 4.11 mL/s. Care was taken to ensure that the pulse width of the ethylene did not change in the series of catalysts whose activity was compared.

Chemisorption Apparatus. The chemisorption of hydrogen was determined by the method of Benson and Boudart[3] in an apparatus given in Figure 2. The main manifold line was attached to the static high vacuum system and had two 1-L flasks (A) for gas storage, a trap (B) with gold foil to trap mercury vapors, and a mercury manometer (C). The secondary manifold had three calibrated bulbs (D′, D″, and D‴); an oil manometer (E) with silicone diffusion oil (Dow Corning 704 Fluid of density 1.06), a capillary hairpin trap (F), a catalyst chamber (G), and an exit tube which could be used for flow treatment of catalysts with gases and then sealed off. The oil for the manometer was first heated under vacuum for several hours to remove the soluble gases. The secondary manifold had a dead space volume of 46.7 mL and the catalyst chamber about 4 mL. In most cases 200–1000 mg of supported catalyst was used containing about 0.5% platinum and this adsorbed about 10 μmol of hydrogen. Pressure measurements changes corresponding to 0.5 mm of oil would correspond to about 0.1 μmol of hydrogen. Thus, the error in the chemisorption measurements were of the order of 1%. Usually the samples were pretreated at the same temperature and with the same gases as in the poison titration experiments except that helium treatment in poisoning experiments was replaced by evacuation. The following procedure was followed for determination of the extent of chemisorption. After the catalyst chamber containing about 500 mg of catalyst was sealed to the system, it was evacuated at room temperature for 30 min, the temperature was raised to 150 or 300 °C, and it was treated with 0.5 atm of oxygen for 0.5 h; then it was evacuated for 15 min and then treated with 0.5 atm of hydrogen for 0.5 h and then evacuated for 2 h. The temperature was lowered to room temperature and the dead space determined with helium. This was followed by a 15-min evacuation. The catalyst was then contacted with 0.5 atm of oxygen for 0.5 h, the system was evacuated for 15 min, and hydrogen was introduced to a pressure of 40–100 mm difference on the oil manometer. The change in pressure was most marked during the first 0.5 h and the value chosen was the change in pressure after 0.5 h. This did not vary with the initial pressure in the range of 40–300 mm difference on the oil manometer. The amount chemisorbed was calculated from the pressure change and the dead volume of the system as determined with helium. The percent surface dispersion was calculated from this data according to the stoichiometry proposed by Benson and Boudart and the chemical analysis of the platinum content.

$$Pt\text{-}O + {}^3/_2H_2 = Pt\text{-}H + H_2O$$

Chemical Platinum Analysis. The determination of the percent dispersion of the platinum not only involves the determination of the number of centers inactivated by the poison but also the amount of platinum in the catalyst. The following procedure due to Ayres and Meyer[6] was adapted for this purpose. It is designed to measure by optical absorbance the complex between stannous chloride and platinic chloride in the platinum concentration range 2–20 ppm. For a catalyst of 0.5 wt % platinum a sample of about 40 mg is weighed out, placed in a 250-mL beaker, treated with 20 mL of aqua regia (freshly prepared from concentrated acids), lightly covered with a watch glass, and heated with an electric mantle until the volume of the liquid is reduced to about 3 mL. It is then treated with 20 mL of 6 M HCl and again evaporated to about 3 mL. This digestion with HCl is repeated. Care must be exercised that during this digestion process the material is *not* evaporated to dryness. Finally, a 20 mL of 6 M HCl is used to transfer the suspension quantitatively into a centrifuge tube. It is then centrifuged for about 12 min at 10000 rpm. The solution is then decanted from the solids and these are further washed with 6 M HCl. The main bulk of the solution and the washings are then evaporated to about 3 mL, again treated with 30 mL of 6 M HCl, evaporated to 10 mL, and transferred to a 25-mL

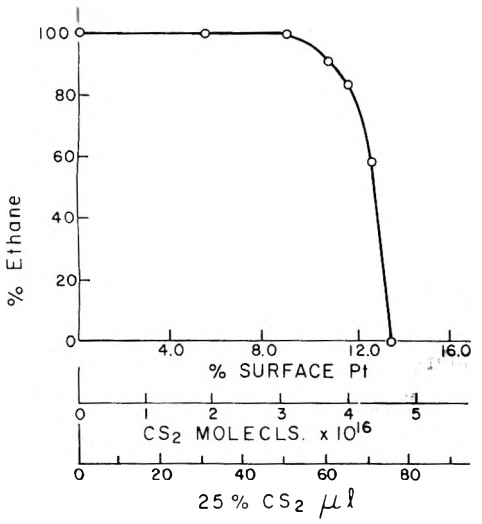

Figure 3. Typical poison titration curve.

DATE	SURFACE Pt / TOTAL Pt	DATE	SURFACE Pt / TOTAL Pt
12/9/74	13.6 %	1/6/75	13.4 %
12/11	12.6	1/7	12.6
12/26	14.4	1/7	14.4
12/29	13.0	1/8	14.6
1/4/75	14.0	1/9	12.6
1/6	14.4	1/9	13.4

AVERAGE 13.6 ± 1.0 %

$\frac{\text{MAX-MIN}}{\text{AVERAGE}}$ = 15.0 %

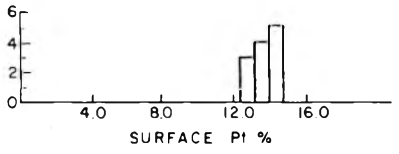

(REPRODUCIBILITY CHECK FOR 1.84 % Pt on Alumina)

Figure 4. Reproducibility check on titration.

volumetric flask containing 2 mL of 12 M HCl and 5 mL of stannous chloride reagent (prepared by dissolving 2.3 g of $SnCl_2 \cdot 2H_2O$ in 50 mL of distilled water and 30 mL of 12 M HCl and diluting this solution to 100 mL; it is stored in a stoppered flask and is layered with xylene to prevent oxidation). 6 M HCl is used to make the transfer quantitative and to dilute the solution to 25.0 mL. After mixing thoroughly, the color develops and the optical transmittance is determined at 403 nm. The platinum content is determined by using a calibration curve prepared with standard platinum solution.

Results

After preliminary work with a variety of poisons, a variety of reactants, and using different temperatures, the following conditions were taken as standard: carbon disulfide as the titrant poison, ethylene hydrogenation as the indicator reaction, hydrogen as the carrier gas. The catalyst was cleaned of both poison and other contaminants by an oxygen stream at 135 °C for 1 h and then reduced with hydrogen at the same temperature. The catalyst was cooled in hydrogen to 0 °C. A typical titration curve is given in Figure 3. It should be noted that the first titer with carbon disulfide is usually slightly higher than the

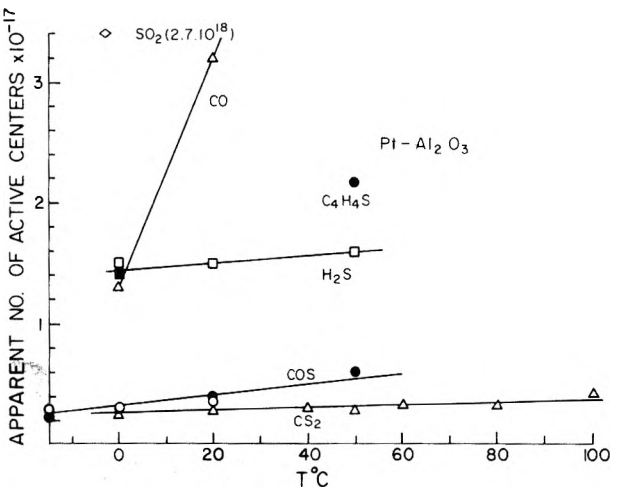

Figure 5. Titration results using different poisons at different temperatures.

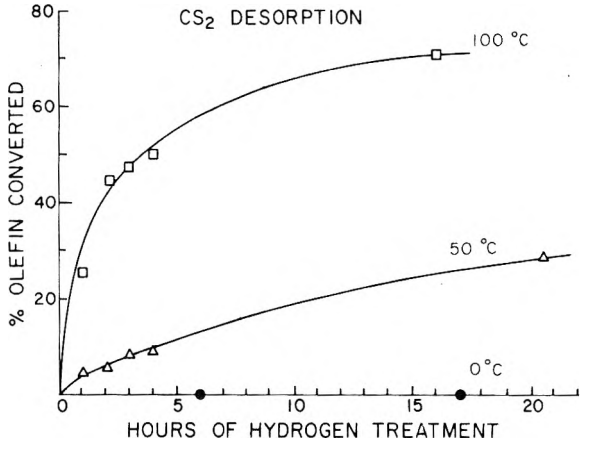

Figure 6. Recovery of catalyst after poisoning.

succeeding one for Pt on Baymal support. The reproducibility of the poison titer is given in Figure 4 and is seen to be 7%. Another sample of a 32-Å platinum (0.5 wt %) on Baymol alumina was used for 11 months without any change in the number of active centers.

The temperature of the titration with carbon disulfide has little influence on the number of active centers, in the range 0–100 °C, as is shown in Figure 5.

The titration technique can be reversed to study the removal of the poison either by desorption or reaction by passing a hydrogen stream over the catalyst at various temperatures for different periods of time and periodically testing the status of the catalyst by introducing a pulse of ethylene to determine the extent of recovery of the activity by the catalyst. It is seen from Figure 6 that there is no activity of the catalyst after passing hydrogen over the poisoned catalyst for 17 h at 0 °C. At 50 °C about 30% of the activity of a poisoned catalyst was recovered after a 24-h hydrogen treatment, while the recovery was 75% after a 17-h hydrogen treatment at 100 °C. The removal of carbon disulfide may be due to desorption or reaction with hydrogen. If we use the activity values at 5 h, we calculate an activation energy for the reactivation process (11% at 50 °C and 55% at 100 °C) of 7.7 kcal/mol. The reactivation curve at 100 °C shows that the poison is not removed completely after 16 h, despite the fact that the platinum particles are monodisperse.

The number of centers (of platinum on alumina) involved in hydrogenation in the temperature range 0–100 °C is to a first approximation the same for the following compounds: ethylene, propylene, butene-1, cyclohexene,

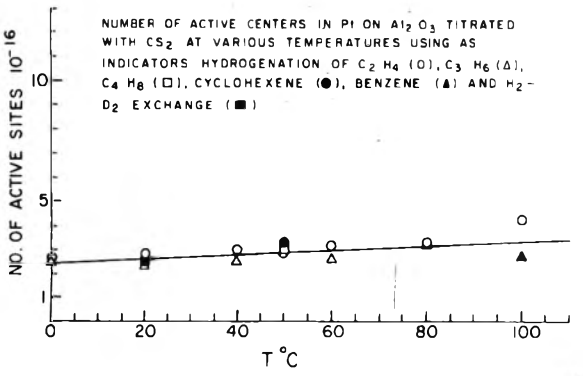

Figure 7. Number of surface atoms poisoned for different reactions.

benzene, and deuterium. Between 0 and 80 °C the number of centers in a given sample of standard 32-Å platinum on Baymol catalysts was in the range of 2.6 to 3.3 × 10^{16} centers. There appears to be a small difference at 100 °C between the number of centers for benzene (2.6 × 10^{16}) and ethylene 4.0 × 10^{16} (Figure 7). This difference is real as the following experiment shows (Figure 8): carbon disulfide was used as a poison for the hydrogenation of benzene on platinum on alumina at 100 °C and the number of centers corresponds to 68 μL of 5% carbon disulfide. The system was cooled to 0 °C and the catalyst was found to have activity for the hydrogenation of ethylene. It took an additional 12 μL of 5% carbon disulfide to poison the centers active for the hydrogenation of ethylene. This would indicate that with carbon disulfide as titrant, the number of active centers for benzene is 85% of those active for the ethylene hydrogenation.

Hydrogen sulfide (25% H_2S in H_2) was also used as a poison on Pt on silica catalyst B67 to determine whether the same number of centers was involved in catalytic hydrogenation of benzene as of ethylene. Using ethylene hydrogenation as an indicator the titre for the number of active centers at 0 °C was 70 μL. The catalyst was then oxidized and reduced at 300 °C. The titration with H_2S at 0 °C was repeated using ethylene as an indicator. The value was 40 μL and the difference (70–40 mL) represents the H_2S fixed by the sodium ions on the silica. The third titration was the hydrogenation of benzene at 100 °C; the titre was 20 μL. The catalyst was again oxidized and reduced at 300 °C and the titre with ethylene as an indicator dropped to 30 μL. The oxidation and reduction was again carried out at 300 °C. The titre with benzene as indicator at 100 °C was again 20 μL. At this stage no oxidation reduction was carried out. The temperature was lowered to 0 °C and the catalyst showed activity for ethylene hydrogenation. An additional titre of 10 μL was necessary to poison the centers which were active for the hydrogenation of ethylene, but not active for benzene hydrogenation. The results obtained with H_2S and CS_2 as the titrant and ethylene and benzene as indicators are mutually consistent if one assumes that carbon disulfide poisons two centers while H_2S poisons only one. Thus with carbon disulfide we obtain for benzene hydrogenation (5% × 2)(60 μL) as 6.7 equiv while with H_2S we obtain (25%)(22) or 5.5 equiv. For ethylene hydrogenation the values are (5% × 2)(80) or 8 equiv and (25%)(32) or 8.0 equiv. The ratio of centers involved in benzene hydrogenation to ethylene hydrogenation are 0.84 and 0.69 for H_2S and CS_2 and are considered the same. These results indicate a contribution of the geometrical factor in the hydrogenation of benzene and can be taken as support for the ideas of Balandin.

It is also of interest to note that the number of centers necessary for the hydrogen deuterium reactions is the same

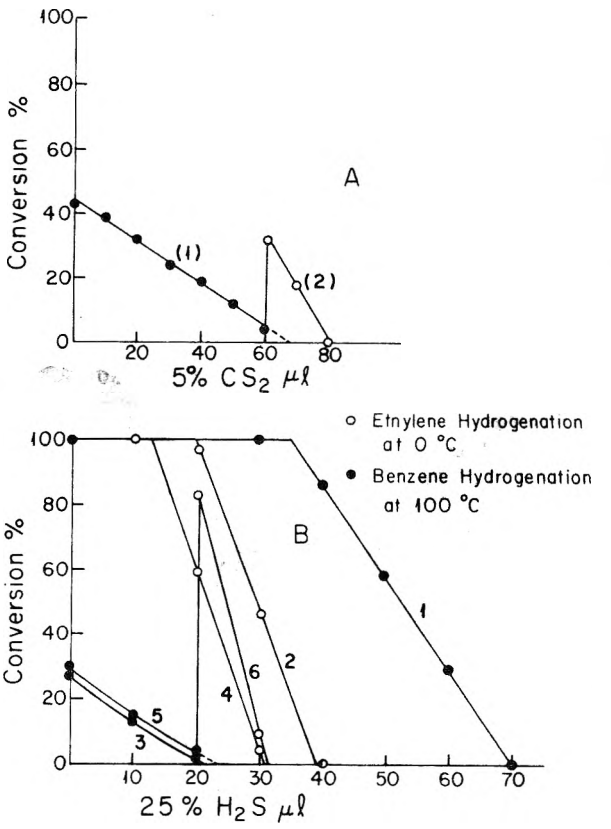

Figure 8. Comparison of a number of active centers for hydrogenation of ethylene and benzene.

as for olefin hydrogenation. This suggests that the activation of hydrogen is the critical step in the hydrogenation reaction.

We have previously reported that the number of sites as determined by carbon disulfide poisoning is a fraction of that determined by hydrogen chemisorption. Now we have extended these investigations to cover a large number of catalysts which had been subjected to different temperature treatment (Table I). It is seen that the results fall into two groups: those (9) in which two surface sites are poisoned by one carbon disulfide molecule and another group (5) in which four to eight sites are poisoned by one carbon disulfide molecule. This ratio does not depend on particle size in the range of particle diameters from 19 to 66 Å. The value of two can be explained on the assumption that one carbon disulfide molecule poisons by adsorption two surface atoms being attached horizontally to the surface. Values lower than two would indicate that the carbon disulfide is attached to one platinum atom and is perpendicular to the surface. Values higher than two would indicate that the carbon disulfide extends it influence over an area of platinum atoms or that some sites determined by chemisorption are inherently catalytically inactive. It was therefore decided to study in detail the effect of temperature and gas treatment on the two components that determine this ratio: the Boudart–Benson hydrogen chemisorption and the carbon disulfide titration. The platinum catalyst was always oxidized at 300 °C prior to reduction at different temperatures. The hydrogen chemisorption (Figure 9) and the carbon disulfide titration (Figure 10) were carried out at 0 °C. The Engelhardt commerical Pt on alumina catalyst gave a constant value both for chemisorption and titre on heat treatment of the catalyst from 0 to 450 °C. The Pt on platelike Baymol alumina catalyst showed a decrease from 27 to 16% dispersion by chemisorption on heating in a hydrogen atmosphere at 450 °C for 0.5 h and to 3% dispersion on

TABLE I

Catalyst	Treatment at °C			Dispersion, %		No. of centers poisoned by a CS_2	Activity at 0 °C		
	O_2	H_2	He or vacuum	H_2	CS_2		Convn/ mg of Pt	10^{17} (convn)/ center (H_2)	10^{17} (convn)/ center (C_1S_2)
B67	150	150	150	53	62	1.7	12.6	0.78	0.7
	300	300	450	62	18	7.2	4.1	0.21	0.8
19 Å	300	0		50	68	1.5	16.5	1.04	0.8
B66	150	150	150	(36)	36	2.0	6.0	(0.55)	0.6
32 Å	300	300	450	36	8	10.3	1.8	0.16	0.8
B70	150	150	150	(24)	18	2.7	3.2	0.44	0.6
47 Å	300	300	450	24	6	8.3	1.4	0.13	0.8
E[a]	150	150	150	58	28	4.1	4.9	0.27	0.6
20 Å	300	300	450	58	28	4.1	6.7	0.38	0.8
N4	150	150	150	30	26	2.4	3.9	0.42	0.5
33 Å	300	300	450	8	10	1.8	2.0	0.82	0.8
M4[a]	300	0		27	26	2.1	7.6	0.91	1.0
43 Å	300	150		27	22	2.4	5.8	0.68	0.8
	300	300		25	24	2.0	5.0	0.67	0.7
	300	150		17	18	1.9	5.3	0.99	1.0
	300	150		26	24	2.1	6.1	0.77	0.8

[a] Diameter calculated by chemisorption. Parentheses indicates value obtained from subsequent run.

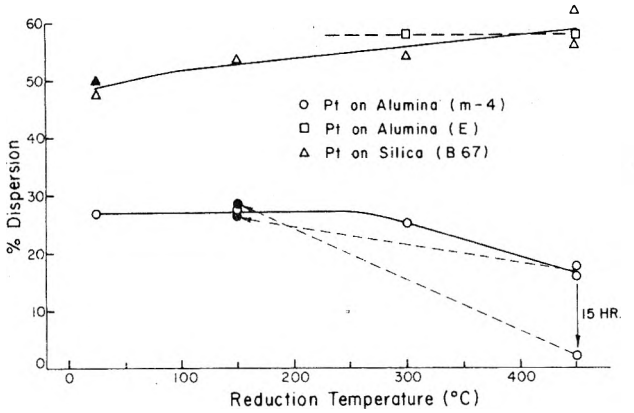

Figure 9. Variation of dispersion from hydrogen chemisorption (by the Benson–Boudart method with heat treatment).

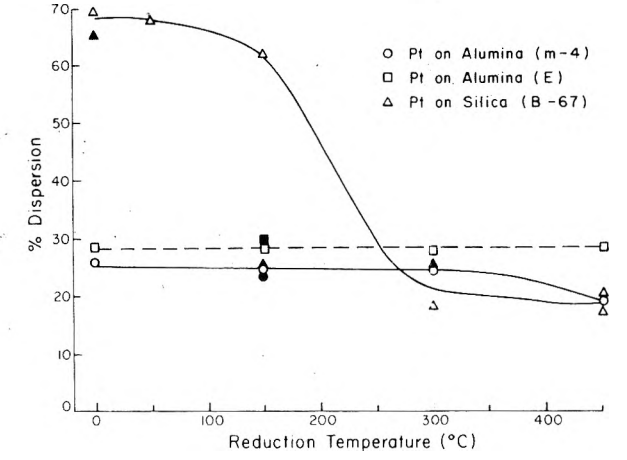

Figure 10. Variations of dispersion from poison titre with heat treatment.

heating for 15 h (open circles). However the catalyst recovered its original value of 26% dispersion by chemisorption on reoxidation at 300 °C and reduction at 150 °C (filled circles). The CS_2 titre also followed the chemisorption values closely. The ease of restoring the original values for chemisorption and catalytic activity by oxidation at 300 °C in 0.5 h and the fact that the platinum particles are isolated from each other (only a single 32-Å particle is located on an alumina plate of 200 by 1000 Å) eliminates sintering of platinum to form larger particles with a smaller dispersion value. We ascribe the loss of dispersion as determined by chemisorption and the loss of a number of catalytic centers due to decomposition of platinum particles (clusters) into an "atomic" form of platinum incorporated into the alumina support. The "atomically" dispersed platinum has lost its ability both to chemisorb hydrogen or catalyze the hydrogenation of ethylene. This phenomenon has also been observed recently in this laboratory with 25-Å diameter particles prepared on platelike alumina by impregnation of the latter with chloroplatinic acid and heating. It has also been observed with platinum in NaY zeolite catalyst. This process does not involve chlorine impurity because it occurs with the platinum colloid supported on platelike Baymol alumina which had no obvious source of chlorine. It is not due to carbon deposition since it occurs after 0.5-h treatment either in a static atmosphere of hydrogen or under evacuation and since it occurs in the "supercages" of the NaY zeolite. It must depend on "acceptor sites" in the alumina which are present in the platelike Baymol alumina and the zeolites where it was shown by the Lyon group[7] to be associated with sodalite cages. We will report on this phenomena in more detail in a subsequent publication.

The behavior of platinum on silica (B67) was similar. The titre using carbon disulfide as poison showed a rather small drop in the number of active centers on reduction, 69% at 0 °C, 67% at 50 °C, 62% at 150 °C, and then a dramatic drop to 18% at 300 °C reduction and 20 and 18% at 450 °C (open triangles in Figure 11). On reoxidation at 300 °C and subsequent reduction at 300 and 150 °C there was only a slight increase in the number of active clusters as determined by the titration. However reduction at 0 °C recovered the active center value of 66% of all the platinum. The chemisorption of hydrogen showed a slight increase from the value of 48% dispersion obtained initially to 57–62% on reduction at 450 °C. Again the process is reversible for a reoxidation at 300 °C for 0.5 h and reduction at 0 °C the dispersion value as determined by hydrogen chemisorption dropped to 50%. This must be an example of a more subtle type of platinum particle decomposition with loss in ability to catalyze hydrogenation of ethylene but retention of its ability to chemisorb hydrogen. We suggest the following mechanism. At temperatures of above 300 °C the platinum particles on silica are unstable. They decompose into "molecular forms" involving platinum diads. These have an ability

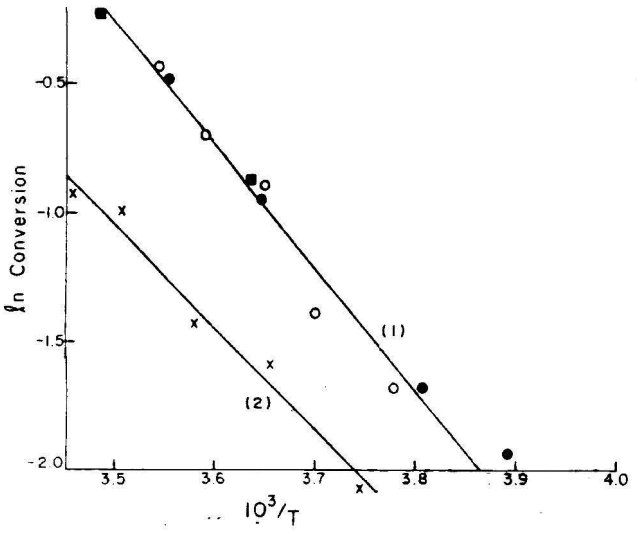

Figure 11. Arrhenius plot of ln conversion of 35-Å Pt on alumina (0.45%): (curve 1) oxidized at 150 °C and reduced at 150 °C, activation energy 9.4 kcal/mol; (curve 2) oxidized at 300 °C, reduced at 300 °C, and heat treatment at 450 °C, activation energy 7.8 kcal/mol. Different symbols represent different runs.

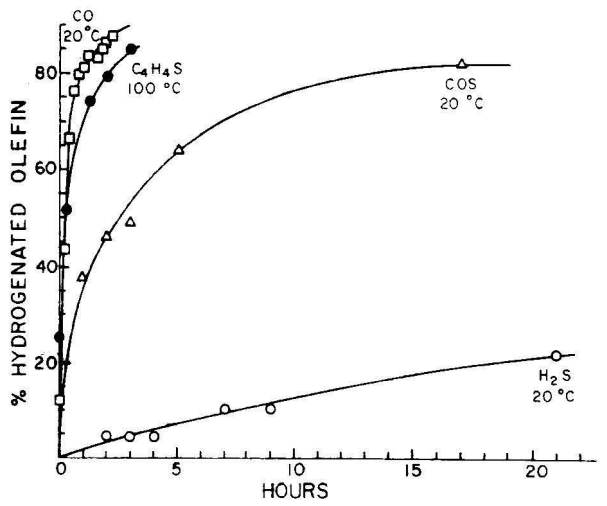

Figure 12. Desorption of various poisons.

to chemisorb hydrogen but lack the ability to chemisorb ethylene at the same time. This would require at least four atom clusters of platinum atoms. Thus the critical size of a cluster for ethylene hydrogenation is less than 216 (6^3 atoms, 16-Å diameter particle) and greater than 2. Work is in progress on synthesis of clusters of platinum atoms to determine the minimum size for catalytic activity. Our results to date indicate that neither "atomically" dispersed nor "molecular diads" of platinum atoms supported on alumina and silica have catalytic activity to hydrogenate ethylene.

The instability of small platinum particles seems to be a function both of size and support. Certainly the smallest platinum particles with a greatest "surface tension" will decompose most readily. This may account for the widely observed catalytic phenomenon that catalysts of highest activity (greatest dispersion) lose this activity most readily. The role of alloys may be to stabilize these small particles (clusters). Furthermore the "atomization" or "molecularization" of the platinum particle may be the mechanism for the transport of platinum from the smallest particles to the largest platinum particles leading to permanent loss in activity. This process of small particle decomposition is also a function of the support. The Engelhardt alumina does not seem to have "acceptor sites" for this "atomic" or "molecular" platinum. They are present in platelike Baymol alumina and the NaY zeolite. In the latter they are identified with sodalite cages. There may be similar acceptor structures in certain aluminas associated with silica impurities. Attempts will be made to observe these "atomically" and "molecularly" dispersed platinum with ultra high resolution electron microscopy.

Catalytic activity per site for ethylene by hydrogenation was determined at a convenient temperature (as low as −30 °C) using pulse technique and Arrhenius plot to obtain "percent conversion" at 0 °C. Pulses of the same size, catalyst bed of the same length, and hydrogen flow rate of the same velocity were used in these experiments. Care was taken to ensure that the pulse width of ethylene was small to ensure the same contact time of the ethylene with the catalyst. The results were reproducible as representative data (Figure 12) show. The turnover numbers calculated as "percent conversion" per milligram of platinum have no absolute value but are useful in comparing catalysts. The activity per catalytically active center was obtained by dividing this number by the number of centers as determined by carbon disulfide poisoning. The results for a large variety of catalysts are given in Table I. It is clearly seen that the values of the turnover number based on carbon disulfide titre of the number of active centers varies from 0.5 to 1.0 by a factor of 2. It is independent of particle size in the range of particles from 19 to 50 Å diameter. From the previous discussion it becomes zero for atomically dispersed and molecular diads. Thus at some diameter between 19 and 2.76 Å (atomic diameter) or between a cluster of 216 and 2 atoms the catalytic activity for ethylene hydrogenation becomes zero.

If one calculates the turnover number on the basis of the number of centers as determined by hydrogen chemisorption the variation is much larger from 0.19 to 1.04. The reason for this, as evident from our previous discussion, is that some centers which chemisorb hydrogen (namely, molecular diads) are not catalytically active for hydrogenation of ethylene.

On the basis of these results we suggest that the carbon disulfide titration gives a better measure of the number of catalytically active sites and reactivity (turnover number) per site since the titration deals with the reaction itself rather than the interaction of hydrogen with catalyst (chemisorption) or with platinum oxide.

Carbon Monoxide as Titrant. Carbon monoxide was used effectively in titrating the active centers of palladium catalysts for ethylene hydrogenation (5). However, it is unsatisfactory for platinum catalysts. The titre based on CO varies markedly with temperature (Figure 5). If the temperature dependence line of the titre is extrapolated to low temperature it crosses the COS and the CS_2 lines at −18 °C. Recent experiments in the Princeton laboratories have shown that the chemisorption of carbon monoxide (obtained in a static system) gives the same dispersion values for platinum of varying size as hydrogen chemisorption. The rapid recovery of the platinum catalyst poisoned by carbon monoxide would indicate that either the carbon monoxide is displaced from the catalyst by hydrogen or that it reacts with hydrogen. This latter point is under investigation.

Hydrogen Sulfide as Titrant. Hydrogen sulfide as a poison was also investigated. The titration value for platinum on alumina was 1.5×10^{17} centers twice that obtained with carbon disulfide. This high value could not be ascribed to weak adsorption of hydrogen sulfide which would lead to a desorption of the poison during the course of titration since the desorption of hydrogen disulfide measured directly was slow (Figure 14). This high value

must be associated with the adsorption of the acidic hydrogen sulfide on the alkali centers present on the alumina. It is interesting to note that these centers adsorb the hydrogen sulfide before the platinum centers are poisoned. Furthermore, on oxidation of the poisoned platinum centers all the sulfide present on the catalyst, that on the platinum and that on the alumina, is removed. Thus, there may be a "spill-over" of the oxygen from the platinum to the alumina support. On platinum on silica the poisoning behavior of hydrogen sulfide is different. The number of platinum surface atoms poisoned by one hydrogen sulfide molecule is just over 1.25 for a 50-Å particle and drops to less than 1 for particles of 19 Å. Thus, in contrast to carbon disulfide, one hydrogen sulfide molecule poisons one surface platinum atom. Furthermore, the number of active centers for hydrogenation of benzene is as determined by H_2S titrant at most two-thirds of those required for the hydrogenation of ethylene (Figure 8).

Carbonyl Sulfide as Titrant. The behavior of carbonyl sulfide on platinum on alumina is similar to that of carbon disulfide. At 50 °C it gives twice the value obtained with carbon disulfide. This may be due to adsorption on one platinum atom by one carbonyl sulfide molecule.

Thiophene as Titrant. Thiophene is not a very effective poison for platinum on alumina and is readily desorbed from the surface.

Sulfur Dioxide as Titrant. Sulfur dioxide on platinum on alumina gives high values for the number of active centers for the hydrogenation of ethylene, about 100 times greater than that obtained for hydrogen sulfide. If we assume that the basic sites associated with the retention of hydrogen sulfide are due to the small amount of sodium introduced in the preparation of the platinum particles and alumina support, very large number associated with the adsorption of sulfur dioxide must be due to certain alumina sulfite complexes. It is of interest to note that the oxidation at 150 °C with oxygen to regenerate the activity removes not only the sulfur dioxide from the platinum but also from the aluminum sites, again illustrating the "spill-over" of the oxygen from the platinum to the alumina support. Thus, the poison titration technique permits a study of the interaction of the active metal on the surface with the support and also for dual catalysts. For instance, it would be of interest to determine at what temperature the "spill-over" of active oxygen ceases.

Acknowledgment. We thank Professor Robert Burwell of Northwestern University for the samples of platinum on silica and for prepublication copy of the paper "Pt/SiO_2 Part 1. Percentage Exposed and Its Effect Upon Reactivity of Adsorbed Oxygen" (T. Ochijima, J. M. Hermann, Y. Inoue, R. L. Burwell, J. B. Butt, and J. B. Cohen, *J. Catal.*, submitted for publication). The sample designations in the above paper are: 63.5-SiO_2-ion X is B67; 40-SiO_2-PtCl-S is B66 and 27-SiO_2-ion X is B70. This work was supported by the U.S. Energy Research and Development Agency.

References and Notes

(1) S. Brunauer, P. H. Emmett, and E. Teller, *J. Am. Chem.* Soc., **60**, 309 (1936).
(2) J. E. Benson and M. Boudart, *J. Catal.*, **14**, 704 (1965); G. K. Boreskov and A. P. Kurnakov, *Zh. Fiz. Khim.*, **26**, 1814 (1952); D. E. Mears and R. C. Hansford, *J. Catal.*, **9**, 125 (1967); G. R. Wilson and W. K. Hall, *Ibid.*, **17**, 190 (1970); Y. Barbaux, B. Roger, J. P. Beaufils, and J. E. Germain, *J. Chim. Phys.*, **67**, 1035 (1970); J. M. Basset, A. Theoller, M. Primet, and M. Prettre, *Catal., Proc. Int. Congr., 5th, 1972*, **2**, 1915 (1973); M. A. Vannice, J. E. Benson, and M. Boudart, *J. Catal.*, **16**, 348 (1970); S. W. Weller and A. A. Montagna, *Ibid.*, 394 (1971); A. Renouprez, C. Hoang-Van, and P. A. Compagnon, *Ibid.*, **34**, 411 (1974).
(3) K. Aika, L. L. Ban, I. Okura, S. Namba, and J. Turkevich, *J. Res. Inst. Catal., Hokkaido Univ.*, **24**, 54 (1976).
(4) J. Turkevich, A. Ichikawa, and T. Ikawa, Abstracts of paper presented at the National Meeting of the American Chemical Society, Chicago, Ill., Sept, 1961; J. Turkevich, F. Nozaki, and D. Stamires, *Proc. Int. Congr. Catal., 3rd, 1964*, **1**, 586 (1965); J. Turkevich, S. Murakami, F. Nozaki, and S. Ciborowski, *Chem. Eng. Prog.*, **63**, 75 (1967); J. Turkevich and S. Ciborowski, *J. Phys. Chem.*, **71**, 3208 (1967); Y. Murakami, *Kogyo Kagaku Zassky*, **71**, 779 (1965); M. P. Rosynek and J. W. Hightower, *Catal., Proc. Int. Congr., 5th, 1972*, (1973).
(5) J. Turkevich and G. Kim, *Science*, **169**, 873 (1970); E. B. Maxted, *Adv. Catal.*, **3**, 129 (1951); A. M. Rubenstein, *Probl. Kinet. Katal., Heterogen. Katal.*, **127**, (1949); Yu. V. Filippov and V. P. Lebedev, *Zh. Fiz. Khim.*, **40**, 1846 (1966); B. V. Romanovski, *Kinet. Katal.*, **8**, 927 (1963).
(6) G. H. Ayres and A. S. Meyer, *Anal. Chem.*, **23**, 299 (1951).
(7) P. Gallezot, A. Alarcon-Diaz, J-A. Dalmon, A. J. Renouprez, and B. Imelik, *J. Catal.*, **39**, 334 (1975); P. Gallezot, J. Datka, J. Massardies, M. Primet, and B. Imelik, "The Sixth International Congress on Catalysis", London, 1976, paper A11.

Preferential Oxidation Characteristics in the Oxidation of Cobalt–Nickel Alloys in Nitric Oxide and in Oxygen

Yoshio Takasu, Hideo Kanagawa, and Yoshiharu Matsuda*

Department of Industrial Chemistry, Faculty of Engineering, Yamaguchi University, Tokiwadai, Ube, Yamaguchi, Japan 755 *(Received November 22, 1976)*

Publication costs assisted by Yamaguchi University

Preferential oxidation characteristics in the oxidation of Co–Ni alloy (80, 60, 40, and 20% Co) in nitric oxide or in oxygen were examined by microgravimetry, x-ray diffractometry, ion microanalysis (IMA), and x-ray photoelectron spectroscopy (XPS). In the case of the oxidation of Co–Ni alloys in NO, the rates of the Ni-rich alloys were extremely rapid obeying a linear rate law, while that of the Co-rich alloys were very slow obeying a parabolic rate law. The oxide layers were composed of (CoO·NiO), or CoO, or a mixed oxide of them. The apparent activation energy of the oxidation in 10 Torr of NO around 700 °C was 17–21 kcal/mol for Ni-rich alloys and 32–33 kcal/mol for Co-rich alloys. In the oxidation of the alloys in O_2, all specimens were oxidized obeying a parabolic rate law. Moreover, the scales were composed of CoO and Co_2O_3, (CoO·NiO) and Co_2O_3, or (CoO·NiO) and Co_3O_4. The reason for the different behaviors of the oxidation between NO and O_2 is discussed.

Introduction

Although many studies have been made on the high temperature oxidation of metals and alloys in oxygen (O_2) or in air, few investigations have been made on reactions in nitric oxide (NO).[1-3] The corrosive characteristics of nitric oxide are much different from that of oxygen. For example, the oxidation of nickel has been found to obey a faster linear rate law in NO (700 °C, 10 Torr) than that in O_2. Moreover, in the case of a Cu–Ni alloy (65% Ni), nickel oxide was preferentially formed in the surface oxide layer in NO, while copper oxide was preferentially formed in the oxidation of the alloy in oxygen.[4]

In this study, the preferential oxidation characteristics in the oxidation of Co–Ni alloys were examined by use of microgravimetry and various surface analyzing techniques, such as x-ray diffractometry, ion microanalysis (IMA), and x-ray photoelectron spectroscopy (XPS). These examinations were carried out in order to compare the oxidation behavior of the alloys in O_2 and in NO.

Experimental Section

Samples. Pure Co (99.8%), pure Ni (99.9%), and four Co–Ni alloys, 80, 60, 40, and 20% Co (weight percent), were used in this study. The alloys were cast from Co and Ni, hot rolled, scalped, cold rolled to a thickness of 0.05–0.02 cm, and annealed. The apparent surface area of each test specimens was about 1 cm^2. It was abraded with emery paper, annealed at 850 °C, electropolished in a mixed acid (H_2SO_4:H_3PO_4:H_2O = 170:540:308 in volume), and then rinsed in water and acetone. Nitric oxide (NO) of a high purity in a glass cylinder, from the Takachiho Co., was used without further purification. The oxygen and argon were purified through bulb-to-bulb distillation with liquid nitrogen coolant. For pretreatment of the sample hydrogen was used as received.

Oxidation Measurements. The oxidation process was followed by a Gulbransen-type microbalance set in a conventional vacuum apparatus which was capable of being evacuated to $\sim 10^{-5}$ Torr. Before the oxidation measurements were made, test specimens were reduced with 20 Torr of hydrogen at 850 °C for 2 h. Argon was used to determine the zero-point of the microbalance.

Observation of the Surface Oxide Layers. The following conditions were adopted for analyzing the surface oxide layers formed on the metals and alloys: (a) x-ray diffractometry, Cu Kα, 0.9 kW; (b) ion microanalysis (IMA), Hitachi IMA-S, Ar^+: 7 kV for Co^+ and Ni^+, 13 kV for O^-, sample current 0.6 $\mu A/0.8$ mm^2; (c) x-ray photoelectron spectroscopy, Du Pont ESCA-650 analyzer, Mg Kα.

Results and Discussion

The oxidation of the Co, Ni, and the four Co–Ni alloys was examined in 10 Torr of O_2 at 700 °C. As shown in Figure 1, all the oxidation curves obeyed a parabolic-like law. Within 15 min from the start of oxidation, these oxidation curves strictly obeyed a parabolic rate law. However, most of them deviated from the law in the later stages, as shown in Figure 2. The rate of oxidation increased with increasing cobalt content. Similar results were also obtained by several investigators.[5] Subsequently, the oxidation behavior was examined in 10 Torr of NO at 700 °C. These results were shown in Figure 3. The oxidation rates of pure Ni and 20% Co and 40% Co alloys were very rapid and obeyed a linear rate law, whereas the oxidation rates of pure Co and Co-rich alloys were very slow, and obeyed a parabolic rate law. It is noteworthy that the relation between the alloy composition and the order of the rate of oxidation in NO was completely contrary to that obtained in O_2. The reason the oxidation rate of the Co-rich alloy in O_2 was much higher than that of Ni-rich alloy could be explained by the fact that the rate of cobalt ions through the oxide layer was much faster than that of nickel.[6,7] The extremely high oxidation rate for the oxidation of Ni-rich alloy by NO must be due to the high reactivity of nickel with NO. The authors have reported in another paper[8] that the main characteristics of the state of the scale formed on nickel in NO could be summarized as follows: (1) a remarkable oxidation along grain boundaries, this was the cause of the change of the specimen to the coarse, bulky, and brittle state; (2) the formation of a large number of lattice defects; and (3) an unequal oxidation behavior among various crystal planes.

In this study, the surfaces of the nickel and Ni-rich alloys, 20 and 40% Co, oxidized in NO were also very coarse, while the surfaces of the other specimens, as well as the specimen oxidized in O_2, were very smooth. Therefore, the oxidation mechanism of the Ni-rich alloy in NO could be similar to that of pure nickel. This

TABLE I: Rate Parameters in Oxidation of Co-Ni Alloys[a]

	O_2		NO	
% Co	Rate constant	Activation energy,[b] kcal/mol	Rate constant	Activation energy, kcal/mol
100	$K_p = 5.1 \times 10^3$	29	$K_p = 0.08 \times 10^3$	43
80	$K_p = 3.9 \times 10^3$	42	$K_p = 0.39 \times 10^3$	32
60	$K_p = 2.3 \times 10^3$	47	$K_p = 0.17 \times 10^3$	33
40	$K_p = 1.3 \times 10^3$	48	$K_l = 30$	17
20	$K_p = 0.53 \times 10^3$	48	$K_l = 53$	21
0	$K_p = 0.37 \times 10^3$	51	$K_l = 122$	18

[a] $P_{O_2,NO}$ = 10 Torr, 700 °C. K_p or K_l shows the rate constant of parabolic or linear law, respectively (K_p, $\mu g^2/cm^4$ min and K_l, $\mu g/cm^2$ min). The values in the parentheses were obtained by Frederic and co-workers.[5] [b] Reference 5.

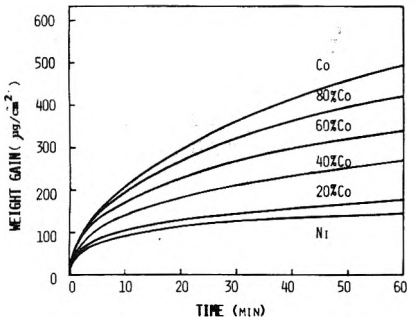

Figure 1. Oxidation curves of Co-Ni alloys in O_2, P_{O_2} = 10 Torr, 700 °C.

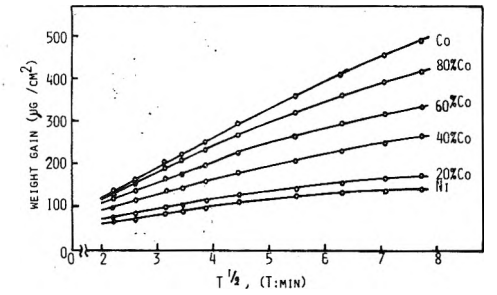

Figure 2. Parabolic plots of the oxidation curves of Co-Ni alloys in O_2.

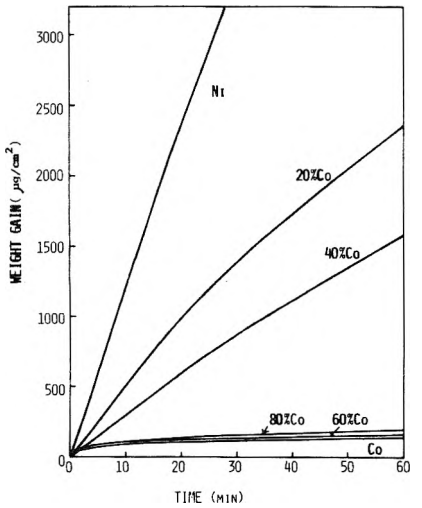

Figure 3. Oxidation curves of Co-Ni alloys in NO, P_{NO} = 10 Torr, 700 °C.

speculation is supported by the values of the activation energy of the oxidation shown below. Table I represents rate parameters of the oxidation of Co-Ni alloys in NO and in O_2. Columns 2 and 4 list the oxidation rate constants which were calculated from the early stages of the oxidation. Columns 3 and 5 list the apparent activation

TABLE II: Chemical Species in the Scales[a]

% Co	NO	O_2
100	CoO	CoO
80	CoO	CoO, Co_2O_3
60	CoO, (CoO·NiO)	(CoO·NiO), Co_2O_3
40	(CoO·NiO)	(CoO·NiO), Co_2O_3
20	(CoO·NiO)	(CoO·NiO), Co_3O_4
0	NiO	NiO

[a] P_{NO,O_2} = 10 Torr, 700 °C, 1 h.

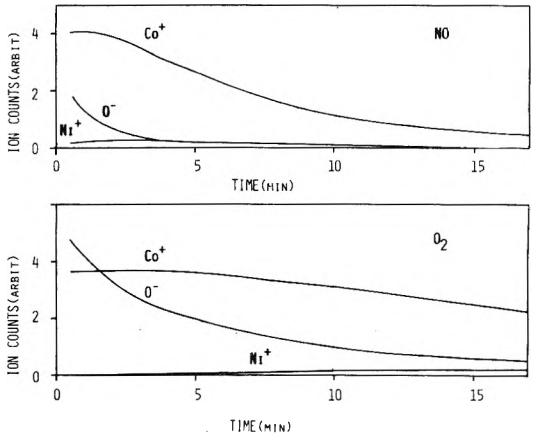

Figure 4. IMA spectra of scales formed on Co-Ni alloys (80% Co): (a) P_{NO} = 10 Torr, 700 °C, 5 min; (b) P_{O_2} = 10 Torr, 700 °C, 5 min.

energy of the oxidation, with the values in parentheses obtained in O_2 by Frederic and Cornet.[5] The apparent activation energies of the Ni-rich alloys in NO, which obeyed the linear rate law, were very small, i.e., 17–21 kcal/mol. The apparent activation energies of the Co-rich alloys were very large, i.e., 32–43 kcal/mol, and the values were close to the values obtained in the oxidation in O_2. These findings suggested that the oxidation mechanism of the Ni-rich alloys in NO was quite different from that of Co-rich alloys.

Table II represents the chemical species in the oxide layer formed in 10 Torr of NO or O_2 at 700 °C for 1 h, identified by x-ray diffractometry. In the scale formed on pure nickel or pure cobalt only NiO or CoO was detected, respectively, regardless of the difference of the corrosive gas. On the other hand, in the scales on the alloys the chemical species were different between the scale formed in NO and that in O_2. That is, the valency of cobalt in the oxide layer formed on Co–Ni alloys in NO was only Co^{2+}, while that in O_2 was Co^{2+} and Co^{3+}. For example, 40% Co alloy, only (CoO·NiO) was found in the scale formed in NO, however, Co_2O_3 was also detected besides (CoO·NiO) in the scale formed in O_2. These findings were also observed for the scales formed under the conditions of various oxidation time (10–120 min). In the oxidation of Fe, analogous results were found, namely, the scale formed

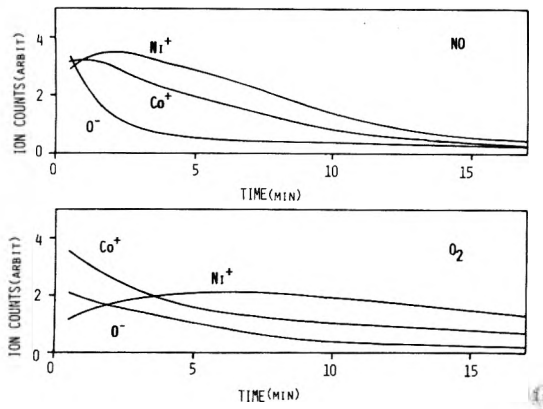

Figure 5. IMA spectra of scales formed on Co–Ni alloys (20% Co): (a) P_{NO} = 10 Torr, 700 °C, 5 min; (b) P_{O_2} = 10 Torr, 700 °C, 5 min.

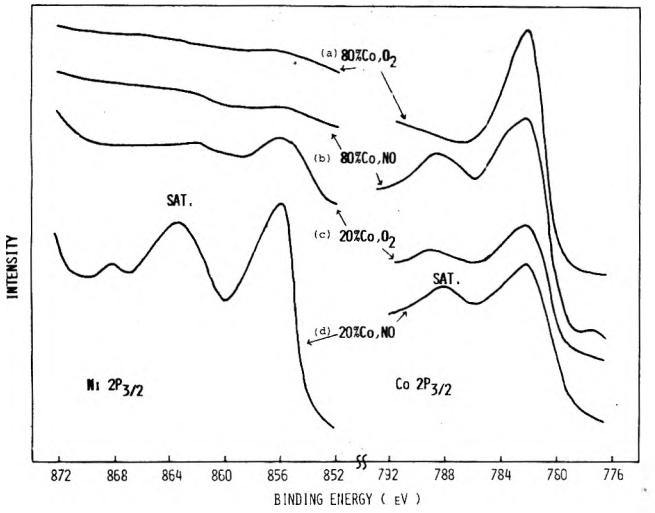

Figure 6. XPS spectra of scales formed on Co–Ni alloys ($Ni2P_{3/2}$, $Co2P_{3/2}$): (a) 80% Co, P_{O_2} = 10 Torr, 700 °C, 5 min; (b) 80% Co, P_{NO} = 10 Torr, 700 °C, 5 min; (c) 20% Co, P_{O_2} = 10 Torr, 700 °C, 5 min; (d) 20% Co, P_{NO} = 10 Torr, 700 °C, 5 min.

in NO was consisted of only Fe_3O_4, while that in O_2 was Fe_3O_4 and Fe_2O_3.[9] Since CoO and NiO have the same crystal structure (NaCl-type) and almost the same lattice parameter (4.25 Å for CoO and 4.17 Å for NiO), mixed oxides $(CoO)_x$·$(NiO)_y$, x, $y > 0$, can be formed.[5]

Figures 4 and 5 show the IMA spectra of the scales (80 and 20% Co) formed in O_2 or NO at 700 °C for 5 min. The abcissa is the sputtering time by argon ions (7 kV for Co^+ and Ni^+, 13 kV for O^-, sample current 0.6 μA/0.8 mm^2). The value of the ion current was influenced by various factors, such as sputtering coefficient, ionization coefficient, surface structure, degree of oxidation of surface species, so that it might show only the outline of the content of each atoms. In these spectra one can find significant information: the surface layers of the scale formed on the alloy in O_2 were much enriched with cobalt oxide, while in case of the scale formed in NO, the degree of enrichment of cobalt oxide was not so high. Then, no peak of nitrogen was also found in the IMA spectra of these scales in this experiment. While IMA spectra can give information about depth profiles, it cannot give information about the surface composition (0–20 Å) of the oxide layer. Therefore, x-ray photoelectron spectroscopy was also carried out. Figure 6 shows the spectra of the surfaces of scales which were formed on Co–Ni alloys, 80 and 20% Co, in 10 Torr of NO or O_2 at 700 °C for 5 min. In the case of the 80% Co alloy, (a) and (b), the shape and the spectral intensity from $Ni2P_{3/2}$ was very similar between (a) and (b), while that from $Co2P_{3/2}$ were much different between them.

TABLE III: Chemical Species of the Surface Scale Estimated by XPS[a]

% Co	Gas NO	O_2
80	NiO (VW) CoO (S) (R = 0.5)	NiO (VW) Co_2O_3 (S) (R = 0)
20	NiO (S) CoO (M) (R = 0.5)	NiO (W) CoO_x (M) $1 < x < 1.5$ (R = 0.3)

[a] P_{NO,O_2} = 10 Torr, 700 °C, 5 min, (S), (M), (W), and (VW) signify strong, medium, weak, and very weak, peak strength respectively. $R = PH_{788.5eV}/PH_{782.5eV}$ where PH is the peak height.

That is, the spectrum (b) had a strong shake-up satellite peak at 788.5 eV, while the spectrum (a) had not. The former was identified to be CoO and the later to be Co_2O_3, using pure samples.

The spectrum of the oxide scale for 20% Co alloys also gave several interesting observation. First, the surface of the scale was more enriched in cobalt oxide by oxidation in O_2, than it was by oxidation in NO. In the case of the Co–Ni alloy, the spectral intensity of $Co2P_{3/2}$ or $Ni2P_{3/2}$ had almost the same ratio value as its alloy composition. Secondly, the mean value of the valence of cobalt ions in the scale formed in O_2 was higher than the scale formed in NO as listed in Table III. Then, the ratio R of the height of the peaks (PH, the height of the top of the peak from the background) at 782.5 eV (multiplet splitting of $Co2P_{3/2}$) and 788.5 eV (shake-up satellite of $Co2P_{3/2}$) should be a rough measure of the mean valency of cobalt, where

$$R = PH_{788.5eV}/PH_{782.5eV}$$

This assignment was based on the findings that the R value of CoO or Co_2O_3 was 0.5 or zero, respectively.

As described above, in the case of the oxidation of Co–Ni alloys in NO, the oxidation rate of the Ni-rich alloys was extremely rapid obeying a linear rate law, while that of the Co-rich alloys were very slow obeying a parabolic rate law. The extremely rapid oxidation rate of Ni-rich alloy must be due to the high reactivity of nickel with NO as described above. Since the oxide layer formed was very coarse, the metallic ions could easily diffuse through the oxide layer, therefore, the oxide layer of the Ni-rich alloy was composed of a relatively homogeneous phase of NiO and CoO. On the other hand, for the oxidation of the alloys in O_2, all the specimens were oxidized obeying the parabolic rate law, and showed the surface layers of the oxide scale were highly enriched with cobalt oxide. The oxide layers were composed of CoO and Co_2O_3 or (CoO·NiO) and Co_2O_3 or Co_3O_4. The enrichment of cobalt oxide in the outer layer of the oxide formed in O_2 would be caused by the difference of the diffusion rates of metallic ions. The diffusion rate of nickel ions through the oxide layer was much slower than that of cobalt ions, so that Co_3O_4 or Co_2O_3 could be also formed.

Acknowledgment. The authors are grateful to Director Dr. Teruo Yasui and Dr. Hideo Kawakami of the Central Research Laboratories of Kuraray Co. Ltd., for their kindness and advice in using the photoelectron spectrometer. Also, they thank Professor Hideo Tamura and Mr. Masaharu Eguchi of the Faculty of Engineering, Osaka University, for making the IMA available for their present work; and they thank Professor Hiromi Shima of the Faculty of Engineering, Yamaguchi University, for his

kindness in using the x-ray diffractometer. This work was supported by the Scientific Research Fund of the Ministry of Education of Japan.

References and Notes

(1) E. Schröder and G. Tamman, *Z. Anorg. Allg. Chem.*, **28**, 179 (1923).
(2) M. Faber, A. J. Darnell, and D. M. Ehremberg, *J. Electrochem. Soc.*, **102**, 446 (1955).
(3) Y. Takasu, Y. Matsuda, S. Maru, and N. Hayashi, *Nature (London)*, **255**, 544 (1975).
(4) Y. Takasu, Y. Matsuda, S. Maru, N. Hayashi, H. Yoneyama, and H. Tamura, *J. Phys. Chem.*, **79**, 1480 (1975).
(5) S. F. Frederic and I. Cornet, *J. Electrochem. Soc.*, **102**, 285 (1955).
(6) W. B. Crow, Ph.D. Thesis, Ohio University, 1969.
(7) A. D. Dalvi and D. E. Coates, *Oxid. Met.*, **2**, 331 (1970).
(8) Y. Takasu, S. Maru, and Y. Matsuda, *Bull. Chem. Soc. Jpn.*, **49**, 3349 (1976).
(9) Y. Takasu, S. Maru, and Y. Matsuda, *Chem. Lett.*, 909 (1975).

Effect of Irradiation Temperatures on Hydrogen Atom Reactions in Neopentane and Its Mixtures Irradiated at 4.2 and 77 K as Studied by Electron Spin Resonance

Machio Iwasaki,* Kazumi Toriyama, Keichi Nunome, Mitsuharu Fukaya, and Hachizo Muto

Government Industrial Research Institute, Nagoya, Hirate, Kita, Nagoya, Japan *(Received February 25, 1977)*

Publication costs assisted by the Government Industrial Research Institute, Nagoya

It has been found that the behavior of hydrogen atoms produced by the homolitic scission of the C–H bond is quite different at 4.2 and 77 K. Neopentane–isobutene (2 mol %) mixtures irradiated at 77 K show that *tert*-butyl radicals are formed by hydrogen atom scavenging in addition to neopentyl radicals. The scavengeable hydrogen atoms are estimated to be about 60–70% of the hydrogen atoms produced in the system. However, the same mixture irradiated at 4.2 K gives only neopentyl radicals which amount to the same as the total radical yield in the mixture irradiated at 77 K. This indicates that the hydrogen atoms which are scavengeable at 77 K are not scavenged at 4.2 K and they reacted with neopentane forming neopentyl radicals. The ESR line width of the neopentyl radicals, their pairwise trapping, and microwave power saturation behavior indicate that the hydrogen atoms reacted with neopentane by a rather short-range reaction at 4.2 K while some of them reacted with solutes via long-range migration at 77 K. Similar effects of irradiation temperature have been also found in neopentane–cyclohexane (2 mol %) mixtures as well as in neopentane containing a small amount of impurity. It is suggested that short-range hot abstraction from neopentane takes place at 4.2 K while a long-range tunneling reaction of thermal hydrogen atoms with solutes takes place at 77 K other than hot abstraction. The results are discussed in relation to guest radical formation in mixed crystals of *n*-decane-d_{22} and *n*-decane-h_{22} previously reported.

To elucidate the mechanisms of solid state radiation-induced reactions, information on the transient reaction intermediates has been compiled mainly at liquid nitrogen temperature (77 K) but little is known at temperatures below 77 K. The mechanisms involved have been discussed based on the information obtained at 77 K. Recently we have found that the mode of radical formation in irradiated saturated hydrocarbons is quite different at liquid helium temperature.[1] The electron spin resonance (ESR) spectra of single crystals of *n*-decane-d_{22} irradiated at 4.2 K indicate that most of alkyl radicals are formed in pairs with random separations distributed from 2.5 to $\simeq$25 Å, while the crystals irradiated at 77 K give spectra mainly attributable to isolated alkyl radicals. When the mixed crystals of *n*-decane-d_{22} containing a small amount of *n*-decane-h_{22} are irradiated at 77 K, guest alkyl radicals are formed with a much higher yield than that expected from the concentration. Irradiation at 4.2 K suppressed the formation of guest radicals giving essentially the same spectra as that obtained from the pure crystals at 4.2 K. What is most unusual in these experiments is that the spectra observed at 77 K after irradiation at 4.2 K are entirely different from those obtained from crystals irradiated at 77 K. Most of the distant radical pairs produced at 4.2 K remain even at 77 K and the spectra of radical pairs change into those of isolated radicals at 200 K. During the change at 200 K the appearance of the guest radical spectra is observed when mixed crystals are used. Similar results have been reported by Gillbro and Lund.[2] These results suggest that the radiation effect is dependent on irradiation temperatures and unknown phenomena might be involved in solid state radiolysis. Assuming homolytic scission of the carbon–hydrogen bonds forming alkyl radicals and hydrogen atoms followed by hydrogen abstraction from the neighboring molecules forming counter alkyl radicals, we have tentatively interpreted the irradiation temperature effect in terms of the difference in the range of hydrogen atom migration which becomes shorter at lower irradiation temperatures.

In relation to these problems, unusual hydrogen atom migration has been recently suggested by Miyazaki et al.[3] in some hydrocarbon mixtures irradiated at 77 K. According to their experiments, when neopentane containing a small amount of cyclohexane is γ irradiated at 77 K, the highly selective formation of cyclohexyl radicals takes place. They have also observed a similar selective formation of solute alkyl radicals in the photolysis of the same mixtures with HI at 77 K. From this similarity, they have suggested that hydrogen atoms produced either by radiolysis or photolysis migrate through the host crystals and selectively react with guest alkane molecules forming predominantly guest radicals. Very recently Willard et al.[4] have also pointed out that thermal deuterium atoms produced by photolysis of 3-methylpentane-d_{14}–DI selectively abstract hydrogen atoms from the impurity C–H bonds with an extremely low activation energy.

In the present studies, we have examined if such a selective formation of guest radicals in irradiated neo-

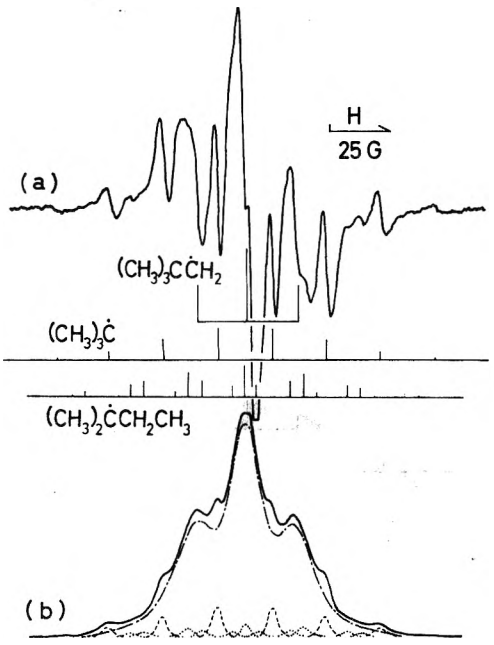

Figure 1. (a) First derivative and (b) integrated ESR spectra of neopentane x irradiated and measured at 77 K. The stick diagram indicates the hyperfine line positions of the three constituent radicals. The dotted curves in (b) indicate the decomposition of the integrated spectrum: microwave power 40 μW; modulation 2.5 G.

pentane mixtures takes place at quite low irradiation temperatures, in relation to our results obtained from *n*-decane-d_{22} and its mixtures with *n*-decane-h_{22}. In addition to 99.9% neopentane and neopentane–cyclohexane mixtures, we have studied neopentane–isobutene mixtures to determine if hydrogen atom reaction with the solute is involved. Analogous to the observation in *n*-decane mixtures, all samples gave solute radicals at 77 K with a higher yield than that expected from the concentration, while at 4.2 K the excess formation of solute radicals was almost completely suppressed. The results seem to be consistent with our previous suggestion that the range of hydrogen atom migration is shorter at 4.2 K.

Experimental Section

Samples of neopentane (99.9%) obtained from Tokyo Kagaku Seiki Co. were distilled by a trap-to-trap method in a vacuum line and then treated with a sodium mirror before transferring into ESR tubes. Samples of cyclohexane (guaranteed reagent) obtained from Wako Junyaku Co. were distilled two times and passed through a 30-cm column of active alumina. Samples of isobutene (guaranteed reagent) obtained from Tokyo Kasei Co. were used without further purification. The samples were irradiated with x-rays (45 kV, 40 mA) to a dose of about 0.3 Mrad. The details of our low temperature irradiation apparatus is described in our previous paper.[5] For quantitative measurements to determine the total radical yield, the samples were irradiated with ^{60}Co γ rays to a dose of 0.5 Mrad at a dose rate of 1.6 Mrad/h. Both x and γ irradiations gave essentially the same ESR spectra. The spectra were measured with a Varian E-12 spectrometer at X-band using 100-kHz field modulation. Double integration of the first derivative ESR spectra was carried out using an on-line computer (Nicolet 1070 spectrum analyzer).

Results

Neopentane (99.9%). Shown in Figures 1 and 2 are the first derivative ESR spectrum (a) and its integrated spectrum (b) for neopentane (99.9%) irradiated at 77 and

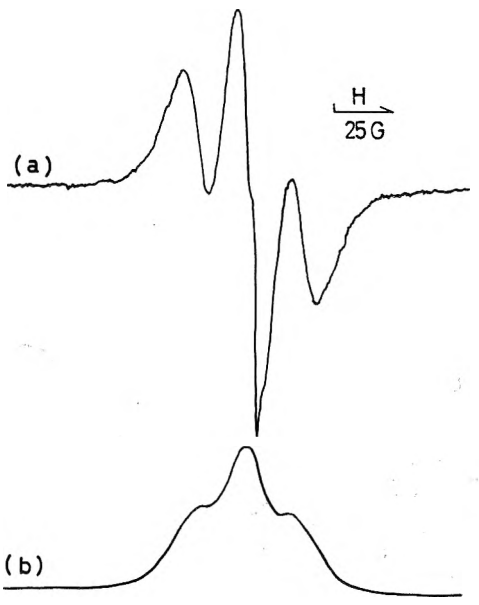

Figure 2. (a) First derivative and (b) integrated ESR spectra of neopentane x irradiated at 4.2 K and measured at 77 K: microwave power 40 μW; modulation 2.5 G.

TABLE I: Relative Amounts (%) of Solute Radicals to the Total Radicals Determined from Spectral Decomposition

Sample irrad temp, K	neo-C_5H_{12}		neo-C_5H_{12}–c-C_6H_{12}		neo-C_5H_{12}–i-C_4H_8	
	77 K	4.2 K	77 K	4.2 K	77 K	4.2 K
t-Bu	~8	<1	~3		36 ± 7	~2
t-Pen	~6		<1			
c-Hex			32 ± 7	3~5		

4.2 K, respectively. All these spectra are measured at 77 K. The three-line spectrum with a separation of 21 G obtained from the sample irradiated at 4.2 K (Figure 2) is quite simple and is attributable to neopentyl radical I.

$$(CH_3)_3C\dot{C}H_2$$
I

As is shown by the stick diagram, the complicated spectrum obtained from the sample irradiated at 77 K consists of three components: a three-line spectrum of I, a ten-line spectrum with a separation of 22.4 G which is attributable to *tert*-butyl radical II, and a spectrum which is attrib-

$$(CH_3)_3\dot{C}\qquad (CH_3)_2\dot{C}CH_2CH_3$$
II III

utable to *tert*-pentyl radical III. The identification of the *tert*-pentyl radical has been recently made by Fujimura et al.[6] using their well-resolved spectra obtained by in-situ irradiation of plastic phase neopentane at −121 °C. The CH_3 and CH_2 proton couplings are estimated to be ~24 and ~18.5 G, respectively, for our crystalline phase neopentane using the second derivative spectrum.

From the decomposition of the integrated spectrum (Figure 1b), it was found that the major species is the neopentyl radical which amounts to about 86%. The amounts of *tert*-butyl and *tert*-pentyl radicals are about 8 and 6%, respectively (Table I). Since the line width of the three-line spectrum of I is extremely broader than those of the two other species, the profile of the first derivative ESR spectrum is greatly modulated by the narrower components, resulting in a quite different profile from the three-line spectrum shown in Figure 2. However, the profiles of the integrated spectra are not very much different from each other.

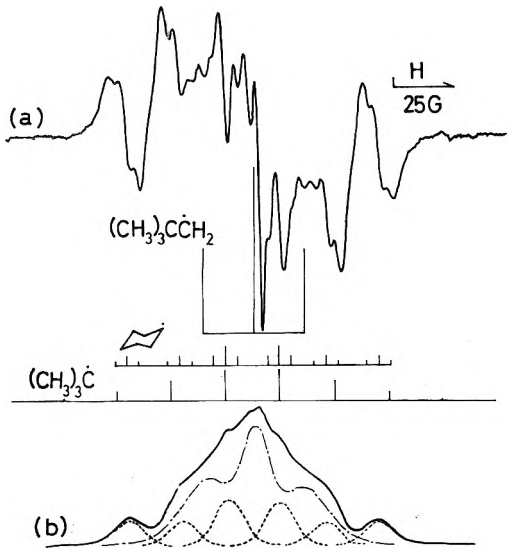

Figure 3. (a) First derivative and (b) integrated ESR spectra of a neopentane–cyclohexane (2 mol %) mixture x-irradiated and measured at 77 K. Other remarks are the same as those in Figure 1.

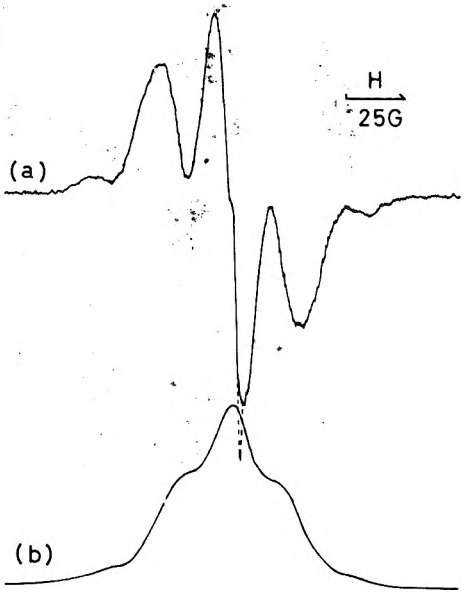

Figure 4. (a) First derivative and (b) integrated ESR spectra of a neopentane–cyclohexane (2 mol %) mixture x-irradiated at 4.2 K and measured at 77 K: microwave power 40 μW; modulation 2.5 G.

Neopentane–Cyclohexane (2 mol %) Mixtures. Shown in Figures 3 and 4 are the spectra obtained at two different irradiation temperatures. The spectrum obtained from the sample irradiated at 4.2 K (Figure 4) is essentially the same as that of 99.9% neopentane irradiated at 4.2 K. It is clear that the main species formed at 4.2 K is the neopentyl radical I. On the other hand, the spectrum obtained from the sample irradiated at 77 K shows the formation of cyclohexyl radicals (IV) as is reported by Miyazaki et al.[3]

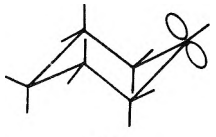

IV

The stick diagrams in Figure 3 illustrate the overlapping of the spectrum arising from cyclohexyl and *tert*-butyl radicals with that of neopentyl radicals. The hyperfine coupling values for cyclohexyl radicals estimated using the second derivative spectrum are $a_{\alpha H}$ = 22 G, $a_{\beta H}$ = 41 G,

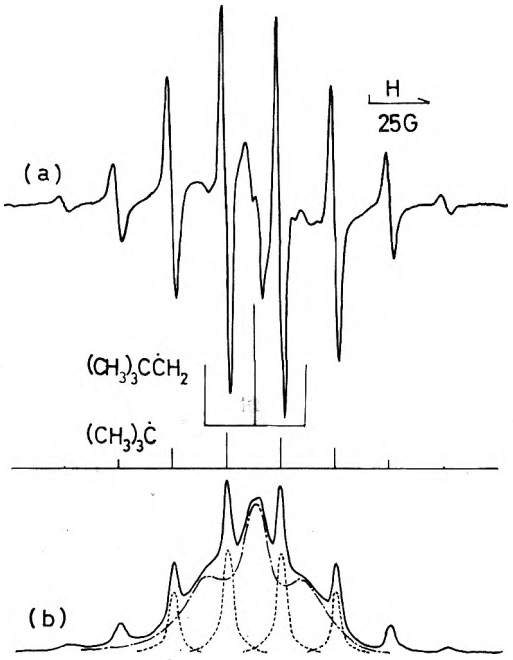

Figure 5. (a) First derivative and (b) integrated ESR spectra of a neopentane–isobutene (2 mol %) mixture x-irradiated and measured at 77 K. Other remarks are the same as those in Figure 1.

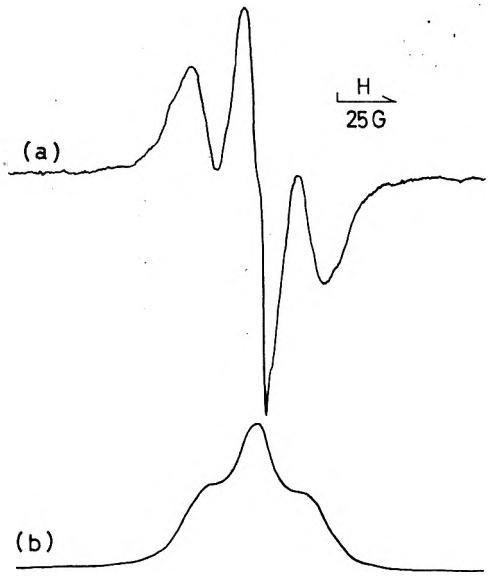

Figure 6. (a) First derivative and (b) integrated ESR spectra of neopentane–isobutene (2 mol %) mixture x-irradiated at 4.2 K and measured at 77 K: microwave power 40 μW; modulation 2.5 G.

and $a_{\beta H'}$ = 5 G in agreement with the values reported by Ogawa and Fessenden.[7]

From the decomposition of the integrated spectrum (Figure 3b) the amount of cyclohexyl radicals is estimated to be 32%. The amount of *tert*-butyl radicals is estimated to be about 3% from the peak height of the first derivative spectrum in referring to the spectrum obtained from the neopentane–isobutene mixtures which will be described in the next section. The amount of cyclohexyl radicals formed at 4.2 K is estimated to be about 3–5% (Table I).

Neopentane–Isobutene (2 mol %) Mixtures. Shown in Figures 5 and 6 are the spectra obtained at two different irradiation temperatures. The spectrum obtained from the sample irradiated at 4.2 K (Figure 6) is essentially the one arising from neopentyl radicals. On the other hand, the first derivative spectrum obtained from the sample irradiated at 77 K (Figure 5a) is essentially the one arising from *tert*-butyl radicals at a glance. However, the inte-

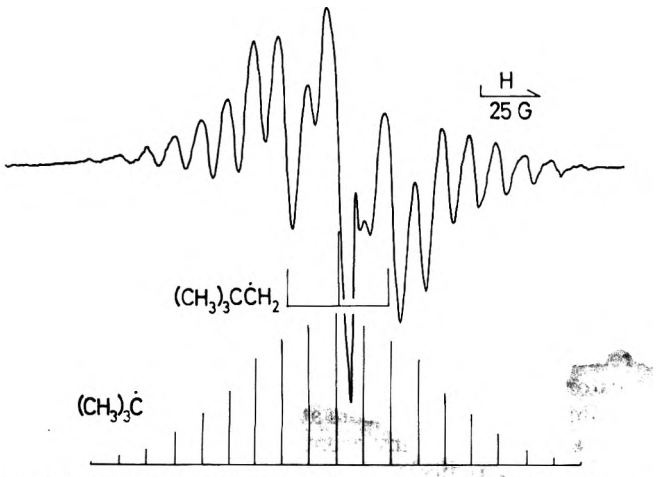

Figure 7. First derivative ESR spectrum of a neopentane–isobutene (2 mol %) mixture x-irradiated at 77 K and measured at 4.2 K. The stick diagram indicates the theoretical line spectra expected from *tert*-butyl radicals in which three methyl groups undergo tunneling rotation: microwave power 1 μW; modulation 2.5 G.

grated spectrum (Figure 5b) clearly shows a major contribution from neopentyl radicals. The amount of *tert*-butyl radicals is estimated to be 36%. A simulation of the first derivative spectrum was also performed and a similar result was obtained. The amount of *tert*-butyl radicals formed at 4.2 K is estimated to be about 2% from the peak height of the first derivative spectrum (Table I).

It is mentioned that careful analysis of the overlapping first derivative spectra of the broad and sharp components is necessary for estimating the relative abundance of the sharp component. Unless otherwise, unusually high selective formation of the radicals giving a sharp component would result.

It may be worthwhile to note here that the spectrum of *tert*-butyl radicals observed at 4.2 K changes from a 10-line spectrum with a binomial intensity ratio into a 19-line spectrum with a half-spacing and intensity ratio which is expected from the tunneling rotation of the three methyl groups (see Figure 7). As is well known, a tunneling methyl group shows a seven-line spectrum with an intensity ratio of 1:1:1:2:1:1:1 when the population of the lowest torsional level is predominant and the tunneling splitting is sufficiently smaller than kT.[8] The stick diagram in Figure 7 is the theoretical spectrum expected from *tert*-butyl radicals in which all three methyl groups undergo tunneling rotation.

Spatial Distribution of the Neopentyl Radicals. As shown in Figure 8, the spectrum measured at 4.2 K for 99.9% neopentane immediately after x irradiation at 4.2 K is much broader than that measured at 4.2 K after annealing at 77 K for 30 min. During annealing at 77 K the total radical amount decreased by about 20%. If the pairwise trapping of neopentyl radicals takes place, it is expected that the spin–spin interaction greatly contributes to the line width. Therefore, the intensity ratio, I_2/I_1, of the $\Delta M_s = \pm 2$ and the $\Delta M_s = \pm 1$ transitions was measured at 4.2 K before and after annealing at 77 K as a crude measure of the pairwise trapping of radicals.[1] The value of I_2/I_1 for 99.9% neopentane decreased from 1.8×10^{-4} to 0.95×10^{-4}, consistent with line width narrowing. It is to be noted that the I_2/I_1 value is comparable with that of *n*-decane-d_{22} in which alkyl radicals are formed in pairs. On the other hand, the I_2/I_1 value for samples irradiated at 77 K was less than 0.5×10^{-4}. The spectra obtained from the neopentane–cyclohexane (2 mol %) and the neopentane–isobutene (2 mol %) mixtures irradiated at 4.2 K behave essentially in the same manner. The I_2/I_1 ratios for all the samples are tabulated in Table II.

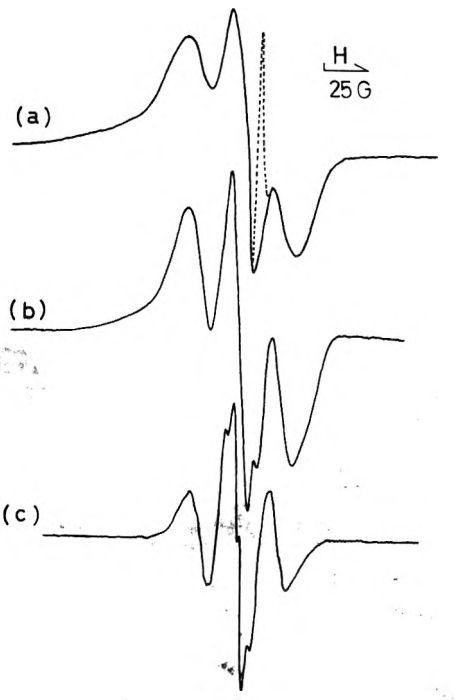

Figure 8. First derivative ESR spectra of neopentane (a) irradiated and measured at 4.2 K, (b) measured at 4.2 K after annealing at 77 K for 30 min, and (c) measured at 77 K after annealing at 145 K for 10 min. The microwave power was 4 μW for (a) and (b), 40 μW for (c); the modulation was 5 G for (a) and (b), 2.5 G for (c).

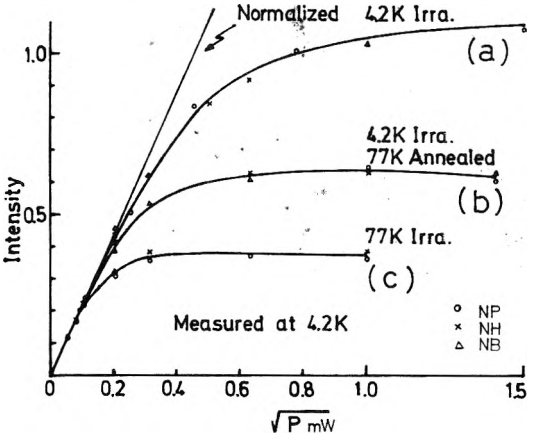

Figure 9. Microwave power saturation curves measured at 4.2 K for (O) neopentane, (×) neopentane–cyclohexane (2 mol %), and (Δ) neopentane–isobutene (2 mol %) mixtures (a) immediately after irradiation at 4.2 K, (b) after annealing at 77 K for 30 min, and (c) immediately after irradiation at 77 K. The ordinates for all the saturation curves are normalized to give the linear portion of the curves the same slope.

TABLE II: I_2/I_1 Ratios and Relative $(T_1T_2)^{1/2}$ for x Irradiated Neopentane (99.9%), Neopentane–Cyclohexane (2 mol %), and Neopentane–Isobutene (2 mol %) Mixtures

Irrad temp, K	I_2/I_1 (× 10^4)[a]	$(T_1T_2)^{1/2}$[a]
4.2	~2.1	1.00
4.2 → 77	~1.3	1.64
77	<0.5	2.56

[a] Since the three samples gave a similar value if the irradiation conditions were the same, the averaged values are given.

In order to check the difference in the spatial distribution of radicals, the microwave power saturation was also measured at 4.2 K. Since the stronger spin–spin interaction decreases T_2 and thus $(T_1T_2)^{1/2}$, it is expected that

TABLE III: Radical Yields in γ Irradiated Neopentane (99.9%), Neopentane-Cyclohexane (2 mol %), Neopentane-Isobutene (2 mol %) Mixtures

Sample irrad temp, K	neo-C_5H_{12}		neo-C_5H_{12}-c-C_6H_{12}		neo-C_5H_{12}-i-C_4H_8	
	4.2 K	77 K	4.2 K	77 K	4.2 K	77 K
Total yield	1.00[a]	0.74	1.1_0	0.97	0.96	0.91
neo-Pen[b]	>0.99	0.64	1.0_6	0.66	0.94	0.58
Solute radicals[b]	<0.01	0.10	0.04_4	0.31	0.02	0.33

[a] The total radical yield for neo-C_5H_{12} irradiated at 4.2 K is taken as 1.00, to which other radical yields are referred. [b] The relative amounts of the solvent and solute radicals are assumed to be the same as those determined from the samples irradiated by x rays (see Table I).

samples with a higher local concentration of radicals exhibit a microwave power saturation behavior which is less saturated than samples with a lower local concentration.[5,9] As shown in Figure 9, all samples irradiated at 4.2 K exhibit the least saturated behavior reflecting the highest local concentration of radicals. After annealing at 77 K, all samples become more easily saturated suggesting a decrease of local concentration. This is consistent with the narrowing of the line width and the decrease of I_2/I_1. Samples irradiated at 77 K exhibit the most saturated behavior, consistent with the lowest I_2/I_1 value. The relative $(T_1T_2)^{1/2}$ values obtained from the saturation curves are tabulated in Table II.

From these results it is concluded that neopentyl radicals are formed in pairs with a much higher local concentration at 4.2 K as is the case for *n*-decane previously reported,[1] while solute radicals are formed as isolated radicals at 77 K.

Annealing above 77 K. The relative abundance of the guest to host radicals in samples x-irradiated at 4.2 K slightly increased after annealing at 77 K. Since the total amount of radicals decreased about 20%, the apparent increase of the guest radical is probably due to a decrease of host radicals which are formed in pairs. Further spectral changes were examined at 77 K after repeating successive annealing at temperatures above 77 K. Although the total amount of radicals gradually decreased, an appreciable change in the relative abundance of the guest to host radicals was not observed at annealing temperatures lower than 145 K. However, during annealing notable line width narrowing of the neopentyl radical spectrum was observed suggesting a decrease of the local concentration of radicals. With this narrowing the substructures which are attributed to γ-proton coupling by Lin and Williams[10] gradually appeared on the central line. Figure 8c shows the spectrum obtained after annealing at 145 K for 10 min for neopentane irradiated at 4.2 K. The mixtures irradiated at 4.2 K gave essentially the same spectra. From these results, it is concluded that an efficient radical conversion from the host to guest radicals does not take place in neopentane mixtures.

Total Radical Yields. The total radical yields of samples γ irradiated at 4.2 K with a dose of 0.5 Mrad were measured at 77 K and compared with those of samples γ irradiated at 77 K with the same dose. The results are summarized in Table III. The results indicate that the total radical yields in all the samples irradiated at 4.2 K are nearly the same. On the other hand, when the samples are irradiated at 77 K, the neopentane–cyclohexane and neopentane–isobutene mixtures give nearly the same total radical yield as that in samples irradiated at 4.2 K while 99.9% neopentane gives considerably smaller yields than the others. It is, however, to be noted that the yield of neopentyl radicals in samples irradiated at 77 K is nearly the same and the difference derives from the yield of radicals other than neopentyl radicals. This difference will be discussed in a later section.

It is mentioned that these measurements are made at 77 K so that some of radicals initially produced in samples irradiated at 4.2 K may be lost upon warming to 77 K. Similarly radicals produced in samples irradiated at 77 K may also be reduced during irradiation at 77 K. The samples x irradiated and measured at 4.2 K show that about 20% of the radicals initially trapped at 4.2 K are lost upon warming to 77 K when the radical amount is remeasured at 4.2 K again. However, because of spectral distortion at 4.2 K due to mixing of the dispersion mode quantitative measurements at 4.2 K are less reliable than those at 77 K. In any event, since it is not possible to estimate the radical yield produced during irradiation at 77 K if some of radicals are lost, the total radical yield was compared at 77 K.

Discussion

What is most remarkable is that irradiation at 4.2 K gives entirely different spectra from those obtained from irradiation at 77 K even after annealing at 77 K as is the case for *n*-decane irradiated at 4.2 K.[1] The formation of radicals other than neopentyl radicals is almost completely suppressed at 4.2 K for all samples examined.

Our results obtained from neopentane–isobutene (2 mol %) suggest that hydrogen atoms produced by the homolytic scission of the C–H bond of neopentane react efficiently with isobutene to form hydrogen addition radicals, that is, *tert*-butyl radicals when irradiation occurs at 77 K. An equal number of hydrogen atoms (0.5) and neopentyl radicals (0.5) must be initially formed (reaction 1). If one assumes that some of the hydrogen atoms react

$$\text{neo-}C_5H_{12} \rightsquigarrow C_5H_{11}\cdot + H\cdot \quad (1)$$

$$H\cdot + \text{neo-}C_5H_{12} \rightarrow C_5H_{11}\cdot + H_2 \quad (2)$$

$$H\cdot + (CH_3)_2C{=}CH_2 \rightarrow (CH_3)_3C\cdot \quad (3)$$

with neopentane (reaction 2) and the rest react with isobutene (reaction 3), our analyses suggest that the number of hydrogen atoms reacted with neopentane and isobutene is 0.14 and 0.36, respectively. On the other hand, the reaction of hydrogen atoms with isobutene is greatly suppressed at 4.2 K. The difference in the spatial distribution of neopentyl radicals at both irradiation temperatures strongly suggests that hydrogen atom migration to the guest molecule is suppressed at 4.2 K and that the rather short-range reaction with host molecules is predominated at 4.2 K. In other words, hydrogen atoms produced at 4.2 K cannot be scavenged by isobutene.

Positive hole trapping by isobutene followed by hydrogen abstraction from the neighboring molecule might also produce *tert*-butyl radicals. However, it is hard to believe that positive hole migration is suppressed at 4.2 K. Our preliminary results obtained from neopentane–tetramethylethylene (hole scavenger[11]) indicate that hole scavenging by tetramethylethylene is not suppressed at 4.2 K.

The behavior of guest radical formation in neopentane–cyclohexane (2 mol %) mixtures at both irradiation temperatures is quite similar to that in neopentane–isobutene (2 mol %) mixtures. This suggests that the reaction of migrating hydrogen atoms with cyclohexane forms cyclohexyl radicals by hydrogen abstraction (reaction 4) at 77 K while hydrogen atom migration is suppressed

$$H\cdot + \text{c-}C_6H_{12} \rightarrow \text{c-}C_6H_{11}\cdot + H_2 \quad (4)$$

at 4.2 K. If this is the case, our results obtained at 77 K indicate that the relative amount of hydrogen atoms which react with neopentane is 0.18 and those with cyclohexane is 0.32, neglecting a minor contribution from *tert*-butyl radical formation. Miyazaki and Hirayama[3d] reported that the formation of cyclohexyl radicals is 86%. This exceeds the number of hydrogen atoms produced in the system. This peculiarity is eliminated by our analyses.

Miyazaki and Hirayama[3d] also reported that the formation of *tert*-butyl and *tert*-pentyl (unidentified by them) radicals in 99.9% neopentane irradiated at 77 K to a dose of 0.5 Mrad is about 50%. They suggested that *tert*-butyl radicals are formed by the reaction of hydrogen atoms with radiation-produced impurities and that *tert*-pentyl radicals are formed by the reaction of hydrogen atoms with initially existing impurities, based on their experiments of the effect of preirradiation dose and sample purity. Although our analyses of the ESR spectra reduced the amount of *tert*-butyl and *tert*-pentyl radicals to about 14% from their value of 50%, this still seems to be unusually higher than expected from the concentration of impurities. However, our experiments indicate that the formation of these radicals is also suppressed at 4.2 K suggesting that both species are formed from the reaction of migrating hydrogen atoms with impurities with high efficiency at 77 K.

$$H\cdot + \text{impurities} \rightarrow (CH_3)_3C\cdot + (CH_3)_2\dot{C}CH_2CH_3 \quad (5)$$

Now, as mentioned before, the total radical yield in 99.9% neopentane irradiated at 77 K is considerably smaller than those in the mixtures although the yield of neopentyl radicals is nearly the same for all samples irradiated at 77 K. This suggests that scavenging of hydrogen atoms by solutes and impurities resulted in the excess formation of radicals other than neopentyl radicals and that some of scavengeable hydrogen atoms are lost in 99.9% neopentane by recombination (reaction 6) forming

$$2H\cdot \rightarrow H_2 \quad (6)$$

hydrogen molecules, since the amount of impurities is not sufficient to react with all the scavengeable hydrogen atoms produced in the system. If this is the case, the lost of hydrogen atoms by reaction 6 without forming radicals is about 0.2–0.3.

It is to be noted that reaction 5 produces one H_2 molecule from one H·, while reaction 6 produces one H_2 molecule from two H·. As a result, the hydrogen yield, $G(H_2)$, should increase upon the addition of cyclohexane. If the hydrogen yield by unimolecular detachment is neglected, the above assumptions predict that $G(H_2)$ in neopentane–cyclohexane (2 mol %) is higher by a factor of 1.25–1.43. According to the product analyses by Miyazaki et al.[3a] $G(H_2)$ in neopentane–cyclopentane mixtures irradiated at 77 K sharply increases upon the addition of a small amount of cyclopentane (see Figure 4 in ref 3a). For example, $G(H_2)$ in neopentane without solutes is about 1.6, while it increases to about 2.1, 2.3, and 2.4 with solute concentrations of 2, 5, and 10 mol %, respectively. $G(H_2)$ in the 2 mol % mixture is higher by a factor of 1.31. This agrees with the above-mentioned prediction for neopentane–cyclohexane (2 mol %) mixtures.

For these reasons, it may be concluded that the scavengeable hydrogen atoms by isobutene reacted with cyclohexane forming cyclohexyl radicals and the amount of scavengeable hydrogen atoms is about 70–72%, the rest reacting with neopentane forming neopentyl radicals at 77 K. Although this estimate assumes that all the radicals initially produced are trapped at 77 K, if it is assumed that neopentyl radicals trapped at 77 K are reduced by a factor of 0.8 and all the solute radicals are trapped without decay, as is suggested from the samples x irradiated at 4.2 K, the amount of scavengeable hydrogen atoms is about 60–62%.

TABLE IV: Relative Rate Constants and Reactivity Ratios of Tunneling Abstraction by Thermal Hydrogen Atoms from Neopentane and Cyclohexane Estimated from the Unsymmetrical Eckart Potential[a]

	Relative rate constants[b]		Reactivity ratios	
T, K	neo-C_5H_{12}[c]	c-C_6H_{12}[d]	k_{CHX}/k_{NP}	Obsd[e]
300	4291	87162 (990)	20.3	(6.6)[f]
77	1	88 (1)	88	$\gtrsim$87
4.2	0.018	1.83 (0.021)	100	$\gtrsim$3

[a] $\bar{V}(x) = -\Delta Hy/(1-y) - [(E_A - \Delta H)^{1/2} + E_A^{1/2}]^2 y/(1-y)^2$ with $y = -\exp(2x/a)$, where E_A, ΔH, a, and x are the activation energy, the heat of reaction, the potential width parameter, and the reaction coordinate, respectively. [b] $k = BT^{1/2}\Gamma(T)\exp(-E_A/RT)$ is assumed, where $\Gamma(T)$ is the tunneling correction factor. B is assumed to be the same for the two compounds. If $B = 10^{13}$ cm^3 mol^{-1} s^{-1} is assumed, the absolute rate constant for neopentane becomes 0.7×10^9 cm^3 mol^{-1} s^{-1} at 300 K in agreement with 1×10^9 cm^3 mol^{-1} s^{-1} estimated by Hardwick.[14c] [c] $E_A = 8.6$ kcal/mol, $\Delta H = -9.8$ kcal/mol, and $a = 0.56$ Å are assumed. [d] $E_a = 6.65$ kcal/mol, $\Delta H = -19.2$ kcal/mol, and $a = 0.56$ Å are assumed. [e] Assuming a simple competition, the reactivity ratios are obtained from the relative radical yield determined from experiments. [f] Calculated value by Hardwick[14c] using the rate constants for the reaction of hydrogen atoms with hydrocarbon structural groups at room temperature.

The results obtained from all samples irradiated at 4.2 K indicate that the total radical yield is nearly the same as those in mixtures irradiated at 77 K. This means that all hydrogen atoms which are scavengeable at 77 K reacted with neopentane forming neopentyl radicals at 4.2 K. The higher local concentration of neopentyl radicals at 4.2 K is consistent with this conclusion if the hydrogen atoms scavengeable at 77 K reacted with neopentane by a rather short-range reaction.

It is quite interesting that the hydrogen atoms produced by homolytic scission behave quite differently at 4.2 and 77 K. Recently Wilkey and Willard[4] have suggested that thermal deuterium atoms can abstract H atoms from the C–H bond at 77 K with a low activation energy. Wang and Williams[12] have reported that an apparent activation energy for the hydrogen abstraction reaction from the C–H bond by $\dot{C}H_3$ radicals in CH_3CN is 1.4 kcal/mol at 90 K. Le Roy, Sprague, and Williams[13a] have explained this by a tunneling mechanism. We have examined the possibility of tunneling abstraction by thermal hydrogen atoms using the unsymmetrical Eckart potential and the analytical expression for permiability.[13b] The results indicate that the fast reaction of thermal hydrogen atoms can occur at 77 K by tunneling through a potential barrier of 6–9 kcal/mol with a potential wall thickness parameter in the reasonable range. It was also found that the difference in activation energies and heat of reactions for the primary C–H bonds of neopentane and for the secondary C–H bonds of cyclohexane leads to a reactivity ratio which is consistent with the selective reaction observed at 77 K. Although the details will be given elsewhere, some of the results are shown in Table IV. It is noted that the reactivity ratio at 77 K becomes larger than that at 300 K. This means that the selectivity is higher at 77 K in agreement with the temperature dependence of the selectivity reported by Miyazaki and Hirayama.[3d] It is well known that the relative reactivity of the hydrogen abstraction reaction from the C–H bond at ordinary temperature increases with decreasing number of C–H bonds at the group which is attacked by atoms or radicals.[14] The

importance of the tunneling correction for proton and hydrogen atom reactions even at ordinary temperature is pointed out by many workers.[15] If a tunneling mechanism is involved, the selective reaction at 77 K seems to be an analogous situation observed at ordinary temperatures, including the higher reactivity of hydrogen addition to the double bond. However, it is mentioned that Miyazaki et al.[3c,16] reported some other selective reactions of hydrogen atoms which do not seem to be explained by this simple relation of relative reactivity at ordinary temperatures.

On the other hand, our experiments at 4.2 K show that the reactivity of hydrogen atoms with neopentane becomes comparable with that of cyclohexane at 4.2 K, if the effect of irradiation temperature originates from the change in reactivity ratio of thermal hydrogen atoms at 77 and 4.2 K. However, as shown in Table IV the trial estimation of the tunneling correction factor at 4.2 K shows that the situation is not very much different at 4.2 K. If one assumes that the potential barrier and width change at 4.2 K, it may be possible to explain the change in the reactivity ratio. However, there seems to be no a priori reason for the potential energy surface changes at 4.2 K. It seems difficult to explain the irradiation temperature effect by a change in the reactivity ratio of thermal hydrogen atoms for solute and solvent molecules.

Another possibility that must be taken into consideration is that irradiation at 4.2 K suppresses the migration of hydrogen atoms or the formation of hydrogen atoms which would migrate to the solutes at 77 K. The difference in the kinetic energy distribution of hydrogen atoms produced and in some matrix effects on hydrogen atom migration in the solid at the two irradiation temperatures might be related to the range of the hydrogen atoms. Suppose that there are two different pathways of dissociative excitation which produce two kinds of hydrogen atoms having different average kinetic energies. For example, Ito et al.[17] have recently observed the formation of two kinds of hydrogen atoms with different average kinetic energies by measuring the Doppler profile of the emission spectra of Balmer α radiation induced by electron impact on H_2. If the formation of two kinds of hydrogen atoms is dependent on irradiation temperatures, there is a possibility that the formation of hydrogen atoms favorable for long-range migration is suppressed at 4.2 K. A sort of cage effects at 4.2 K may preclude escape of hydrogen atoms to react with solutes and may result in a rather short-range reaction. The radiation-induced deformation of the lattice which may not be relaxed and may be accumulated during irradiation at 4.2 K might also hinder hydrogen atom migration. To reach a proper understanding of the problem, consideration of atomic collisions in solids may be required.

Timm and Willard[18] reported that hydrogen atoms produced in radiolysis of CH_4 can be trapped at 4.2 K but they are not scavenged by the addition of 0.3 mol % of isobutene at 4.2 K. They have explained this by low reactivity of thermal hydrogen atoms with isobutene at 4.2 K. However, if hydrogen atoms produced are thermalized before migrating a long distance to reach solute molecules and thermal hydrogen atoms cannot react with CH_4, the implication of their observation is similar to that of the present work, except that hydrogen atoms can react with solvent molecules in our case. Our preliminary calculation of tunneling correction factors indicates that the reactivity of thermal hydrogen atoms at 4.2 K is extremely low for CH_4 having the highest bond dissociation energy among simple saturated hydrocarbons. The formation of radical pairs between $\dot{C}H_3$ and H· in irradiated CH_4[19] also suggests that the thermalization distance of hydrogen atoms in CH_4 is short at 4.2 K. In solvents in which even thermal hydrogen atoms can react with solvent at 4.2 K, the range of hydrogen atom migration may be shorter than that in CH_4.

Taking the initial kinetic energy of hydrogen atoms into consideration, it may be concluded that short-range hot abstraction by hydrogen atoms from the matrix takes place at 4.2 K while long-range tunneling abstraction by hydrogen atoms with low kinetic energy takes place at 77 K other than by hot abstraction.

Guest Radical Formation in Mixed Crystals of n-Decane. Gillbro and Lund[2] have explained the selective formation of protiated radicals at 77 K in mixed crystals of *n*-decane-d_{22} and *n*-decane-h_{22} by excitation transfer to guest molecules. However, similarity in the irradiation temperature effect to that observed for neopentane mixtures suggests that a similar mechanism is involved in both mixtures. The observation by Wilkey and Willard[4] in 3-methylpentane-d_{14} containing a small amount of protiated impurity is also quite similar to that in decane mixtures especially in the marked mass effect. It is suggested that deuterium atom migration to guest molecules is the main cause of the selective formation of protiated radicals as proposed in our previous paper.[1] The mass effect of hydrogen abstraction from C–H and C–D bonds is expected to be quite large for tunneling reactions.[12,13] In addition, it is noted that guest radicals are also selectively formed at the C_2 atom, that is, $CH_3\dot{C}HCH_2$– is predominant rather than –CH_2–$\dot{C}H$–CH_2– and $\dot{C}H_2$–CH_2–.[2] This is also understandable from the difference in the reactivity of hydrogen atoms with hydrocarbon structural groups.[14]

Since we have observed radical site transfer in the irradiated crystals of *n*-decane-d_{22} at low temperatures and thermal radical conversion at 200 K from the host to guest radicals in mixed crystals irradiated at 4.2 K,[1] the possibility of radical site transfer to guest molecules during irradiation at 77 K might not be neglected. However, our recent study on mixed crystals of *n*-decane-d_{22} and *n*-decylbromide-h_{21} suggested that the contribution from radical site transfer to selective formation of guest radicals during irradiation is not appreciable.

NOTE ADDED IN PROOF: After completing the manuscript, the authors have received a preprint of a paper from Dr. Miyazaki.[20] He has performed product analysis of the hydrogen produced in mixed crystals of *n*-decane-d_{22} and *n*-decane-h_{22} irradiated at 77 K. It was found that DH increased while D_2 decreased with increasing addition of *n*-decane-h_{22}. In addition, DH formation is parallel to the formation guest radicals. From these results it was concluded that deuterium atoms abstract hydrogen atoms from guest molecules in agreement with our previous suggestion.[1]

References and Notes

(1) M. Iwasaki, K. Toriyama, H. Muto, and K. Nunome, *Chem. Phys. Lett.*, **39**, 90 (1976); *J. Chem. Phys.*, **65**, 596 (1976).
(2) T. Gillbro and A. Lund, *Chem. Phys. Lett.*, **39**, 357 (1975); *Int. J. Radiat. Phys. Chem.*, **8**, 625 (1976).
(3) (a) T. Miyazaki, T. Wakayama, M. Fukaya, Y. Saitake, and Z. Kuri, *Bull. Chem. Soc. Jpn.*, **46**, 1030 (1973); (b) K. Kato, Y. Saitake, T. Miyazaki, and Z. Kuri, *ibid.*, **46**, 2004 (1973); (c) T. Wakayama, T. Miyazaki, K. Fueki, and Z. Kuri, *J. Phys. Chem.*, **77**, 2365 (1973); (d) T. Miyazaki and T. Hirayama, *ibid.*, **79**, 566 (1975); (e) T. Miyazaki, K. Kinugawa, M. Eguchi, and S. M. L. Guedes, *Bull. Chem. Soc. Jpn.*, **49**, 2970 (1976).
(4) D. D. Wilkey and J. E. Willard, *J. Chem. Phys.*, **64**, 3976 (1976).
(5) K. Nunome, H. Muto, K. Toriyama, and M. Iwasaki, *Chem. Phys. Lett.*, **39**, 542 (1976).
(6) Y. Fujimura, H. Kadoi, H. Ishigure, and Y. Tabata, Abstract of 18th Symposium on Radiation Chemistry held in Tokyo, Oct 1975, p 87.
(7) S. Ogawa and R. W. Fessenden, *J. Chem. Phys.*, **41**, 994 (1964).

(8) J. H. Freed, *J. Chem. Phys.*, **43**, 1710 (1965); M. Iwasaki, K. Nunome, H. Muto, and K. Toriyama, *ibid.*, **54**, 1839 (1971).
(9) D. P. Lin and L. Kevan, *J. Chem. Phys.*, **55**, 2629 (1971).
(10) J. Lin and F. Williams, *J. Phys. Chem.*, **72**, 3707 (1968).
(11) T. Ichikawa and P. K. Ludwig, *J. Am. Chem. Soc.*, **91**, 1023 (1969).
(12) J. Wang and F. Williams, *J. Am. Chem. Soc.*, **94**, 2930 (1972).
(13) (a) J. Le Roy, E. D. S. Sprague, and F. Williams, *J. Phys. Chem.*, **76**, 546 (1972); (b) C. Eckart, *Phys. Rev.*, **35**, 1303 (1930).
(14) (a) G. A. Russell, "Free Radicals", J. K. Kochi, Ed., Vol. 1, Wiley, New York, N.Y., 1973, p 275; (b) K. Yang, *J. Phys. Chem.*, **67**, 562 (1963); (c) T. J. Hardwick, *ibid.*, **65**, 101 (1961).
(15) E. F. Daldin, *Chem. Rev.*, **69**, 135 (1969).
(16) T. Wakayama, T. Miyazaki, K. Fueki, and Z. Kuri, *Bull. Chem. Soc. Jpn.*, **44**, 2619 (1971).
(17) K. Ito, N. Oda, Y. Hatano, and T. Tsubol, *Chem. Phys.*, **17**, 35 (1976).
(18) D. Timm and S. E. Willard, *J. Phys. Chem.*, **73**, 2403 (1969).
(19) W. Gordy and R. Morehouse, *Phys. Rev.*, **151**, 207 (1966).
(20) T. Miyazaki, *Int. J. Radiat. Phys. Chem.*, in press.

Electron Spin Resonance Characterization of Superoxide Ions in Some Oxygenated Apatites

J. Dugas*

Département de physique, Université Mohammed V, Faculté des Sciences, Rabat, Morocco

and C. Rey

Laboratoire de Physico-Chimie des Solides et des Hautes Températures, 31078, Toulouse, France *(Received April 14, 1976; Revised Manuscript Received March 16, 1977)*

Electron spin resonance studies of calcium, strontium, and barium phosphate and arsenate oxygenated apatites containing superoxide ions were used to determine the position and the orientation of these ions in the channels of the apatite lattice. The angle between the O_2^- bond and the c axis was studied in the different compounds.

Introduction

The apatites constitute a large family of isomorphous compounds which may be found in phosphate rocks and in calcified tissues. They correspond to the general formula

$$Me_{10}(XO_4)_6Y_2$$

$Me^{2+} = Ca^{2+}, Sr^{2+}, Ba^{2+}, \ldots$
$XO_4^{3-} = PO_4^{3-}, AsO_4^{3-}, VO_4^{3-}, \ldots$
$Y_2^{2-} = 2F^-, 2Cl^-, 2Br^-, 2OH^-, CO_3^{2-}, O^{2-}, O_2^{2-}, \ldots$

The apatites generally crystallize in a hexagonal system (spatial group $P_{6_3/m}$). The structure of calcium hydroxylapatite, for instance, was described by Kay et al.[1]

The most important feature in this structure is the presence of channels running along the c (6_3) axis. These channels may be empty, or partially or completely filled with Y ions which form linear chains. They also may be partially occupied by molecular oxygen, as shown recently.[2] These apatites are referred to as oxygenated apatites. Moreover their channels contain OH^-, O_2^{2-}, O_2^-, ...,[3] the latter being observed by ESR.[4]

In this paper electron paramagnetic resonance studies of O_2^- superoxide ions in the channels of calcium, strontium, and barium phosphate and arsenate oxygenated apatites are presented. For the sake of simplification we shall henceforth call (P,Ca)Ap the oxygenated apatite whose skeleton is built with phosphate and calcium, (As,Ba)Ap the one built with arsenate and barium, etc.

The superoxide ion has been intensively studied either in single crystals of alkali halides[5-7] and alkaline earth fluoride[8] or absorbed at the surface of powdered samples of MgO,[9] ZnO, and TiO_2[10] as implied by catalytic processes. In every case it was ascertained that the axial molecular symmetry was lowered by the crystalline environment.

Sample Preparation

Oxygenated apatites were precipitated by dropwise addition of an alkaline earth nitrate solution (70 mL, 0.125 M) into a stirred solution of diammonium hydrogen phosphate (or arsenate) (700 mL; 0.010 M) containing hydrogen peroxide (10%). All reagents were analytical grade. Precipitations were performed at 80 °C with pH values of 11.8. The products were separated by filtration or centrifugation, washed, and dried at room temperature.

X-ray analysis has shown the precipitates to be pure apatites. Hexagonal a and c parameters were determined using NaCl (a = 5.6402 Å) as an internal standard. The values thus obtained are reported in Table I.

Experimental Results

The difficulty of obtaining, till now, sufficiently large single crystals of these apatites has lead us to study ESR spectra of powdered samples and thus there is a great loss of information. Such averaged spectra, without hyperfine structure, present only lines corresponding to the "**g** tensor" principal components and thus give only some pictures of the symmetry of the defect.

In this work the ESR spectra were obtained with a conventional X-band homodyne spectrometer built in the Laboratoire de Physique des Solides, Toulouse. The frequency of the magnetic field modulation was 100 kHz. Measurements have been achieved either at room temperature or at liquid nitrogen temperature using a Varian variable temperature accessory. In this last case, the intensity of spectra was strongly enhanced. For both the barium apatites (P,Ba)Ap and (As,Ba)Ap spectra are observable only at liquid nitrogen temperature.

All spectra are characteristic of an anisotropic g factor with two generally well-resolved components, except for (As,Ca)Ap. g values are given in Table I also. We shall see later that with such g values so close to the free electron one, there may exist two distinct values for g_x and g_y, but they are not resolved. The low field line (corresponding to g_z) is generally anomalously broader and flatter than those attributable to the perpendicular (g_x and g_y) component. Moreover, in the (As,Ca)Ap spectra, the main line is widened on its low field side and it is very difficult to determine a correct g_z value. For the apatites the spectra are very intense, especially at low temperature, indicating

* On leave from Laboratoire de Physique des Solides, Université Paul Sabatier, Toulouse, France.

TABLE I

Apatite	(P,Ca)	(P,Sr)	(P,Ba)	(As,Ca)	(As,Sr)	(As,Ba)
a, Å	9.47_0	9.80_9	10.22_5	9.87_5	10.09_3	10.51_5
c, Å	6.88_0	7.28_7	7.73_0	6.94_1	7.40_2	7.82_5
g_z	2.05_8	2.08_1	2.14_7	2.0_6	2.09_0	2.15_8
$g_x = g_y$	2.00_3	2.000_2	1.99_8	2.00_1	2.001_5	1.99_9
L_1	4.101	4.247	4.427	4.276	4.370	4.553
L_2	4.176	4.392	4.634	4.259	4.479	4.714
L_1/L_2	0.982	0.967	0.955	1.004	0.975	0.966
tan 2α	0.028	0.039	0.072	0.03	0.044	0.078
Δ/λ	35.8	25.6	13.9	33.	22.7	12.8
$a/2c = \tan\theta$	0.688	0.673	0.661	0.711	0.682	0.672

the presence of a great number of centers in the samples. Such a density may explain the anomalous broadening of the lines.

The g_z values in Table I lead us to ascertain that the g shift regularly grows in both series from (P,Ca)Ap to (P,Ba)Ap and from (As,Ca)Ap to (As,Ba)Ap, and that there are only very slight differences between phosphate and arsenate apatites having the same alkaline-earth metal.

Interpretation

The more detailed ESR study on O_2^- superoxide ions, due to Känzig et al.,[5] has been carried on a wide series of alkali halides.

The free molecular O_2^- ion has an unpaired electron in a Π_g orbital, so its ground state is an orbitally degenerate $^2\Pi^*_g$.

If, as it might be thought at first sight, the superoxide ions were lying in the apatite channels with their internuclear O–O axis (that we shall label O_z) parallel to the c crystal direction, that is to say in C_3 symmetry, this degeneracy would largely contribute to the g factor. The "g tensor" components might reach $g_x = g_y = 0$ and $g_z = 4$. Actually the obtained g values mean that the electronic spin almost alone plays a part in the interaction of the paramagnetic center with the static magnetic field. Thus the orbital momentum must be nearly quenched. For this, the molecular Π_g orbital must be split. That may happen if an external crystal field lowers the molecular symmetry. Such a crystal field can be seen by the superoxide ion only if its internuclear O_z axis is inclined with respect to the c direction in the apatite channel.

Then the important question arises: what is the superoxide ion position in the channel? It is well known that in various apatites, the anion position in the channel changes with its nature. For instance, in calcium phosphate fluoroapatite, fluoride ions are located along the c axis at $c/4$ and $3c/4$. In chloroapatite, the chloride ions sit roughly in the middle of triangles formed by oxygens of phosphate ions.

In our case, if the O_2^- ion was centered in the middle of alkaline-earth triangle, for symmetry reasons, attractive and repulsive forces would keep it parallel to the c axis. We have seen that such a possibility must be discarded. A more favorable situation occurs when the ion is located in the channel at the $z = c/2$ level. Then, it is at the center of an octahedron formed by six alkaline-earth cations (Figure 1). If we assume the relative position of Me^{2+} along the a axis is the same in oxygenated apatites as in the other apatites ($x_{Me} = a/4$),[1,11] we are able to compute the dimension of each edge of the octaedron. These edges can be grouped into two series of equal length, either parallel to the (00.1) plane or not. If we label the edge length L_1 in the former series, L_2 in the latter one, we find

$$L_1 = a\sqrt{3}/4 \qquad L_2 = \sqrt{(a/4)^2 + (c/2)^2}$$

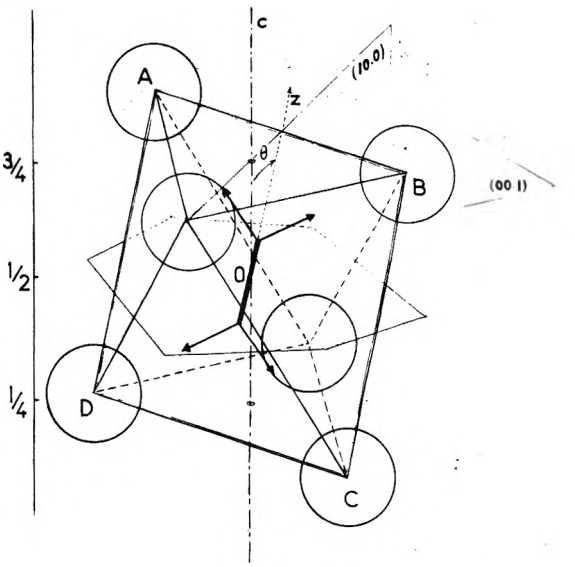

Figure 1. Proposed orientation of an O_2^- superoxide ion in the channel of an oxygenated apatite. The circles represent the alkaline earth ions forming an octahedron. The six corners of the warped hexagon are at the sites of oxygens belonging to phosphates (or arsenates) ions around the channel. The arrows are drawn for the lobes of the antibonding Π g_x orbital.

The L_1 and L_2 values corresponding to the different apatites are also given in Table I. The ratio L_1/L_2 is 1 for a regular octahedron. We can see that in the apatites studied the octahedron formed by six Me^{2+} ions surrounding the channels is nearly regular. It is only slightly stretched along c for all the apatites except (As,Ca)Ap. This situation looks like the one existing in some alkali halides where the O_2^- ions are exactly at the center of a regular octahedron of alkaline ions.[6]

Considering the above position along the c axis, the orientation corresponding to an energy minimum consists in placing the superoxide ion along a median of a Me^{2+} rectangle such as ABCD (Figure 1). Indeed in this case the lobes of the Π g_x molecular orbital are oriented toward Me^{2+} cations and the energy of this orbital is lowered; on the other hand, the energy level of the Π_{g_y} orbital, directed toward oxygen atoms, is higher. As only the Π_{g_x} orbital is completely filled it appears that this position leads to a lowering of energy. Moreover the superoxide ion can be assumed to lie along the median of the rectangle ABCD which is parallel to the AD side (i.e., the median of the ABCD rectangle which lie in the 10.0 plane) and never along that which is parallel to the AB side (i.e., the median which is perpendicular to the c axis); in this last case, indeed the ion would lie entirely inside a warped hexagon formed by six oxygens and its energy would be increased. Moreover the available space is generally slightly larger in the first position than in the last one (except for (AsCa)Ap).

In this hypothesis O_2^- makes an angle θ with the c axis. This angle would be 35° 16′ for a regular octahedron. In the apatites it is given by the relation

$$\tan \theta = a/2c$$

and can be calculated from the crystallographic parameters for every apatites (Table I, last line). Furthermore for symmetry reasons there may exist three directions for the superoxides, one in each of the three planes equivalent to 10.0 (i.e., 10.0, 01.0, $\bar{1}\bar{1}$.0). If the transition from one site to another by a $2\pi/3$ rotation about the c axis does not require a large energy, successive thermal jumps could contribute to the anomalous width of the "g_z lines" whose positions, as we shall see, are most sensitive to crystal field variations.

To describe the system, as Zeller and Kanzig[6] have already done, we take eigenfunctions of the free molecule as basis functions. Two terms whose effects are opposite are taken as perturbations: the crystal field which splits the orbitaly degenerate doublet in two sublevels $^2\Pi_{g_x}$ and $^2\Pi_{g_y}$ and thus quenches the orbital angular momentum; the spin–orbit interaction which tends to unquench it again.

If $^2\Pi_{g_x}$ is the lowest orbital level arising from the doublet, it is still spin degenerate. This ultimate degeneracy is completely removed by the external magnetic field in the ESR experiment. We can write both spin sublevels as

$$|\psi_+\rangle = \cos\alpha\,|\Pi_{g_x}, +\rangle + i \sin\alpha\,|\Pi_{g_y}, +\rangle$$

$$|\psi_-\rangle = \cos\alpha\,|\Pi_{g_x}, -\rangle - i \sin\alpha\,|\Pi_{g_y}, -\rangle$$

with α defined by $\tan 2\alpha = \lambda/\Delta$, the ratio of the spin–orbit parameter λ to the crystal field splitting Δ.

The ESR transitions occur between these sublevels so that, to a first approximation, we can obtain the "g tensor" components as

$$g_x = g_e \cos 2\alpha + A \cos 2\alpha - B(1 - \sin 2\alpha)$$

$$g_y = g_e \cos 2\alpha + A \cos 2\alpha + B(1 - \sin 2\alpha)$$

$$g_z = g_e + 2 \sin 2\alpha$$

where A and B are sums of matrix elements between ground and excited states divided by the corresponding energy differences. The smaller these constants are, the more the x and y components of g approach one another. By this way we explain the observation of a single unresolved line for g_x and g_y components in our powdered samples. Besides these components are too near to g_e and too sensitive to poorly localized excited states to arrive at any conclusion.

On the other hand, using the g_z experimental values we can calculate sin 2α and then evaluate the variations of the crystal field effect Δ when the crystal parameters change from one apatite to another. In Table I we reported the different values of tan 2α and $\Delta/\lambda = 1/\tan 2\alpha$ obtained from the measurements of g_z. The spin–orbit coupling parameter λ is characteristic of O_2^- and may be assumed constant in all the apatites. So we can represent $\Delta \propto 1/\tan 2\alpha$ vs. the tangent of the slope angle θ of the superoxide ion on the c axis. This is done in Figure 2. One obtains two different curves for phosphate and arsenate apatites. The representative points of the first series are aligned. The (As,Sr)Ap and (As,Ba)Ap points are on a parallel line but the (As,Ca)Ap point is not. This exceptional behavior may be associated, at the same time, with the difficulty of measuring g_z and with the L_1/L_2 ratio which we showed to be greater than 1 for this apatite alone. Does it mean that in (As,Ca)Ap superoxide ion has a different orientation? At present we are not able to answer this. In all the other cases the crystal field splitting seems to be proportional to tan θ and grows with the slope of the superoxide on the c axis. On another hand the two lines are shifted with respect to each other; for a given alkaline earth, the crystal field is more important for phosphates than for arsenates. That may be well understood taking into account the relatively greater size of the arsenate ions.

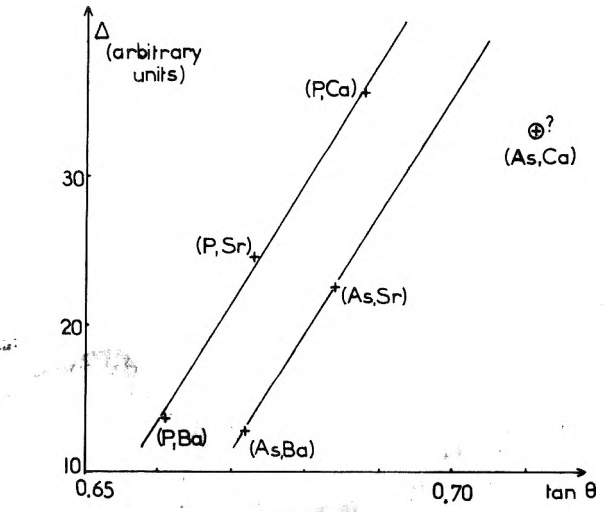

Figure 2. Variation of the crystal field parameter vs. the slope of the O_2^- molecular axis in the apatite channel.

These conclusions are quite in agreement with the model proposed for the superoxide ion in apatites.

Conclusion

In this work the O_2^- superoxide ion was studied by electron paramagnetic resonance in six different oxygenated apatites. For five of them, in spite of using powdered samples, an extended interpretation of the experimental results permits the determination of the position of these ions in the channels and to propose a model in which the O–O axis is inclined with respect to the c axis of the apatites.

Within the precision of our measurements, the crystal field effect appears to be proportional to the tangent of the angle between the molecular and channel axes. However, it must be said that the variation of this angle is weak enough on the whole set of studied apatites to consider this proportionality only as a first approximation.

The calcium arsenate oxygenated apatite constitutes a particular case. Here the flattening of the calcium octahedron around the channel perhaps permits the superoxide ion to take a lot of bearings. Then that could give greater values for Δ and consequently a lot of g_z nearer of g_e. That might correspond to the observed broadening of the line on the low field side. However, at this time, this possibility remains a purely hypothetic explanation.

References and Notes

(1) M. I. Gay, R. A. Young, and A. S. Posner, *Nature (London)*, **208**, 1050 (1964).
(2) C. Rey and J. C. Trombe, unpublished results.
(3) C. Rey, J. C. Trombe, and G. Montel, *C.R. Acad. Sci., Ser. C*, **273**, 1081 (1971).
(4) J. C. Gourdon, C. Rey, C. Chachaty, J. C. Trombe, and J. Pescia, *C.R. Acad. Sci., Ser. B*, **276**, 559 (1973).
(5) W. Kanzig and M. H. Cohen, *Phys. Rev. Lett.*, **3** -11, 509 (1959).
(6) H. R. Zeller and W. Kanzig, *Helv. Phys. Acta*, **40**, 845 (1967).
(7) R. T. Shuey and H. R. Zeller, *Helv. Phys. Acta*, **40**, 873 (1967).
(8) H. Bill, *C.R. Seances Soc. Phys. Hist. Nat. Geneve*, **5** -2-3, 165 (1970).
(9) A. J. Tench, T. Lawson, and J. F. J. Kibblewhite, *Trans. Faraday Soc.*, **68**, 1169 (1972).
(10) J. H. Lunsford and J. P. Jayne, *J. Chem. Phys.*, **44**, 1487 (1966).
(11) C. Feltin and P. Charpin, *C.R. Acad. Sci.*, to be published.

An Electron Paramagnetic Resonance Study of Manganese(II) in the Aragonite Lattice of a Clam Shell, *Mya arenaria*

L. K. White, A. Szabo, P. Carkner, and N. D. Chasteen*

Department of Chemistry, University of New Hampshire, Durham, New Hampshire 03824 *(Received January 3, 1977)*

Publication costs assisted by the National Science Foundation

The electron paramagnetic resonance spectra of Mn(II) in the aragonite lattice of clam shell, *Mya arenaria*, is examined at X-band (9.5 GHz) and Q-band (35.0 GHz) frequencies. The powdered and oriented section EPR spectra for the nine-coordinate, low symmetry site can adequately be interpreted with the spin Hamiltonian: $\mathcal{H}_S = g_{iso}\beta B\cdot S + A_{iso}(I\cdot S) + D(S_z^2 - {}^1/_3S(S+1)) + E(S_x^2 - S_y^2)$. The EPR parameters obtained from perturbation expressions are $g_{iso} = 2.006 \pm 0.001$, $A_{iso} = 94 \pm 1.0$ G, $D = 250 \pm 10$ G, and $E = 42 \pm 5$ G. Approximate directions for the principle zero-field splitting tensor axes with respect to the c crystallographic axis are also obtained. Finally, the ordering of the aragonite microcrystallites with respect to the clam shell's morphology has been determined. The only preferential orientation for the aragonite microcrystallites is with their c axes normal to the shell surface.

Introduction

Manganese(II) doped into calcite, the most stable mineral form of $CaCO_3$, has been extensively studied by electron paramagnetic resonance (EPR) spectroscopy.[1-7] On the other hand, Mn(II) in the thermodynamically less stable mineral aragonite has escaped examination because it is difficult to obtain isomorphous substitution of Mn(II) for Ca(II). Mn(II) in aragonite is normally found associated with small regions of calcite.[8] Mn(II) readily substitutes for Ca(II) in calcite since $CaCO_3$ (calcite) and $MnCO_3$ (rhodochrosite) are isomorphous with the same unit cell parameters.[10]

Recently, we have become interested in the EPR spectra of trace transition metals in the exoskeletons of marine organisms and have observed an unusual Mn(II) spectrum with sea shells comprised of aragonite. As will be demonstrated, these Mn(II) signals arise from the unusual circumstance of isomorphous replacement of Ca(II) in the aragonite lattice. Apparently, Mn(II) can be doped into aragonite formed during the biomineralization process of shell formation whereas substitution of Mn(II) for Ca(II) in this mineral does not appear to be possible in normal geological processes.

Sea shells are found as two common mineral forms of $CaCO_3$, calcite and aragonite. The crystal structures of calcite and aragonite and their interconversion have been studied extensively.[8-12] Aragonite shells and aragonite mineral deposits are known to undergo a slow metamorphosis into calcite. Heating aragonite at temperatures greater than 400 °C produces an irreversible conversion to calcite without any apparent change in crystalline morphology. Essentially, the calcium atom positions remain fixed and only a reorientation of the CO_3^{2-} anions produces the change from aragonite to calcite. The crystallographic c axis in aragonite converts to the c hexagonal axis in calcite, i.e., the threefold rotation axis. The Ca^{2+} sites in calcite have localized D_{3d} symmetry, with six nearest-neighbor oxygen atoms while the Ca^{2+} site in aragonite has nine nearest-neighbor oxygen atoms with C_s symmetry. Here, in the clam shell of *Mya arenaria* we have the opportunity to observe the Mn(II) doped into an unusual, nine-coordinate, low-symmetry site.

Experimental Section

X-band (9.5 GHz) spectra were recorded with a Varian E-4 spectrometer. Q-band (35.0 GHz) spectra were recorded on a Varian E-9 spectrometer with high-field pole caps. DPPH ($g = 2.0036$) was used as the standard field marker. The magnetic fields were calibrated with a hydrogen/lithium NMR probe. Specimens were gathered from Hampton Beach, N.H., and typically contained 10 ppm Mn as determined by atomic absorption spectroscopy.

Results

A. *EPR Spectra.* The EPR spectra of oriented sections of shells *Mya arenaria* were taken in three mutually perpendicular planes at 10° intervals at both X-band and Q-band frequencies. The three mutually perpendicular planes (1, 2, 3) are shown in Figure 1, in relation to the clam shell's morphology. Only the $M_S = -1/2 \leftrightarrow 1/2$ transitions were observed for our oriented clam shell. The relative intensity of Mn(II) lines is weaker than that observed for calcite shells.[13] The line widths are also broader due to misaligned crystallites in the shell and a larger zero-field splitting term. The X-band EPR spectra appear to be very complex (Figure 2) but many of the observed features are due to the forbidden, $\Delta M_I \neq 0$ transitions. The $\Delta M_I = \pm 1$ forbidden lines, here called *secondary* lines, are observed at some orientations with intensities exceeding those of the allowed $\Delta M_I = 0$ transitions, here called *primary* lines.

The intensity of the forbidden lines is dependent upon the relative magnitude of the zero-field splitting term, D, in relation to the electronic Zeeman term. At Q-band microwave frequencies (35 GHz), the magnitude of D remains constant while the electronic Zeeman term is approximately a factor of 4 larger than at X-band (9.5 GHz). Thus, the relative magnitude of D in relation to the electronic Zeeman term is less and a dramatic reduction in the forbidden lines' intensity is observed in Q-band EPR spectra[14] (Figure 3). At Q-band frequencies the spectra are much less complex and the *primary* lines can easily be distinguished from the *secondary* lines.

The EPR spectra observed in plane 1 (see Figure 1) were invarient with orientation. X-band and Q-band spectra taken in planes 2 and 3 were anisotropic and showed the *same* orientation dependence. At least two magnetically nonequivalent sites are observed in these planes consistent with structure of the aragonite lattice.[11] EPR spectra of powdered clam shell samples were also recorded at X-band and Q-band frequencies (see Figures 4 and 5). The oriented shell and powdered Mn(II) EPR spectra can be

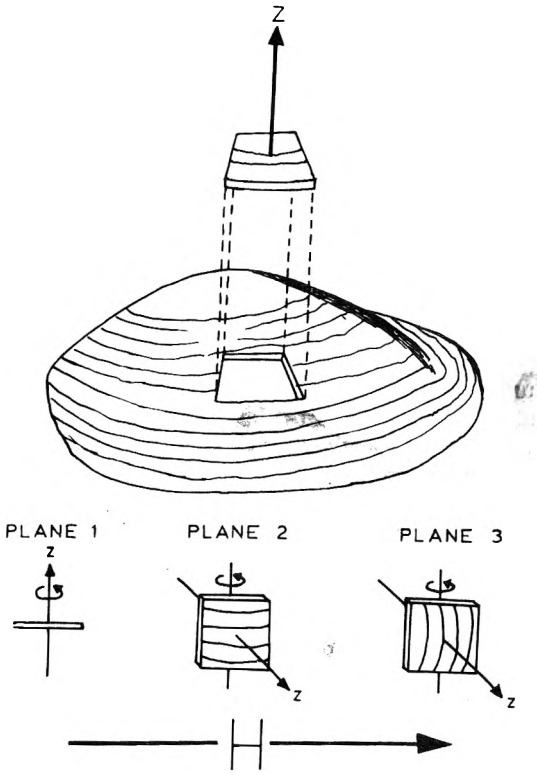

Figure 1. The three mutually perpendicular planes in which EPR spectra were recorded are shown with respect to the clam shell's morphology. The z axis is considered to be normal to the shell surface. Plane 1 has the z axis perpendicular to the applied field at all orientations. Planes 2 and 3 both contain the z axis orientation.

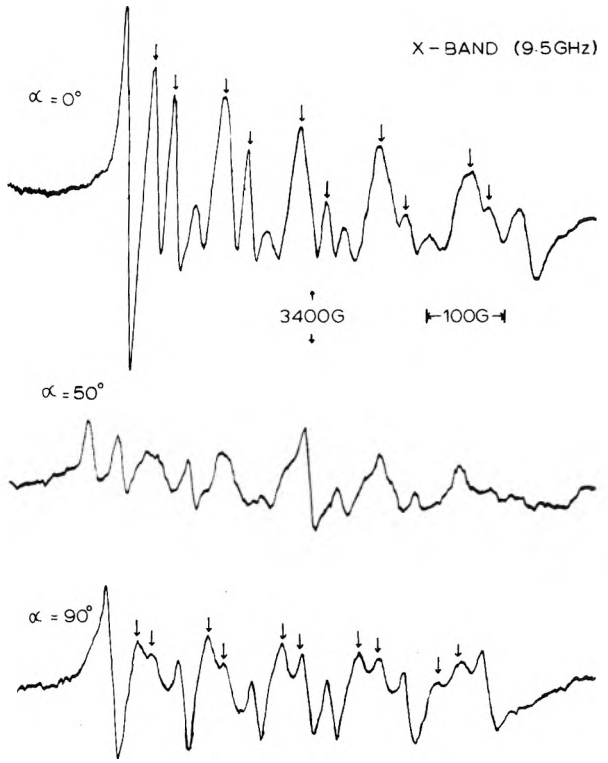

Figure 2. Selected X-band spectra recorded in plane 2 (or 3) are shown. The angle α refers to the angle between the z axis and the applied magnetic field. The microwave frequency is 9.534 GHz. The modulation amplitude is 5 G with 100-kHz modulation frequency. Arrows denote secondary (forbidden) lines.

interpreted with an isotropic electronic Zeeman and hyperfine interaction and a much larger zero-field splitting, D value, than is observed for Mn(II) doped into calcite (see Table I). Since the cation site in aragonite has low

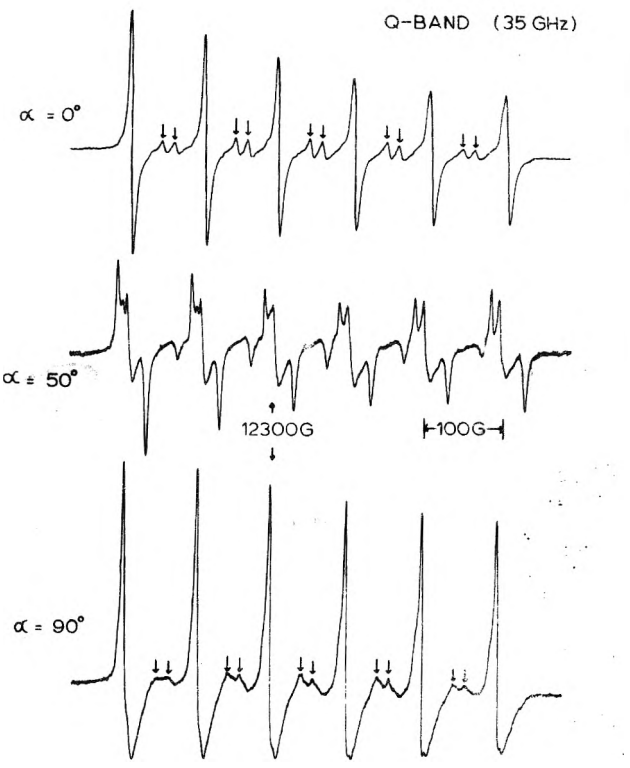

Figure 3. The corresponding Q-band EPR spectra at the same α orientations as shown in Figure 2. The microwave frequency is 34.672 GHz. The modulation amplitude is 5 G with a 100-kHz modulation frequency. Arrows denote secondary (forbidden) lines.

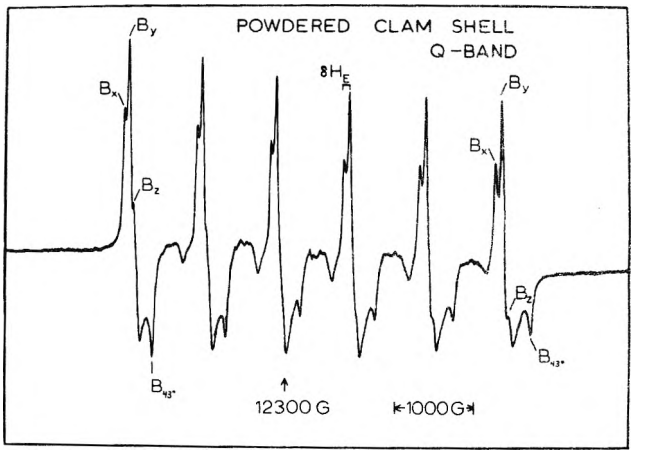

Figure 4. The Q-band powdered clam shell EPR spectrum. The microwave frequency is 34.688 GHz. B_z, B_x, B_y, and $B(43°)$ are marked. Note the splitting of the low field $\theta = 90°$ feature ($B_x - B_y = \delta H_E$) due to the E asymmetry term.

TABLE I: EPR Parameters for Calcite and Aragonite

	g_{iso}	A_{iso}, G	D, G
Calcite[a]	2.0018	−94 ± 1.0	91 ± 1.0
Aragonite[b]	2.006 ± 0.001	(−)94 ± 1.0	250 ± 10.0
			E = 42 ± 5.0

[a] Reference 7. [b] This work.

symmetry, the higher order crystal field terms for Mn(II), $S = 5/2$, are possible, but our EPR spectra can be interpreted with only the zero-field splitting terms, D_z, D_x, and D_y, in addition to the Zeeman and the nuclear hyperfine interactions. The spin Hamiltonian is

$$\mathcal{H}_S = g_{iso}\beta B\cdot S + A_{iso}(I\cdot S) - D_z(S_z^2) - D_x(S_x^2) - D_y(S_y^2)$$

Because the zero-field splitting tensor is traceless (i.e., D_x

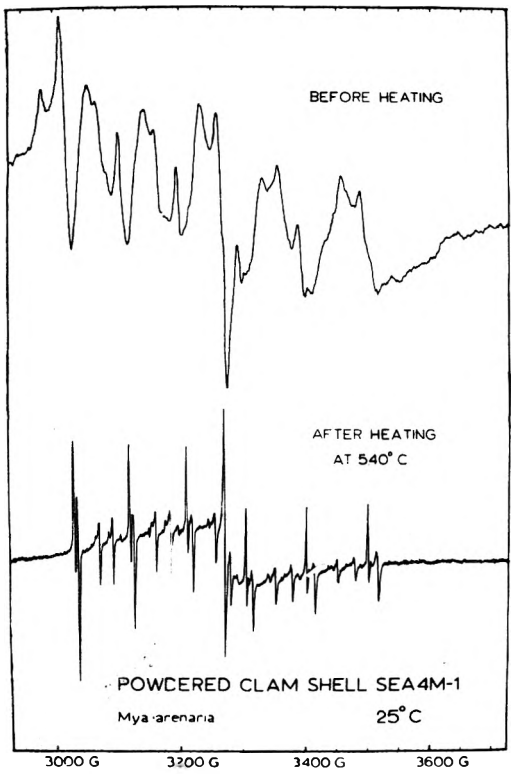

Figure 5. The X-band powdered clam shell EPR spectrum. The top scan is the Mn(II) in aragonite spectrum before heating. The bottom scan is the Mn(II) in calcite spectrum after heating.

$+ D_y + D_z = 0$), only two parameters, D and E, are necessary, where $D = {}^1/_2(D_x + D_y) - D_z$ and $E = -{}^1/_2(D_x - D_y)$. Thus, we have the spin Hamiltonian

$$\mathcal{H}_S = g_{iso}\beta B\cdot S + A_{iso}(I\cdot S) + D(S_z^2 - {}^1/_3 S(S+1)) + E(S_x^2 - S_y^2)$$

A_{iso} and g_{iso} are, respectively, the isotropic metal hyperfine parameter and the isotropic g value. B is the magnetic field inside the sample.

Although the orientation dependence of the *primary* $M_s = -1/2 \leftrightarrow 1/2$ line positions is more substantial at X-band frequencies, the Q-band powder and oriented shell spectra were analyzed in the most detail since the resonance lines are sharper than observed at X-band and their *primary* lines are not obscured by forbidden lines. The third-order perturbation treatment for the axial case outlined in our previous calcite shell studies[13] and elsewhere,[1,15,16] along with second-order perturbation treatment for the rhombic case,[17,18] was used to obtain EPR parameters from the line positions of the *primary* lines in the Q-band powder spectrum (Figure 4). Essentially, A_{iso} was obtained from the spacing between the hyperfine lines and g_{iso} from the center of the parallel ($\theta = 0°$ feature, B_z) hyperfine manifold. D was estimated from the second- and third-order zero field splitting of the primary $M_S = -1/2 \leftrightarrow 1/2$ parallel line, B_z, and the high field line ($\theta \approx 43°$), B (43°), feature. E was estimated from the splitting of the $\theta = 90°$ orientation powder feature, $(B_x - B_y)$, using second-order terms (i.e., $\delta H_{90°} \approx 8DE/B_0$, $B_0 = h\nu/g\beta$).[19] Our parameters are listed in Table I. The principal features of the spectra from oriented shell samples are in accord with the parameters in Table I.

No attempt was made to analyze the *secondary* lines, since at most orientations the primary resonances of at least two magnetic sites overlap them. The absolute nor the relative signs of A_{iso} and D can be determined from our data. In addition, since the aragonite metal site bears little resemblance to the metal site of calcite, it is conceivable that the sign of D may be different than that observed for Mn(II) in a calcite lattice.

B. *Orientation of the Aragonite c-Crystalline Axis.* Oriented shell fragments do not exhibit well-defined precession photographs and consequently the orientation of the aragonite c-crystallographic axis cannot be determined directly from x-ray diffraction studies. However, we were able to use the conversion of aragonite into calcite to obtain information about the aragonites lattice's orientation. A clam shell was heated at 540 °C for 1 h. No loss of the shell's morphology was observed and an x-ray powder pattern confirmed complete conversion to calcite. Figure 5 shows the powdered, X-band, Mn(II) EPR spectrum before and after heating. A subsequent EPR study of oriented sections of our now calcite clam shell also showed the sharp well-known Mn(II) in calcite anisotropic spectrum.

By measuring the EPR spectrum of the converted shell as a function of angle as outlined previously,[13] the c hexagonal axis of calcite was determined to be normal to the shell surface which is the same as the c axis of aragonite (see Introduction). The immediate conversion of the aragonite Mn(II) spectrum to the calcite Mn(II) spectrum is strong evidence that Mn(II) replaces the Ca(II) in aragonite.

From x-ray structural data[10,11] both of the magnetic sites are equivalent in aragonite, when the c axis is parallel to the applied magnetic field. Our oriented section EPR spectrum at this orientation show just one set of resonances.

No information can be obtained about the preferential orientation of the a and b aragonite crystal axes from calcite conversion studies, since the metal site in calcite has axial symmetry. However, examination of the EPR spectra of oriented sections of the aragonite shell in plane 1 (i.e., where the a and b crystalline axis would lie in aragonite's orthorhombic P_{mcn} space group) reveals little or no variation in the spectra. This observation, along with the *same* anisotropic behavior being observed in the EPR spectra taken in planes 2 and 3, leads us to believe that there is a random orientation of the a and b axes in the aragonite lattice of the shell. The only preferential orientation of the microcrystallites is along the c axis. This conclusion is confirmed by the observation that thin shell sections do not extinguish when viewed down the c axis under a polarizing microscope. The peculiar asymmetric line shapes and the numerous features associated with a single resonance at most orientations is consistent with this type of random orientation behavior.

Accordingly, we conclude that, with oriented samples, we are observing a partially powder-like spectrum of many orientations. The principal D_z axes of all the microcrystallites form a "ring" of orientations about the c aragonite axis with each D_z axis being tilted at a constant angle, α_D, away from c.

C. *Orientation of the Principal Zero-Field Splitting Tensor Axes.* The aragonitic clam shell, having order only along the c axis, makes the normal detailed single-crystal analysis to determine the directions of the rhombic zero-field tensor axes difficult. However, by using the site symmetry of the aragonite cation site, C_S, and an analysis of the EPR spectra of two specific orientations of sections of the clam shell, we can obtain some information about the directions for the principal D axes.

The *bc* plane is the reflection plane of symmetry for the aragonite cation site; thus two of the principal D tensor axes must lie in this plane and the third must be normal

to this plane (i.e., coaxial with the crystallographic a axis). We have been able to determine the orientation of the principal D_z axis with respect to the c axis, α_D, by analyzing the orientation dependence of the line positions of the *primary* resonances. However, at most orientations the *primary* lines have several features associated with a "powder" spectrum. A superficial analysis is difficult because these "powder" features are dependent upon both the angle, α_D (i.e., between the principal D_z axis and the crystallographic c axis) and the angle, θ, between the magnetic field direction and the D axes of every microcrystallite. However, it is sufficient for our purposes to look at the one magnetic field orientation where all the microcrystallites appear to be magnetically equivalent, $\alpha = 0°$.

At this orientation the line position is approximately 3-G upfield from the $\theta = 0°$ line position, B_z. The $\theta = 0°$ can easily be computed since it is independent of the values of D and E. Any upfield line position has two possible orientations as shown in Figure 7 of ref 13. Our computations show the two choices are: $\theta = 9 \pm 1°$ or the region near $\theta \approx 65 \pm 5°$. The expected orientation dependence of the intensities of the *secondary* lines can help us choose the proper α_D. With axial symmetries the intensity of the secondary lines have a $(\sin 2\theta)^2$ dependence[14,15] (i.e., zero intensity at $\theta = 0°$ and $\theta = 90°$ and a maximum intensity at $\theta = 45°$).[12,13] θ is the angle between the principal D_z axis of the zero-field tensor and the magnetic field vector. The addition of the E asymmetry parameter also gives the *secondary* lines intensity in the xy plane with a $(\sin 2\phi)^2$ dependence. When the applied magnetic field is parallel to c, $\alpha = 0°$, the *secondary* lines have a large intensity particularly at X-band frequencies, indicating that the principal D_z axis is a substantial angle away from the c axis. Thus, D_z tensor axis direction most likely has an $\alpha_D \approx 65 \pm 5°$. (For the alternate choice of $\alpha_D = 9°$ little or no intensity is expected for the secondary lines.)

What remains is to determine which tensor axis (D_x or D_y) also lies in bc plane. If we look at the $\alpha = 90°$ oriented shell spectrum (Figure 3) taken in plane 2 or 3, the $\theta = 90°$ B_y feature observed in Q-band powder spectrum (Figure 4) is strongly favored while the B_x feature is absent. The strongly favored feature in this powder-like spectrum must correspond to the principal D_y axis which *does not* lie in the bc plane. The principal D_x axis therefore lies in the bc plane and is tilted approximately 25° away from c, and thus the applied magnetic for the $\alpha = 90°$ orientation is always between 65 and 90° away from D_x; accordingly the B_x feature contributes very little to the $\alpha = 90°$ spectrum. The high field D_y feature therefore dominates the spectrum at $\alpha = 90°$. Thus, D_y is coaxial with the crystallographic a axis and D_x is in the bc plane, for a positive E parameter.

In spite of obtaining approximate directions for the principal D tensors with respect to the aragonite c crystallographic axis, we still cannot assign with certainty the directions relative to the b crystallographic axis. Two choices still exist for the D_z and D_x directions in bc plane. Figure 6 shows one choice for the orientation of the principal D axes with respect to the cation site in aragonite. D_z is tilted $65 \pm 5°$ away from c and D_x $25 \pm 5°$ away from c. As a reference, projections of the Ca–O bond vectors on to the bc plane[11] make the following angles with respect to c axis: Ca–O(1), 32.4°; Ca–O(5), 22.2°; Ca–O(3), 61.9°; Ca–O(4), 67.3°; and Ca–O(2), 3.6°. The other choice for D_z and D_x tensors directions would be the reflection of the D_z and D_x axes through the ac plane. The D_y axis is coaxial with the a axis in both cases. We choose not to speculate about the correct choice for the D_z and D_x directions at this time.

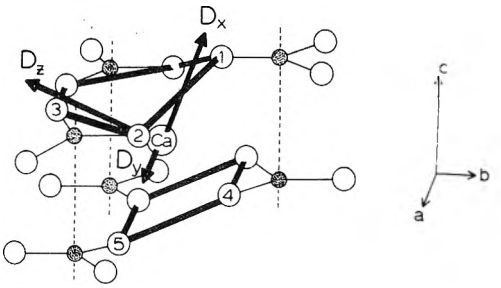

Figure 6. The metal site of the aragonite lattice is shown with one of the two possible choices for the principal D_z and D_x directions. The solid circles are carbon atoms, the open circles oxygen atoms. The five- and four-membered rings above and below the calcium atom depict the cation site. The dashed lines are coaxial with c. The Ca atom and O(1) lie in the bc reflection plane. D_z and D_x also lie in the bc plane with D_y being coaxial with a.

Discussion

A comparison of the EPR parameters of the Mn(II) doped in calcite and aragonite lattice (see Table I) shows that the zero-field splitting parameters, D, are substantially different. In S state ions, D reflects the deviation of the crystalline electric field from spherical symmetry. In the calcite lattice there is a trigonal distortion from octahedral symmetry; the crystal field has been elongated along the threefold axis. It is not particularly surprising that the low-symmetry aragonite lattice has a large zero-field splitting parameter. Indeed, the cation site is distorted substantially from a spherical crystalline electric field. The large E asymmetry parameter is a further reflection of the low-symmetry site. For aragonite we find that $E/D = 0.17$. An E/D ratio of 0.333 corresponds to a completely rhombic ligand field.

The similar magnitudes of the isotropic metal hyperfine coupling constant, A_{iso}, of Mn(II) in calcite and aragonite is also noteworthy. The spin polarization mechanism gives rise to the expected negative sign for A_{iso} in Mn(II) complexes.[20] The magnitude of A_{iso} is also sensitive to covalency of donor atoms,[18,21,22] i.e., the amount of spin density delocalized onto the ligands. With increased covalency a smaller A_{iso} value is observed. Since the average Ca–O bond distance in aragonite is 2.53 Å compared to the calcite Ca–O bond distance of 2.36 Å, one might expect a substantially different A_{iso} for the two lattices. However, in fact, the A_{iso} for aragonite and calcite lattices are the same within experimental error. The expected diminished covalency of a single Ca–O bond in aragonite is apparently made up for by the increased number of oxygen donor atoms (i.e., nine for the aragonite vs. six for calcite). It appears that although the cation sites differ appreciably in size, the Mn(II) spin delocalization (i.e., overall covalency) is nearly the same for both lattices.

Aside from information obtained about the Mn(II) site from the EPR parameters, we have used the anisotropic nature of the oriented shell section Mn(II) EPR spectra to elucidate the crystalline organization within a clam shell. The oriented shell section EPR spectra have been interpreted as a ring of D axis orientations about the c crystallographic axis of aragonite. It is known that exoskeletons of marine animals are made up microcrystallites separated from one another by an organic matrix. For our clam shell, there is obvious preference for the aragonite microcrystallites to orient themselves so that their c axes are normal to the shell surface. We have also shown that there is no ordering of the a and b axes. This random orientation behavior may be due to a random micro-

crystallite distribution and/or "twinning" of the aragonite lattice within the microcrystallites. Twinning on the (110) face is common in mineral aragonite deposits.[9]

It is reasonable to expect some crystalline organization with mineralized tissues, but perhaps not as much as in the minerals themselves. We have observed a similar preferencial orientation in the calcitic shells of the barnacle *Balanas balanoides*[23] and the mussel *Mytilus edulis*.[13] It is also evident from these Mn(II) EPR studies, as well as from microscopic examination of the exoskeleton, that some marine organisms have more organization within their exoskeletons than others. It may be possible to examine other more ordered aragonitic exoskeletons to further refine the Mn(II) EPR parameters and the principal zero-field splitting tensor directions.

Acknowledgment The authors thank the National Science Foundation, Grant No. CHE75-03475 A01, and the National Institutes of Health, Grant No. GM20194-05, for support of this research.

References and Notes

(1) F. K. Hurd, M. Sachs, and W. D. Hershberger, *Phys. Rev.*, **93**, 373 (1954).
(2) C. Kikuchi, *Phys. Rev.*, **100**, 1243 (1955).
(3) H. M. McConnell, *J. Chem. Phys.*, **24**, 904 (1956).
(4) C. Kikuchi and L. M. Matanese, *J. Chem. Phys.*, **33**, 601 (1960).
(5) J. A. Hodges, *J. Chem. Phys.*, **49**, 2857 (1968).
(6) V. Lupei, A. Lupei, and I. Ursu, *Phys. Rev. B*, **6**, 4125 (1972).
(7) G. E. Barberis, R. Calvo, H. G. Maldonado, and C. E. Zarate, *Phys. Rev. B*, **12**, 853 (1975).
(8) G. T. Fonda, *J. Phys. Chem.*, **44**, 435 (1940).
(9) H. A. Deer, R. A. Howie, and J. Zurrman, "Rock Forming Minerals", Vol. 5, "Non-Silicates", 1963, pp 230–255, 305–315.
(10) F. Lippman, "Minerals, Rocks, and Inorganic Materials", Vol. 6, "Sedimentary Carbonate Minerals", Springer-Verlag, New York, N.Y., 1973, pp 6–13, 53–66, and references therein.
(11) J. P. R. de Villiers, *Am. Mineral.*, **56**, 758 (1971).
(12) H. Shoji, *Z. Kristallogr.*, **84**, 74 (1932).
(13) S. C. Blanchard and N. D. Chasteen, *J. Phys. Chem.*, **80**, 1362 (1976).
(14) A. Abragam and B. Bleaney, "Electron Paramagnetic Resonance of Transition Ions", Oxford University Press, London, 1970, pp 186–205.
(15) F. Tsay, S. L. Manatt, and S. I. Chan, *Chem. Phys. Lett.*, **17**, 223 (1972).
(16) G. C. Upreti, *J. Mag. Reson.*, **18**, 287 (1975).
(17) A. Chatelain and R. A. Weeks, *J. Chem. Phys.*, **52**, 3758 (1970).
(18) G. M. Woltermann and J. R. Wasson, *Inorg. Chem.*, **12**, 2366 (1973).
(19) These expressions are not rigorously true for a rhombic powder pattern, but they give us a good estimate of the zero-field splitting parameters within the listed experimental errors.
(20) R. E. Watson and A. J. Freeman, *Phys. Rev.*, **123**, 2027 (1961).
(21) J. S. Van Wieringen, *Discuss. Faraday. Soc.*, **19**, 118 (1955).
(22) R. S. Title, *Phys. Rev.*, **136**, 623 (1963).
(23) S. C. Blanchard and N. D. Chasteen, to be published.

Positron Annihilation Studies on Coordination Compounds. 1. Investigation of Positron Lifetime and Angular Correlation of Annihilation γ Photons on the Mixed Complexes of Bis(dimethylglyoximato)cobalt(III) with Unidentate Ligands

K. Burger,[†] B. Lévay,[‡] A. Vértes,*[‡] and C. Várhelyi[§]

Institute of Inorganic and Analytical Chemistry and Institute of Physical Chemistry and Radiology, L. Eötvös University, Budapest, Hungary and Chemistry Department, Babes Bolyai University, Cluj, Roumania *(Received August 24, 1976; Revised Manuscript Received December 8, 1976)*

Positron annihilation investigation of bis(dimethylglyoximato)cobalt(III) mixed complexes formed with unidentate ligands, compared with ESCA results on the same complexes, suggested that the cobalt(III) central atom and the nitrogen donor atom of the parent complex have a negligible effect on the change of the positron lifetime. Mainly electrons of halide, pseudohalide, and S-bonded sulfite ion, each coordinated along the Z axis of the mixed complex, affect the annihilation rate of positrons. The positron lifetime decreasing effect of the unidentate ligands water, ammonia, nitrite, and organic bases was found to be negligible. It has been demonstrated that the positron lifetime decreases parallel to the increasing negative character of the halides I^-, Br^-, and Cl^- and to the increasing π-acceptor ability of S- and Se-bound pseudohalides SCN, SeCN. Halides bound in the outer coordination sphere have the effect of decreasing the positron lifetime lower than those in the inner sphere. The positron lifetime of mixed complexes containing one halide ion is longer than those containing two halides. Considering angular correlation data it seems that the localization of positrons on halide ligands decreases (the curves become narrower) in the order Cl^-, Br^-, I^-. From this respect pseudohalide ligands lie between Cl^- and Br^- in accordance with their optical electronegativity values. These results suggest the possible role of positron–halide and positron–pseudohalide bound states in the positron annihilation process.

Introduction

In the course of positron annihilation, generally two γ photons are produced each with an energy of 0.511 MeV corresponding to the rest mass of the electron–positron pair. The angle between the two emitted photons is nearly 180° to fulfill momentum-conservation requirements. The deviation from 180° is determined by the momentum of the electron–positron pair annihilating. Consequently the distribution of electron momenta can be obtained from the angular distribution curve.

Since the probability of positron annihilation depends very much on the electron density at the site of the positron, the rate of the annihilation process and the angular distribution of the annihilation γ photons are closely related to the electronic structure of the substance studied and are influenced very sensitively by its changes. Studying the annihilation process one can obtain information about the structure of the material; thus this

[†] Institute of Inorganic and Analytical Chemistry, L. Eötvös University.
[‡] Institute of Physical Chemistry and Radiology, L. Eötvös University.
[§] Chemistry Department, Babes Bolyai University.

method is becoming more widely used.[1]

The average lifetime of the positrons is a few tenths of a nanosecond in the condensed phase when the "free annihilation" of an electron–positron pair takes place. The annihilation process, however, can be preceded either by the formation of a bound state (e^+M) between a positron and an atom or molecule (M), or the formation of the lightest element, the positronium "atom" (Ps), which is a combination of a positron and an electron. When the spins of the electron and positron are parallel ortho-positronium (o-Ps) is formed and when the particle spins are opposite parapositronium (p-Ps) is formed. The average lifetime of o-Ps is 1.4×10^{-7} s in vacuo, and that of p-Ps is only 1.25×10^{-10} s.

In the condensed phase the relatively long lifetime of o-Ps decreases due to different interactions and falls generally into the 0.5–5-ns range. The formation of Ps in the medium is indicated quite often by the long lifetime component of the spectrum. In the case of angular correlation measurements the "narrow" component of the spectra resulting from the annihilation of p-Ps atoms indicates the formation of positronium.[1]

The fundamental processes of positron annihilation in liquids have been clarified already in many aspects. Mogensen's "spur" model[2] deals with the factors influencing the probability of positronium formation; in addition the rate of the pick-off annihilation of o-Ps atoms can be explained by the bubble model.[3] The chemical reactions of Ps atom are elucidated properly, and recently experiments were carried out for studying the chemistry of positrons as well.[4]

In solids (except metals, ionic alkali halides, metal oxides, and polymers) only a few systematic investigations have been made. Positron annihilation measurements carried out so far in solids attempted mainly the study of the correlation with the physical parameters of the substance. The effects of, e.g., vacancies, dislocations or collective imperfections (voids) in metals, F-centers in ionic crystals, the degree of crystallization of polymers, or the granule size of oxide powders on positron annihilation was investigated.[1]

It was shown that positron annihilation is very sensitive to the changes occurring in the physical state of the environment, and thus the method can be used with good results in an investigation of the physical structure of substances. At the same time the high sensitivity of this method to minor changes in the physical state makes it more difficult to study the chemical structure of the substance.

This kind of systematic measurements had not been made yet, and that is why we do not know too much about the correlations between the chemical structure of the substance and the parameters of positron annihilation in solids.

The aim of the present work is to study positron annihilation on solid coordination compounds where, if possible, only a few ligands of one parent complex can be exchanged with chemically considerably different ones in such way that the basic structure of the complex remains practically unchanged. Under such circumstances one can expect that the changes occurring in the parameters of the positron annihilation (lifetime, angular distribution) can be correlated mainly with coordination chemical changes.

For the first model system the mixed complexes of bis(dimethylglyoximato)cobalt(III) were chosen, which have already been investigated with different methods.[5]

Dimethylglyoxime forms square-planar complexes of high stability with transition metals. The two dioxime ligands are bound to the metal not only with coordinative bonds, but also to each other with H bonds. This structure hinders the binding of a third bidentate ligand to the central atom. The square-planar parent complexes are able to coordinate two unidentate ligands along their Z axis (e.g., hydroxide, halide, pseudohalide, or nitrogen base, etc.).[6-8] The nickel complex is an exception in this respect. The cobalt(III)–dioxime complexes investigated are low spin compounds. To correlate the measured annihilation lifetime or the changes in the parameters of the angular distribution curves with the chemical changes in the coordination sphere, it would be necessary to know the active sites of this complicated molecule where positron annihilation predominantly takes place.

To solve this problem the data and experience obtained by other methods with the same complexes can offer some important additional information.

The previously determined electron-binding energies measured by the ESCA method on the central cobalt atom and donor atoms provided valuable information on the electronic structure of the complex, and the electron density of the individual atoms.[9] Consequently the interpretation of the results of the positron annihilation investigations was supported by the correlations with the data of ESCA measurements.

Experimental Section

The complexes investigated were prepared as described in the literature;[9-16] their composition was checked by elemental analysis.[9]

Positron lifetime spectra and angular distribution curves were measured by the usual methods. The details of the apparatus have been published elsewhere.[4,17] The ^{22}Na positron source used for lifetime measurements was evaporated onto an approximately 1 mg/cm^2 thick Kapton polyimid foil, and was covered with another sheet of the foil. This source was placed between two samples (tablet or powderlike) with a thickness of more than 200 mg/cm^2. Lifetime spectra were evaluated by the POSITRONFIT EXTENDED[18] computer program.

For the characterization of the angular correlation curves the peak heights normalized to equal areas are given.

Results and Discussion

I. Lifetime spectra were analyzed for two components but the intensity of the long lifetime component ($\tau_2 \sim 1$ ns) was only about 1% for all the compounds investigated. This result indicates that, practically, there is no positronium formation in these compounds.

The lifetime data obtained for samples of the original polycrystalline powder form and the ones pressed into pills agreed within the limit of errors. This result indicates the fact that, in the course of high pressure pressing, no new imperfections and positron traps were formed in the substances investigated, consequently they had probably been saturated with them.

Thus it would likely not be a great error to assume that the saturation concentration of imperfections were practically the same in chemically different samples. At any rate this uncertainty factor must be considered when explaining the data.

II. In Table I, lifetime data are compared with the previously obtained[9] ESCA data, i.e., the electron binding energies on the central cobalt atom, on the nitrogens of the dioxime ligands, and on the iodide coordinated along the Z axis.

The data do not indicate a clear cut correlation between the positron lifetimes and the electron-binding energies on the central cobalt atom and on the nitrogen donor

TABLE I: Comparison of the Results of Positron Lifetime and ESCA Measurements

Compd investigated[a]	τ_1,[b] ps	ESCA[c] Co $2p_{3/2}$-C 1s	N 1s-C 1s	I $3d_{3/2}$-C 1s
$H[Co(HD)_2Cl_2]$ (I)	334 ± 1	495.2 ± 0.1	115.6 ± 0.1	
$H[Co(HD)_2Br_2]$ (II)	337 ± 1	494.75 ± 0.1	115.15 ± 0.1	
$[Co(HD)_2(NH_3)_2]Cl$ (III)	353 ± 2	495.0 ± 0.2	115.0 ± 0.1	
$H[Co(HD)_2I_2]$ (IV)	368 ± 3	494.5 ± 0.1	115.2 ± 0.2	
$H[Co(HD)_2CNI]$ (V)	350 ± 2	495.0 ± 0.1	115.3 ± 0.1	344.5 ± 0.1
$H[Co(HD)_2I_2]$ (IV)	368 ± 3	494.5 ± 0.1	115.2 ± 0.1	344.6 ± 0.1
$H[Co(HD)_2NO_2I]$ (VI)	373 ± 1	494.5 ± 0.1	115.1 ± 0.1	344.8 ± 0.1
$[Co(HD)_2NH_3I]$ (VII)	384 ± 1	494.6 ± 0.2	115.0 ± 0.1	345.8 ± 0.1
$H[Co(HD)_2Cl_2]$ (I)	334 ± 1	495.2 ± 0.1	115.6 ± 0.1	
$H[Co(HD)_2NO_2Cl]$ (VIII)	338 ± 1	494.5 ± 0.1	115.9 ± 0.2	
$H[Co(HD)_2CNCl]$ (IX)	348 ± 2	495.7 ± 0.1	115.8 ± 0.2	

[a] HD is the dimethylglyoximato ion (with one negative charge). [b] Positron lifetime. [c] Electron bonding energies in eV. The carbon atom of the methyl group of the ligands is taken as reference atom.

atoms, respectively. On the other hand, the ESCA data of the ligands on the Z axis, e.g., those of iodide in compounds IV–VII, indicate a decreased electronic density with increasing positron lifetime. A similar trend is reflected by the data of compounds XVII and XX in Table III.

Since it can be supposed that the increase of electron density on the given atom decreases the positron lifetime, the comparison of the ESCA data with the positron lifetimes indicate that neither the cobalt nor the oxime ligand are responsible for the change of the positron lifetime but it is caused by the unidentate ligands coordinated along the Z axis. It is very likely that the coordination of the strong field ligands resulting in the formation of a low spin electronic structure of the central cobalt atom decreased the interaction of the cobalt with the positrons.

III. In most cases angular correlation data are in the expected correlation with the lifetimes. Narrower angular correlation curves with higher peaks indicate a weaker localization and, accordingly, a lesser momentum of positrons while broadened curves show a more pronounced localization of positrons. The annihilation rate of localized positrons increases, that is, their lifetime decreases. This correlation seems to be valid considering the data in Table II obtained for complexes containing halides, particularly if the same type of series are compared. Some further relationships can also be deduced from Table II.

1. Comparing complexes with two halides in their inner coordination sphere it can be seen that the angular distribution curves become narrower in the order of Cl^-, Br^-, I^-; consequently the localization of positrons decreases in the same order. This result is in agreement with those of the theoretical calculations[19,20] and the experimentally found angular correlation curves[4,21] for the positron–halide bound state. This facts suggests the possible role of the positron–halide bound state also in our case. The tendency is similar for the halides in the outer coordination sphere.

2. The connection expected can be observed between the lifetime and the peak height of the angular correlation for the complexes containing only a single halide ligand in the inner sphere, too. In this case, however, the angular correlation curves are a bit broader when comparing them with the complexes with two halide ligands or one in the outer sphere.

3. The angular correlation curves of the pseudohalide containing complexes (XIII–XV) were similar to that of the chloride complex (I) indicating that the positron–pseudohalide bound state has about the same strength as that formed with the chloride. The angular correlation results for I, II, IV, XIII, and XV show a trend similar to that of Jørgensen's[22] optical electronegativity data for the ions (Cl^-, 3.0; NCO^-, 3.0; SCN^-, 2.8; Br^-, 2.8; I^-, 2.5).

TABLE II: Comparison of Lifetime and Angular Correlation Data

Compd investigated	τ_1,[a] ps	Peak height[b]
$H[Co(HD)_2Cl_2]$ (I)	334 ± 1	17460
$H[Co(HD)_2Br_2]$ (II)	337 ± 1	17960
$H[Co(HD)_2I_2]$ (IV)	368 ± 3	19270
$[Co(HD)_2(H_2O)Br]$ (X)	361 ± 2	17910
$H[Co(HD)_2(CN)I]$ (V)	350 ± 2	18690
$[Co(HD)_2(H_2O)I]$ (XI)	373 ± 2	18750
$[Co(HD)_2(NH_3)I]$ (VII)	384 ± 1	18950
$[Co(HD)_2(NH_3)_2]Cl$ (III)	353 ± 2	18120
$[Co(HD)_2(Py)_2]Br$ (XII)	373 ± 2	19350
$[Co(HD)_2(H_2O)(NCO)]$ (XIII)	374 ± 1	17230
$H[Co(HD)_2(SeCN)_2]$ (XIV)	349 ± 1	17470
$[Co(HD)_2(SCN)]$ (XV)	345 ± 3	17540
$[Co(HD)_2(H_2O)(SCN)]$ (XVI)	333 ± 2	

[a] Lifetime. [b] Angular correlation. The curves are normalized to equal areas. The uncertainties in peak heights are estimated to be about ±100.

IV. The following qualitative relationships can be given for the effect of ligands on positron lifetime:

1. The positron lifetime decreasing effect of halide ions decreases in the order of Cl^-, Br^-, I^- irrespective of whether the complex contains one or two halides. Probably this is due to the negative character of the ligands decreasing in the same fashion (Table I and II). It can be seen that the halide ion plays a decisive role in determining the positron lifetime. The effect of nitrite, ammonia, and coordinated water can be neglected, but cyanide acts like halides and decreases the positron lifetime.

Thus it seems likely that the effect of "hard" anions on positron lifetime is smaller or even negligible in contrast to that of the "soft" polarizable or π-acceptor ligands.

Furthermore, an increase in positron lifetime is caused by the exchange of one halide of the dihalide mixed complex for an inert ligand. When comparing chloride and iodide mixed complexes containing cyanide with the appropriate dihalide complexes it is obvious that the positron lifetime decreasing effect of the cyanide is lower than that of the chloride but higher than that of the iodide. Thus in case of the chloride–cyanide complex, the positron lifetime is longer, in the iodide–cyanide complex it is shorter than that of the appropriate dihalide.

2. The positron lifetime decreasing effect of the halide depends on the character of the coordination of halide. Such an effect of the halide coordinated in the inner sphere

TABLE III: Positron Lifetime Values of Sulfite Complexes and the Electron Binding Energies of S $2p_{1/2\ 3/2}$ Orbitals

Complex	Lifetime, τ_1, ps	C 1s-S $2p_{1/2\ 3/2}$
$NH_4[Co(HD)_2H_2OSO_3]$ (XVII)	348 ± 2	116.9 ± 0.1
$[Co(HD)_2NH_3SO_3]$ (XVIII)	348 ± 2	
$NH_4[Co(HD)_2an(SO_3)]$ (XIX)	336 ± 1	
$NH_4[Co(HD)_2(\gamma\text{-picolin})SO_3]$ (XX)	333 ± 2	118.3 ± 0.1
$NH_4[Co(HD)_2(m\text{-toluidin})SO_3]$ (XXI)	336 ± 2	
$NH_4[Co(HD)_2(p\text{-fenetidin})SO_3]$ (XXII)	334 ± 1	

is greater than that in the outer sphere. Compare, e.g., the lifetimes of VIII (338 ± 1 ps) and III (353 ± 2 ps), or those of X (361 ± 2 ps) and XII (373 ± 2 ps).

The more pronounced effect of the halide ion in the inner coordination sphere can be explained by the stronger polarization of the halide which makes the electrons of the halide more suitable for the reaction with positrons. It can be also seen from the data that the quality of the halide is more dominant than the nature of its bonding.

The chloride, bonded in the outer sphere, is more efficient than the bromide in the inner sphere and the bromide coordinated in the outer sphere is more efficient than the iodide in the inner sphere. (See also VII, 384 ± 1 ps.)

3. The positron lifetime of S- and Se-containing pseudohalides increases in the same way as their π-acceptor ability (SCN < SeCN). The N-bonded NCO^- complex showed however a higher positron lifetime than the SCN^- and $SeCN^-$ compounds.

4. Besides halides and pseudohalides the S-bonded sulfite ion having a great π-acceptor ability shows a considerable decreasing effect on the positron lifetime (Table III). As shown from the data of XVII and XVIII and comparing them with those of VIII and X, the effect of sulfite is smaller than that of chloride but larger than that of bromide.

The identical data of the two sulfite mixed complexes indicate again the negligible effect of coordinated water and ammonia on the positron lifetime (XVII, XVIII).

The lifetime data of mixed sulfite complexes XIX–XXII, however, show that the bases substituted with a nucleofil substituent having a relatively loose π-electron structure slightly enhance the decreasing effect of the complex on the positron lifetime.

5. The longest lifetimes were obtained in the following *p*-chloroaniline and *p*-bromoaniline mixed complexes:

$[Co(HD)_2(p\text{-Cl-an})_2]ClO_4$ (XXIII) $\tau_1 = 394 \pm 2$ ps

$[Co(HD)_2(p\text{-Br-an})_2]ClO_4$ (XXIV) $\tau_1 = 392 \pm 1$ ps

It is clear from the data that the organic halogens have a negligible effect on positron lifetime. The chlorine atoms of perchlorate positioned in the outer sphere also have little or no effect. Comparing these data with the results of aniline–sulfite and amine–sulfite mixed complexes mentioned previously, it seems that electrophillic halides quench the slight positron lifetime decreasing effect of aniline.

Conclusions

Both positron lifetimes and the data obtained by measuring the angular distribution of annihilation γ radiation reflect sensitively the changes occurring in the chemical features of bis(dimethylglyoximato)cobalt(III) mixed complexes caused by the coordination of unidentate ligands along their *Z* axes. Thus the positron annihilation method seems to be suitable to investigate the chemical structure of the substance even in the solid phase.

In our opinion, the changes observed in the course of positron annihilation measurements cannot be attributed simply to random differences in the physical state of the complexes but rather to the changes resulting from different ligands. This is supported by the correlation with the ESCA results and by the similarity of the lifetime data found for the chemically similar groups of compounds (e.g., for XVII–XVIII; XIX–XXII; XXIII–XXIV).

Further systematic investigations are planned to obtain a more exact explanation of the connection between annihilation data and chemical structure in the solid phase.

Acknowledgment. One of the authors (B.L.) acknowledges the hospitality of the Chemistry Department of the Danish Atomic Energy Commission Research Establishment, Risø, where he had the opportunity to carry out the positron annihilation measurements. He thanks Drs. Ole Mogensen and Peter Jansen for useful discussions and Niels-Jörgen Pedersen for valuable technical assistance.

References and Notes

(1) J. H. Green and J. Lee, "Positronium Chemistry", Academic Press, New York, N.Y., 1964; V. I. Goldanskii, *At. Energy Rev.*, **6**, 3 (1968); R. N. West, *Adv. Phys.*, **22**, 263 (1973); J. A. Merrigan, J. H. Green, and S. J. Tao, in "Physical Methods of Chemistry", Vol. 1, Part IIID, A. Weissberger and B. W. Rossitter, Ed., Wiley, New York, N.Y., 1972, p 501.
(2) O. E. Mogensen, *J. Chem. Phys.*, **60**, 998 (1974).
(3) See B. Lévay and A. Vértes, *J. Phys. Chem.*, **80**, 37 (1976), and the references given therein.
(4) O. E. Mogensen and V. P. Shantarovich, *Chem. Phys.*, **6**, 100 (1974).
(5) K. Burger, "Coordination Chemistry: Experimental Methods", Butterworths, London, 1973.
(6) K. Burger and I. Ruff, *Talanta*, **10**, 329 (1963).
(7) K. Burger and B. Pintér, *J. Inorg. Nucl. Chem.*, **29**, 1717 (1967).
(8) K. Burger, B. Zelei, G. Szántó-Horváth, and T. T. Binh, *J. Inorg. Nucl. Chem.*, **33**, 2573 (1971).
(9) K. Burger, E. Fluck, Cs. Várhelyi, H. Binder, and I. Speyer, *Z. Anorg. Allg. Chem.*, **408**, 304 (1974).
(10) E. Cambi and C. Coriselli, *Gazz. Chim. Ital.*, **66**, 81 (1936).
(11) F. Feigl and H. Rubinstein, *Justus Liebigs Ann. Chem.*, **433**, 183 (1923).
(12) A. V. Ablov, *Bull. Soc. Chim. Fr.*, (5) **7**, 151 (1940).
(13) Z. Finta and Cs. Várhelyi, *Acta Chim. Acad. Sci. Hung.*, submitted for publication.
(14) A. K. Babko and V. Korotum, *Z. Obscsej Him.*, **24**, 597 (1954).
(15) A. V. Ablov, *Dokl. Akad. Nauk SSSR*, (2) **97**, 1019 (1954).
(16) Cs. Várhelyi, I. Genescu, and L. Szotyori, *Z. Anorg. Allg. Chem.*, **386**, 232 (1971).
(17) M. Eldrup, O. E. Mogensen, and G. Trumpy, *J. Chem. Phys.*, **57**, 495 (1972).
(18) P. Kirkegaard and M. Eldrup, *Comp. Phys. Commun.*, **3**, 240 (1972).
(19) P. Cade and A. Farazdel, *J. Chem. Phys.*, in press.
(20) A. Farazdel and P. Cade, *J. Chem. Phys.*, in press.
(21) O. E. Mogensen and P. Jansen, Paper G 13, presented at the Forth International Conference on Positron Annihilation, Aug 1976, Helsingör, Denmark.
(22) C. K. Jørgensen, "Modern Aspects of Ligand Field Theory", North Holland Publishing Co., London, 1971, pp 362–369.

A Test of the Scaled Particle Theory Results for Dense Mixtures of Convex-Shaped Molecules

Saul Goldman

Guelph-Waterloo Centre for Graduate Work in Chemistry, Guelph Campus, Department of Chemistry, University of Guelph, Guelph, Ontario N1G 2W1, Canada *(Received February 16, 1977)*

Publication costs assisted by the National Research Council of Canada

First-order perturbation theory is used to derive an expression for the Henry's law constant, K, and for the partial molar volume at infinite dilution, $\bar{V}_2^\bullet$, of a gas in a liquid, for systems where both species can be considered to be convex shaped. The properties of the reference state are calculated by the scaled particle theory expressions derived recently by Boublík. The terms that arise due to the perturbing potentials are evaluated semiempirically by fitting the expression for K to experimental data. Values of $\bar{V}_2^\bullet$ were calculated for the following systems at 25 °C: Ar, N_2, and CH_4 in C_6H_6; Ar, N_2, CH_4, and O_2 in CCl_4. Ar and CH_4 were taken to be spheres; N_2 and O_2 were approximated by oblate spherocylinders; C_6H_6 and CCl_4 were assumed to contain hexagonal and tetrahedral cores, respectively. In every case the agreement between the calculated and the experimental values of $\bar{V}_2^\bullet$ was very good. This agreement lends support to the validity of Boublík's expressions.

Introduction

Recently Tomáš Boublík applied scaled particle theory[1-5] to dense fluid mixtures comprised of hard convex molecules of different shapes in order to derive expressions for the equation of state for such mixtures, and for the chemical potentials of the components in such mixtures.[6,7] The only completely unambiguous test of the accuracy of these equations is comparison with computer simulations. Unfortunately such simulations for mixtures are not available, and it would be costly to do these simulations for a range of conditions and types of particles. However, in view of the importance of statistical mechanical descriptions of dense fluid mixtures comprised of nonspherical particles, it was considered worthwhile to construct a test, albeit and indirect one, for Boublík's mixture results.

The approach we will take is to use themodynamic perturbation theory to derive an expression for the Henry's law constant (K),[8] of a gas in a liquid. The reference state chosen will be the hard-convex body mixture, and Boublík's results will be used to obtain the properties of the reference state. The energy integrals that are needed will be determined semiempirically by fitting our derived expression for K to experimental data. Subsequently our expression for K will be differentiated with respect to pressure, in order to obtain an explicit equation for the partial molar volume at infinite dilution of a gas in a liquid ($\bar{V}_2^\bullet$). Thus values of $\bar{V}_2^\bullet$ will be calculated for a number of systems wherein the geometry of the components can be reasonably approximated by convex shapes, and the results will be compared with experimental data.

Theory

For a mixture of convex molecules that interact through a pairwise additive Kihara-type potential, the Helmholtz free energy can be expressed to the first order by[9]

$$\beta A = \beta A^{\mathrm{ref}} + {}^1/_2\beta \sum_{i,j=1}^{2} N_i\rho_j \int_0^\infty W_{ij}(\ell) g_{\mathrm{av}\,ij}^{\mathrm{ref}}(\ell) S_{i+\ell+j}\, \mathrm{d}\ell \quad (1)$$

where $\beta = 1/kT$, A, and A^{ref} are respectively the Helmholtz free energy of the real system and of the hard-convex body reference system, N_i and ρ_j are respectively the number of particles of species i, and the particle number density of species j, $W_{ij}(\ell)$ is the intermolecular potential between particles i and j, ℓ is the shortest distance between the surfaces of particles i and j, $g_{\mathrm{av}\,ij}^{\mathrm{ref}}(\ell)$ is the angle-averaged correlation function between particles i and j in the reference system, and $S_{i+\ell+j}$ is the surface resulting from the motion of the centre of particle j at a constant distance ℓ between the surfaces of the particles i and j, averaged over all mutual orientations of both particles. The defining expressions for $g_{\mathrm{av}\,ij}^{\mathrm{ref}}(\ell)$ and for $S_{i+\ell+j}$ are given in ref 9.[10]

The basic idea implicit in eq 1 is that nonspherical particles can, as a first approximation, be replaced by convex-shaped particles whose intermolecular pair potential depends only on the shortest distance between the surfaces of the two particles. The surfaces of these convex-shaped particles are parallel to and surround an impenetrable convex-shaped "core". The cores used for the particles in this study are described in the footnotes given with Table I.

From eq 1 and the definition of the chemical potential in a binary system

$$\mu_2 = (\partial A/\partial N_2)_{N_1,T,V}$$

it follows that

$$(\mu_2)_1 = (\mu_2^{\mathrm{ref}})_1 + {}^1/_2 \frac{\partial}{\partial N_2}\left(\sum_{i,j=1}^{2} N_i\rho_j \times \int_0^\infty W_{ij}(\ell) g_{\mathrm{av}\,ij}^{\mathrm{ref}}(\ell) S_{i+\ell+j}\, \mathrm{d}\ell \right)_{N_1,T,V} \quad (2)$$

The subscripts 1 and 2 denote solvent and solute, respectively, and l and g will denote the liquid and gas phases, respectively.

From thermodynamics and the definition of the Henry's law constant K,[8] one obtains

$$\ln K = \beta[(\mu_2^\circ)_l - (\mu_2^\circ)_g] \quad (3)$$

where

$$(\mu_2^\circ)_l = \lim_{X_2 \to 0} [(\mu_2)_l - \beta^{-1} \ln X_2]$$

In eq 3 the superscript degree denotes standard state and X denotes mole fraction. The standard state for the solute in the gas is the ideal gas at 1 atm and temperature

TABLE I: Parameters Used for the Solvents and Solutes[a]

Solvents	R_1[b]	S_1[b]	V_1[b]	$\bar{V}$[c]	$\beta_T \times 10^4$[d]
C_6H_6	2.805	91.825	70.029	89.408	0.9798
CCl_4	2.845	94.387	78.552	97.098	1.0811

Solutes[e]	R_2			S_2			V_2		
Ar		1.703[f]	1.619[g]		36.424[f]	32.925[g]		20.670[f]	17.765[g]
CH_4		1.871[f]	1.800[g]		43.993[f]	40.715[g]		27.437[f]	24.430[g]
O_2	1.683[i]	1.735[f]	1.685[h]	34.757[i]	36.860[f]	34.712[h]	18.706[i]	20.362[f]	18.601[h]
N_2	1.836[i]	1.847[f]	1.754[h]	41.685[i]	41.916[f]	37.708[h]	24.787[i]	24.828[f]	21.114[h]

[a] R is in Å, S in Å^2, V in Å^3, $\bar{V}$ in cm^3/mol, β_T in atm^{-1}. $\bar{V}$ and β_T are for 25 °C. [b] Taken from Boublík[9] who obtained them by fitting theoretically derived expressions to equilibrum vaporization data for the pure liquids. The benzene molecule is pictured as a convex body whose surface is parallel to and encloses a "core" that is taken to be the hexagon formed by joining the midpoints of the CH bonds in benzene. Similarly the surface of the carbon tetrachloride molecule is parallel to and encloses a core taken to be the tetrahedron formed by the Cl atoms in CCl_4. [c] Reference 13. [d] Reference 14. [e] Ar and CH_4 were taken to be spheres (a sphere is a convex body whose core is a point). O_2 and N_2 were taken to be oblate spherocylinders (convex bodies whose cores are straight lines joining the two atoms). [f] These values were obtained by assuming that V_2 was given by $^4/_3\pi(\sigma/2)^3$ where σ is the Lennard-Jones distance parameter. The σ's were taken from ref 15 and the cores for O_2 and N_2 were taken from ref 16. [g] Obtained from the Barker-Henderson prescription for calculating hard-sphere diameters.[20] [h] Taken from Kihara,[16] who obtained them from diffusion coefficients. [i] Taken from Table I of ref 23 with shell thickness ξ obtained from $\xi = (^1/_2)^{1/6}(\rho_0/2)$. These values derive from second virial coefficient data and theoretically based estimates of the core lengths.

T, and its standard state in solution is the hypothetical unit mole fraction solution at T.

Since in all the systems studied here the gas phase will be sufficiently attenuated to be considered ideal

$$(\mu_2^\circ)_g = -\beta^{-1} \ln [(2\pi m_2 kT/h^2)^{3/2}\beta^{-1}] \quad (4)$$

Combining eq 2-4, using eq 84 of ref 6 for $(\mu_2^{ref})_l$, and using the superscript • to denote the limit $X_2 \to 0$, one obtains after rearrangement

$$\ln K = \ln (RT/\bar{V}_1) + \beta\mu_2^\bullet(\text{ref}) + \beta\mu_2^\bullet(\text{corr}) \quad (5)$$

where $\bar{V}_1$ is the molar volume of the pure solvent

$$\beta\mu_2^\bullet(\text{ref}) = -\ln (1 - \rho_1^\bullet V_1) + \frac{\rho_1^\bullet(R_2S_1 + R_1S_2 + V_2)}{(1 - \rho_1^\bullet V_1)} + \frac{\rho_1^{\bullet 2}(S_1^2R_2^2 + 2V_2R_1S_1)}{2(1 - \rho_1^\bullet V_1)^2} + \frac{\rho_1^{\bullet 3}V_2R_1^2S_1^2}{3(1 - \rho_1^\bullet V_1)^3}$$

$$\beta\mu_2^\bullet(\text{corr}) = \frac{\rho_1^\bullet}{kT}(I_{12}^\bullet + I_{11}^\bullet) \equiv \frac{\rho_1^\bullet I^\bullet}{kT}$$

$$I_{12}^\bullet = \int_0^\infty W_{12}(\ell)(g_{av\,12}^{ref}(\ell))^\bullet S_{1+\ell+2}\, d\ell$$

$$I_{11}^\bullet = \frac{N_1}{2}\int_0^\infty W_{11}(\ell)\left(\frac{\partial g_{av\,11}^{ref}(\ell)}{\partial N_2}\right)^\bullet_{N_1TV} S_{1+\ell+1}\, d\ell$$

The first term in eq 5 accounts for the difference in the standard state of the solute in the two phases.

The term $\beta\mu_2^\bullet$(ref) gives the contribution to ln K made by the chemical potential of the solute at infinite dilution in the hard-convex body reference mixture. The terms R_i, S_i, and V_i denote the $(1/4\pi)$ multiple of the integral of mean curvature, the surface area, and the volume of the convex body i, respectively. The defining expressions for these geometric functionals have been given elsewhere.[6]

The term $\beta\mu_2^\bullet$(corr) gives the correction to ln K due to the solute–solvent pair potentials (the $I_{12}^\bullet$ term) and the solvent–solvent pair potentials (the $I_{11}^\bullet$ term) in the real system.

The problem with using eq 5 directly is that expressions for $g_{av\,ij}^{ref}(\ell)$ are not available for nonspherical convex-particle mixtures, and also the pair potentials $W_{ij}(\ell)$ are not known for the systems we plan to examine. Consequently the term $I^\bullet$ had to be determined by fitting eq 5 to experimental data and a derivative of eq 5 was the equation actually tested.

The partial molar volume of a solute at infinite dilution, $\bar{V}_2^\bullet$, is related to K by

$$\bar{V}_2^\bullet = RT(\partial \ln K/\partial P)_T \quad (6)$$

Thus if $I^\bullet$, R_i, S_i, V_i $(i = 1, 2)$ are assumed to be independent of pressure, one obtains from eq 5 and 6

$$\bar{V}_2^\bullet = RT\left\{\beta_T + \frac{V_1}{1 - \rho_1^\bullet V_1}\left(\frac{\tilde{N}}{\bar{V}}\right)\beta_T + F(R_2S_1 + R_1S_2 + V_2) + \frac{F\rho_1^\bullet}{1 - \rho_1^\bullet V_1}(S_1^2R_2^2 + 2V_2R_1S_1) + F\left(\frac{\rho_1^\bullet}{1 - \rho_1^\bullet V_1}\right)^2 V_2R_1^2S_1^2 + \left(\frac{\partial\rho_1^\bullet}{\partial P}\right)_T\left(\frac{I^\bullet}{kT}\right)\right\} \quad (7)$$

where

$$F \equiv \left(\frac{\partial\rho_1^\bullet}{\partial P}\right)_T\left(\frac{1}{1 - \rho_1^\bullet V_1} + \frac{\rho_1^\bullet V_1}{(1 - \rho_1^\bullet V_1)^2}\right)$$

$$(\partial\rho_1^\bullet/\partial P)_T = \tilde{N}\beta_T/\bar{V}$$

$\beta_T = -(1/\bar{V})(\partial\bar{V}/\partial P)_T$ is this coefficient of isothermal compressibility of the pure solvent. $\tilde{N}$ is Avogadro's number.

Calculations and Results

The systems analyzed here are Ar, N_2, and CH_4 in C_6H_6, and Ar, N_2, CH_4, and O_2 in CCl_4. These systems were selected because the values of K and $\bar{V}_2^\bullet$ are available at 25 °C, because the shapes of the solutes and solvents can be approximated by convex bodies and because the geometric functionals R_i, S_i, and V_i are available or can be estimated from other work.

The values of the solvent and solute parameters that were used are given in Table I. The solvent functionals (R_1, S_1, V_1) were taken from Boublík[9] who determined them semiempirically. Three sets of solute functionals (R_2, S_2, V_2) were chosen for each solute. This was done because accurate values of R_2, S_2, and V_2 did not exist for the solutes, so that some estimate of the effect of solute parameter choice on the calculated value of $\bar{V}_2^\bullet$ was desireable.

The value of $I^\bullet$ was determined for each system and for each set of parameters by fitting eq 5 to the experimental ln K values listed in Table II. Subsequently these values of $I^\bullet$ were used in eq 7 to predict values for $\bar{V}_2^\bullet$.

TABLE II: Comparison of Calculated and Experimental Values of $\bar{V}_2^{\infty}$[a]

System	ln K	$\bar{V}_2^{\infty}$ Calcd			$\bar{V}_2^{\infty}$ Exptl[d]
Ar in C_6H_6	7.05[b]		43.7[e]	39.6[f]	43
N_2 in C_6H_6	7.73[b]	51.7[h]	51.9[e]	46.8[g]	53
CH_4 in C_6H_6	6.17[b]		50.9[e]	46.9[f]	52
Ar in CCl_4	6.62[b]		46.9[e]	42.5[f]	44
N_2 in CCl_4	7.33[b]	55.6[h]	55.9[e]	50.4[g]	52.5
CH_4 in CCl_4	5.87[b]		55.0[e]	50.6[f]	52.4
O_2 in CCl_4	6.73[c]	45.0[h]	47.6[e]	44.9[g]	45.3

[a] All entries are for 25 °C. K is in atm, $\bar{V}_2^{\infty}$ in cm³/mol. [b,c] Obtained from values quoted in ref 17 and 18, respectively. The values of I^* (see text) were obtained from these values, the appropriate parameters in Table I, and eq 5. [d] Obtained from values quoted in ref 19. [e-h] These values were obtained from eq 7, the appropriate value of I^*, the relevant solvent parameters in Table I, and the solute parameters labeled f, g, h, and i, respectively, in Table I.

The results are entered in Table II. It is seen from this table that the calculated values of $\bar{V}_2^{\bullet}$ are in very good agreement with the corresponding experimental values. While the values of $\bar{V}_2^{\bullet}$ show some sensitivity the set of R_2, S_2, and V_2 used, the worst errors are only of the order of 10%. The average absolute error for all the calculated values of $\bar{V}_2^{\bullet}$ is about 5%.

Discussion

It is necessary to explain at this point why enthalpies of solution were not also predicted. The enthalpy of solution of a solute at infinite dilution, $\Delta H_s^{\bullet}$, is related to K by

$$\Delta H_s^{\bullet} = -RT^2(\partial \ln K/\partial T)_P$$

so that at first sight it may seem that once $I^{\bullet}$ is obtained from K, eq 5 could be differentiated with respect to temperature to provide values for $\Delta H_s^{\bullet}$. In fact this was done in preliminary calculations where it was found that the accuracy of the predicted enthalpies was much worse than that of the volumes. The reason for this can be found in perturbation theory, from which it is known (for spherical particles) that the size of the particles in the reference state (i.e., the hard-sphere diameters) are much more strongly temperature dependent than they are pressure dependent.[11] Consequently, taking a temperature derivative of eq 5 necessitates the questionable assumption that the functionals R_i, S_i, and V_i ($i = 1, 2$) are temperature independent. The assumption made here, that the functionals are independent of pressure, should be much better than the corresponding temperature-independence assumption, so that this accounts for the success of the $\bar{V}_2^{\bullet}$ predictions relative to those for $\Delta H_s^{\bullet}$.

In view of the variety of systems and particle shapes considered here it is unlikely that the good agreement between the experimental and predicted $\bar{V}_2^{\bullet}$'s resulted from fortuitous cancellation of errors. Rather, one can reasonably conclude that these results support the validity of Boublík's derived equations. Fairly recently, Sandler has developed a statistical mechanical perturbation theory for systems of nonspherical particles based on a nonspherical reference state.[12] The positive result found in this work suggests that Boublík's equations can be used to calculate the thermodynamic properties of these nonspherical reference states.

Acknowledgment. The author is grateful to the National Research Council of Canada for financial assistance.

References and Notes

(1) H. Reiss, H. L. Frisch, and J. L. Lebowitz, *J. Chem. Phys.*, **31**, 369 (1959).
(2) H. L. Frisch, *Adv. Chem. Phys.*, **6**, 229 (1964).
(3) H. Reiss, *Adv. Chem. Phys.*, **9**, 1 (1965).
(4) R. M. Gibbons, *Mol. Phys.*, **17**, 81 (1969).
(5) R. M. Gibbons, *Mol. Phys.*, **18**, 809 (1970).
(6) T. Boublík, *Mol. Phys.*, **27**, 1415 (1974).
(7) T. Boublík, *J. Chem. Phys.*, **63**, 4084 (1975).
(8) The Henry's law constant K of a solute is defined by

$$K \equiv \lim_{X_2 \to 0} p_2/X_2$$

where p_2 is the partial pressure of the solute over the solution and X_2 is the mole fraction of the solute in the solution.
(9) T. Boublík, *Collect. Czech. Chem. Commun.*, **39**, 2333 (1974).
(10) It should be noted that the expression given in ref 9 for $g_{av\ ij}^{ref}(\ell)$ is in terms of $g_{ij}^{ref}(\ell, \theta, \varphi, \omega)$ where θ, φ, and ω are the angles required to specify the relative orientation of the convex bodies i and j. Neither $g^{ref}(\ell, \theta, \varphi, \omega)$ nor $g_{av}^{ref}(\ell)$ are presently known.
(11) In the Barker–Henderson[20] theory, the diameters are functions of temperature only, and have no pressure-dependence whatever. In the variational[21] and Chandler–Weeks–Andersen[22] theories the diameters are both temperature and pressure dependent, but the temperature dependence is stronger than the pressure dependence.
(12) S. I. Sandler, *Mol. Phys.*, **28**, 1207 (1974).
(13) A. Weissberger and E. S. Proskauer, "Organic Solvents," 2nd ed, Vol. VII, Interscience, New York, N.Y., 1955, pp 72, 194.
(14) "Handbook of Chemistry and Physics", 50th ed, The Chemical Rubber Co., Cleveland, Ohio, 1969–1970, p F-12.
(15) D. Henderson, and P. J. Leonard in "Physical Chemistry, An Advanced Treatise", Vol. VIIIB, H. Eyring, D. Henderson, and W. Jost, Ed., Academic Press, New York, N.Y., 1971, p 420.
(16) T. Kihara, *Adv. Chem. Phys.*, **5**, 147 (1963).
(17) R. A. Pierrotti, *J. Phys. Chem.*, **67**, 1840 (1963).
(18) J. H. Hildebrand and R. L. Scott, "The Solubility of Nonelectrolytes", 3rd ed, Dover Publications, New York, N.Y., 1964, p 243.
(19) E. B. Smith and J. Walkley, *J. Phys. Chem.*, **66**, 597 (1962).
(20) J. A. Barker and D. Henderson, *J. Chem. Phys.*, **47**, 4714 (1967).
(21) G. A. Mansoori and F. B. Canfield, *J. Chem. Phys.*, **51**, 4958 (1969).
(22) J. D. Weeks, D. Chandler, and H. C. Andersen, *J. Chem. Phys.*, **54**, 5237 (1971).
(23) A. Kolde and T. Kihara, *Chem. Phys.*, **5**, 34 (1974).

A Diffusional Model of "Water Splitting" in Electrodialysis

I. Rubinstein

Department of Applied Mathematics, The Weizmann Institute of Science, Rehovot, Israel *(Received November 3, 1976; Revised Manuscript Received March 21, 1977)*

A diffusional model of water dissociation within an unstirred layer in a cross electric field is considered. It is concluded that for realistic values of the bulk salt concentration, the salt ions are potential determining over a wide range of voltages, in particular deeply within the domain of "water splitting". As a corollary, the shift of pH in the unstirred layer is determined by voltage and does not depend on the bulk concentration of the salt. The efficiency of the current depends strongly on the latter. It is shown that the diffusional overvoltage approximation leads to overestimated values of the current carried by the H^+ and OH^- ions, compared with those obtained by numerical solution of the exact problem.

Introduction

In the course of electrodialysis the solution near the membrane is depleted, and a concentration gradient arises in the boundary layer close to the membrane–a phenomenon called polarization of electrolyte. One might think that as the concentration of electrolyte on the membrane solution interface approaches zero, the voltage–current curve will become saturated, the current in the system reaching its limit value. Actually[1,2] after a plateau in the voltage–current curve one observes a region of rapid current increase. This is usually said[1,3,4] to be due to a progressing participation of dissociated (split) water in charge transfer, as the voltage increases.[2,3]

Together with the voltage–current changes just mentioned one observes a considerable shift of pH in the layers near the membranes (there arises an excess of H^+ (OH^-) near the anion (cation) exchange membrane). This phenomenon is usually called "water splitting" or "acid–base generation". It is obvious that an understanding of the water splitting phenomenon is impossible without a clear knowledge of the properties of electrodiffusional ion transfer in the solution layers near the membranes, when reversible water dissociation takes place.

Here we present a theory of such a transfer in an idealized system. We regard this theory as a qualitive one, built in order to clarify the general properties of a pure diffusional mechanism. In a sense we have proceeded one step further than Isaakson,[5] who analyzed theoretically water dissociation in the solution, and Grossman[6] who did the same for a uniform and composite membrane in a constant electric field, both under conditions of chemical equilibrium for the water.

Statement of the Problem

Let us consider an ideally permselective ion-exchange membrane, for example, an anion exchange membrane, with an adjacent unstirred layer of a strong 1,1 valent electrolyte (salt). Let a reversible reaction of water dissociation take place throughout the unstirred layer according to

$$H_2O \underset{k}{\overset{Kk}{\rightleftharpoons}} OH^- + H^+ \qquad (I)$$

where $K_p = [H_2O]K \simeq 10^{-14}$ M^2 is the equilibrium ionic product for water and $k \simeq 1.3 \times 10^{11}$ mol^{-1} s^{-1} [7] is the OH^- and H^+ recombination rate constant and K is the corresponding equilibrium constant. Let a cross electric field be applied from the membrane to the solution.

We direct the x axis normally to the membrane and identify $x = 0$ with the outer boundary of the unstirred layer. Let $x = \delta$ represent the membrane–solution interface, where δ denotes the thickness of the unstirred layer.

The steady diffusional ion transfer in our system will be described by the following equations

$$\frac{d}{dx}\left[D_i\frac{d\tilde{C}_i}{dx} + \frac{D_i(-1)^{i+1}F}{RT}\tilde{C}_i\frac{d\tilde{\varphi}}{dx}\right] = 0 \qquad i = 1, 2 \qquad (1a,b)$$

$$\frac{d}{dx}\left[D_i\frac{d\tilde{C}_i}{dx} + \frac{D_i(-1)^{i+1}F}{RT}\tilde{C}_i\frac{d\tilde{\varphi}}{dx}\right] = k\tilde{C}_3\tilde{C}_4 - K_p k \qquad i = 3, 4 \qquad (2a,b)$$

$$\tilde{C}_1 + \tilde{C}_3 = \tilde{C}_2 + \tilde{C}_4 \qquad (3)$$

Here $i = 1$ corresponds to the cation of the salt, $i = 2$ corresponds to the anion of the salt, $i = 3$ corresponds to H^+, and $i = 4$ corresponds to OH^-, $\tilde{C}_i$ and D_i are respectively the concentration and the diffusion constants of component i, and $\tilde{\varphi}$ is the electrical potential in the system.

Equations 1a,b describe the electrodiffusion of the salt ions, eq 2a,b that of the proton and hydroxyl ion, taking into account reaction I. Equation 3 expresses the condition of electroneutrality.

Equations 1–3 are supplemented by the boundary conditions

$$\tilde{C}_i|_{x=0} = \tilde{C}_{i0} \qquad i = 1, 2, 3, 4 \qquad (4a\text{–}d)$$

$$\tilde{\varphi}|_{x=0} = 0 \qquad (4e)$$

$$\left(D_i\frac{d\tilde{C}_i}{dx} + \frac{D_iFC_i}{RT}\frac{d\tilde{\varphi}}{dx}\right)\Bigg|_{x=\delta} = 0 \qquad i = 1, 3 \qquad (5a,b)$$

$$(\tilde{C}_2 + \tilde{C}_4)|_{x=\delta+0} = \tilde{p}^* \qquad (6a)$$

$$\tilde{\varphi}|_{x=\delta+0} = \tilde{A} \qquad (6b)$$

$$\frac{\tilde{j}_4}{\tilde{j}_2}\Bigg|_{x=\delta-0} = \left(\frac{\tilde{C}_4}{\tilde{C}_2}\right)\Bigg|_{x=\delta+0}\frac{D_4'}{D_2'} \qquad (7)$$

Here C_{i0}s are the bulk concentrations of the corresponding components $\tilde{C}_{10} = \tilde{C}_{20} = C$, $\tilde{C}_{30} = \tilde{C}_{40} = n_0$, $j_i = -D_i(d\tilde{C}_i/dx) - [D_i(-1)^{i+1}F/RT]\tilde{C}_i(d\tilde{\varphi}/dx)$ is the flux of the i component, the D_i's ($i = 2, 4$) are the diffusion constants within the membrane, $\tilde{p}^*$ is the effective concentration of fixed charges within the membrane according to usual concepts of the theory of polyelectrolytes,[8] $\tilde{A}$ is the voltage applied, and $x = \delta + 0$ denotes the interior of the membrane.

Boundary conditions (5a,b) express the nonpenetrability of an ideal anion exchange membrane for cations and (6) corresponds to electroneutrality within the membrane. Condition (7) states that the fluxes of penetrating ions in the membrane are proportional to the concentrations of these ions in it, and conditions (4a–e) imply that the concentrations of ions and the electric potential in the bulk are fixed.

Finally, from the continuity of electrochemical potentials of the penetrating ions on the membrane–solution interface one has

$$[RT \ln \tilde{C}_i + (-1)^{i+1} F\tilde{\varphi}]_{x=\delta} = 0 \qquad i = 2, 4 \qquad (8a,b)$$

where [] denote a jump. We have assumed that the activity coefficients are equal to one everywhere and that the standard potentials are constant within the unstirred layer and equal to those within the membrane.

In terms of dimensionless variables where the various scales have been chosen in a reasonable fashion, (1)–(8) take the form

$$\frac{d}{dy}\left(\frac{dC_i}{dy} + (-1)^{i+1} C_i \frac{d\varphi}{dy}\right) = 0 \qquad i = 1, 2 \qquad (9a,b)$$

$$\epsilon_i^2 \frac{d}{dy}\left(\frac{dC_i}{dy} + (-1)^{i+1} C_i \frac{d\varphi}{dy}\right) = C_3 C_4 - 1$$
$$i = 3, 4 \qquad (10a,b)$$

$$C_1 - C_2 = (C_4 - C_3)\alpha \qquad (11)$$

$$C_i|_{y=0} = 1 \qquad i = 1, 2, 3, 4 \qquad (12a\text{–}d)$$

$$\varphi|_{y=0} = 0 \qquad (13)$$

$$\left(\frac{dC_i}{dy} + (-1)^{i+1} C_i \frac{d\varphi}{dy}\right)\Big|_{y=1} = 0 \qquad i = 1, 3 \qquad (14a,b)$$

$$C_2|_{y=1+0} + \alpha C_4|_{y=1+0} = p^* \qquad (15)$$

$$\frac{j_4}{j_2}\Big|_{y=1-0} = \left(\frac{C_4}{C_2}\right)\Big|_{y=1+0} \theta \qquad (16)$$

$$[\ln C_i + (-1)^{i+1} \varphi]_{y=1} = 0 \qquad i = 2, 4 \qquad (17a,b)$$

$$\varphi|_{y=1+0} = A \qquad (17c)$$

where

$$C_i = \tilde{C}_i / C_{i0}, \qquad \varphi = F\tilde{\varphi}/RT, \qquad y = x/\delta$$

$$j_i = -\frac{dC_i}{dy} - (-1)^{i+1} C_i \frac{d\varphi}{dy} \qquad i = 2, 4$$

$$\epsilon_i^2 = D_i / k\delta^2 n_0$$

$$\alpha = n_0 / C_0, \qquad p^* = p^*/C_0$$

$$A = F\tilde{A}/RT, \qquad \theta = D_4' D_2 / D_4 D_2'$$

One obtains immediately from (8a) and (13a)

$$C_1 = e^{-\varphi} \qquad (18)$$

Evaluating the dimensionless parameters ϵ_i^2 and α for the reasonable values of $C_0 \simeq 10^{-3}$–10^{-2} mol L^{-1}, $n_0 \simeq 10^{-7}$ mol L^{-1}, $k = 1.3 \times 10^{11}$ mol^{-1} s^{-1}, $K_p \simeq 10^{-4}$ mol^2 L^{-2}, and $D_3 \simeq D_4 = 10^{-4}$ cm^2/s one obtains $10^{-5} < \epsilon^2 < 10^{-4}$ and $10^{-5} < \alpha < 10^{-4}$. One concludes from (11), taking into account the smallness of α, that unless $C_1, C_2 \gg C_3, C_4$ the local electroneutrality in the system is guaranteed by the salt ions ($i = 1, 2$), and that these salt ions are (as we shall see) the "potential determining" ions. We conclude from (10a,b) taking into account the smallness of ϵ_i^2, that within most of unstirred layer there holds a chemical equilibrium for the water ($C_3 C_4 \simeq 1$) and that only in a narrow layer near the membrane (order of thickness ϵ_i) is this equilibrium essentially disturbed.

Perturbation Procedure

Since α_1, ϵ_1, and ϵ_2 are so small, we shall look for a solution of system 9–17 in terms of expansions in power of α, ϵ_i. Such an "outer" expansion[9] should be valid everywhere except in a narrow layer, of the order of thickness ϵ, adjacent to the membrane. Let us suppose for simplicity that $D_3 = D_4$. Then $\epsilon_3 = \epsilon_4 = \epsilon$. Equations 9a,b and 10a,b can be written, taking into account (14a) as

$$\frac{dC_i}{dy} + (-1)^{i+1} C_i \frac{d\varphi}{dy} = -j_i \qquad i = 1, 2 \qquad (19a,b)$$

$$j_1 = 0 \qquad j_2 = \text{constant}$$

$$C_1 - C_2 = \alpha(C_4 - C_3) \qquad (20)$$

$$\frac{d}{dy}(C_3 - C_4) + (C_3 + C_4)\frac{d\varphi}{dy} = I_w$$
$$I_w = \text{constant} \qquad (21a)$$

$$\epsilon^2\left[\frac{d^2 C_3}{dy^2} + \frac{d}{dy}\left(C_3 \frac{d\varphi}{dy}\right)\right] = C_3 C_4 - 1 \qquad (21b)$$

Here j_2 is a dimensionless flux of the salt anions and I_w is a dimensionless current carried by the ions of water. j_2 and I_w have to be determined from the boundary conditions. The total dimensionless current in the system is

$$I_w = j_2 + (D_4/D_2)\alpha I_w \qquad (21c)$$

Let us look for an outer expansion of the form

$$C_i = \overline{C}_i^0(y) + \overline{C}_{i\alpha}(y)\alpha + \overline{C}_{i\epsilon}(y)\epsilon + \overline{C}_{i\alpha\alpha}(y)\alpha^2 + \overline{C}_{i\epsilon\epsilon}(y)\epsilon^2 + \overline{C}_{i\alpha\epsilon}(y)\alpha\epsilon + \ldots \qquad (22a)$$

$$\varphi = \overline{\varphi}^0(y) + \overline{\varphi}_\alpha(y)\alpha + \overline{\varphi}_\epsilon(y)\epsilon + \overline{\varphi}_{\alpha\alpha}(y)\alpha^2 + \overline{\varphi}_{\epsilon\epsilon}(y)\epsilon^2 + \overline{\varphi}_{\alpha\epsilon}(y)\alpha\epsilon + \ldots \qquad (22b)$$

$$j_2 = j^0 + j_\alpha \alpha + j_\epsilon \epsilon + \ldots \qquad (22c)$$

$$I_w = i^0 + i_\alpha \alpha + i_\epsilon \epsilon + \ldots \qquad (22d)$$

One obtains, substituting (22a–d) into (19)–(21) and equating the coefficients at α^0, ϵ^0

$$\frac{d\overline{C}_1^0}{dy} + \overline{C}_1^0 \frac{d\overline{\varphi}^0}{dy} = 0 \qquad (23a)$$

$$\frac{d\overline{C}_2^0}{dy} - \overline{C}_2^0 \frac{d\overline{\varphi}^0}{dy} = j^0 \qquad (23b)$$

$$\overline{C}_1^0 = \overline{C}_2^0 \qquad (23c)$$

$$\frac{d}{dy}(\overline{C}_3^0 - \overline{C}_4^0) + (\overline{C}_3^0 + \overline{C}_4^0)\frac{d\overline{\varphi}^0}{dy} = i^0 \qquad (24a)$$

$$\overline{C}_3^0 \overline{C}_4^0 = 1 \qquad (24b)$$

From (23a–c), taking into account (12a–d) and (13), one obtains easily

$$\overline{C}_1 = \overline{C}_2^0 = 1 - \frac{j^0}{2} y \qquad (25a,b)$$

$$\overline{\varphi}^0 = -\ln\left(1 - \frac{j^0}{2} y\right) \qquad (26)$$

Substituting (25a,b) and (26), into (24a) one finds that

$$\frac{d}{dy}(\overline{C}_3^0 - \overline{C}_4^0) + (\overline{C}_3^0 + \overline{C}_4^0)\frac{j^0/2}{1 - \frac{j^0}{2} y} = i^0 \qquad (27)$$

Let us introduce the abbreviation

$$1 - \frac{j^0}{2} y \equiv z \tag{28}$$

and make the substitution

$$\overline{C}_3{}^0 = zu \qquad \overline{C}_4{}^0 = v/z \tag{29a,b}$$

One then obtains from (27) and (24b)

$$\frac{1}{z}\frac{dv}{dz} - z\frac{du}{dz} = 2i' \tag{30a}$$

$$uv = 1 \tag{30b}$$

where

$$i' = i^0/j^0 \tag{30c}$$

From (30a,b) one has

$$u'\left(\frac{1}{zu^2} + z\right) = -2i'$$

and after substituting $z^2 \equiv t$ one obtains

$$\frac{du}{dt} = -\frac{i'u^2}{1 + tu^2} \quad \text{or} \quad \frac{dt}{du} = -\frac{1 + tu^2}{i'u^2} \tag{32}$$

From boundary conditions (12c–d)

$$t|_{u=1} = 1 \tag{33}$$

Solution of (32) with (33) yields

$$\left(1 - \frac{j^0}{2} y\right)^2 = \exp[-u(y)/i'] \left\{ \exp(1/i') - \frac{1}{i'^2} \int_{1/i'}^{u(y)/i} \frac{e^\zeta}{\zeta^2}\, d\zeta \right\} \qquad 0 < y < 1 \tag{34}$$

This determines u and hence $\bar{C}_3{}^0$ and $\bar{C}_4{}^0$ as functions of y and i' everywhere except in the boundary layer of order of thickness ϵ adjacent to the membrane.

In order to determine the solution in the boundary layer, let us introduce a new variable

$$\zeta = (1 - y)/\epsilon \tag{35}$$

In terms of ζ the system (19)–(21) takes the form

$$\frac{dC_1}{d\zeta} + C_1 \frac{d\varphi}{d\zeta} = 0 \tag{36}$$

$$\frac{dC_2}{d\zeta} - C_2 \frac{d\varphi}{d\zeta} = \epsilon J_2 \tag{37}$$

$$C_1 - C_2 = \alpha(C_4 - C_3) \tag{38}$$

$$\frac{d}{d\zeta}(C_3 - C_4) + (C_3 + C_4)\frac{d\varphi}{d\zeta} = -\epsilon I \tag{39}$$

$$\frac{d^2C_3}{d\zeta} + \frac{d}{d\zeta}\left(C_3 \frac{d\varphi}{d\zeta}\right) = C_3C_4 - 1 \tag{40}$$

Again we seek the series solution

$$C_i(\zeta) = \mathbf{C}_1{}^0(\zeta) + \mathbf{C}_{i\alpha}(\zeta)\alpha + \mathbf{C}_{i\epsilon}\epsilon + \ldots \qquad i = 1, 2, 3, 4 \tag{41}$$

$$\varphi(\zeta) = \varphi^0(\zeta) + \varphi_\alpha(\zeta)\alpha + \varphi_\epsilon(\zeta)\epsilon + \ldots \tag{42}$$

These "inner" expansions must satisfy the boundary conditions (14)–(17) on the membrane at each order in α,ϵ and must be matched with the outer expansions (22a,b). Substituting (41) and (42) into (36)–(40) and equating the coefficents at α^0, ϵ^0, we obtain

$$\frac{d\mathbf{C}_1{}^0}{d\zeta} + \mathbf{C}_1 \frac{d\varphi^0}{d\zeta} = 0 \tag{43a}$$

$$\frac{d\mathbf{C}_2{}^0}{d\zeta} - \mathbf{C}_2{}^0 \frac{d\varphi^0}{d\zeta} = 0 \tag{43b}$$

$$\mathbf{C}_1{}^0 = \mathbf{C}_2{}^0 \tag{43c}$$

$$\frac{d}{d\zeta}(\mathbf{C}_3{}^0 - \mathbf{C}_4{}^0) + (\mathbf{C}_3{}^0 + \mathbf{C}_4{}^0)\frac{d\varphi^0}{dy} = 0 \tag{44}$$

$$\frac{d^2\mathbf{C}_3{}^0}{d\zeta^2} + \frac{d}{d\zeta}\left(\mathbf{C}_3{}^0 \frac{d\varphi^0}{d\zeta}\right) = \mathbf{C}_3{}^0\mathbf{C}_4{}^0 - 1 \tag{45}$$

with the boundary conditions

$$\varphi^0|_{\zeta=0-0} = A \tag{46a}$$

$$(\ln \mathbf{C}_2{}^0 - A)|_{\zeta=0-0} = (\ln \mathbf{C}_2{}^0 - \varphi^0)|_{\zeta=0+0} \tag{46b}$$

$$\mathbf{C}_2{}^0|_{\zeta=0-0} = p^* \tag{46c}$$

$$\left(\frac{d}{d\zeta}\mathbf{C}_3{}^0 + \mathbf{C}_3{}^0 \frac{d\varphi^0}{d\zeta}\right)\Big|_{\zeta=0+0} = 0 \tag{47}$$

$$\frac{i^0}{j^0} = \frac{\mathbf{C}_4{}^0}{\mathbf{C}_2{}^0}\Big|_{\zeta=0-0}\theta \tag{48}$$

We conclude that $\mathbf{C}_i{}^0$ $(i = 1, 2, 3, 4)$ and φ^0 are constants that have to be determined from the matching with appropriate terms in the outer expansion. This matching yields

$$\mathbf{C}_1{}^0 = \mathbf{C}_2{}^0 = 1 - \frac{j^0}{2} \tag{49a}$$

$$\varphi^0 = -\ln\left(1 - \frac{j^0}{2}\right) \tag{49b}$$

$$j^0 = 2(1 - e^{(p^* - A)/2}) \tag{50}$$

Furthermore

$$\mathbf{C}_i{}^0 = \overline{C}_i{}^0|_{y=1} \qquad i = 3, 4 \tag{51}$$

$$\frac{i^0}{j^0} = \frac{\mathbf{C}_4{}^0}{1 - (j^0/2)}\theta \tag{52}$$

Thus (34) implies that i^0 can be determined by

$$\frac{1}{\beta^2} = \exp[-\beta^2\theta/i'^2] \left\{ \exp(1/i') - \frac{1}{i'^2} \int_{1/i'}^{\beta^2\theta/i'^2} \frac{e^\zeta}{\zeta^2}\, d\zeta \right\} \tag{53a}$$

Here

$$\beta = \exp[(A - \ln p^*)/2] \tag{53b}$$

Recall, that i^0 is the zeroth order approximation (in α and ϵ) to the dimensionless current carried by the H^+ and OH^- ions. Indeed the construction of the zeroth order approximation has been fully accomplished. This approximation corresponds to the so-called kinetics of diffusional overvoltage with a homogeneous chemical equilibrium implied, according to electrochemical terminology.[10] It is easy to check that the approximation constructed guarantees a matching of algebraic terms in $\mathbf{C}_{i\epsilon}$ $(i = 1, 2, 3, 4)$, φ, with corresponding terms in $\bar{C}_i^0$, $\bar{\varphi}^0$. We are not going to construct $\mathbf{C}_{i\epsilon}$ $(i = 1, 2, 3, 4)$, φ_ϵ, i, explicitly although this can be done in a straightforward way.

Let us emphasize that to any approximation in α in both the inner and outer expansions the system (19)–(21),

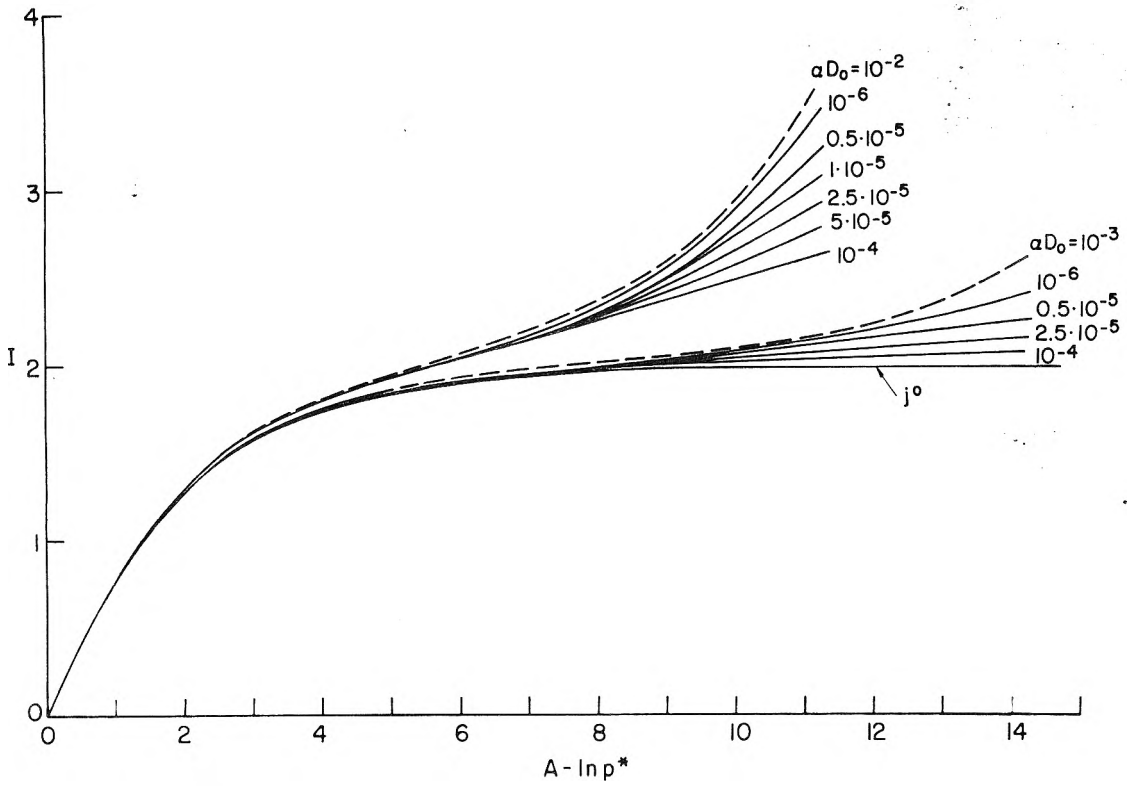

Figure 1. Computed voltage–current curves in terms of dimensionless voltage $A - \ln p^*$ and dimensionless current I: (— 10^{-4}) numerical solution of the exact problem for $\epsilon^2 = 10^{-4}$; (- - -) approximation of diffusion overvoltage.

(12)–(17) splits into two parts. The first part, arising from (19), (20), (12a,b), (13), (14a), (15), (17a,c), describes the transfer of salt ions and determines the electrical potential in the system. To zero order in α the electric potential and the current carried by the salt ions (expressions 25, 26, and 50) conforms with those in a system "without water dissociation". The second part arising from (21a,b), (14b), (16), and (17b) describes the transfer of H^+ and OH^-. We have carried out a singular perturbation procedure in all the system (19a,b), (20), (21a,b), and not in (21a,b) only, in order to avoid an artificial nonuniformity in the inner expansion for C_3, C_4 arising from the behavior of φ at large ζ. If only (21a,b) were perturbed one would have for the potential at zeroth order in α

$$\varphi^0(y) = -\ln\left(1 - \frac{j^0}{2}y\right) \tag{A}$$

This expression would hold everywhere, not only outside a boundary layer of thickness $0(\epsilon)$. After substituting (A) into (21b) one would obtain in terms of $\zeta = (i - y)/\epsilon$, $0 \leq \zeta < \infty$

$$\frac{d^2C_3}{d\zeta^2}(\zeta, \epsilon, \alpha = 0) + \frac{d}{d\zeta}\left[C_3(\zeta, \epsilon, \alpha = 0) \times \frac{j^0/2}{1 - (j^0/2)(1 - \epsilon\zeta)}\right] = C_3C_4 - 1 \tag{B}$$

This equation has a nonuniformity due to the term $\epsilon\zeta$.

Let us return now to expression (21c). It can easily be shown that $j_\epsilon = 0$. Furthermore, taking into consideration that D_4 is about ten times as large as D_2 one can neglect αj_α as compared with $(D_4/D_2)\alpha i^0$. Neglecting quadratic terms, we then find that the current is given by the equation

$$I = j^0 + \alpha\frac{D_2}{D_4}i^0 \tag{54}$$

where j^0 and i^0 are defined by (50) and (53).

Let us now consider the asymptotic behavior of i^0 (A) for large A (which is only of interest for $10^{-6} < \alpha(D_4/D_2) \equiv \alpha D_0 < 10^{-2}$. One can easily show from (53) that for $A \to \infty$ $(\beta \to \infty)$

$$i^0 \approx j^0\theta^{1/2}\exp[(A - \ln p^*)](A - \ln p^*)^{-1/2} \tag{55}$$

Hence from (50) and (52)

$$C_4^0 \approx \frac{1}{C_3^0} \approx \frac{1}{\theta^{1/2}(A - \ln p^*)^{1/2}} \tag{56}$$

In the next section the results predicted by the asymptotic expressions (34), (53), (54), (55), and (56) will be compared with the results of a numerical solution of the system (9)–(17).

Numerical Solution and Discussion

The system (9)–(17) was solved by finite differences using the quasi-linearization method[11] for a sequence of voltages A. As an initial approximation for each new A we took the solution obtained for the previous value of A. The parameters α, ϵ, and θ were widely varied ($10^{-6} < \alpha < 10^{-3}$, $10^{-7} < \epsilon^2 < 4 \times 10^{-4}$, $0.5 < \theta < 10$). In Figure 1 we present two families (for two values of α) of computed voltage–current curves at different values of ϵ. The dashed line corresponds to the zeroth term (54), (55) of the asymptotic expansion (22d) in the limit $A \to \infty$. We see from Figure 1 that the computed voltage–current curves tend to their asymptotic form, defined by (53) as ϵ decreases. However, for realistic values of ϵ^2 between 10^{-5} and 10^{-4}, the asymptotic formula (55) overestimates the current.

Figure 2 show that changing the parameter θ (i.e., altering transport properties within the membrane) does not appreciably affect the form of the computed voltage–current curves. Here formula 55 correctly predicts a shift in i^0 along the A axes.

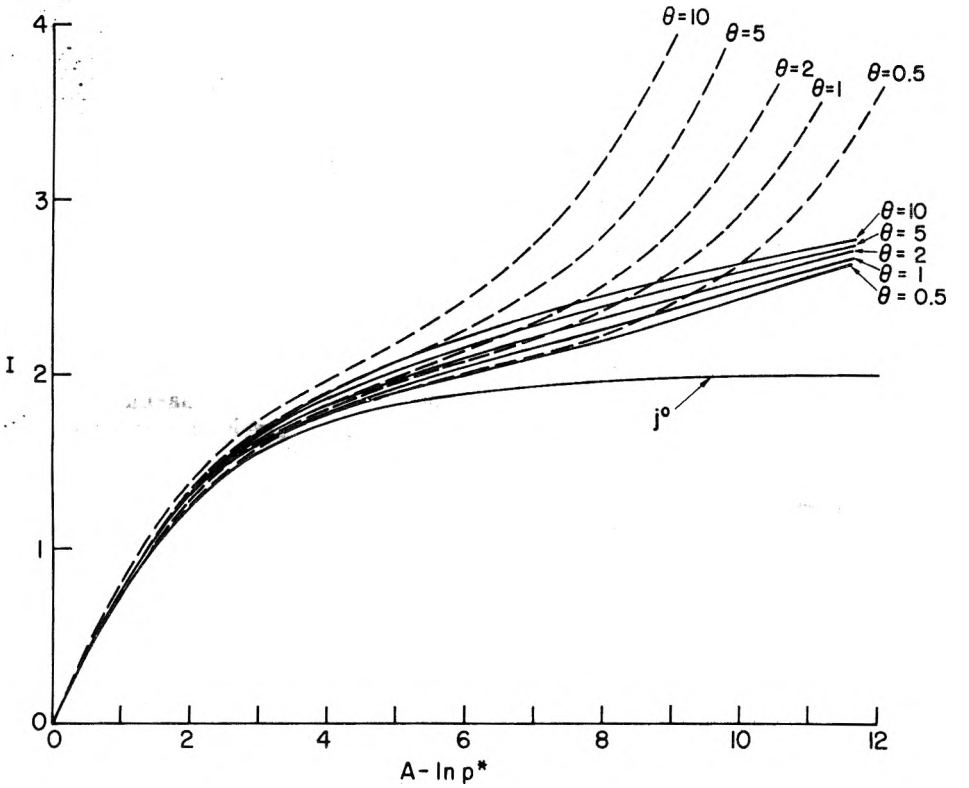

Figure 2. Computed voltage–current curves for different values of the parameter $\theta = (D_4'/D_4)(D_2'D_2)$, characterizing the transport properties of ions within the membrane: (—) numerical solution of the exact problem; (– – –) approximation of diffusion overvoltage.

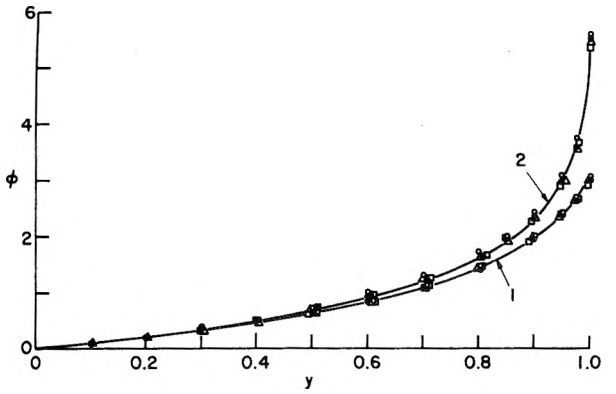

Figure 3. Profiles of dimensionless electric potential within the unstirred layer of different bulk concentration C_0 at two values of dimensionless voltage A: (O) numerical solution, $\alpha = n/C_0 = 10^{-3}$; (●) numerical solution, $\alpha = 10^{-4}$; (□) numerical solution, $\alpha = 10^{-5}$; (Δ) approximation $\varphi = -\ln[1 - (\alpha^2/2)y]$; curve 1 corresponds to $A = 6$; curve 2 corresponds to $A = 11$.

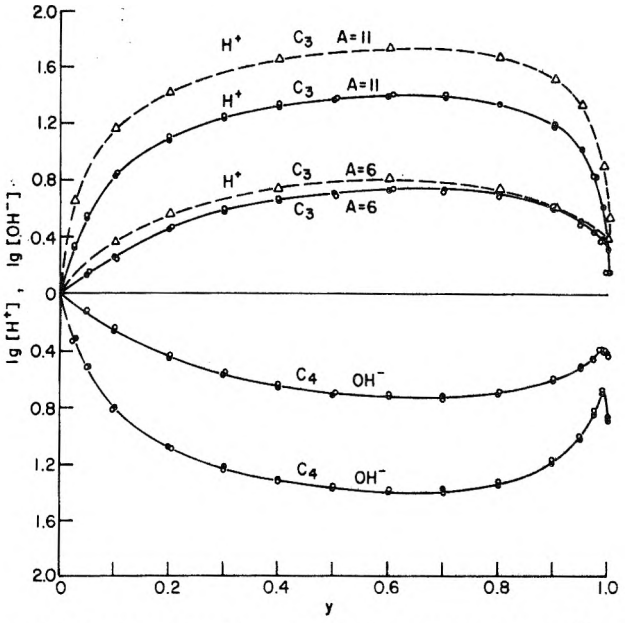

Figure 4. Logaritmic profiles of dimensionless concentration of H^+ and OH^- within the unstirred layer for different bulk concentrations C_0 at two values of dimensionless voltage A: (O) $\alpha = n_0/C_0 = 10^{-3}$; (●) $\alpha = 10^{-4}$; (– Δ –) approximation of diffusion overvoltage.

Let us turn now to considering profiles of electric potential and ion concentration within the unstirred layer. A few characteristic examples of such profiles for different values of the parameter α and of the dimensionless voltage A are presented in Figure 3. The computations show that, even when water splitting is quite extensive, in all the given ranges of α and A the electrical potential within the unstirred layer is determined practically exclusively by the salt ions and can be very well approximated by the expressions 26 and 50. This means that in studies of water splitting one can use as a good approximation the system of equations

$$\epsilon_1^2 \frac{d}{dy}\left[\frac{dC_3}{dy} + C_3\frac{j^0/2}{1-(j^0/2)y}\right] = C_3C_4 - 1 \qquad (57)$$

$$\epsilon_2^2 \frac{d}{dy}\left[\frac{dC_4}{dy} - C_4\frac{j^0/2}{1-(j^0/2)y}\right] = C_3C_4 - 1 \qquad (58)$$

with boundary conditions, (12c,d), (14), (15), (16), and (17a,b), at

$$\varphi = -\ln\left(1 - \frac{j^0}{2}y\right) \qquad C_2 = 1 - \frac{j^0}{2}y$$

$$j^0 = 2\{1 - \exp[(\ln p^* - A)/2]\} \qquad \alpha = 0$$

in them.

Physically our results stem from the fact that because of the high mobility of H^+ and OH^- their contribution to the total current becomes appreciable as the voltage is increased, much earlier than their concentration in the unstirred layer becomes locally comparable with that of

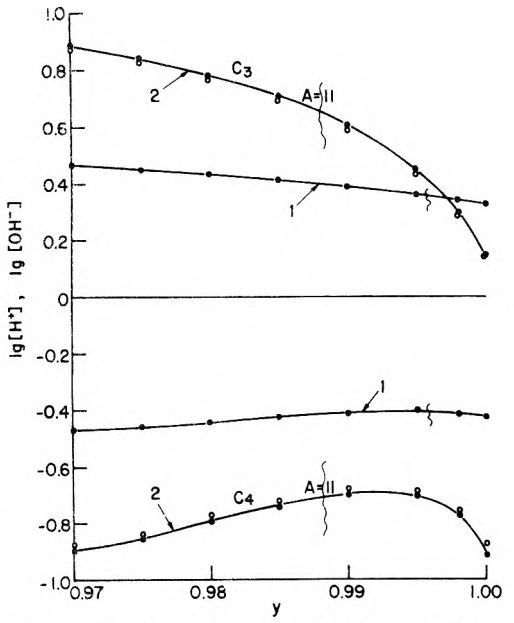

Figure 5. Logaritmic profiles of dimensionless concentration of H^+ and OH^- within the reactive zone: (○) $\alpha = n_0/C_0 = 10^{-3}$; (●) $\alpha = 10^{-4}$; curve 1 corresponds to $A = 6$; curve 2 corresponds to $A = 11$.

the salt. This assertion is affirmed by the data from Figure 4, where we present two families (for two values of the voltage) of H^+, and OH^- concentration profiles, obtained by numerical solution of (9)–(17) at different values of α. The results show that the form of the profiles within the unstirred layer practically does not depend on α and only varies with the applied voltage. In other words, since for the voltage range in question the potential determining ions are those of the salt, the shift of pH in the unstirred layer depends on the voltage (A) only and practically does not depend on the bulk salt concentration (α). In the example in Figure 4, this shift is about 1.4 for $A = 11$ and 0.7 for $A = 6$. At the same time the current efficiency depends very much on α. (See Figure 1).

Note that in most of the unstirred layer (except for a narrow reactive zone) the product C_3C_4 practically equals one. In Figure 4 we present a few profiles computed from the asymptotic formulas (29), and (34). As one can see, these expressions predict in a qualitatively correct way the character of the change in concentrations of H^+ and OH^- in the unstirred layer out of the reactive zone. There is a slowly varying central region in the concentration profiles with a fast initial increase (decrease) and a fast decrease (increase) of the concentration of H^+ (OH^-) near the membrane. It is worthwhile considering in more detail the concentration profiles within the reactive zone. Indeed we see in Figure 5 the non-monotonic character of the change of the OH^- concentration within this zone. This could have been anticipated from the form of the boundary condition (16) for OH^- and from what was said above concerning the potential in our system.

Indeed we have seen that the electric potential within our system in the range of voltages considered can be approximated with high accuracy by the expression

$$\varphi \simeq \ln\left(1 - \frac{j^0}{2}y\right) \tag{59a}$$

similarly

$$C_2 \simeq 1 - \frac{j^0}{2}y \tag{59b}$$

$$j_2 \simeq j^0 < 2 \tag{59c}$$

substituting (59a–c) into (16), (17a,c), one obtains

$$\left.\frac{dC_4}{dy}\right|_{y=1} + C_4|_{y=1}\frac{j^0/2}{1-(j^0/2)} = 0 \tag{59d}$$

and hence

$$\left.\frac{dC_4}{dy}\right|_{y=1} < 0 \tag{60}$$

At the same time one has, according to (34), outside of the reactive zone $dC_4/dy > 0$, for y close enough to 1 (see Figure 4). This means that within the reactive layer there must be at least one maximum in C_4.

Note that there is a reactive zone of considerable extent for $10^{-5} < \epsilon^2 < 10^{-4}$, wherein one cannot speak about any chemical equilibrium for the water ($C_3C_4 \neq 1$). This explains the discrepancy, for these values of ϵ, between the curves obtained by a numerical integration of the system (9)–(17) and those computed from the asymptotic expression (53). That is, although $\epsilon \simeq 10^{-2}$, in this case it is not truly a small parameter.

Conclusions

Summarizing we conclude that for realistic values of parameters ($\alpha < 10^{-3}$) the salt ions are potential determining over a wide range of voltages, in particular deeply within the domain of "water splitting". As a corollary the shift of pH in the unstirred layer is determined by the voltage and does not depend on the bulk concentration of the salt. The efficiency of the current depends strongly on the latter.

Furthermore, one concludes that the approximation of diffusional overvoltage leads, for realistic values of the parameter ϵ ($10^{-5} < \epsilon^2 < 10^{-4}$), to poor quantative results (the current carried by H^+ and OH^- is overestimated). One can, however, use this approximation for certain qualitative estimates in that it gives for realistic ϵ qualitatively reasonable forms for the voltage–current curves and for the H^+ and OH^- concentration profiles out of the reactive zone.

Generally speaking, computations have shown that we are dealing with an essentially intermediate kinetics where the concentration of reacting components on the boundary of the reactive zone is established by diffusion in the presence of a homogeneous chemical equilibrium of the water; on the other hand, this diffusion depends on the course of the reaction in the reactive zone.

Acknowledgment. The author thanks Professors O. Kedem and L. Segel for their advice.

References and Notes

(1) A. M. Peers, *Discuss. Faraday Soc.*, **21**, 124 (1956).
(2) C. Forgues, N. Ishibashi, J. Leibovitz, J. Sinkovic, and K. S. Spiegler, *Desalination*, **10**, 2, 181 (1972).
(3) L. H. Shaffer and M. S. Mintz, "Electrodialysis", in "Principles of Desalination", K. S. Spiegler, Ed., Academic Press, New York, N.Y., 1966, p 199.
(4) C. Forgues, J. Leibovitz, R. O'Brien, and K. S. Spiegler, *Electrochimica*, **20**, 555 (1975).
(5) M. S. Isaakson, M.Sc. Thesis, Massachusetts Institute of Technology, Department of Mechanical Engineering, 1970.
(6) G. Grossman, *J. Phys. Chem.*, **80**, 1625 (1976).
(7) M. Eigen and L. De Maeyer, *Z. Elektrochem.*, 59, 986 (1955).
(8) Y. Toyoshima and M. Nozaki, *J. Phys. Chem.*, **74**, 2704 (1970).
(9) J. Cole, "Perturbation Methods in Applied Mathematics", Blaisdell, Waltham, Mass., 1968, p 27.
(10) K. J. Wetter, "Elektrochemiche Kinetik", Springer-Verlag, Berlin, 1961, p 133.
(11) R. E. Bellman and R. E. Kalaba, "Quasilinearization and Nonlinear Boundary Value Problem", American Elsevier, New York, N.Y., 1965, p 29.

IT'S JUST A MATTER OF TIME

You have a choice. You can spend hours checking out tables of contents, looking for articles of special interest in your field—the ones you must read—or . . . . . you can accomplish the same result in a matter of minutes—by using the ACS SINGLE ARTICLE ANNOUNCEMENT.

Lere's how it works: In the ACS SINGLE ARTICLE ANNOUNCEMENT you'll find are contents pages from the latest issues of all 18 ACS primary journals. Chances are good you'll see several articles that can help you in your work. Just send your order to ACS. We'll see to it that you get the material in a hurry. And the price is low.

Every issue includes an easy-to-use order form to save you even more time.

The ACS SINGLE ARTICLES ANNOUNCEMENT is published twice a month.

Mail the coupon now.

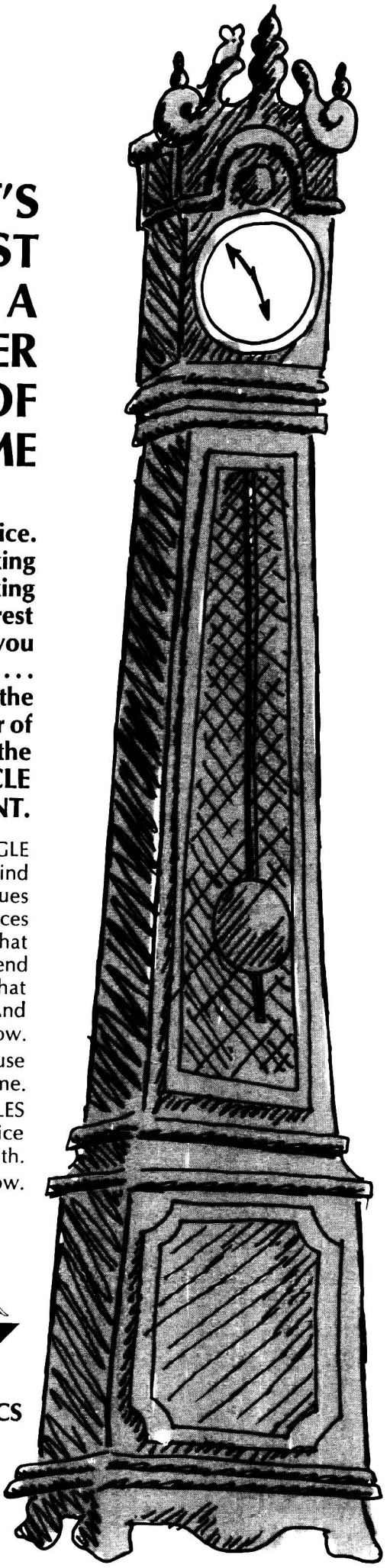

Another service of ACS

18 Participating Journals

- Accounts of Chemical Research
- Analytical Chemistry
- Biochemistry
- Chemical Reviews
- Chemical Technology
- Environmental Science & Technology
- I&EC Fundamentals
- I&EC Process Design and Development
- I&EC Product Research and Development
- Inorganic Chemistry
- Journal of Agricultural and Food Chemistry
- Journal of the American Chemical Society
- Journal of Chemical Information and Computer Sciences
- Journal of Chemical and Engineering Data
- Journal of Medicinal Chemistry
- The Journal of Organic Chemistry
- The Journal of Physical Chemistry
- Macromolecules

SINGLE ARTICLE ANNOUNCEMENT 197
American Chemical Society
1155 Sixteenth Street, N.W.
Washington, D.C. 20036

Yes—I wish to receive the ACS SINGL ARTICLE ANNOUNCEMENT at the one-yea rate checked below:

	U.S.	Canada Foreign	PUAS
ACS Member*	☐ $12.00	☐ $16.50	☐ $16.0
Nonmember	☐ $24.00	☐ $28.50	☐ $28.0

☐ Payment enclosed ☐ Bill me ☐ Bil company ☐ I am an ACS member ☐ am not an ACS member

Air freight rates available on request

Name Position

Address ☐ Home ☐ Business (Specific title please

City State/Country Zip

Journal subscriptions start in January '77.
Allow 90 days for your first copy to be mailed.
*NOTE: Subscriptions at ACS member rates are for personal use only.